Purdue University
Purdue e-Pubs

Open Access Dissertations | Theses and Dissertations

12-2016

Fundamental studies of flame propagation in lean-burn natural gas engines

Zhiyan Wang
Purdue University

Follow this and additional works at: https://docs.lib.purdue.edu/open_access_dissertations

 Part of the Chemical Engineering Commons, and the Mechanical Engineering Commons

Recommended Citation
Wang, Zhiyan, "Fundamental studies of flame propagation in lean-burn natural gas engines" (2016). *Open Access Dissertations*. 1027.
https://docs.lib.purdue.edu/open_access_dissertations/1027

This document has been made available through Purdue e-Pubs, a service of the Purdue University Libraries. Please contact epubs@purdue.edu for additional information.

Graduate School Form
30 Updated 12/26/2015

PURDUE UNIVERSITY
GRADUATE SCHOOL
Thesis/Dissertation Acceptance

This is to certify that the thesis/dissertation prepared

By Zhiyan Wang

Entitled

FUNDAMENTAL STUDIES OF FLAME PROPAGATION IN LEAN-BURN NATURAL GAS ENGINES

For the degree of Doctor of Philosophy

Is approved by the final examining committee:

John Abraham
Chair

Haifeng Wang

Peter H. Meckl

Steven Son

To the best of my knowledge and as understood by the student in the Thesis/Dissertation Agreement, Publication Delay, and Certification Disclaimer (Graduate School Form 32), this thesis/dissertation adheres to the provisions of Purdue University's "Policy of Integrity in Research" and the use of copyright material.

Approved by Major Professor(s): John Abraham

Approved by: Jay P. Gore 10/12/2016

Head of the Departmental Graduate Program Date

FUNDAMENTAL STUDIES OF FLAME PROPAGATION IN LEAN-BURN NATURAL GAS ENGINES

A Dissertation

Submitted to the Faculty

of

Purdue University

by

Zhiyan Wang

In Partial Fulfillment of the

Requirements for the Degree

of

Doctor of Philosophy

December 2016

Purdue University

West Lafayette, Indiana

ACKNOWLEDGMENTS

My utmost thanks and gratitude go to my major advisor, Prof. John Abraham, whose continued support has made this work possible. His words of wisdom and advice have been instrumental to my graduate research and its successful completion. His understanding, encouragement and confidence in me have been invaluable. He has taken every step to nurture my personal as well as professional growth. I am also thankful to him for providing a research environment conducive to independent study.

I would like to extend my gratitude to Professors Peter Meckl, Steven Son and Haifeng Wang for serving on my PhD advisory committee and for providing many valuable feedback on the dissertation. I am grateful to Prof. Vinicio Magi and Dr. Emmanuel Motheau for their contributions to the numerical code employed in this work. Discussions with Prof. Vinicio Magi have greatly improved my understanding of the numerical aspects of the code. I would like to thank Prof. Carlo Scalo for valuable suggestions on the implementation of the feedback control employed in this work, and for providing computational resources.

This research was partly supported by Caterpillar, Inc. Their financial support is gratefully acknowledged. I am also indebted to the Department of Mechanical Engineering at Purdue University for direct financial aid through teaching assistantships. I would like to acknowledge the Rosen Center for Advanced Computing (RCAC) at Purdue University, Extreme Science and Engineering Discovery Environment (XSEDE) at Texas Advanced Computing Center (TACC) and National Computational Infrastructure (NCI), Australia for providing computational resources.

My gratitude goes to my fellow student colleagues, Dr. Muhsin Ameen, May Yen, Anand Jebakumar and Jiacheng Zhang, for their friendship and inspirations. In par-

ticular, I would like to thank Dr. Muhsin Ameen and May Yen for useful discussions and feedback that improved this work.

Last but not least, special thanks to my parents Wenyi Wang and Shaoai Chen, and my girlfriend Xing Ge, whose unconditional support to me served as a driving force in the completion of this work.

TABLE OF CONTENTS

LIST OF TABLES

LIST OF FIGURES

Figure Page

SYMBOLS

Upper-Case Roman

A	area
$\mathrm{A_L}$	laminar flame area
A_{ref}	reference area
$\mathrm{A_T}$	turbulent flame area
B	forcing coefficient
$C_\mu, C_{\epsilon_1}, C_{\epsilon_2}$	constants in the k-ϵ model
C_{EBU}	constant in eddy-break-up model
C_I	constant in the Smagorinsky model
CFL	CFL number
D, D_k	mass diffusivity
D_3	fractal dimension
D_T	turbulent mass diffusivity
Da	Damköhler number
Da_{ign}	ignition Damköhler number
Da_{ext}	extinction Damköhler number
E	total energy
F_i	external force
F_{ij}	Gaussian filter
$F(\vec{x})$	Fávre filter
G	scalar field in level-set equation
$\mathcal{H}^{C-D}_{\Delta t/2}$	integration with convective and diffusion terms over half a time step
$\mathcal{H}^{R}_{\Delta t}$	integration with reaction term over a full time step
$\mathbf{H}$	total curvature

I_o	Efficiency factor
K	flame stretch
$\mathbf{K}$	Gaussian curvature
K_Σ	constant in algebraic model
Ka	Karlovitz number
$\mathcal{L}$	Markstein length
$\mathcal{L}_i$	amplitude of the characteristic wave
Le, Le_k	Lewis number
$\mathrm{L}, \mathrm{L_x}, \mathrm{L_y}, \mathrm{L_z}$	domain length
$\mathrm{L_o}$	turbulence integral length scale
M, Ma	Mach number
P	pressure
P_o, P_{ref}	reference pressure
P_∞	pressure at infinity
$P()$	probability density function
$\mathcal{R}$	universal gas constant
R_{ij}	auto-correlation function
Re	Reynolds number
Re_T	turbulent Reynolds number
Re_L	Reynolds number based on integral scale
Re_λ	Reynolds number based on Taylor microscale
Re_η	Reynolds number based on Kolmogorov scale
$\mathcal{S}$	surface
$\check{\mathrm{S}}_{ij}$	filtered strain rate
$\|\check{\mathrm{S}}\|$	magnitude of filtered strain rate
$\mathrm{S_{GC}}$	global consumption speed
$\mathrm{S_L}$	laminar flame speed
$\mathrm{S_{LC}}$	local consumption speed
$\mathrm{S_{LD}}$	local displacement speed

S_T	Turbulent flame speed
S_d	flame displacement speed
S_n	flame displacement speed due to normal diffusion
S_r	flame displacement speed due to chemical reaction
S_t	flame displacement speed due to tangential diffusion
Sc	Schmidt number
T	temperature
T_o	reference temperature
T_u	temperature of unburnt gas
T_b	temperature of burned gas
T_{ad}	adiabatic flame temperature
T_{peak}	temperature of maximum temperature gradient
T_{eval}	evaluation temperature
T_i	terms in TKE transport equation
U_0	mean inflow velocity
V_f	speed of the mean flame front
V_{in}	mean inflow velocity
W, W_k	molecular weight
Y, Y_k, Y_m	mass fraction
Y_f, Y_F	fuel mass fraction
Y_F^u	fuel mass fraction in the fresh gas
Y_F^b	fuel mass fraction in the burned gas
Y_p	product mass fraction
Y_m^*	equilibrium mass fraction
Z	mixture fraction
Z	enstrophy

Lower-Case Roman

a_N	normal strain rate
a_T	tangential strain rate

c	reaction progress variable
c	speed of sound
c_m	reaction rate-averaged progress variable
c_p	specific heat
c_{st}	stoichiometric progress variable
d_{max}	distance from ignition location to location of peak temperature
e	internal energy
h	enthalpy
h°	entalpy of formation
h	grid spacing
k	wavenumber
k	turbulent kinetic energy
k_o	steady-state turbulent kinetic energy
k_i	constant in integral control loop
k_p	constant in proportional control loop
k_u	turbulent kinetic energy in the unburned mixture
k_b	turbulent kinetic energy in the burned mixture
l_I	turbulence integral length scale
l_k	Kolmogorov length scale
$l_{uu}, l_{vv}, l_{ww}, l_{uv}, l_{uw}, l_{vw}$	integral scale
m	mass
$\mathbf{n}, n_i, n_j$	flame surface normal direction
t	time
p	pressure
p_0	thermodynamic part of pressure
p_1	hydrodynamic part of pressure
u, u_i, u_j	velocity in the Cartesian coordinate direction
u'	velocity fluctuation

u_{rms}	root-mean-square velocity
w	flame front propagation speed
x_f	location of the mean flame front
x_i	distance in the Cartesian coordinate direction
x_{slice}	location of slicing

Upper-Case Greek

Δ	filter width
Δ	sampling width
Δ_t	time step
$\Delta_x, \Delta_y, \Delta_z$	grid spacing
$\dot{\Omega}$	burning rate per unit flame area
Σ	flame surface density
Σ_{SGS}	subgrid-scale flame surface density
Ξ	sensible energy per unit mass

Lower-Case Greek

α	molecular thermal diffusivity
χ	scalar dissipation rate
χ_{st}	stoichiometric scalar dissipation rate
δ	mixing layer thickness
δ_{ij}	Dirac delta function
δ_L, δ_f	laminar flame thickness
δ_T	turbulent flame brush thickness
ϵ	turbulent dissipation rate
ϵ_i	inner cut-off length
η	Kolmogorov length scale
γ	specific heat ratio
γ	skewness
κ	curvature
κ_1, κ_2	principal curvatures

κ_m	mean curvature
λ	thermal conductivity
λ_1	most extensive principal strain rate
λ_2	intermediate principal strain rate
λ_3	most compressive principal strain rate
λ_i	velocity of the characteristic wave
μ	dynamic viscosity
ν	kinematic viscosity
ν_T	turbulent viscosity
$\dot{\omega}$	reaction rate
$\dot{\omega}_F$	fuel reaction rate
$\vec{\omega}$	vorticity
ϕ	equivalence ratio
ρ	density
σ	standard deviation
$\sigma_k, \sigma_\epsilon$	constants in the k-ϵ model
τ	temperature rise coefficient
τ_{ij}	stress tensor
τ_T	turbulence time scale
τ_o	eddy turnover time
τ_c	chemsitry time scale
τ_f	flame time scale
τ_η	Kolmogorov time scale
τ_{ig}	time to autoignition
τ_{max}	time to attain peak temperature
τ_{st}	time to steady flame propagation
τ_{prop}	total time required for steady flame propagation
τ_i	time interval of integral feedback
τ_p	time interval of proportional feedback

ξ	coordinate of uniform grid space
ξ_1	most extensive principal strain rate direction
ξ_2	intermediate principal strain rate direction
ξ_3	most compressive principal strain rate direction
ζ_t	constant in Adams-Bashforth scheme

Symbols

$\sim$	Fávre mean
$\bar{}$	mean
$''$	Fávre fluctuation
$\langle \vert \rangle$	conditional mean
$\langle \rangle_s$	average on the flame surface
$'$	first derivative
$''$	second derivative
$\cdot$	rate of change
$*$	density-weighted

ABBREVIATIONS

AB	Adams-Bashforth
BMEP	brake mean effective pressure
BML	Bray-Moss-Libby
CFL	Courant-Friederichs-Lewey
CFM	coherent flame modeling
CI	compression-ignited
CN	cetane number
CO	carbon monoxide
COV	coefficient of variation
CTC	characteristic time combustion
DNS	direct numerical simulation
EIA	Energy Information Administration
FFT	fast Fourier transform
FLEDS	flow large-eddy and direct-simulations
FSD	flame surface density
HCCI	homogeneous change compression ignition
HOLOMAC	high-order low-Mach combustion
HPC	high performance computing
HRR	heat release rate
IMEP	indicated mean effective pressure
JPDF	joint probability density function
LECT	local equilibrium characteristic time
LES	large-eddy simulation
LODI	local one-dimensional inviscid
LTC	low temperature combustion

MIE	minimum ignition energy
MPI	message passing interface
NO_x	nitric oxides
NSCBC	Navier-Stokes characteristic boundary condition
NTC	negative temperature coefficient
OH	hydroxyl
PDF	probability density function
PM	particulate matter
RANS	Reynolds-averaged Navier-Stokes
RK	Runge-Kutta
RKC	Runge-Kutta-Chebyshev
SGS	subgrid-scale
SI	spark-ignited
Tcf	trillion cubic feet
TDC	top-dead-center
TDMA	tri-diagonal matrix algorithm
TFC	turbulent flame closure
TRZ	thin reaction zone
UHC	unburned hydrocarbon

ABSTRACT

Wang, Zhiyan PhD, Purdue University, December 2016. Fundamental Studies of Flame Propagation in Lean-Burn Natural Gas Engines. Major Professor: John Abraham, School of Mechanical Engineering.

Lean-burn natural gas engines offer enhanced thermal efficiencies and reduced soot and NOx emissions. However, cycle-to-cycle variability in combustion that can result from unreliable ignition, variability in equivalence ratio and quenching is a challenge. Reliability of ignition can be improved by employing a dual-fuel ignition strategy in which a small quantity of diesel fuel is injected to initiate ignition. Computational studies of n-heptane/methane-air mixing layers are performed to provide insight into the fundamental physics of dual-fuel ignition. The results show that the characteristic time required for steady premixed flame propagation has three components: time for autoignition to occur, time for peak temperature to be achieved following autoignition, and time for steady flame propagation in the premixed fuel/air mixture to be achieved. The autoignition time correlates well with pressure and temperature of the unburned premixed charge. The time to achieve peak temperature is relatively short, but correlates with mixing layer thickness and premixed equivalence ratio. The time to achieve steady propagation correlates with mixing layer thickness and laminar flame speed and thickness.

Subsequent work focuses on turbulent flame propagation in lean homogeneous mixtures by employing direct numerical simulations (DNS) under conditions that are relevant to lean-burn engines. Attention is specifically focused on the turbulent flame speed (S_T) as a parameter of interest because of its importance in modeling combustion in engines. The studies are carried out in the thin reaction zone (TRZ) regime of turbulent premixed combustion. Normalized turbulence intensity (u_{rms}/S_L) varies from 2 to 25 and the ratio of integral length scale to flame thickness (L_o/δ_L)

varies from 3.2 to 12.8. Initial studies show that the normalized turbulent flame speed (S_T/S_L) depends on more parameters than u_{rms}/S_L suggested by some models.

Although it is known that the turbulent flame speed varies with equivalence ratio (ϕ), it is shown that the normalized turbulent flame speed does not change with ϕ provided the Karlovitz (Ka) and Damköhler (Da) numbers are fixed. This suggests that Ka and/or Da are important parameters in characterizing the turbulent flame speed. Furthermore, S_T/S_L can be related to the flame area enhancement A_T/A_L and an efficiency factor I_o which is close to unity. A_T/A_L is raised by increasing turbulent Reynolds number Re_T and by reducing Ka. Increasing Re_T leads to a broader spectrum of turbulent eddies that generate flame surface area. Increasing Ka results in fine wrinkling at the expense of larger scale wrinkling. This results in a net reduction in the effective surface area enhancement. Based on these insights, a correlation for S_T that shows a dependence on Re_T and Ka is proposed. Modeling of the Flame Surface Density (FSD) evolution is also considered. FSD is influenced by tangential strain rate and flame displacement speed. Surface averaged tangential strain rate is found to scale linearly with Ka. The effects of Ka on flame displacement speed are modeled using a Probability Density Function (PDF) based approach.

The effects of premixed combustion on turbulence are investigated. For flames in the TRZ regime, the turbulence kinetic energy (TKE) decays monotonically across the flame brush. Scaling analyses of the terms in the transport equation of TKE reveal that viscous dissipation is the dominant contribution in the TKE equation. The relative importance of the other terms in the TKE equation decreases with increasing Ka.

1. INTRODUCTION

1.1 Background and Motivation

In recent years, natural gas has gained increased attention in the United States for use as an alternative fuel in internal combustion engines for ground transportation and power generation applications. According to the U.S. Energy Information Administration (EIA), total dry natural gas production in the United States has increased by 35% from 2005 to 2013 while the share of natural gas consumption as a fraction of gross national energy consumption has risen from 23% to 28% [1]. This is in part due to the fact that natural gas is domestically abundant. U.S. total proved reserves of dry natural gas equaled a record high of 338 trillion cubic feet (Tcf) while 1,932 Tcf of undiscovered technically-recoverable resources of dry natural gas have been identified as of January 2012 [1]. Based on the current consumption rate, this will fulfill the demands for the next 87 years.

Other factors to consider include the fact that increasing utilization of domestically produced natural gas helps to strengthen national energy security as it weans of dependence on imported energy resources. In addition, natural gas has less impact on the environment than other fossil fuels, producing 29% less greenhouse emissions than petroleum-based fuels and 44% less than coal [1]. Natural gas combustion also produces low smoke and particulate matter and its contribution to smog formation is minimal compared with gasoline and diesel [1].

Burning natural gas at lean conditions in engines is particularly attractive as it reduces in-cylinder temperature which results in reduced nitric oxides (NO_x). Lean burn also results in enhanced thermal efficiency and reduced soot emissions [2]. However, operating at lean-burn conditions poses several challenges. Misfire is more likely, and beyond a certain limit, lean conditions generate increased unburned hydrocarbon

(UHC) and carbon monoxide (CO) emissions. Furthermore, cycle-to-cycle variations are greater and combustion phasing is more difficult to control with lean combustion [2, 3]. Therefore, optimization of lean-burn engines is critical. In this work, we aim to provide a better fundamental understanding of natural gas combustion under lean engine-like environments.

An important consideration in the fundamental study of natural gas combustion is the composition of the fuel. Natural gas is a naturally occurring fossil fuel that can be found in the subsurface of earth trapped in porous rock formation. Its composition is variable. Table 1.1 presents the volumetric composition of natural gas from various sources (identified as Gas 1, 2, 3, and 4). Although the composition of natural gas varies from place to place, its properties are generally approximated to be similar to those of methane which is its primary constituent [4]. Consequently, methane has been conveniently adopted as a surrogate for natural gas fuel in the combustion research community.

1.2 Lean-Burn Natural Gas Engines

To achieve optimal fuel economy and meet the stringent government emission regulations, natural gas engines are often operated at the lean misfire limit [9]. NO_x formation which is temperature-sensitive can be reduced as a result of lower combustion temperature. The presence of excess oxygen in the exhaust allows for oxidation catalyst to be applied to oxidize CO and UHC existing in the tailpipe. However, lean-burn in engines poses several challenges, of which the most significant is the increased cycle-to-cycle variations [2] which results in "rough" engine operation and reduced efficiency. Furthermore, greater cyclic variations have adverse effects on CO, UHC and NO_x emissions [10]. Figure 1.1 plots the coefficient of variation (COV) in indicated mean effective pressure (IMEP) in engines running on gasoline and natural gas at 2100 rpm and brake mean effective pressure (BMEP) of 250 kPa. It can be

Table 1.1. Composition of natural gas at various sources.

Component in %	Gas1	Gas 2	Gas 3	Gas 4
Methane	87.0–96.0	83.96–94.80	70–90	92.7
Ethane	1.5–5.1	3.03–5.72		4.34
Propane	0.1–1.5	0.58–1.07	0–20	0.93
iso-Butane	0.01–0.3	0.09-0.10		0.29
n-Butane	0.01–0.3	0.11–0.13		
Nitrogen	0.7–5.6	0.56–6.05	0–5	1.12
Carbon	0.1–1.0	0.65–1.40	0–8	0.54
Oxygen	0.01–0.1	0–1.53	0–0.2	0.00
Source	Western Canada	Continental US	World data	Continental US
Reference	[5]	[6]	[7]	[8]

seen that when natural gas is inducted into the intake manifold using a mixer, the COV in IMEP remains small at 4% as long as the mixture equivalence ratio is larger than 0.7. However, as the mixture equivalence ratio is lowered below 0.7, the COV in IMEP increases significantly. It is believed that COV larger than 10% would affect the operation of the vehicle [11]. It is interesting to note that lower COV is observed if natural gas is injected as opposed to being inducted into the cylinder. This is because direct injection allows for a more precise control over the distribution of fuel-air ratio thereby enhancing stability [12, 13].

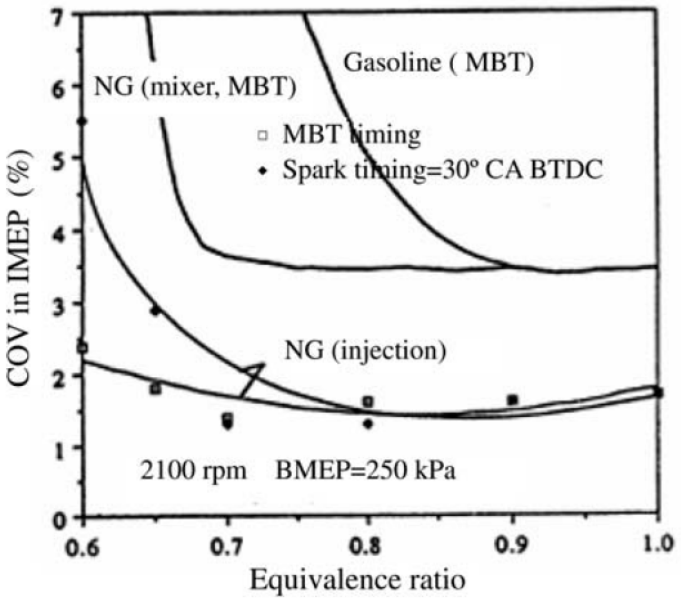

Figure 1.1. Coefficient of variation (COV) over a range of equivalence ratio [14].

Cycle-to-cycle variations are largely due to combustion variations resulting from the slow burning velocities accentuated especially under lean conditions. One way to address the issue is by adding hydrogen to the natural gas. Hydrogen with its higher burning velocity will increase the mixture flame speed [15] and this is most effective in the early stage of flame development from spark ignition. Hydrogen blending also contributes to higher burning speed through the addition of hydrogen and hydroxyl (OH) radicals which enhance overall reactivity [16].

Another way to promote burning rate and hence reduce variability is by increasing turbulence. This can be achieved in several ways. Sakurai *et al.* (1993) [17] tested various combustion chamber geometries and found that by placing two dents on the piston head, dual swirling flows are formed during the intake stroke and they subsequently interact with each other and break down during compression stroke to generate turbulence. Evans (1992) [18] introduced the chamber design that forces the working fluid through narrow exit channels at top-dead-center as a series of "squish-jets" which generate high levels of turbulence. Johansson and Olsson (1995) [19] found that a combustion chamber with a square cross-section results in the fastest combustion. It is well known that moderate levels of turbulence will enhance the local diffusion of heat as well as radical species and hence accelerating the global reaction rate. On the other hand, extremely high turbulence can result in local extinction due to high strain rate. Understanding the effects of flow turbulence on flame propagation will be one of the objectives of this work.

1.3 Dual-Fuel Compression-Ignited Natural Gas Engines

Natural gas can be utilized in both spark-ignited (SI) engines where combustion is initiated through energy deposition from a spark plug, and compression-ignited (CI) engines where combustion is achieved by autoignition of fuel at high pressure and temperature. Reddy (2011) [20] and Chen (2009) [21] have extensively studied ignition/extinction characteristics of premixed natural gas flames in their doctoral dissertations. Specifically, they have characterized the minimum ignition energy (MIE) as a function of flame and turbulence parameters and examined ignition kernel development under the influence of turbulence. Their studies are of relevance to spark-ignited engines. In the current work, combustion initiated by autoignition will also be studied.

Since methane, the primary constituent of natural gas, has a cetane number (CN) that is much lower than petroleum-based fuels [3], natural gas does not ignite spon-

taneously for typical engine compression ratios. In general, this is an advantage since higher compression ratios which lead to higher efficiency can be employed in natural gas engines. However, this property makes it challenging to auto-ignite the mixture. This challenge can be overcome by employing a dual-fuel ignition strategy [22]. In this approach, a pilot quantity of a high CN fuel (e.g., diesel) is directly injected into the combustion chamber that is filled with natural gas/air mixture introduced through the port. After the initial ignition delay, the pilot fuel will auto-ignite generating ignition kernels from which flames will propagate. Multiple kernels can accelerate the overall combustion process.

Extensive experimental studies have been carried out with lean-burn natural gas engines operating in dual-fuel mode. The results have shown that dual-fuel operation can effectively reduce NO_x and particulate matter (PM) emissions while maintaining a competitive thermal efficiency over a range of load conditions compared with conventional SI and CI engines [22, 23, 24, 25, 26, 27]. Furthermore, the formation of multiple ignition kernels and thereby faster burning rate [3] reduces cycle-to-cycle variation of dual-fuel engines to levels that are similar to those of conventional CI engines with approximately 1% of COV in IMEP [28]. While dual-fuel engines can attain thermal efficiencies comparable to those of normal CI engines at high loads [29, 30], it suffers at part-load conditions. This happens because the pilot fuel may fail to ignite the lean premixed natural gas-air charge. Hence, understanding how flame develops and propagates in the dual-fuel mixture is important. This motivates the work in this thesis.

1.4 Objectives of the Work

In this work, computational studies will be carried out to investigate flame propagation in lean-burn mixtures under conditions of relevance to lean-burn natural gas engines. The studies will be relevant to dual-fuel engines and conventionally ignited engines. In the case of the studies relevant to dual-fuel engines, n-heptane will be

used as a surrogate for diesel and methane for natural gas. The specific objectives are the following:

1. To understand the differences in autoignition behavior in dual-fuel and single-fuel mixtures.

2. To investigate the influence of thermodynamic quantities and fuel-air ratio on flame development following autoignition in dual-fuel mixtures.

3. To establish the fundamental physics of turbulent flame propagation in lean mixtures.

The insight gained from this work can be applied, in future work, to the design of reliable and robust multi-dimensional engine simulation tools.

1.5 Thesis Outline

Chapter 2 provides a review of prior work relevant to these studies. This will include a review of studies on dual-fuel combustion in natural gas engines. While fundamental studies on autoignition in dual fuel mixtures are virtually non-existent, existing engine studies and an understanding of autoignition, in general, will be integrated to provide insights into autoignition when a pilot fuel of a high cetane number fuel is employed to autoignite natural gas. The existing understanding of turbulent flame propagation in homogeneous fuel/air mixtures will be discussed through a review of the literature. Existing turbulent flame speed correlations will also be presented. The wide variability in the predictions of these correlations will be highlighted.

In Chapter 3, the computational tools employed in the present work will be described. In particular, two numerical codes are used: one for fully compressible flows and the other for weakly compressible flows. The set of conservation equation being solved by the codes will be presented and various numerical schemes will be discussed.

Chapter 4 presents the results of studies on autoignition and flame development in n-heptane/methane-air dual fuel mixtures under typical engine environments. A correlation for the characteristic time required to reach steady flame propagation without the influence of turbulence will be established.

In Chapter 5, a computational methodology to simulate statistically-stationary turbulent premixed flames in an inflow/outflow configuration will be developed and evaluated. A technique for synthesizing pseudo-turbulent flow fields will be described. Generation of homogeneous isotropic turbulence using linear forcing will also be discussed.

Chapter 6 presents simulation results of turbulent flame speed in lean premixed mixtures over a range of turbulence intensities using a 2-dimensional (2D) setup. Different combustion regimes and controlling physical parameters will be discussed.

Chapter 7 presents 3-dimensional (3D) DNS studies of lean premixed flames over a range of equivalence ratios. The effects of equivalence ratio on turbulent flame speed will be discussed.

In Chapter 8, 3D DNS studies of lean premixed flames with parametric variation of turbulence intensities and length scales are presented. The dependencies of turbulent flame speeds will be discussed and a correlation will be formulated.

Chapter 9 presents the studies on the evolution of flame surface area. The effects of Karlovitz number on the tangential strain and surface propagation will be discussed. Model implications will also be considered.

Chapter 10 discusses the effects of premixed flame on turbulence. The transport equation of turbulent kinetic energy will be examined. The influence of Karlovitz number on the terms in the transport equation will be discussed.

Chapter 11 presents the summary and conclusions from this thesis. Directions for future work are considered.

2. LITERATURE REVIEW

2.1 Introduction

The dual-fuel natural gas engine utilizes lean homogeneous primary gaseous fuel/air mixture but combustion is initiated by injecting a pilot quantity of liquid fuel, usually diesel fuel, which self-ignites. Thus it combines features of both spark-ignition (SI) and compression-ignition (CI) combustion. During the compression process, local temperature inhomogeneity in the premixed charge results in different heat capacities throughout the combustion chamber. Ignition of the pilot fuel is initiated in the hotter zones [31]. The flame kernel growth following ignition is considered to be primarily controlled by the chemical kinetics of the mixture and little influenced by turbulence [32]. In the case of the dual fuel engine, multiple ignition fronts develop and merge with one another forming a flame front. As the front propagates farther into the homogeneous charge, the influence of the pilot fuel diminishes and the flame front transitions into a steady premixed turbulent flame. Therefore, dual-fuel combustion is a multi-faceted phenomenon which includes aspects of chemical kinetics, transient ignition and flame development, and fully-developed turbulent flame propagation.

In order to gain a better understanding of dual-fuel ignition and more generally turbulent flame propagation in premixed charges, a comprehensive literature review will be provided in this chapter. In Section 2.2, we will summarize the autoignition characteristics of inhomogeneous n-heptane/air mixtures. The effects of scalar dissipation rate on the ignition delay will be reviewed. Existing studies on ignition process in dual-fuel diesel/natural gas engines will be discussed in Section 2.3. It will be shown that the interactions between the pilot fuel, i.e., diesel, and the primary fuel, i.e., natural gas, plays a non-trivial role in the ignition process. In Section 2.4, the method of simulating reacting flows using Reynolds-averaged Navier-Stokes (RANS)

simulations and large-eddy simulations (LES) will be briefly outlined. Section 2.5 will provide a review of various groups of models for simulating premixed combustion, particularly the interactions between chemistry and turbulence. Section 2.6 will discuss the significance of the "turbulent flame speed concept" and discuss correlations for the speed from the literature. Section 2.7 will be dedicated to the most recent progress in premixed combustion research using direct numerical simulations (DNS). The chapter closes with a summary in Section 2.8.

2.2 Non-Premixed Ignition Fundamentals

In this section, we will present some basics of n-heptane autoignition in laminar non-premixed mixtures. The most widely studied configuration for this type of problem is the counterflow diffusion flame formed when an oxidizing stream impinges on a fuel stream. Liñán (1974) [33] analyzed the structure of the counterflow flame using asymptotic analysis. He noted that a critical strain rate exists below which a low temperature non-energetic state, referred to as the "froze" state, will not exist. This implies that autoignition can take place when Damköhler number (Da), which is defined as the ratio of mixing timescale and chemical timescale, exceeds a certain threshold Da_{ign}. On the other hand, quenching will occur when strain rate is too high or equivalently when Da is below a critical value, i.e., $Da < Da_{ext}$. This is famously described by the S-shaped curve of maximum temperature to Damköhler number as shown in Fig. 2.1 [33]. Interestingly the critical Da for ignition is higher than that for quenching. As a result, there exists a branch, indicated by the dash line, where a solution does not exist, i.e., the solution "jumps" from one state to the other when critical condition is reached.

The autoignition characteristics of n-heptane/air mixture under engine combustion conditions have been investigated using a single-pulse high-pressure shock tube [34]. The band emission traces of CH were registered and the state behind the reflected shock wave were measured. The influence of initial pressure and temperature

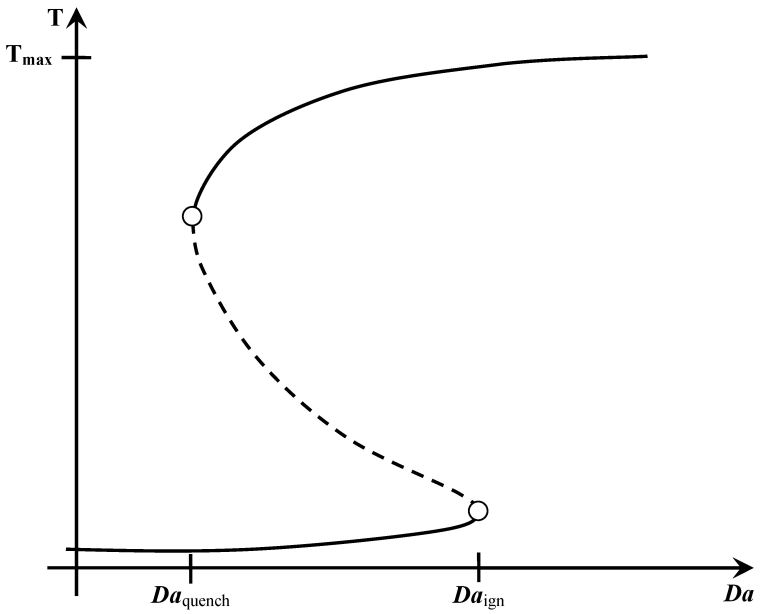

Figure 2.1. S-shaped curve describing the autoignition and quenching behavior dependence on critical Damköhler number.

and the equivalence ratios on ignition delay was studied. The range of initial pressure was between 3.2 and 42 bar. It was found that in the intermediate temperature range where the initial temperature is between 700 K and 950 K, ignition delay increases with increasing temperature. This so-called "negative temperature coefficient" (NTC) in an intermediate temperature range is due to the transition from a low-temperature kinetics dominated regime to a high-temperature kinetics regime. Equivalence ratio has little effect on ignition delay in the high-temperature region, i.e., T $>$ 950 K. In the intermediate temperature region, the shortest ignition delay is observed in the fuel rich mixture whereas in the low-temperature region, i.e., T $<$ 700 K, ignition is the fastest in the stoichiometric mixture.

A two-stage ignition process which transitions from "mild" to "strong ignition" is reflected in n-heptane autoignition. This process is illustrated in Fig. 2.2 for autoignition inside n-heptane/air mixing layer initially at 900 K and pressure of 40 bar. During the first stage of ignition which occurs just before 0.1 ms, the peak temperature in the mixture increases by approximately 200 K above the initial temperature.

The second stage ignition, i.e., the "strong ignition" does not follow immediately after the "mild" ignition, but occurs at 0.17 ms. Similar trends have been reported in other experimental studies of n-heptane oxidation which employ jet-stirred reactors [35, 36], rapid compression machines [37, 38], test engines [39, 40, 41], plug flow reactors [42, 43] and jet-stirred flow reactors [44].

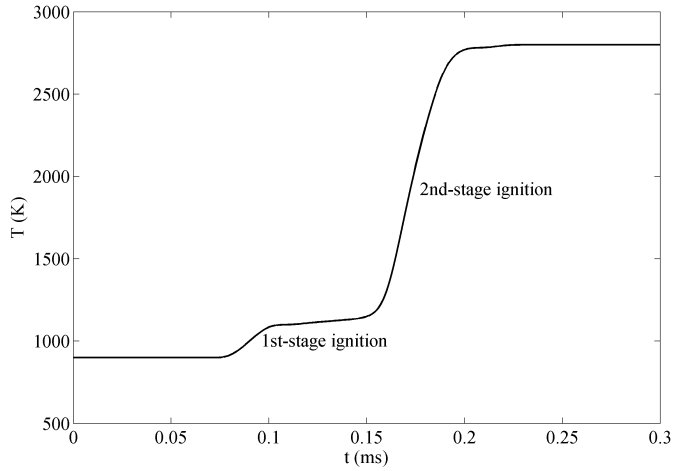

Figure 2.2. Evolution of peak temperature inside n-heptane/air mixing layers initially at 900 K at pressure of 40 bar displaying two-stage ignition characteristics.

Based on the available experimental data, detailed and reduced kinetic mechanisms have been developed to model n-heptane oxidation. Curran *et al.* (1998) [42] developed a detailed chemical kinetic model for n-heptane oxidation and validated its behavior against experiments data. Seiser *et al.* (2000) [45] developed a reduced mechanism consisting of 159 species and 770 elementary reactions and Peters *et al.* (2002) [46] has performed further reduction and derived a 30-step mechanism. Maroteaux and Noel (2006) [47] developed a 61-step and a 26-step reduced mechanism. Yoo *et al.* (2011) [48] developed a 88-species skeletal mechanism for n-heptane oxidation that is suitable for homogeneous charge compression ignition (HCCI) engine conditions.

The effects of steady strain on the autoignition of n-heptane have been studied numerically using a counterflow configuration at high pressure (P = 40 bar) conditions by Liu *et al.* (2004) [49]. They found that when the scalar dissipation rate defined as

$$\chi = 2D(\frac{\partial Z}{\partial x})^2 \tag{2.1}$$

where D is the thermal diffusivity and Z is the mixture fraction, increases, the ignition delay also increases in all temperature regimes, i.e., low-, intermediate- and high-temperature regimes, defined above. This is because the spatial gradients present in the counterflow configuration act as a diffusive term in the energy conservation equation, and hence inhibit the evolution of temperature towards thermal runaway. When the diffusion is sufficiently large to counterbalance the heat generation due to chemical kinetics, ignition cannot occur at all. In addition, the second stage of the two-stage ignition is found to be more susceptible to the scalar dissipation rate [50]. In the case where the temperature of the fuel stream is lower than that of the oxidizer as is common in direct-injected engines, ignition delay is further delayed because of the additional temperature gradient. Bansal *et al.* (2009) [51] have investigated the effects of unsteady strain rate on the ignition delay in non-premixed n-heptane/air mixtures. Oscillatory scalar dissipation rates were imposed by time-varying the velocities of the fuel and air streams in the counterflow configuration. It was found that for a two-stage ignition, ignition delay is positively correlated with mean scalar dissipation rate for frequencies less than 650 Hz. At intermediate frequencies, ignition becomes highly unsteady. At even higher frequencies ($>$ 1700 Hz), the system becomes quasi-steady as the ignition kernel no longer responds to the rapid unsteady fluctuations in the scalar dissipation rate. The positive correlation of ignition delay with scalar dissipation rate is regained.

Autoignition in non-strained laminar n-heptane/air mixing layers has also been studied by many groups. Mastorakos *et al.* (1997) [52] performed 2-D direct numerical simulations of laminar and turbulent mixing layers using a global chemistry mechanism and observed that ignition delay decreases with increase in initial mixing layer thickness at high temperatures (1000–1200 K). Pitsch and Peters (1998) [53]

numerically investigated ignition under conditions relevant to diesel engines using reduced n-heptane chemistry. They concluded that increasing scalar dissipation rate χ, as a result of reducing diffusion layer thickness, would delay ignition. Gopalakrishnan and Abraham (2002) [54] carried out numerical computations of ignition in a diesel spray in a constant volume chamber using n-heptane as a surrogate for the fuel. They found that ignition always occurs in the rich mixture of equivalence ratio around 3.0 and downstream of the maximum penetration of the liquid drops. The exact location of ignition depends on a set of variables including local equivalence ratio, scalar dissipation rate and mixture temperature. Gopalakrishnan and Abraham (2004) [55] also evaluated the role of differential diffusion in n-heptane ignition numerically using a 1-D setup. They found that the unity Lewis number assumption in general overpredicts the ignition delay in contrast to the cases where multi-component transport models are employed, and it is most accurate under conditions where ignition delay is relatively short.

Mukhopadhyay and Abraham (2011) [50] investigated the influence of compositional and thermal stratification in 1-D laminar mixing layers on the ignition characteristics under high pressure and temperature conditions relevant to conventional and low temperature combustion (LTC) engines. They found that for high gradients, ignition is delayed by increasing gradients which is consistent with prior work. However, when the gradients are small, ignition is facilitated by increasing gradients. This effect was accounted for by the fact that upon ignition, an "ignition front" propagates from the initial ignition location in the rich mixture to the stabilization location near stoichiometric point. This shift of ignition front, i.e., the location of peak heat release rate, reflects fundamental changes in the mode of chemical kinetics, e.g., switching from a chain-branching to a thermal explosion mode [56]. In the case of low gradients, the physical distance from the ignition location to the stabilization location is large and propagation time becomes the limiting factor. Consequently increasing stratification reduces the distance and hence, the time to reach the stable flame condition.

In summary, n-heptane autoignition in non-premixed laminar flows has been extensively studied both experimentally and numerically. Two stage ignition has been observed and an NTC regime exists where ignition delay is negatively correlated with temperature. Increasing scalar dissipation rate retards ignition in general and a critical strain rate exists beyond which ignition cannot occur. In unstrained laminar mixing layers, the initial location of autoignition in the mixture fraction space has been characterized and found to be always in the rich mixtures. An "ignition front" is then formed and it propagates to the stabilization location. This understanding of ignition is important in dual-fuel engines where direct injection of diesel fuel and its autoignition is employed to ignite the fuel/air mixture in the chamber.

2.3 Dual-Fuel Engine Ignition

While performance and emission characteristics of dual-fuel natural gas engines with diesel injection have been extensively studied using experiments [22, 24, 25, 26, 27, 57, 58, 59], there is limited work in the literature discussing the ignition behavior of dual-fuel mixtures. The dual-fuel combustion system essentially features a homogeneous natural gas-air mixture compressed below its autoignition conditions, and ignited by the injection of pilot fuel near the top-dead-center (TDC) position. Karim (2003) [23] characterized the combustion heat release rate as a combination of three overlapping components: (1) energy release due to the combustion of the pilot fuel, (2) that due to the combustion of primary fuel in the close vicinity of ignition kernels of the pilot and (3) subsequent turbulent flame propagation through the homogeneous mixture. Figure 2.3 shows the schematic representation of the three components in a dual-fuel engine at high load conditions.

Although the injected pilot fuel only contributed to a small fraction (less than 10%) of the total heat released [22], it can bring about substantial speedup of the overall rates of combustion. This is illustrated using a constant volume chamber in which premixed n-heptane/methane/air mixture of varying compositions is initially

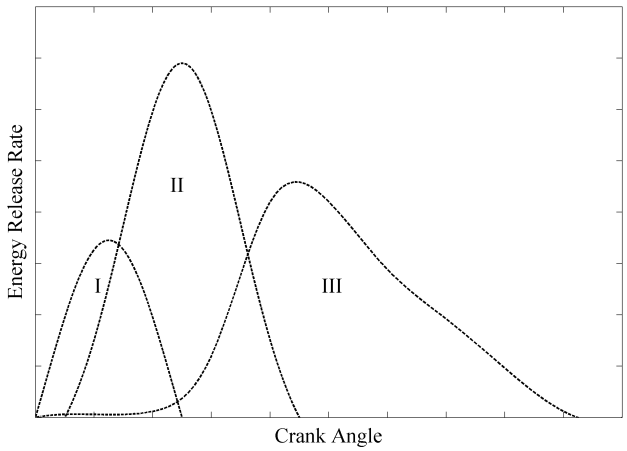

Figure 2.3. Schematic representation of different components of combustion energy release rate in a dual-fuel engine under heavy load [23].

held at 800 K and 2.8 MPa. The overall mixture is stoichiometric but the percentage of n-heptane out of the total fuel mass is varied from 0% to 100%. Figure 2.4 plots the evolution of peak temperature inside the domain as a function of time for 13 different compositions [60]. It is seen that less than 5% of n-heptane substitution into stoichiometric methane-air mixtures is capable of reducing the overall ignition delay by one order of magnitude. Such phenomenon is explained by Karim [23] by the argument that small quantities of n-heptane present would be oxidized spontaneously. The released heat in addition to key transient radicals would greatly accelerate methane oxidation.

The presence of the primary fuel also influences both the pre-ignition and post-ignition processes in a complex manner. Karim (1980) [22] noted that the temperature of the homogeneous mixture has the most significant effect on the ignition delay of pilot fuel. More interestingly, it is reported that the ignition delay of the pilot fuel, i.e., diesel, is initially extended by increasing the quantity of primary fuel into air, i.e., with increasing equivalence ratio, but then reduced with higher equivalence ratio for several fuels [22]. This trend is captured in Fig. 2.5 where ignition delays (in terms of Crank Angle degrees) are graphed against the overall equivalence ratios for various

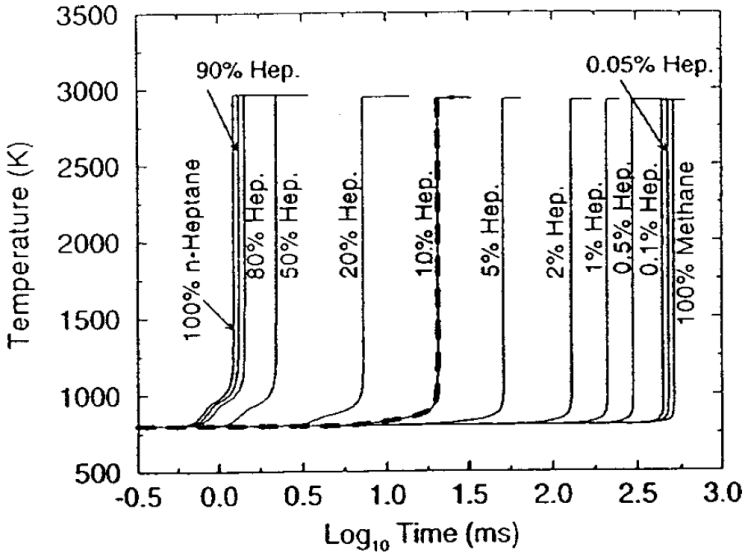

Figure 2.4. Evolution of temperature in mixtures of n-heptane, methane and air of varying composition at initial temperature of 800 K, initial pressure of 2.8 MPa and a total equivalence ratio of 1.0 [60].

combinations of fuels. It is shown that pure diesel would ignite more readily by increasing its equivalence ratio. When a secondary fuel such as methane, ethylene, hydrogen or propane is added to a given amount of diesel, the overall equivalence ratio of the mixture increases but the ignition is retarded initially until a certain threshold equivalence ratio is reached, after which ignition is accelerated with further addition of the secondary fuel. The reason for this is not well understood. Karim (1980) [22] attempted to provide an explanation by arguing that the addition of the secondary fuel would alter the cold mixture properties, such as specific heat ratio and heat transfer parameters. These changes can lower the charge temperature and in-cylinder pressure at the instant of pilot fuel injection and result in longer ignition delay. Liu and Karim (1998) [61] provided further explanation relating to the residual gas effects. They claimed that the residual gas remaining inside the chamber would raise the charge temperature when they are mixed with the fresh charge. With further increase in the mixture equivalence ratio by adding secondary fuel, the residual gas

becomes hotter. As a result, charge temperature also increases after mixing and thereby accelerates ignition.

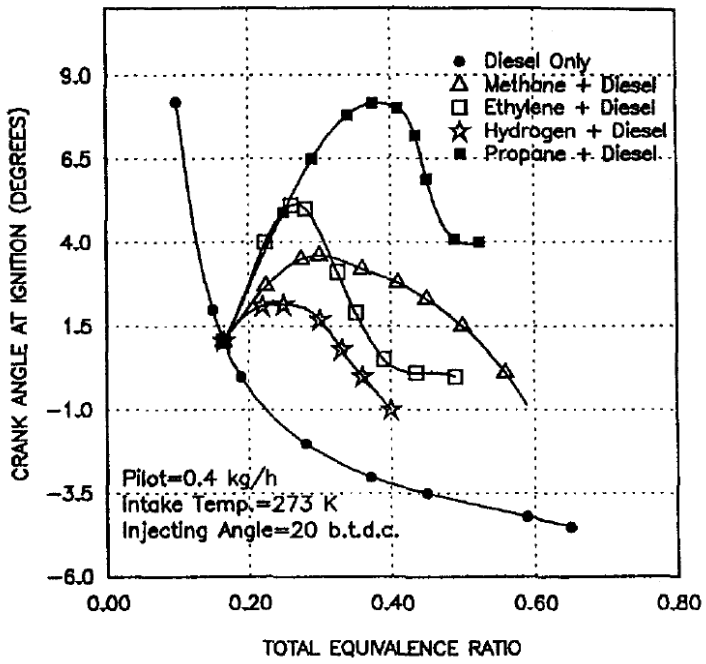

Figure 2.5. Ignition delay of dual-fuel mixtures in crank angle degrees with different fuel substitutions [22].

Khalil and Karim (2002) [60] numerically examined the role of natural gas composition on the ignition delay in the dual-fuel mixtures. They reported that the higher alkanes, e.g., ethane, propane and butane, present in natural gas undergo rapid oxidation to generate OH and HO_2 molecules which then combine with slower-oxidizing methane to form CH_3 radicals. These radicals significantly accelerate the oxidation of methane via H-abstraction as opposed to the much slower initiation reactions that would have been in the pure methane-air mixture. The speed-up brought by H-abstraction is most dominant at low temperature.

In summary, the existing work suggests that in a n-heptane/methane-air dual-fuel engine, n-heptane autoignition is affected by the presence of the primary fuel in a complex manner. Fundamental understanding on the ignition of the pilot fuel

and subsequent flame development into a steady propagating turbulent flame in the premixed primary fuel/air mixture is still lacking. This is an area of interest in our work.

2.4 Modeling of Turbulent Premixed Flames

In the lean-burn natural gas engines, a turbulent flame front will eventually develop after ignition and propagate into the homogeneous mixture. After ignition, the flame kernel grows in size and as it does so, it comes under the influence of an increasing spectrum of turbulent eddies inside the combustion chamber, i.e., the flame propagation becomes that of a fully-developed turbulent premixed flame (in a statistical sense). When studying the propagation of the premixed flame, it is computationally impractical to use spatial and temporal resolution that resolves all physical scales of the problem. For instance, the physical size of the combustion chamber is of the order of 10^{-1} m and so are the largest turbulent eddies. On the other hand, the physical scale over which reactions occur, i.e., the reaction zone thickness, is only a few micrometers under high pressure and temperature conditions [62] and the size of the smallest turbulent eddy, i.e., the Kolmogorov length scale, is of similar magnitude. The duration of combustion in each engine cycle is of the order of milliseconds [11] whereas the chemical reaction takes place within the timeframe of nanoseconds. Evidently there exists a considerable separation of spatial and temporal scales and therefore combustion models which capture the essence of the physical phenomena without incurring excessive computational costs are of great importance.

In the case of chemical kinetics, this implies that reaction time scales on the order of nanoseconds are not resolved but their effects are captured in the reduced mechanism by adjusting, for example, the reaction rate parameters. In the case of turbulent flows, this implies that small scales are averaged and their effects have to be captured through sub-grid scale models. This is the premise of large-eddy simulations (LES) where the direct solution captures only the larger scales of the flow and the effects of

the smaller scales, whose behavior is more universal in character, are modeled. In fact, it may be sufficient to average the effect of all the scales and numerically solve only the averaged equations. In this case, a model is required to capture the effect of all the unresolved scales. This is the premise of Reynolds-averaged Navier-Stokes (RANS) models. The numerical solution of the RANS equations provides only the Reynolds-averaged values of the variables. For compressible flow problems, as in engines, the need to resolve the acoustic scales of the problem typically require the numerical temporal resolution to be shorter than the shortest time scales of the physical problem. Hence, temporal averaging is not generally employed in multidimensional simulations of engine combustion. Irrespective of whether it is LES or RANS simulations, the fact remains that the chemical reactions occur on molecular scales comparable to those within turbulent dissipation range, and are generally smaller than the finest resolution used in the numerical simulation. This implies that the effects of turbulence on the chemistry and on the transport of the reaction zones are not directly resolved, but need to be modeled. Hence, there is a need for turbulence/chemistry interaction models.

To summarize, there are three components to the modeling of turbulent premixed (or non-premixed) combustion: the *chemistry sub-model*, the *turbulence sub-model*, and the *turbulence/chemistry interaction sub-model*. In this work, we will briefly describe the strategies of turbulence modeling in the context of RANS and LES in Sections 2.4.1 and 2.4.2. More details will be provided on the discussion of the turbulence/chemistry interaction sub-models in Section 2.5.

2.4.1 Modeling of turbulent flow by RANS methods

RANS simulations aim to solve for the ensemble average values of the flow variables whose evolution in space and time is described by the set of Reynolds-averaged equations for compressible flows. When considering reacting flows, mass-weighted

(Fávre) averaging can be employed to simplify the decomposition of nonlinear terms. The Fávre mean of an arbitrary quantity ϕ is defined as

$$\bar{\rho}\tilde{\phi} = \overline{\rho\phi} \tag{2.2}$$

and the Fávre fluctuation is

$$\phi'' = \phi - \tilde{\phi} \tag{2.3}$$

With this averaging, the RANS equations can be written as follows:

(i) Reynolds-averaged continuity equation

$$\frac{\partial \bar{\rho}}{\partial t} + \frac{\partial \bar{\rho}\tilde{u}_j}{\partial x_j} = 0. \tag{2.4}$$

(ii) Reynolds-averaged Navier Stokes equation

$$\frac{\partial \bar{\rho}\tilde{u}_j}{\partial t} + \frac{\partial \bar{\rho}\tilde{u}_j\tilde{u}_i}{\partial x_j} = -\frac{\partial \bar{\rho}\widetilde{u_j'' u_i''}}{\partial x_j} - \frac{\partial \bar{p}}{\partial x_i} + \frac{\partial \bar{\tau}_{ij}}{\partial x_j} + \bar{F}_i. \tag{2.5}$$

(iii) Reynolds-averaged conservation equation for energy (enthalpy)

$$\begin{aligned}\frac{\partial \bar{\rho}\tilde{h}}{\partial t} + \frac{\partial \bar{\rho}\tilde{u}_j\tilde{h}}{\partial x_j} &= -\frac{\partial \bar{\rho}\widetilde{u_j'' h''}}{\partial x_j} + \frac{\partial \bar{p}}{\partial t} \\ &+ \frac{\partial}{\partial x_j}\left(- \frac{\lambda}{c_p}\Big[\frac{\partial \bar{\rho}\tilde{h}}{\partial x_j} + \sum_{k=1}^{N}(\frac{1}{Le_k} - 1)h_k\frac{\partial \bar{\rho}\tilde{\mathrm{Y}}_k}{\partial x_j}\Big] + \overline{u_i\tau_{ij}}\right) + \overline{u_j F_j}.\end{aligned} \tag{2.6}$$

(iv) Reynolds-averaged conservation equation for species

$$\frac{\partial \bar{\rho}\tilde{\mathrm{Y}}_k}{\partial t} + \frac{\partial \bar{\rho}\tilde{u}_j\tilde{\mathrm{Y}}_k}{\partial x_j} = -\frac{\partial \bar{\rho}\widetilde{u_j''\mathrm{Y}_k''}}{\partial x_j} + \frac{\partial}{\partial x_j}\left(\rho D_k\frac{\partial \tilde{\mathrm{Y}}_k}{\partial x_j}\right) + \bar{\dot{\omega}}_k. \tag{2.7}$$

Note that the first term on the RHS of Eqs. (2.5), (2.6), and (2.7) need to be modeled, in addition to the average reaction rate. Closure models are required in which the modeled terms can be related to the mean variables. The modeling of the Reynolds stress term, i.e., $\widetilde{u_i'' u_j''}$, typically employs the Boussinesq approximation which expresses the turbulent stress in terms of mean turbulent kinetic energy $\tilde{k} = \frac{1}{2}\widetilde{u_i'' u_i''}$ and turbulent viscosity ν_{T} , i.e.,

$$\widetilde{u_i'' u_j''} = \frac{2}{3}\tilde{k}\delta_{ij} - 2\nu_{\mathrm{T}}(\tilde{\mathrm{S}}_{ij} - \frac{\delta_{ij}}{3}\tilde{\mathrm{S}}_{kk}). \tag{2.8}$$

The terms in the energy and species equations can be closed through an analogy to the gradient transport formulation by employing a turbulent diffusivity D_{T}, under the assumption that Lewis number is unity. The estimation of the turbulent transport properties requires a turbulent length scale and velocity scale. These can be estimated from a simple algebraic model like the mixing length model [63] or obtained by solving a set of transport equations. The most widely used model is a two-equation $k-\epsilon$ model which solves the transport equations for turbulent kinetic energy k and dissipation rate ϵ which are in turn used to specify turbulent viscosity ν_{T} as

$$\nu_{\mathrm{T}} = C_{\mu}\frac{\tilde{k}^2}{\tilde{\epsilon}}. \tag{2.9}$$

The transport equations of turbulent kinetic energy and turbulent dissipation are given as

$$\frac{\partial\bar{\rho}\tilde{k}}{\partial t} + \frac{\partial\bar{\rho}\tilde{u}_j\tilde{k}}{\partial x_j} = -\frac{\partial}{\partial x_j}\Big[\frac{\bar{\rho}\nu_{\mathrm{T}}}{\sigma_k}\frac{\partial\tilde{k}}{\partial x_i}\Big] + 2\bar{\rho}\nu_{\mathrm{T}}\tilde{\mathrm{S}}_{ij}\tilde{\mathrm{S}}_{ij} - \bar{\rho}\tilde{\epsilon}. \tag{2.10}$$

$$\frac{\partial\bar{\rho}\tilde{\epsilon}}{\partial t} + \frac{\partial\bar{\rho}\tilde{u}_j\tilde{\epsilon}}{\partial x_j} = -\frac{\partial}{\partial x_j}\Big[\frac{\bar{\rho}\nu_{\mathrm{T}}}{\sigma_\epsilon}\frac{\partial\tilde{\epsilon}}{\partial x_i}\Big] + C_{\epsilon_1}\frac{\tilde{\epsilon}}{\tilde{k}}2\bar{\rho}\nu_{\mathrm{T}}\tilde{\mathrm{S}}_{ij}\tilde{\mathrm{S}}_{ij} - C_{\epsilon_2}\bar{\rho}\frac{\tilde{\epsilon}^2}{\tilde{k}}. \tag{2.11}$$

The equations contain adjustable constants which are derived by fitting experiment data. The standard values are $C_\mu = 0.09, \sigma_k = 1.00, \sigma_\epsilon = 1.30, C_{\epsilon_1} = 1.44, C_{\epsilon_2} = 1.92$ [64].

2.4.2 Modeling of turbulent flow by LES methods

Large eddy simulation (LES) is based on filtering the full set of conservation equations in the physical space over a control volume of size Δ. For reacting flows where density changes are significant, it is more desirable to perform Fávre averaging to eliminate the extra term arising from the linearization of the triple products involving density. For instance, applying a Fávre filter $F(\vec{x})$ on an arbitrary quantity ϕ would yield

$$\bar{\rho}\tilde{\phi} = \int_{-\infty}^{\infty}\rho\phi F(\vec{x})d\vec{x}. \tag{2.12}$$

Application of the spatial Fávre filtering procedure to the conservation equations gives

(i) Filtered continuity equation

$$\frac{\partial \bar{\rho}}{\partial t} + \frac{\partial \bar{\rho}\tilde{u}_j}{\partial x_j} = 0. \tag{2.13}$$

(ii) Filtered Navier Stokes equation

$$\frac{\partial \bar{\rho}\tilde{u}_j}{\partial t} + \frac{\partial \bar{\rho}\tilde{u}_j\tilde{u}_i}{\partial x_j} = -\frac{\partial \bar{\rho}(\widetilde{u_i u_j} - \tilde{u}_i\tilde{u}_j)}{\partial x_j} - \frac{\partial \bar{p}}{\partial x_i} + \frac{\partial \bar{\tau}_{ij} - \tilde{\tau}_{ij}}{\partial x_j} + \frac{\partial \tilde{\tau}_{ij}}{\partial x_j} + \bar{F}_i. \tag{2.14}$$

(iii) Reynolds-averaged conservation equation for energy (enthalpy)

$$\begin{aligned}\frac{\partial \bar{\rho}\tilde{h}}{\partial t} + \frac{\partial \bar{\rho}\tilde{u}_j\tilde{h}}{\partial x_j} &= -\frac{\partial \bar{\rho}(\widetilde{u_j h} - \tilde{u}_j\tilde{h})}{\partial x_j} + \frac{\partial \bar{p}}{\partial t} \\ &+ \frac{\partial}{\partial x_j}\left(- \frac{\lambda}{c_p}\Big[\frac{\partial \bar{\rho}\tilde{h}}{\partial x_j} + \sum_{k=1}^{N}(\frac{1}{Le_k} - 1)h_k\frac{\partial \bar{\rho}\tilde{\mathrm{Y}}_k}{\partial x_j}\Big] + \overline{u_i\tau_{ij}}\right) + \overline{u_j F_j}.\end{aligned} \tag{2.15}$$

(iv) Reynolds-averaged conservation equation for species

$$\frac{\partial \bar{\rho}\tilde{\mathrm{Y}}_k}{\partial t} + \frac{\partial \bar{\rho}\tilde{u}_j\tilde{\mathrm{Y}}_k}{\partial x_j} = -\frac{\partial \bar{\rho}(\widetilde{u_j\mathrm{Y}_k} - \tilde{u}_j\tilde{\mathrm{Y}}_k)}{\partial x_j} + \frac{\partial}{\partial x_j}\left(\rho D_k\frac{\partial \tilde{\mathrm{Y}}_k}{\partial x_j}\right) + \bar{\dot{\omega}}_k. \tag{2.16}$$

As in the RANS equations earlier, terms arise in Eqs. (2.14), (2.15) and (2.16) which have to be modeled. These unresolved terms are called the subgrid-scale (SGS) quantities and physically represent the effects of unresolved small scales on the resolved flow quantities. In the filtered Navier-Stokes equation, there are two SGS terms which require modeling. The first term is

$$\frac{\partial \bar{\tau}_{ij} - \tilde{\tau}_{ij}}{\partial x_j}. \tag{2.17}$$

This arises in Eq. (2.14) because Fávre filtering and partial differentiation do not commute. This term is generally neglected in engineering applications. The second term is

$$-\frac{\partial}{\partial x_j}\left[\bar{\rho}(\widetilde{u_i u_j} - \tilde{u}_i\tilde{u}_j)\right] \tag{2.18}$$

It arises from filtering the nonlinear convective term. The expression inside the brackets is often called the SGS stress σ_{ij}. The earliest closure for the SGS stress was proposed by Smagorinsky (1963) [65] in which the momentum fluxes are related to

depend linearly on the rate of strain of the large scales. Hence, the Smagorinsky model is expressed as

$$\sigma_{ij} = -2\bar{\rho}\nu_t\left(\check{\mathrm{S}}_{ij} - \frac{\delta_{ij}}{3}\check{\mathrm{S}}_{kk}\right) + \frac{\delta_{ij}}{3}\sigma_{kk}, \tag{2.19}$$

where

$$\nu_t = (C_s\Delta)^2\|\check{\mathrm{S}}\|, \tag{2.20}$$

represents the eddy viscosity. $\|\check{\mathrm{S}}\|$ is the magnitude of filtered strain rate given by

$$\|\check{\mathrm{S}}\| = \sqrt{2\check{\mathrm{S}}_{ij}\check{\mathrm{S}}_{ij}}, \tag{2.21}$$

and it represents a Galilean invariant estimation of velocity differences over the length scale of Δ. The constant C_s is problem-dependent and generally lies within the range of 0.1 and 0.25 [66, 67, 68]. Yoshizawa (1986) [69] postulated the relation for the trace of the SGS stress as

$$\sigma_{kk} = 2\bar{\rho}C_I\Delta^2\|\check{\mathrm{S}}\|^2, \tag{2.22}$$

where C_I is a constant between 0.005–0.0066. The premise of the Smagorinsky model is that SGS turbulence is approximately balanced by the energy cascades from larger scales which take place at the scale similar to the filter width.

2.5 Sub-Models for Turbulence-Chemistry Interactions

The earliest models (prior to the early 1970s) for premixed-engine combustion were primarily single-zone phenomenological models based on *á priori* specified heat release rate models, e.g., Wiebe functions [11, 70]. Incidentally, such models are still extensively used in industry. Subsequently, two-zone models were developed in which a burning speed was specified *á priori* [71, 72]. With the increase in computational power, a transition to multidimensional models, in which partial differential equations are directly solved, occurred in the second half of the 1970s [73, 74]. Within the context of these multidimensional models, it also became necessary to model turbulence/chemistry interactions.

2.5.1 Premixed combustion regime maps

The extent to which the flame is affected by the turbulence can be characterized by various non-dimensional parameters using a regime map. These non-dimensional parameters define the length and time scales in the flame relative to those in the turbulent flow field. For instance, time scales of turbulence and chemistry are given as

$$\tau_{\mathrm{T}} = \mathrm{L_o}/u', \tag{2.23}$$

$$\tau_c = \delta_{\mathrm{L}}/\mathrm{S_L}, \tag{2.24}$$

where $\mathrm{L_o}$ is the turbulence integral length scale, δ_{L} is the flame thermal thickness commonly regarded as the length scale of chemistry, u' is the turbulence intensity and $\mathrm{S_L}$ is the unstrained laminar flame speed. The smallest length and time scales of turbulence, i.e., the Kolmogorov scales, are given by

$$\eta = \left(\frac{\nu^3}{\epsilon}\right)^{\frac{1}{4}}, \tag{2.25}$$

$$\tau_\eta = \left(\frac{\nu}{\epsilon}\right)^{\frac{1}{2}}, \tag{2.26}$$

With these scales in space and time, three important non-dimensional parameters can be constructed that are of interest for our discussion:

(1) The turbulent Reynolds number

$$Re_{\mathrm{T}} = \frac{u'\mathrm{L_o}}{\nu}, \tag{2.27}$$

compares turbulent inertial forces with viscous forces. Note that under the assumption of unity Schmidt number, i.e., $Sc \equiv \nu/D = 1$, the following relation holds:

$$Re_{\mathrm{T}} = \frac{u'}{\mathrm{S_L}}\frac{\mathrm{L_o}}{\delta_{\mathrm{L}}}. \tag{2.28}$$

(2) The Damköhler number, Da, compares the turbulent time scale with the chemical time scale, i.e.,

$$Da = \frac{\tau_{\mathrm{T}}}{\tau_c} = \frac{\mathrm{L_o}/u'}{\delta_{\mathrm{L}}/\mathrm{S_L}}. \tag{2.29}$$

(3) The Karlovitz number, Ka, compares the chemical time scale with the time scale associated with the smallest eddy of turbulence,

$$Ka = \frac{\tau_c}{\tau_\eta} = \left(\frac{u'}{\mathrm{S_L}}\right)^{\frac{3}{2}} \left(\frac{\mathrm{L_o}}{\delta_\mathrm{L}}\right)^{-\frac{1}{2}}. \tag{2.30}$$

These non-dimensional numbers among others can be employed to develop physically motivated regime maps which identify various regimes of turbulent premixed charge combustion. The earliest such regime map was proposed by Libby and Williams (1981) [75] for turbulent premixed charge combustion. The regimes were identified on a turbulent Damköhler number (Da) - Reynolds number (Re) plot. Abraham *et al.* (1985) [76] adapted the regime map proposed by Libby and Williams and identified premixed-charge engine operating conditions on the map shown in Fig. 2.6(a). The line $l_k/\delta_\mathrm{L} = 1$ demarcates the region of wrinkled reaction sheets, i.e., when $\delta_\mathrm{L} < l_k$, the reaction zone of the flame is not affected by the smallest scales of turbulence and it remains a wrinkled (convoluted) reaction sheet. On the other hand, when $\delta_\mathrm{L} > l_k$, the local structure of the flame is affected and the reaction zone is either thickened or broken up. The line $u'/\mathrm{S_L} = 1$ separates the regions of singly connected and multiply connected reaction sheets, i.e., when $u' > \mathrm{S_L}$, the reaction sheet is multiply connected. The line $l_I/\delta_\mathrm{L} = 1$ separates the region of distributed combustion from the region where there are broken reaction zones. In other words, if the largest scale of the turbulence is smaller than the thermal thickness of the flame, the flame cannot exist and combustion occurs in a distributed combustion zone. This regime is rarely encountered in engines. This showed that premixed charge flames in engines primarily lie in the wrinkled/reaction sheet (singly and/or multiply connected) flame regime. The conditions considered in identifying the engine regime are those that are far from the lean limit. An important point to note is that as the lean limit is approached, the chemistry time scales become longer relative to the flow time scale, which decreases the Da, and move the shaded area into the combustion regimes where extinction and re-ignition resulting from turbulent strain of the flames, become more dominant.

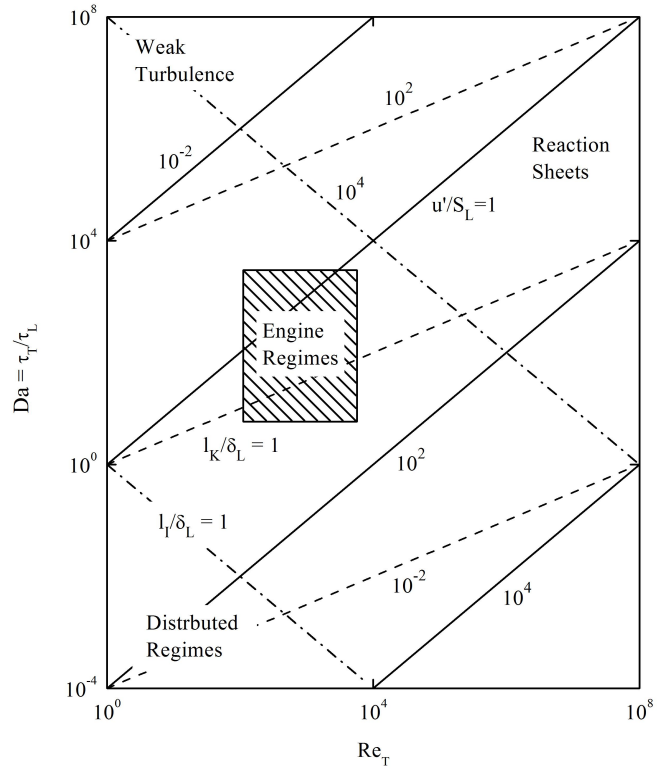

(a)

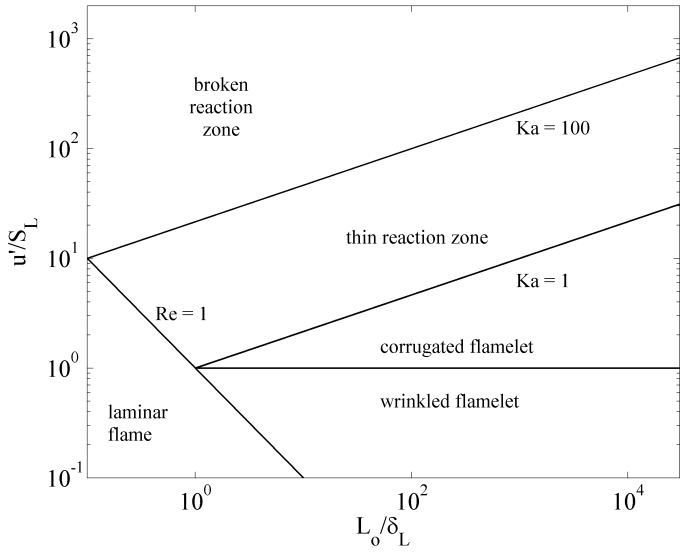

(b)

Figure 2.6. (a) Regimes of turbulent combustion in premixed charges. The regime of combustion in spark-ignited engines is identified by the shaded area [76]. (b) Regime map of premixed turbulent combustion [77].

Other turbulent regime maps have been presented in the literature [78, 79]. For our discussion, the regime map modified by Peters (2000) [77] is used. In Fig. 2.6(b), four reference lines $Re = 1$, $Da = 1$, $Ka = 1$ and $Ka = 100$ are mapped onto the regime diagram and the lines demarcate five distinct characteristic combustion regimes:

(1) Laminar flame regime: $Re_{\mathrm{T}} < 1$. In this regime, the flame behaves as a laminar flame whose behavior has been well characterized.

(2) (Weakly-) Wrinkled flame regime: $Re_{\mathrm{T}} > 1$, $Ka < 1$ and $u' < \mathrm{S_L}$. In this regime, the thermal thickness of the flame is smaller than the size of the smallest eddy such that the flame is embedded inside the Kolmogorov eddies and the reaction zone is essentially unaffected by turbulence. This would correspond to the singly connected region of Fig. 2.6(a).

(3) Corrugated flamelet regime: $Re_{\mathrm{T}} > 1$, $Ka < 1$ and $u' > \mathrm{S_L}$. It is similar to the wrinkled flame regime in that flame is embedded in the smallest eddies of turbulence field. However the larger turbulent motions, too, could affect the flame front, resulting in the formation of pockets of fresh and burnt gas. This would correspond to the multiply-connected region of Fig. 2.6(a).

(4) Thin reaction zone regime: $Re_{\mathrm{T}} > 1$ and $1 < Ka < 100$. In this regime, the chemical time scale is smaller than the turbulent integral time scale, but larger than the Kolmogorov time scale. The smallest eddies can penetrate into the preheat zone of the flame but not the inner reaction zone, and hence able to significantly impact flame structure. Alternatively, the Kolmogorov length scale is shorter than the thermal thickness of the flame, but larger than the reaction zone thickness. This region is not explicitly identified in Fig. 2.6(a), but would correspond to the region where the reaction zones are broken up.

(5) Broken reaction zone regime: $Re_{\mathrm{T}} > 1$ and $Ka > 100$. In this regime, the smallest eddy of turbulence is smaller than the thickness of the reaction zone of

the flame and hence is able to penetrate inside and break up the reaction sheet into separated zones. This corresponds to the region where the reaction zones are broken up. Notice that the "distributed" combustion regime of Fig. 2.6(b) is not identified in Fig. 2.6(a).

2.5.2 Eddy-Break-Up (EBU)/Mixing-controlled models

The turbulence/chemistry interaction sub-models are developed with a physical picture of the turbulent flame in mind. For example, it was assumed in earlier models (developed in the 1970s) that the turbulent flame is broken up, which implies that there would be pockets of burned products and of unburned reactants. This picture would fit either the distributed combustion regime or the broken-sheet regime. The mixing of these pockets of burned products and reactants would then control the average reaction rate and the propagation of the flame brush where the pockets existed. From this physical picture, it is a natural extension to assume that the mixing of the reactants and products is turbulence-controlled and so a turbulent mixing time scale was employed to formulate the reaction rate. This model was applied assuming that the products were formed in a global reaction, i.e.,

$$Reactants \Longrightarrow Products.$$

The eddy-break-up model first proposed by Spalding (1971) [80] was based on this assumption. Under the assumption of fast chemistry and one-step global reaction, the chemical time scale was replaced by the turbulent mixing time scale, i.e., $\tau = k/\epsilon$. Global mean reaction rate of products ($\dot{\omega}_p$) could be cast as follows,

$$\overline{\dot{\omega}}_p = C_{EBU} \frac{\epsilon}{k} \sqrt{\mathrm{Y}_p''^2} \tag{2.31}$$

where $\mathrm{Y}_p''^2$ represents the fluctuations in the product mass fraction. The application of this model requires the modeling of the concentration fluctuations. The constant C_{EBU} is a problem-dependent variable that must be tuned in order to obtain accurate result for specific combustors. Magnussen and Hjertager (1976) [81] generalized the

model for premixed and diffusion flames by using the limiting concentration (fuel, oxygen, products) in the reaction rate expression. They used the mean concentration of the species instead of the fluctuations thereby avoiding the need for modeling the concentration fluctuations. This model was first applied to engine combustion by Grasso and Bracco (1982) [82].

The mixing-controlled models proposed above were applicable only in the fast-chemistry limit. This assumption would break down near walls and in the lean limit. A simple extension of the model was proposed to include local effects of chemical time scale. The proposal was to include a chemical time scale such that the longer of two time scales, the mixing time scale and the chemical time scale, would control the progress of reaction. Another assumption employed by the eddy-break-up model was that of a single-step global reaction mechanism. This assumption was limiting because in rich mixtures, in particular, incomplete combustion of hydrocarbons would lead to the formation of other products like CO and H_2. In lean mixtures, incomplete combustion can lead to the formation of CO and unburned hydrocarbons. The eddy-breakup class of models with a single-step reaction mechanism could not handle these situations.

Abraham *et al.* (1985) [76] suggested an approach to include multiple species in the product mixture by making the assumption that the product mixture is at chemical equilibrium at the local pressure and temperature conditions of the mixture, i.e.,

$$\frac{d\mathrm{Y}_m}{dt} = -\frac{\mathrm{Y}_m - \mathrm{Y}_m^*}{\tau_c}, \tag{2.32}$$

where Y_m and Y_m^* represent the local and the thermodynamic equilibrium value of the mass fraction, and τ_c is the characteristic time for the achievement of equilibrium. The characteristic time τ_c is assumed to be a combination of a laminar timescale and a turbulent timescale, such that the longer of the two time scales controls the combustion rate. The laminar timescale is of Arrhenius form, and the turbulent timescale is assumed to be proportional to the eddy turnover time, i.e., k/ϵ, where ϵ is the dissipation of turbulent kinetic energy and k is the turbulent kinetic energy, similar to the approach adopted in the eddy break-up models discussed earlier. The model has been

applied to premixed-charge and diesel engines. While the application to premixed-charge engines is intuitive, the application to diesel engines is possible because in conventional high-temperature high-pressure diesel engines, the combustion is mixing controlled as implied by the model. The model has been referred to as the characteristic time combustion (CTC) model [83] or the local equilibrium characteristic time (LECT) model [84, 85] in the literature when applied to diesel combustion.

All these models were developed within the context of RANS modeling in the 1970s and early 80s. In one way or another they implicitly assume that the turbulent flame front is a thickened flame brush. The reason why they work is that they are able to reproduce the flame speed. This can be seen as follows. The turbulent flame speed S_T can be expressed as

$$S_T = \sqrt{D_T/\tau_c}, \tag{2.33}$$

where D_T is the turbulent diffusivity and τ_c is a chemical conversion time. The turbulent diffusivity D_T can be expressed as the product of a turbulent length scale l_T and a velocity scale (the turbulence intensity), i.e., $D_T \sim l_T \cdot u'$. When the eddy-breakup model is employed, the conversion time can be approximated as l_T/u'. This would then imply that

$$S_T \sim u'. \tag{2.34}$$

Hence, in situations where the turbulent flame speed is proportional to the turbulence intensity the eddy-breakup class of models works well. In an engine, this approximation is generally applicable. In fact, this is the reason why the burn duration in crank angle degrees is approximately constant as speed is changed because $u' \sim$ flame speed. However, under lean-burn limit conditions, this approximation can break down. To the extent that the structure of the flame is not accurately modeled, there is likely to be an error during the early period of kernel development when the "flame brush" is not fully developed and in the later period of combustion when the "flame brush" interacts with the wall.

In the mid-1980s, the structure of the flame was experimentally observed in an optical engine through planar two-dimensional [86] and three-dimensional imaging

[87, 88]. It was observed that the flame is indeed a highly convoluted "thin" flame in each cycle and not the "thickened" flame visualized earlier. This "thin" flame was consistent with the suggestions made by Abraham *et al.* (1985) [76]. This has led to the development and application of new models, which revolve around the so-called "flamelet" concept that the reacting flame front is thin relative to the turbulence length scale such that the primary effects of turbulence are only to wrinkle and strain the embedded flame surface. In fact, many of these models were developed outside of the engine community.

2.5.3 The Bray-Moss-Libby (BML) model

One approach is to represent the combustion at the flame front in terms of a progress variable c. The progress variable can be expressed in terms of the local fuel mass fraction $\mathrm{Y_F}$ with respect to the fuel mass fractions in the fresh gas, $\mathrm{Y_F^u}$ and burnt gas, $\mathrm{Y_F^b}$ as follows:

$$c = \frac{\mathrm{Y_F} - \mathrm{Y_F^u}}{\mathrm{Y_F^b} - \mathrm{Y_F^u}}. \tag{2.35}$$

This progress variable ranges from 0 to 1 with $c = 0$ in the fresh gas and $c = 1$ in the complete burnt mixture. The concept of progress variable became popular in modeling as it reduced the complexity of chemical kinetics into representation by a single variable and conversely with the knowledge of the progress variable in time and in space, the full map of mean temperature and mean concentration of major species can be reconstructed. The transport equation for progress variable can be written as,

$$\frac{\partial \rho c}{\partial t} + \frac{\partial \rho u_j c}{\partial x_j} = \frac{\partial}{\partial x_j}\left(\rho D \frac{\partial c}{\partial x_j}\right) + \dot{\omega}, \tag{2.36}$$

and the averaged transport equation for RANS simulation and the filtered transport equation for LES are, respectively, given as

$$\frac{\partial \bar{\rho}\tilde{c}}{\partial t} + \frac{\partial \bar{\rho}\tilde{u}_j\tilde{c}}{\partial x_j} = -\frac{\partial \bar{\rho}\widetilde{u_j'' c''}}{\partial x_j} + \frac{\partial}{\partial x_j}\left(\bar{\rho} D \frac{\partial \tilde{c}}{\partial x_j}\right) + \tilde{\dot{\omega}}, \tag{2.37}$$

$$\frac{\partial \bar{\rho}\tilde{c}}{\partial t} + \frac{\partial \bar{\rho}\tilde{u}_j\tilde{c}}{\partial x_j} = -\frac{\partial \bar{\rho}(\widetilde{u_j c} - \tilde{u}_j\tilde{c})}{\partial x_j} + \frac{\partial}{\partial x_j}\left(\bar{\rho} D \frac{\partial \tilde{c}}{\partial x_j}\right) + \tilde{\dot{\omega}}. \tag{2.38}$$

With the objective of formulating a model capable of describing combustion in both the distributed flame and flamelet (thin reaction sheet) regimes, Bray, Moss and Libby (1985) [89] combined a statistical approach using probability density functions (pdf) and the analysis on progress variable presented earlier. Within this framework, the model assumes that the pdf of the progress variable c at location $\vec{x}$ and time t is given as the sum of the contributions from fresh, fully burnt and burning gases:

$$P(c,\vec{x},t) = \alpha(\vec{x},t)\delta(c) + \beta(\vec{x},t)\delta(1-c) + \gamma(\vec{x},t)f(c,\vec{x},t). \tag{2.39}$$

where α, β, γ represents the probability of finding fresh, fully burnt and burning gases at that particular location and time instant. For fresh and fully burnt gas, the pdfs of the progress variable are assumed to be two Dirac-delta functions centered at $c = 0$ and $c = 1$ respectively. The following relations must also be satisfied:

$$\alpha + \beta + \gamma = 1, \tag{2.40}$$

$$\int_0^1 P(c,\vec{x},t)dc = \alpha + \beta + \int_0^1 \gamma(\vec{x},t)f(c,\vec{x},t)dc = 1. \tag{2.41}$$

For the special case of infinitely fast chemistry and infinitely thin flame front, the mixture either exists in the fresh or the fully-combusted state, i.e., $\gamma(\vec{x},t) \cong 0$. With that, the probabilities α and β can be solved:

$$\begin{aligned} \alpha &= \frac{1-\tilde{c}}{1+\tau\tilde{c}}; \\ \beta &= \frac{(1+\tau)\tilde{c}}{1+\tau\tilde{c}}, \end{aligned} \tag{2.42}$$

where $\tau = \rho_u/\rho_b - 1$. Through some clever manipulation of the two transport equations for c and c^2, the following balance equation is derived:

$$\frac{\partial}{\partial t}\Big[\rho c(1-c)\Big] + \nabla\cdot\Big[\rho\vec{u}c(1-c)\Big] = \nabla\cdot\Big(\rho D\nabla[c(1-c)]\Big) + 2\rho D\nabla c\cdot\nabla c - 2c\dot{\omega} + \dot{\omega}. \tag{2.43}$$

Since the pdf of c is assumed to be a bimodal distribution (and hence the name BiModaL), $c(1-c)$ is universally zero by definition and thus Eq. (2.43) becomes,

$$\dot{\omega} = \frac{2\overline{\rho D\nabla c\cdot\nabla c}}{2c_m - 1} = \frac{2\overline{\rho\chi}}{2c_m - 1}. \tag{2.44}$$

Here, c_m represents a reaction rate-averaged progress variable:

$$c_m = \frac{\int_0^1 c \cdot \dot{\omega} f(c) dc}{\int_0^1 \dot{\omega} f(c) dc}, \tag{2.45}$$

and is often estimated from an unstrained laminar flame. The term $\overline{\rho\chi}$ represents the scalar dissipation of progress variable which characterizes the effects of turbulent mixing. It is unclosed and can be solved from its transport equation [90].

2.5.4 Level set (G-equation) model

Based on the assumption that the flame is a thin reaction sheet, it was proposed that the flame could be represented by the level surface of a scalar field G [32, 62]. The G-equation model, also known as the level set method, is based on flame tracking technique where the instantaneous flame front is represented by an isosurface of a scalar field G. For convenience, the flame is assumed to be located at $G \equiv 0$ and inside the fresh gas, G carries a negative sign as opposed to a positive sign in the burnt gas. In the laminar case, this isosurface of G is convected by the velocity field as it propagates normal to itself at the laminar burning velocity. Yakhot (1988) [91] suggested the use of filtered G-equation to be applied to LES of combustion. Peters (2000) [77] formulated the filtered G-equation as,

$$\bar{\rho}\frac{\partial \tilde{G}}{\partial t} + \bar{\rho}\tilde{u} \cdot \nabla \tilde{G} = \bar{\rho} \mathrm{S_T} \|\nabla \tilde{G}\| - \bar{\rho} D_t \tilde{\kappa} \|\nabla \tilde{G}\|. \tag{2.46}$$

On the right hand side of the filtered equation, the first term involves the turbulent burning velocity while the second term represents the curvature effects. The equation for subgrid variance of G is derived as,

$$\bar{\rho}\frac{\partial \widetilde{G''^2}}{\partial t} + \bar{\rho}\tilde{u} \cdot \nabla \widetilde{G''^2} + \nabla \cdot \left(\bar{\rho} \widetilde{u'' G''^2} \right) = 2\bar{\rho} D_{\mathrm{T}} (\nabla \tilde{G})^2 - \bar{\rho}\tilde{\omega} - \bar{\rho}\tilde{\chi}. \tag{2.47}$$

The scaling of terms developed by Peters (2000) [77] showed that the kinematic restoration term, $-\bar{\rho}\tilde{\omega}$, is proportional to the mean propagation and independent

of the small scales whereas the scalar dissipation term, $-\bar{\rho}\tilde{\chi}$ involves a molecular diffusivity. Assuming that the production term in the G''^2-equation is balanced by the kinematic restoration and scalar dissipation, the turbulent burning velocity can be given as

$$\frac{\mathrm{S_T} - \mathrm{S_L}}{\mathrm{S_L}} = \begin{cases} b_1 \nu'_\Delta / \mathrm{S_L} & Da_\Delta \gg 1; \\ b_3 \sqrt{D_t / D} & Da_\Delta \ll 1; \end{cases} \tag{2.48}$$

where constants of value $b_1 = 2.0$ and $b_3 = 1.0$ have been reported by Peters (2000) [77].

Tan *et al.* (2003) [92] have employed this approach to model kernel ignition and premixed combustion of propane/air mixtures in a homogeneous charge engine. Once the ignition kernel had reached a critical size of an order as the integral turbulent length scale, the flame was considered as fully developed and the G-equation model was employed. The authors reported good agreement between measured and predicted in-cylinder pressure and measured and computed exhaust $\mathrm{NO_x}$. Ewald and Peters (2007) [93] also employed a G-equation model to predict premixed-charge engine combustion. They derived an expression for turbulent burning velocity for unsteady flame development in an engine accounting for small and large scale turbulence effects on the flame, the Damköhler number, and curvature effects. A criterion for successful ignition was also proposed. The model was employed to predict combustion from ignition, through fully developed flame propagation, and end of burning. Comparisons of computed and measured in-cylinder pressure for two equivalence ratios with varying dilution levels were presented.

2.5.5 Flame surface density model

One of the early implementations of the flamelet assumption for SI engine modeling was by Cheng and Diringer (1991) [94] who assumed that the combustion is occurring through multiple flamelets and then derived an expression for the flame surface density, and employed an equation for its transport. This approach is not very

different from the coherent flame modeling (CFM) approach of Marble and Broadwell (1977) [95] which also views the flow field to be composed of multiple laminar flamelets stretched by the turbulent flow. Cheng and Diringer (1991) [94] also derived a phenomenological model relating the flame surface density to the size of the kernel during the ignition process. Three-dimensional computations of flame propagation in a spark-ignition engine were presented and predicted pressure and heat release rates were found to be in close agreement with measured results. Boudier *et al.* (1992) [96] employed the CFM model to predict combustion in SI engines. Their implementation included a model for laminar ignition followed by laminar to turbulent transition and then turbulent flame propagation. While flame locations have been well predicted, significant differences were seen suggesting that the laminar to turbulent transition model may be at fault. Another application of the coherent flame modeling to SI engines was presented by Zhao *et al.* (1993) [97] who employed the model of Cheng and Diringer with a modified flame surface production term. They presented comparisons of predicted and measured in-cylinder pressures and reported good agreement for all cases except one with lean swirling flow.

In fact, the CFM model has evolved into the flame surface density (FSD) model [98, 99]. In this type of model, the reacting flame front is assumed to be thin relative to the turbulence length scale such that the primary effect of turbulence is only to wrinkle and strain the embedded flame surface. Chemical reactions take place in the collection of thin reacting sheets or the flamelets, which propagates at the laminar flame speed S_L. With this assumption, the mean burning rate of a species i is expressed as the product of the available flame area per unit volume Σ, and the mean local burning rate per unit flame area integrated along the normal direction to the flame surface $\dot{\Omega}_i$, i.e., $\overline{\dot{\omega}}_i = \dot{\Omega}_i \Sigma$. Such a formulation decouples the chemical effect which is solely described by $\dot{\Omega}_i$ from the flame-turbulence interaction that is accounted for by Σ. For practical purposes, $\dot{\Omega}_i$ is often estimated using a planar laminar flame as

$$\dot{\Omega}_i = \bar{\rho}\tilde{\mathrm{Y}}_i \mathrm{S_L}, \tag{2.49}$$

where $\tilde{\mathrm{Y}}_i$ is the Fávre-averaged mass fraction of species i.

In the case of RANS simulation, flame surface density is determined by numerically solving the averaged transport equation for Σ. For premixed flames in which the locations are defined by the surface of iso-c^* value, the flame surface density is related to the gradient of the progress variable c conditioned at c^* through the following relation:

$$\Sigma(c^*) = \overline{|\nabla c|_{c=c^*}}\overline{P}(c^*). \tag{2.50}$$

The balance equation for Σ is derived from the balance equation for progress variable by Candel and Poinsot (1990) [98], taking the form as follows,

$$\frac{\partial \Sigma}{\partial t} + \nabla \cdot \left(\langle \vec{\mathbf{u}} \rangle_s \Sigma\right) = \langle \nabla \cdot \vec{\mathbf{u}} - nn \colon \nabla \vec{\mathbf{u}} \rangle_s - \nabla \cdot \left[\langle wn \rangle_s \Sigma\right] + \langle w \nabla \cdot n \rangle_s \Sigma. \tag{2.51}$$

Here, $\langle \cdot \rangle_s$ represents averaging along the flame surface and for any quantity Q that

$$\langle Q \rangle_s = \frac{\overline{Q|\nabla c|_{c=c^*}}}{\overline{|\nabla c|_{c=c^*}}}. \tag{2.52}$$

Note that the balance equations for Σ are unclosed and require modeling. Performing Reynolds decomposition to split terms into their mean and fluctuation, the balance equation is recast as follows:

$$\begin{aligned} \frac{\partial \Sigma}{\partial t} + \nabla \cdot (\tilde{\mathbf{u}}\Sigma) = &-\nabla \cdot (\langle \mathbf{u}'' \rangle_s \Sigma) + (\nabla \cdot \tilde{\mathbf{u}} - \langle nn \rangle_s \colon \nabla \tilde{\mathbf{u}})\Sigma \\ &+ \langle \nabla \cdot \mathbf{u}'' - nn \colon \nabla \mathbf{u}'' \rangle_s \Sigma - \nabla \cdot [\langle wn \rangle_s \Sigma] + \langle w \nabla \cdot n \rangle_s \Sigma. \end{aligned} \tag{2.53}$$

The five terms on the R.H.S. of the balance equation represent turbulent transport of FSD, strain-generated FSD by the mean flow, strain-generated FSD by the turbulent motions, propagation of FSD and FSD created by curvature, respectively. All of these terms require closure.

Flame surface density concepts could also be employed in LES simulations. By applying LES filtering operation to the exact balance equation for progress variable c, the Fávre-filtered transport equation is derived:

$$\frac{\partial \bar{\rho}\tilde{c}}{\partial t} + \frac{\partial \bar{\rho}\tilde{u}_i\tilde{c}}{\partial x_i} + \frac{\partial}{\partial x_i}\bar{\rho}(\widetilde{u_i c} - \tilde{u}_i\tilde{c}) = \bar{\dot{\omega}} + \overline{\frac{\partial}{\partial x_i}\rho D \frac{\partial c}{\partial x_i}}. \tag{2.54}$$

The unclosed reaction and diffusion terms on the R.H.S. of the above equation may then be written as

$$\bar{\dot{\omega}} + \overline{\frac{\partial}{\partial x_i}\rho D \frac{\partial c}{\partial x_i}} = \overline{\rho w \|\nabla c\|} = \int_0^1 \overline{(\rho w)_s} \Sigma_{sgs} dc^*, \tag{2.55}$$

where w is the local flame propagation speed. Inside flamelet regimes where flame front is assumed to be very thin, $(\rho w)_s$ and Σ_{sgs} can be approximated as constant across the flame and

$$\int_0^1 \overline{(\rho w)_s} \Sigma_{sgs} dc^* \approx \rho_r \mathrm{S_L} \Sigma_{sgs}. \tag{2.56}$$

The problem remains to determine the unresolved flame surface density Σ_{sgs}. There were two approaches being proposed: using an algebraic model or solving the flame surface density transport equation.

(a) Algebraic model

Boger *et al.* (1998) [100] suggested a simple formulation similar to the eddy-break-up model or Bray-Moss-Libby model employed in RANS modeling that

$$\Sigma_{sgs} = K_\Sigma \frac{\tilde{c}(1-\tilde{c})}{\Delta}. \tag{2.57}$$

Charlette (2002) [101] modified it by including a term that accounts for the resolved flame surface density:

$$\Sigma_{sgs} = \|\nabla \tilde{c}\| + \alpha \Gamma_k \left(\frac{\delta_\mathrm{L}}{\Delta}, \frac{\sqrt{2\tilde{k}/3}}{\mathrm{S_L}} \right) \frac{\sqrt{\tilde{k}}}{\mathrm{S_L}} \frac{\tilde{c}(1-\tilde{c})}{\Delta}. \tag{2.58}$$

Angelberger (1998) [102] proposed a model with the form:

$$\Sigma_{sgs} = \left[1 + \alpha \frac{u'}{\mathrm{S_L}} \Gamma\left(\frac{\delta_\mathrm{L}}{\Delta}, \frac{u'}{\mathrm{S_L}} \right) \right] \|\nabla \tilde{c}\|. \tag{2.59}$$

(b) Transport equation for FSD

Hawkes and Cant (2000) [103] derived the unclosed transport equation for Σ_{sgs}:

$$\begin{aligned} &\frac{\partial \Sigma_{sgs}}{\partial t} + \frac{\partial}{\partial x_i}\left(\tilde{u}_i \Sigma_{sgs} \right) + \frac{\partial}{\partial x_i}\left[(\overline{(u_i)_s} - \tilde{u}_i)\Sigma_{sgs} \right] \\ &= \overline{\left((\delta_{ij} - n_i n_j) \frac{\partial u_i}{\partial x_j} \right)_s} \Sigma_{sgs} - \frac{\partial}{\partial x_i}\left[\overline{(w n_i)_s} \Sigma_{sgs} \right] + \overline{\left(w \frac{\partial n_k}{\partial x_k} \right)_s} \Sigma_{sgs}. \end{aligned} \tag{2.60}$$

The last two terms on the R.H.S. of the equation represent the propagation of flame surface density and the creation of flame surface density due to curvature and propagation respectively. The term $\overline{\left((\delta_{ij} - n_i n_j)\frac{\partial u_i}{\partial x_j}\right)_s}\Sigma_{sgs}$ represents the straining effects on the flame surface caused by the surrounding fluid. All these terms are unresolved and require modeling. The unresolved flux of flame surface density due to $\left(\overline{(u_i)_s} - \tilde{u}_i\right)\Sigma_{sgs}$ is the last piece that requires closure. This term is strongly related to the subgrid-scale flux of progress variable $\widetilde{uc} - \tilde{u}\tilde{c}$ and is modeled as a contribution due to turbulent fluctuations and a non-gradient transport contribution due to heat release.

2.5.6 Tabulated chemistry approaches

A fundamental problem with all the models discussed above is that it is difficult to include complex chemistry. These become important in predicting pollutants and also turbulence/chemistry interactions, especially under limit conditions. Recognize that the instantaneous reaction rate $\dot{\omega}_i$ is a function of temperature T, pressure p, and species mass fractions Y_i, i.e.,

$$\dot{\omega}_i = f(\mathrm{T}, \mathrm{p}, \mathrm{Y}_1, \mathrm{Y}_2, \ldots, \mathrm{Y}_N) \tag{2.61}$$

The Fávre-averaged reaction rate $\dot{\omega}_i$ can then be expressed as

$$\tilde{\dot{\omega}}_i = \int \ldots \iiint \dot{\omega}_i P(\mathrm{T}, \mathrm{p}, \mathrm{Y}_1, \mathrm{Y}_2, \ldots, \mathrm{Y}_N) d\mathrm{T} d\mathrm{p} d\mathrm{Y}_1 d\mathrm{Y}_2 \ldots d\mathrm{Y}_N, \tag{2.62}$$

where $P(\mathrm{T}, \mathrm{p}, \mathrm{Y}_1, \mathrm{Y}_2, \ldots, \mathrm{Y}_N)$ is the joint pdf of the scalars. This is now a problem with the reaction rate depending on $N+2$ variables, i.e., the problem involves finding solutions on an $N+2$ dimensional manifold. In fact, a transport equation for the joint pdf has been developed [104, 105]. Assumptions have to be made to solve the equation. For example, gradient diffusion is usually assumed and a model for molecular mixing has to be employed. This approach is suitable for relatively simple problems, but is unrealistic for complex problems like premixed-charge engines. A simpler approach is to identify a low-dimensional manifold which would be adequate. In the case of

non-premixed charge combustion, e.g., as in diesel engines, this is often done by recognizing that to a first approximation, the scalar quantities of temperature and species mass fractions can be related to the mixture fraction. Furthermore, the local influence of turbulence can be accounted for by a strain rate or scalar dissipation rate. In time-dependent problems, the progress of the manifold in time can be accounted for by using a reaction progress variable. If this simplification is made, the reaction rate can be expression in terms of a low-dimensional manifold, e.g., 3 dimensions for the case we just discussed. In fact, this approach has been successfully applied for gas turbines and diesel engines [106, 107].

For premixed-charge combustion, it is recognized that the flames behave as reaction sheets. They are locally one-dimensional with the scalar variables and temperature that are dependent on the reaction progress variable through the flame. Hence, this reaction progress variable becomes an independent parameter. In addition the turbulent strain rate influences the reaction rate and becomes a second independent parameter characterizing the manifold. Local reactant mixture composition, as characterized by an equivalence ratio and/or the exhaust gas recirculated fraction, can be another independent parameter. The instantaneous reaction rate can be tabulated in terms of these three independent parameters and the average reaction rates obtained by assuming *á priori* pdfs, just as done in the unsteady flamelet progress variable method or unsteady flamelet-generated manifold method in diesel engines. These approaches have been considered in recent studies [108, 109, 110, 111].

2.6 Turbulent Flame Speed Correlations

As discussed in Section 2.4, the turbulent flame speed S_T is a parameter that is employed as a model input in the G-equation to represent the interplay of the diffusional-chemical effects between the local flow field and flamelets. The use of a single variable S_T greatly simplifies the numerical solution by eliminating the need to solve stiff source terms. Indeed by assuming *á priori* closure for turbulent flame

speeds, multi-dimensional simulations were possible in rather complex geometries applicable to bombs [112, 113], SI engines [114, 115] and industrial burners [116, 117]. Similar to the G-equation, the approach to model progress variable transport can also benefit from the specification of a single turbulent speed for characterizing global chemical effects in a fluctuating turbulent flow. Zimont (1977) [118] has proposed that a locally known turbulent burning velocity S_T can be used to close the balance equation of Fávre-averaged progress variable:

$$\frac{\partial \bar{\rho}\tilde{c}}{\partial t} + \frac{\partial \bar{\rho}\tilde{u}_j\tilde{c}}{\partial x_j} = \frac{\partial}{\partial x_j}\left[\bar{\rho}D_T\frac{\partial \tilde{c}}{\partial x_i}\right] + \rho_u S_T\|\nabla\tilde{c}\|. \tag{2.63}$$

It is important to note that many definitions for the turbulent flame speed exist in the literature. Driscoll (2008) [119] summarized three definitions:

1. Global consumption speed (S_{GC}) is defined as the integral mass consumption rate of reactants across the mean flame front and is given by

$$S_{GC} = \frac{1}{\rho_u A_{ref}}\int \dot{\omega} dV, \tag{2.64}$$

   where A_{ref} is the area of the mean flame front.

2. Local consumption speed (S_{LC}) is the local mass consumption per unit area of the turbulent flame brush along the direction normal to the mean flame brush, $\vec{\mathbf{n}}$,

$$S_{LC} = \frac{1}{\rho_u}\int_{-\infty}^{\infty} \dot{\omega} d\vec{\mathbf{n}}, \tag{2.65}$$

3. Leading edge displacement speed (S_{LD}) is the propagation speed of the flame brush leading edge ($\tilde{c} \approx 0$ isosurface) relative to the unburned mixture velocity. This definition is similar to the definition of laminar flame speed except that the mean turbulent flame brush is used instead of the laminar flame front.

Generally, S_{GC} is different from S_{LC} since the area of the mean flame front A_{ref} is dependent on the choice of progress variable isosurface employed to represent the flame front [120]. Moreover, Kim and Bilger (2007) [121] showed that the local consumption speed varies with locations on the flame surface in multi-dimensional flames. The

leading edge displacement speed is also a function of locations in multi-dimensional flames [122]. However, for the case of a statistically stationary 1-D planar flame brush which is the focus of this work, the above three definitions are equal [119] and hence the three definitions can be used interchangeably.

It is also important to recognize the differences between the turbulent flame speed S_T and the front propagation speed w, also known as the displacement speed, used in the flame surface density model, as discussed in Section 2.5.5. The front propagation speed characterizes the propagation of the local flamelet whereas S_T is the velocity pertaining to the mean turbulent brush propagation.

Most early correlations for turbulent flame speeds are phenomenological. Damköhler (1940) [123] first suggested that the increase in flame speed is proportional to the increase in surface area A_T, which in turn is related to the turbulence intensity that

$$\frac{S_T}{S_L} = \frac{A_T}{A_L} = 1 + c\Big(\frac{u'}{S_L}\Big)^q \tag{2.66}$$

Within this framework, Clavin and Williams (1979) [124] derived $q = 2$ based on geometrical considerations. Later they integrated the effects of thermal expansion into the model [125] and suggested that

$$\frac{S_T}{S_L} = \frac{1}{2}\Big[1 + \Big(\big(1 + c(u'/S_L)^2\big)\Big)^{0.5}\Big]^{0.5}. \tag{2.67}$$

Kerstein and Ashurst (1994) [126] proposed a similar form to Damköhler's correlation with $q = 4/3$ by considering the mean passage rate of a propagating interface subject to random advection. Klimov (1983) [127] employed a simplified model of turbulence characterized by a single length and velocity scale and derived the turbulent flame speed as

$$\frac{S_T}{S_L} = 3.5\Big(\frac{u'}{S_L}\Big)^{0.7}. \tag{2.68}$$

Pope and Anand (1985) [105] solved the modeled transport equation for the joint pdf of velocity and progress variable using a Monte Carlo method. They found that in the flamelet regime when $Da > 5$,

$$\frac{S_T}{S_L} = 2.1\Big(\frac{u'}{S_L}\Big). \tag{2.69}$$

Kerstein (1988) [128] modeled the turbulent convection with random exchanges of state (burnt or unburnt) between fluid elements along a discrete line in the streamwise direction. Using the so-called "pair-exchange" model, he formulated

$$\frac{\mathrm{S_T}}{\mathrm{S_L}} = \Big(\frac{u'}{\mathrm{S_L}}\Big)^{0.5} Re_\eta^{1.5}. \tag{2.70}$$

Gouldin's approach (1987) [129] used a fractal description of wrinkled flame surface to predict the flame speed that

$$\frac{\mathrm{S_T}}{\mathrm{S_L}} = \Big\{\big[1-(1-{\mathrm{A_T}}^{0.25} Re_\mathrm{L}^{0.75})e^{-(\mathrm{A_T}/Re_\mathrm{L})^{0.25}(u'/\mathrm{S_L})}\big]{\mathrm{A_T}}^{0.25} Re_\mathrm{L}^{0.75}\Big\}^{D_3-2}. \tag{2.71}$$

in which he suggested a fractal dimension D_3 between 2.32 to 2.4. In the late 1980s, experimental measurements of premixed flame speeds are available. Liu and Lenze (1989) [130] curve-fitted the experimental data and obtained

$$\frac{\mathrm{S_T}}{\mathrm{S_L}} = 1 + 5.3\frac{u'}{{\mathrm{S_L}}^{0.5}}. \tag{2.72}$$

Gülder (1991) [131] found using experimental curve fit, that in the distributed combustion regime

$$\frac{\mathrm{S_T}}{\mathrm{S_L}} = 6.4\Big(\frac{\mathrm{S_L}}{u'}\Big)^{3/4}. \tag{2.73}$$

It was also recognized that turbulent flame speeds potentially not only depend on turbulence intensities, but also on other turbulence or thermodynamic quantities. Zimont *et al.* (1997) [116] proposed a correlation which takes into account the effect of Damköhler number:

$$\frac{\mathrm{S_T}}{\mathrm{S_L}} = 0.52u'Da^{1/4} \sim {u'}^{3/4}{\mathrm{L_o}}^{1/4}{\mathrm{S_L}}^{-1/2}\alpha^{-1/4}, \tag{2.74}$$

where α is the molecular heat diffusivity. Daniele *et al.* (2011) [132] conducted experimental investigation of syngas combustion at pressure up to 20 bar and inlet temperature up to 773 K while turbulence intensity to laminar speed ratio exceeds 100. Their results showed a trend of turbulent flame speed of

$$\frac{\mathrm{S_T}}{\mathrm{S_L}} = 337.5\Big(\frac{u'}{\mathrm{S_L}}\Big)^{0.63}\Big(\frac{\mathrm{L_o}}{\delta_\mathrm{L}}\Big)^{-0.37}\Big(\frac{P}{P_o}\Big)^{0.63}\Big(\frac{\mathrm{T}}{\mathrm{T}_o}\Big)^{-0.63}, \tag{2.75}$$

which is negatively correlated with turbulence length scale and temperature but increases with higher pressure. This is consistent with Ballal and Lefebvre (1975) [133] and Ballal (1979) [134] that turbulent flame speed is reduced by increasing integral length scales at high turbulence levels in a channel. Shepherd *et al.* (1998) [135] also found the same trend from the burning rate measurements in Bunsen flames. On the contrary, increase in burning velocity has been seen with larger integral length scales by other groups [136, 137, 138, 139].

Furthermore, laminar flame speed has shown some impact on S_T. This was confirmed by Lipatnikov and Chomiak (2002) [120] who curve-fitted various experimental databases. Despite of the wide scattering of experimental measurements, a general positive trend is observed between dS_T/du_{rms} and the laminar flame speed S_L. Explicit dependence of turbulent flame speed on pressure has also been reported, i.e., the effects of pressure are not solely manifested in the modifications of laminar flame speed alone:

$$\frac{S_T}{S_L} \sim \Big(S_L\Big)^m \Big(\frac{P}{P_{ref}}\Big)^n. \tag{2.76}$$

Daniele *et al.* (2011) [132] used a power coefficient $n = 0.63$ in their correlation function whereas a weaker dependence on pressure has been reported by Kobayashi (2002) [140], Muppala *et al.* (2005) [141] and Ritzinger (2012) [142] who used values of 0.38, 0.2 and 0.1 respectively for n.

Figure 2.7 graphs fourteen correlations of the turbulent flame speed normalized by the laminar flame speed, i.e., S_T/S_L with increasing turbulence intensities [62, 77, 79, 105, 116, 124, 125, 127, 128, 129, 130, 132, 143]. It is evident that there exists large variation among the predictions of the correlations. The lack of an established model for turbulent flame speed motivates this work where we seek to provide a more fundamental insight on the premixed turbulent flame propagation.

In summary, the turbulent flame speed has been a subject of inquiry in turbulent premixed combustion research in the past decades. Nevertheless, the understanding is far from complete and a universally accepted expression for the speed is not available. In recent years, direct numerical simulations have been employed to study the more

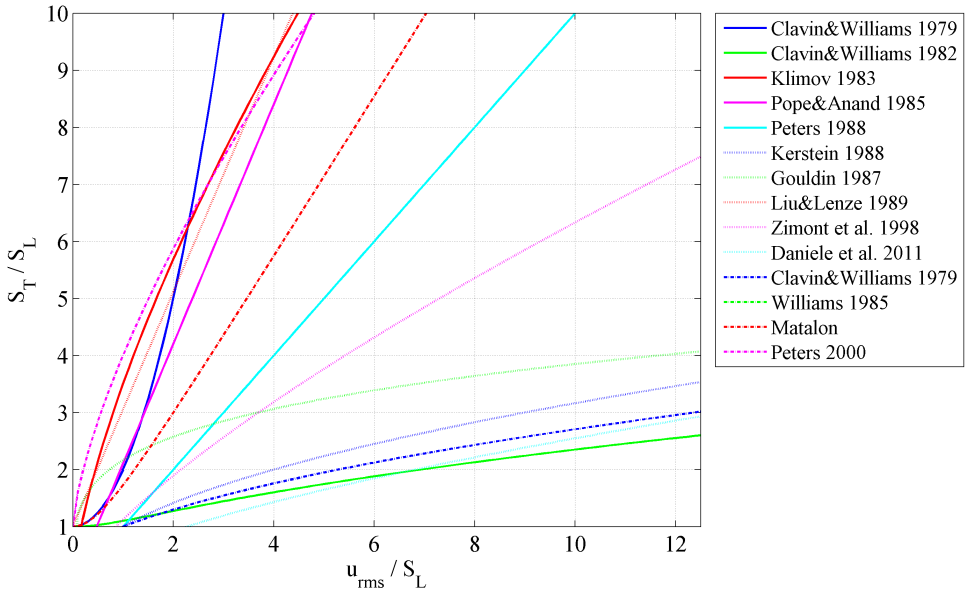

Figure 2.7. Normalized turbulent flame speeds with increasing turbulence intensities by various sources.

fundamental aspects of turbulent flame propagation. These studies will be reviewed in the next section. Similar studies will be carried out in this work.

2.7 DNS of Turbulent Premixed Flames

Direct numerical simulation is a useful tool for studying turbulent combustion. In DNS, all physical length and time scales of the flow are resolved without the use of *á priori* model constants. The major limitation of DNS is the computational cost which renders it impractical for most engineering applications. However, with recent development in high performance computing (HPC), computational resources have become more accessible and affordable for national labs and university research groups. As a result, DNS of turbulent premixed flames at moderate Reynolds numbers have been carried out which allows for in-depth investigation of the turbulence-chemistry inter-

action. In this section, we will summarize the 3D DNS work relevant to premixed combustion.

Tanahashi *et al.* (2005) [144] performed 3D DNS of methane-air premixed flames and studied the statistics of local flame structure. A 23-species 19-step mechanism is used to describe methane oxidation. The highest turbulence intensity considered is 5.8 times the laminar flame speed which gives a Taylor scale Reynolds number Re_λ of 37.4. A large region of low heat release rate was observed on the flame front which is defined as the isothermal contour where heat release rate is maximum in the respective laminar flame. The probability density function of the heat release rate displayed a peak, i.e., the most likely heat release rate, located at 70% of the peak heat release rate of the laminar flame. In addition, higher local heat release rate was observed at locations where the flame surface is convex toward the burned side.

Poludenenko and Oran (2010) [145] performed three DNS of stoichiometric H_2-air flames to investigate the global properties as well as the internal structures of turbulent flame brush when the flame is subjected to high turbulence intensities ($u_{rms}/S_L = 34.5$). A spectral turbulence-driving method is employed to inject turbulent kinetic energy into the domain. This method entails performing inverse Fourier transform on an assumed Kolmogorov-type spectrum to obtain the velocity perturbations. The non-solenoidal components of the generated velocity perturbations are then removed to fulfill the divergence-free condition before being added onto the velocity field on every time step. The flames are simulated over 16 eddy turnover times. It was observed that the flame surface on the fuel side becomes wrinkled on progressively smaller scales with increasing grid resolution whereas the flame surface on the burned side is only curved on scales comparable to the integral length scale. This indicates that the effects of the smaller scales are more pronounced in the preheat zone than in the reaction zone. Turbulent brush thickness grew to a steady value around 16 times the laminar flame thickness after 2 eddy turnover times. Turbulent flame speed, on the other hand, exhibits large variability and no meaningful statistics can be extracted. This is due to the fact that neither the domain size nor the flow period is sufficiently

large to generate a significant statistical sample size to eliminate spatial and temporal variability. It was also shown that the time-averaged mass fraction and temperature profiles in the turbulent flame brush are very close to the laminar profiles inside the reaction zone suggesting that small-scale turbulence fails to penetrate into the reaction zone, and thereby, to modify its internal structure and local speed. These profiles of mass fraction and temperature, however, showed deviation in the preheat zone. Indeed, the total preheat zone width was increased by less than a factor of two compared to the laminar baseline, indicating the broadening of preheat zone by the small eddies typical to the thin reaction zone (TRZ) in the combustion regime diagram of Fig 2.6b.

Poludenenko and Oran (2011) [146] further investigated the results which are presented in their previous work [145] with a focus on the turbulent flame speeds. Isosurfaces of fuel mass fractions were extracted using the "marching cube" algorithm and the areas were plotted as a function of fuel mass fractions. An "inverted-S" shaped curve was seen which suggests the highly convoluted flame surface on the fuel side. In addition, it was shown that the instantaneous turbulent flame speed is primarily determined by the increase in the flame surface area. Turbulent flame speed increment also exhibits exaggerated response to the flame surface augmentation, i.e., $I_o > 1$ where I_o is the stretch factor defined as follows:

$$\frac{\mathrm{S_T}}{\mathrm{S_L}} = I_o(\frac{\mathrm{A_T}}{\mathrm{A_L}}). \tag{2.77}$$

In some cases, I_o can be 30% higher than unity suggesting that there are other mechanisms involved other than surface wrinkling in increasing turbulent flame speed for flames categorized in the TRZ regime. Poludenenko and Oran suggested that the accelerated burning is caused by frequent flame collisions occurring in flow with high turbulence intensity, which resulted in the formation of "cusps." The cusp is a region where local curvature is larger than the inverse of the laminar flame thickness. i.e., $> 1/\delta_{\mathrm{L}}$. Inside a cusp, the focusing of the thermal flux over an extended region of the flame surface results in increase of local burning velocity, and thereby accelerating the overall burning speed.

Aspen *et al.* (2015) [147] performed 3D DNS of lean premixed hydrogen flames at equivalence ratio of 0.4. A range of turbulence conditions is considered when Karlovitz number is between 1 and 36. With increasing Ka, individual structure becomes smaller and thinner flames are observed but the total volume of reacting fluid is much greater. Local extinction events, manifested as breaks in the flame surface, are less pronounced at higher Ka. This is due to higher turbulence reduces the tendency of flame extinction by thermo-diffusive instability (characteristic of hydrogen flame) in regions with negative curvatures. This was contrary to the belief that high Ka would promote local extinction. A decorrelation of fuel consumption and heat release was observed in high Ka flame. In particular, high intensity burning, albeit with a small probability, was seen in the high Ka flame.

Shim *et al.* (2013) [148] carried out 3D DNS of turbulent premixed hydrogen flames under thin reaction zone regime. It was observed that heat release rate is high fluctuating in the region of low temperature. In addition, the mass fractions of radical species such as H_2O_2 and HO_2 are distributed ahead of the flame front in the unburned region. This suggests that small-scale eddies transport species from the preheat zone into the unburned mixture, and thereby enhance local reaction rate. This causes the large fluctuations in the heat release rate inside unburned mixture.

2.8 Summary

In summary, combustion in dual-fuel engines is a multi-faceted problem and the understanding of this subject is still lacking. The pilot fuel autoignites and forms multiple ignition fronts. These fronts then merge to form a flame propagating into the lean homogeneous charge. As the front grows in size, it interacts with an increasing spectrum of turbulent eddies inside the combustion chamber and develops into a fully-developed turbulent premixed flame. Enhanced burning rates result from the wrinkling of the flame front. At the same time, local quenching is possible due to flame stretch. To the best of the author's knowledge, no studies have been carried

out to investigate the ignition behavior and subsequent front propagation in the dual-fuel mixtures on a fundamental level. This work will attempt to fill the gap. Furthermore, propagation of the turbulent premixed flame in the lean homogeneous mixture are not well understood. In particular, there is no universally accepted closure for turbulent flame speed. Due to the limitations on computational resources, studies of turbulence-chemistry interactions using fully-resolved 3D DNS have only started to appear in recent years but are still scarce. In this work, a novel method is developed to alleviate the computational expenses of DNS of premixed flames. This is achieved by simulating statistically-stationary turbulent flames using a feedback mechanism. Within this framework, parametric studies will be carried out to characterize the dependence of turbulent flame speeds on various parameters. Turbulence-chemistry interactions will also be investigated.

3. COMPUTATIONAL METHODS

3.1 Introduction

The current chapter provides the details of the computational methods employed in this work. Two in-house numerical codes have been used to perform the direct numerical simulations. The first is a codenamed Flow Large-Eddy and Direct Simulations (FLEDS) code [149, 150, 151] and is a fully-compressible code. Note that the discussion on FLEDS follows that given in Anders (2006) [151]. The second is named High-Order LOw-MAch Combustion (HOLOMAC) code and has been recently developed by Motheau and Abraham [152]. It solves the reactive compressible Navier-Stokes equations under the low-Mach number assumption. This is also known as the weakly-compressible formulation in which compressibility effects are not considered but the flow density is allowed to vary. The rest of Chapter 3 is organized as follows: Section 3.2 presents the common set of conservation equations solved by these two numerical codes. Section 3.3 discusses the discretization strategies together with filtering schemes employed in FLEDS. Implementation of various boundary conditions in FLEDS is described in Section 3.4. Parallelization performance is briefly described in Section 3.5. Section 3.6 is dedicated to the discussion of the numerics employed in HOLOMAC. Section 3.7 lists some of the prior studies carried out using the two in-house codes.

3.2 Governing Equations

The two in-house codes solve the equations for the conservation of mass, momentum, energy and species together with the equations of state given by Eqs. (3.1–3.5). Note that under the low-Ma number assumption, the pressure $p(\vec{x}, t)$ can be split into a spatially-uniform thermodynamic part, i.e., $p_0(t)$, and a hydrodynamic part,

i.e., $p_1(\vec{x}, t)$, and thereby resulting in some slight modifications to Eqs. (3.2, 3.3 and 3.5). More details will be provided in the discussion of numerics of HOLOMAC under Section 3.6.

i. Continuity equation

$$\frac{\partial \rho}{\partial t} + \frac{\partial \rho u_j}{\partial x_j} = 0. \tag{3.1}$$

ii. Navier-Stokes equation

$$\frac{\partial \rho u_i}{\partial t} + \frac{\partial \rho u_j u_i}{\partial x_j} = -\frac{\partial p}{\partial x_i} + \frac{\partial \tau_{ij}}{\partial x_j} + F_i. \tag{3.2}$$

iii. Conservation of energy

$$\frac{\partial \rho E}{\partial t} + \frac{\partial \rho u_j E}{\partial x_j} = -\frac{\partial u_j p}{\partial x_j} + \frac{\partial u_i \tau_{ij}}{\partial x_j} + \frac{\partial}{\partial x_j}\left(\lambda \frac{\partial \mathrm{T}}{\partial x_j}\right) + \frac{\partial}{\partial x_j}\left(\rho \sum_k h_k D_k \frac{\partial \mathrm{Y}_k}{\partial x_j}\right) + u_j F_j. \tag{3.3}$$

iv. Conservation of species

$$\frac{\partial \rho \mathrm{Y}_k}{\partial t} + \frac{\partial \rho u_j \mathrm{Y}_k}{\partial x_j} = \frac{\partial}{\partial x_j}\left(\rho D_k \frac{\partial \mathrm{Y}_k}{\partial x_j}\right) + \dot{\omega}_k. \tag{3.4}$$

v. Equations of state

$$p = \rho \mathcal{R} \mathrm{T} \sum_k \frac{\mathrm{Y}_k}{\mathrm{W}_k}. \tag{3.5}$$

Here, ρ, u_j and T are the density, velocity component in the j_{th} ($j = 1, 2, 3$) direction and temperature of the mixture, respectively. F_i is the external force on the flow in the i_{th} direction. τ_{ij} is the viscous stress tensor and is given by

$$\tau_{ij} = \mu\left(\frac{\partial u_i}{\partial x_j} + \frac{\partial u_j}{\partial x_i}\right) - \frac{2}{3}\mu \frac{\partial u_l}{\partial x_l}\delta_{ij}. \tag{3.6}$$

The total energy E is defined as the sum of kinetic energy and internal energy e, i.e.,

$$E = e + \frac{1}{2} u_i u_i. \tag{3.7}$$

Thermal conductivity of the mixture is denoted by λ and h_k, D_k, Y_k and W_k are the enthalpy, molecular diffusivity, mass fraction and molecular weight of the k_{th} species,

respectively. Specific heat capacity, thermal conductivity and molecular diffusivity of each species are provided as a function of temperature in the CHEMKIN format to start the simulation. Corresponding enthalpy of species k is evaluated as

$$h_k = h_k^\circ + \int_{298}^{\mathrm{T}} c_{p,k} d\mathrm{T}, \tag{3.8}$$

where h_k° is the enthalpy of formation of the k_{th} species. $\mathcal{R}$ is the universal gas constant. Some simplifying assumptions are employed in the computational model. For instance, heat fluxes due to the Dufour effect and mass fluxes due to the Soret effect are neglected. Radiation heat loss is not accounted for in this model. Ideal gas behavior is also assumed which is generally true at high temperature conditions.

3.3 Numerics of FLEDS

The FLEDS code solves the equations of motion using a non-staggered 3-D Cartesian grid. The governing equations are discretized in space using a 6th-order compact finite-difference scheme developed by Lele (1992) [153]. In this particular formulation, stencils of only five points are needed to evaluate the first and the second derivatives at the non-boundary nodes, i.e., nodes that are at least two points away from the boundary. Consider a generic quantity f at node i along a certain direction. The first and the second derivatives in this direction can be evaluated using the compact scheme as, respectively:

$$\frac{1}{3}f'_{i-1} + f'_i + \frac{1}{3}f'_{i+1} = \frac{7}{9h}(f_{i+1} - f_{i-1}) + \frac{1}{36h}(f_{i+2} - f_{i-2}), \tag{3.9}$$

$$\frac{2}{11}f''_{i-1} + f''_i + \frac{2}{11}f''_{i+1} = \frac{12}{11h^2}(f_{i+1} - 2f_i + f_{i-1}) + \frac{3}{44h^2}(f_{i+2} - 2f_i + f_{i-2}). \tag{3.10}$$

Here, h represents the grid spacing of a uniform grid in the direction of differentiation. In the case of non-uniform grid, grid transformation can be employed to map derivatives in the physical space x_i to those in the uniform space ξ_i using the simple relation:

$$f' = \frac{\partial f}{\partial \xi} \cdot \left(\frac{dx}{d\xi}\right)^{-1}, \tag{3.11}$$

$$f'' = \frac{\partial^2 f}{\partial \xi^2} \cdot \left(\frac{dx}{d\xi}\right)^{-2} - \frac{\partial f}{\partial \xi} \cdot \left(\frac{dx}{d\xi}\right)^{-3} \cdot \frac{d^2x}{d\xi^2}, \tag{3.12}$$

where $x(\xi)$ is the known transformation function and must be continuous and differentiable. For nodes that are close to the boundaries, lower orders of discretization are used. For $i = 1$ or $i = N$, the first and the second derivatives are evaluated using a 3rd-order biased scheme:

$$\begin{cases} f'_i + 2f'_{i+1} = -\frac{5}{2h} f_i + \frac{2}{h} f_{i+1} + \frac{1}{2h} f_{i+2} & \text{if } i = 1; \\ f'_i + 2f'_{i-1} = +\frac{5}{2h} f_i - \frac{2}{h} f_{i-1} - \frac{1}{2h} f_{i-2} & \text{if } i = N; \end{cases} \tag{3.13}$$

$$\begin{cases} f''_i + 11f''_{i+1} = \frac{13}{h^2} f_i - \frac{27}{h^2} f_{i+1} + \frac{15}{h^2} f_{i+2} - \frac{1}{h^2} f_{i+3} & \text{if } i = 1; \\ f''_i + 11f''_{i-1} = \frac{13}{h^2} f_i - \frac{27}{h^2} f_{i-1} + \frac{15}{h^2} f_{i-2} - \frac{1}{h^2} f_{i-3} & \text{if } i = 1; \end{cases} \tag{3.14}$$

For $i = 2$ and $i = N - 1$ points, a 4th-order central-difference approximation is used to compute the first and the second derivatives, respectively:

$$\frac{1}{4} f'_{i-1} + f'_i + \frac{1}{4} f'_{i+1} = \frac{3}{4h}\Big(f_{i+1} - f_{i-1}\Big), \tag{3.15}$$

$$\frac{1}{10} f''_{i-1} + f''_i + \frac{1}{10} f''_{i+1} = \frac{12}{10h^2}\Big(f_{i+1} - 2f_i + f_{i-1}\Big). \tag{3.16}$$

For $i = 3$ and $i = N - 2$ points, a 4th-order central-difference approximation is used to compute the first derivative:

$$\frac{37}{112} f'_{i-1} + f'_i + \frac{37}{112} f'_{i+1} = \frac{87}{112h}\Big(f_{i+1} - f_{i-1}\Big) + \frac{3}{112h}\Big(f_{i+2} - f_{i-2}\Big), \tag{3.17}$$

The one-sided scheme used at the two boundaries, i.e., $i = 1$ and $i = N$ allows the system of linear equations to be written in terms of the product of a tri-diagonal matrix and a vector. These spatial derivatives are then solved using the Tri-diagonal Matrix Algorithm (TDMA), also known as the Thomas algorithm. The solution can be obtained much faster with merely $\mathcal{O}(N)$ operations where N is the total number of grid points as opposed to $\mathcal{O}(N^3)$ operations required by the standard Gaussian elimination technique [154].

The time integration of ρu_i, ρE and $\rho \mathrm{Y}_k$ in Eqs. (3.2–3.4) is carried out using a compact storage 4th-order Runge-Kutta scheme in FLEDS [155]. The constants

are given by Gill (1951) [156]. The implementation is briefly described as follows. Consider an initial value problem specified by

$$\frac{\partial y}{\partial t} = f(t, y); \quad y(t^n) = y^n, \tag{3.18}$$

where a generic variable y needs to be advanced from the n_{th} to the subsequent step over a time-step of Δ_t. Four intermediate increments (k_1, k_2, k_3 and k_4) are made within each time-step and the solution at the next iteration, i.e., y^{n+1} is written as a weighted average of the four predictions which are shown in Eqs. (3.19–3.22):

$$k_1 = f(t^n, y^n), \tag{3.19}$$

$$k_2 = f\Big(t^n + \frac{1}{2}\Delta_t, y^n + \frac{1}{2}\Delta_t k_1\Big), \tag{3.20}$$

$$k_3 = f\Big(t^n + \frac{1}{2}\Delta_t, y^n + (-\frac{1}{2} + \frac{1}{\sqrt{2}})\Delta_t k_1 + (1 - \frac{1}{\sqrt{2}})\Delta_t k_2\Big), \tag{3.21}$$

$$k_4 = f\Big(t^n + \Delta_t, y^n - \frac{1}{\sqrt{2}}\Delta_t k_2 + (1 + \frac{1}{\sqrt{2}})\Delta_t k_3\Big), \tag{3.22}$$

$$y^{n+1} = y^n + \frac{\Delta_t}{6}\Big[k_1 + 2(1 - \frac{1}{\sqrt{2}})k_2 + 2(1 + \frac{1}{\sqrt{2}})k_3 + k_4\Big]. \tag{3.23}$$

The step size of time advancement is determined on-the-fly in FLEDS to satisfy the stability constraints imposed by the Courant-Friederichs-Lewey (CFL) criterion [157], i.e.,

$$\Delta_t \cdot \max\Big\{\frac{1}{\delta_{ix}} + \frac{1}{\delta_{iy}} + \frac{1}{\delta_{iz}}\Big\} \leq \text{CFL}, \tag{3.24}$$

where CFL is the CFL number and is selected to be 0.9 in this work. Here δ_{ix} is estimated as:

$$\delta_{ix} = \frac{\Delta_x \Delta_y \Delta_z}{(|u_i| + c)\Delta_y \Delta_z + (\frac{2\lambda}{\rho c_p} + \nu)\Delta_x}, \tag{3.25}$$

where Δ_x, Δ_y and Δ_z denote the grid spacing in the x, y and z directions, respectively, and c is the speed of sound given by

$$c = \sqrt{\gamma \mathcal{R} \text{T}}. \tag{3.26}$$

It is important to point out that since the speed of sound is present in the denominator of Eq. (3.25), the time step employed in FLEDS is acoustically limited, i.e., acoustic

waves are resolved in time. While this is necessary for simulating compressible flows, e.g., turbulent diesel jet, it is an overkill in incompressible simulations and significantly increases the numerical burden.

A spatial filter is applied at the end of each iterative step. It is meant to remove any spurious waves close to the grid scales similar to a low-pass filter (filtering out the high frequencies). In this way, the spatial filtering prevents energy build-up at the small scales which will lead to numerical instabilities. In this work, we employed a compact scheme which preserved the 6th-order spatial accuracy [153]. The general form of the filtering operation is described as:

$$\begin{aligned}\beta\hat{f}_{i-2} + \alpha\hat{f}_{i-1} + \hat{f}_i + \alpha\hat{f}_{i+1} + \beta\hat{f}_{i+2} \\ = af_i + \frac{d}{2}(f_{i+3} + f_{i-3}) + \frac{c}{2}(f_{i+2} + f_{i-2}) + \frac{b}{2}(f_{i+1} + f_{i-1}),\end{aligned} \tag{3.27}$$

where $\hat{f}_i$ represents the filtered quantity at node x_i. By Taylor-expanding Eq. (3.27) and matching the terms of the same orders, a 6th-order accurate scheme requires that

$$\begin{aligned} a &= \frac{1}{16}(11 + 10\alpha - 10\beta); \\ b &= \frac{1}{32}(15 + 34\alpha + 30\beta); \\ c &= \frac{1}{16}(-3 + 6\alpha + 26\beta); \\ d &= \frac{1}{32}(1 - 2\alpha + 2\beta); \end{aligned} \tag{3.28}$$

With some clever choice of coefficient, i.e., $\beta = 0$, a tri-diagonal system of equations is restored which can again be solved using TDMA. The only free parameter α is used to determine the cut-off frequency of the low-pass filter. A value of $\alpha = 0.5$ results in no filtering at all and as α grows smaller, energy dissipation becomes active at larger length scales (smaller wavenumbers). This is depicted in Fig. 3.1 that as α decreases, the transfer function representing the filtering operation in the Fourier space deviates more from unity, especially at high wavenumbers.

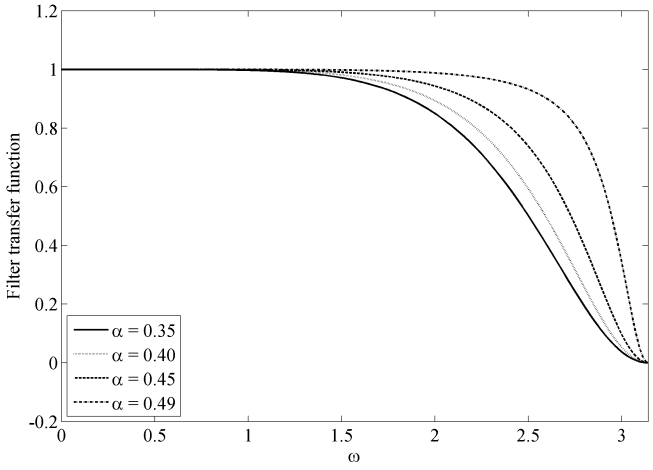

Figure 3.1. Filter transfer function in the spectral space for $\alpha = 0.35$, 0.40, 0.45 and 0.49.

3.4 Boundary Conditions in FLEDS

The computational domain employed in a numerical code is often smaller than the natural domain of the fluid flow of interest. This can be done by making assumptions about the flow field. For example, if there exists symmetry in the flow, e.g., axisymmetry in pipe flow or infinitely large box of homogeneous isotropic turbulence, periodic boundaries can be employed to reflect this similarity. Inflow and outflow boundaries are used to account for the behavior of the fluid outside the computational domain and its interaction with the flow inside. In particular, ideal inflow boundaries should guide the flow into the domain consistent with what would have occurred should the computational domain extend to infinity. Ideal outflow boundaries, on the other hand, should cause no disturbance to the flow exiting the domain as if the boundaries are absent.

Handling of inflow and outflow boundary conditions is particularly challenging in transient compressible flow simulations. This is because the acoustic waves which are resolved in the direct numerical simulations (DNS) are strongly coupled with other flow properties, e.g., velocity and temperature. In the field of reacting flows, inter-

actions between turbulent combustion and acoustic waves may lead to combustion instabilities if the waves are not handled properly by the imposed boundary conditions [158]. In addition, incorrect set of boundary conditions applied to the Navier-Stokes equations may lead to ill-posed formulations. In this study, we employed the Navier-Stokes characteristic boundary conditions (NSCBC) method proposed by Poinsot and Lele (1992) [159], which is based on the analysis of characteristic waves crossing the boundary [160]. Anders *et al.* (2007) [161] modified the method to account for characteristic waves of multi-component species across the boundary in FLEDS. Within the scope of this work, we will only discuss the two relevant types of boundary condition, i.e., subsonic inflow and subsonic outflow.

3.4.1 Wave analysis on Navier-Stokes equations

For 3D flows governed by the Navier-Stokes equation, five physical boundary conditions are needed for a subsonic inflow type to ensure well-posedness while for a subsonic outflow type four physical boundary conditions are needed [162]. Physical boundary condition means the explicit specification of a known physical variable at the boundary [159]. This is in contrast to the concept of "soft" boundary condition which is employed when the number of physical boundary conditions to ensure well-posedness is less than the number of conditions required for numerically solving the system, i.e., in the case of subsonic outflow. Another level of complication to this problem is that at each boundary some of the waves are propagating out while others are entering into the domain. Figure 3.2 shows that for a subsonic flow, four characteristic waves, i.e., $\mathcal{L}_2$, $\mathcal{L}_3$, $\mathcal{L}_4$ and $\mathcal{L}_5$ are entering the computational domain at the inflow boundary whereas one, i.e., $\mathcal{L}_1$ is entering from the outflow boundary. Here, $\mathcal{L}_i$ represents the amplitude of the characteristic waves following Thompson's analysis (1977) [160].

Poinsot and Lele's method [159] to specify soft boundary conditions is by relating the unknown quantity to the set of physical boundary conditions using the conserva-

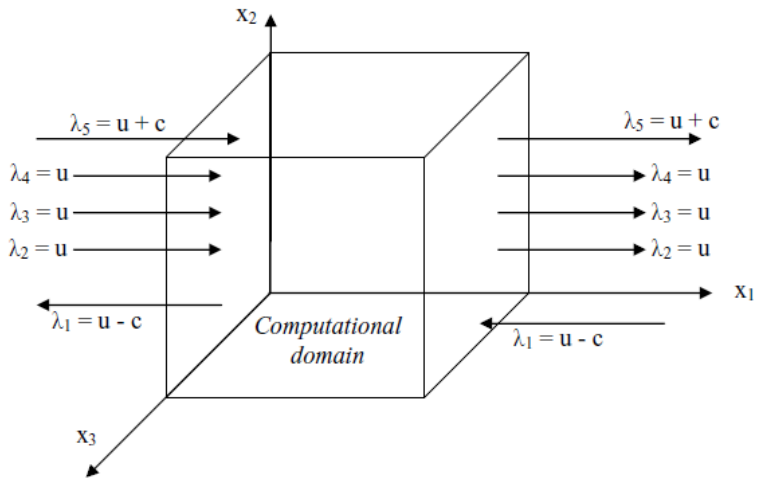

Figure 3.2. Schematic representations of the characteristic waves entering or leaving the computational domain at the subsonic inflow (left) and the subsonic outflow (right) boundaries.

tion equations. For characteristic waves travelling in x_1 direction as shown in Figure 3.2, the full set of governing equation, i.e., Eqs. (3.1–3.4) can be recast into the following forms:

$$\frac{\partial \rho_k}{\partial t} + d_1^k + \frac{\partial m_2}{\partial x_2} + \frac{\partial m_3}{\partial x_3} = 0, \tag{3.29}$$

$$\frac{\partial m_1}{\partial t} + u_1 \sum_k d_1^k + \rho d_3 + \frac{\partial m_1 u_2}{\partial x_2} + \frac{\partial m_1 u_3}{\partial x_3} = \frac{\partial \tau_{11}}{\partial x_1} + \frac{\partial \tau_{12}}{\partial x_2} + \frac{\partial \tau_{13}}{\partial x_3}, \tag{3.30}$$

$$\frac{\partial m_2}{\partial t} + u_2 \sum_k d_1^k + \rho d_4 + \frac{\partial m_2 u_2}{\partial x_2} + \frac{\partial m_2 u_3}{\partial x_3} = \frac{\partial \tau_{21}}{\partial x_1} + \frac{\partial \tau_{22}}{\partial x_2} + \frac{\partial \tau_{23}}{\partial x_3}, \tag{3.31}$$

$$\frac{\partial m_3}{\partial t} + u_3 \sum_k d_1^k + \rho d_5 + \frac{\partial m_3 u_2}{\partial x_2} + \frac{\partial m_3 u_3}{\partial x_3} = \frac{\partial \tau_{31}}{\partial x_1} + \frac{\partial \tau_{32}}{\partial x_2} + \frac{\partial \tau_{33}}{\partial x_3}, \tag{3.32}$$

$$\begin{aligned} &\frac{\partial \rho E}{\partial t} + \frac{1}{2}(u_l u_l) \sum_k d_1^k + \frac{d_2}{\kappa} + m_1 d_3 + m_2 d_4 + m_3 d_5 \\ &\quad - \frac{1}{\kappa} \sum_k \chi_k d_1^k + \frac{\partial (\rho E + p) u_2}{\partial x_2} + \frac{\partial (\rho E + p) u_3}{\partial x_3} = \frac{\partial u_j \tau_{ij}}{\partial x_i} - \frac{\partial q_i}{\partial x_i}, \end{aligned} \tag{3.33}$$

Here, d_i ($i = 1, \ldots, 5$) are the derivative terms parallel to the x_1 direction in the conservation equations and can be expressed in terms of the amplitudes of characteristic waves:

$$d_1^k \equiv \frac{\partial \rho^k u_1}{\partial x_1} = \frac{1}{c^2}\Big[\mathcal{L}_2^k + \frac{\mathrm{Y}_k}{2}(\mathcal{L}_5 + \mathcal{L}_1)\Big], \tag{3.34}$$

$$d_2 \equiv \frac{\partial c^2 \rho u_1}{\partial x_1} + (1-\gamma)\mu \frac{\partial p}{\partial x_1} = \frac{1}{2}(\mathcal{L}_5 + \mathcal{L}_1), \tag{3.35}$$

$$d_3 \equiv u_1 \frac{\partial u_1}{\partial x_1} + \frac{1}{\rho}\frac{\partial p}{\partial x_1} = \frac{1}{2\rho c}(\mathcal{L}_5 - \mathcal{L}_1), \tag{3.36}$$

$$d_4 \equiv u_1 \frac{\partial u_2}{\partial x_1} = \mathcal{L}_3, \tag{3.37}$$

$$d_5 \equiv u_1 \frac{\partial u_3}{\partial x_1} = \mathcal{L}_4, \tag{3.38}$$

where c is the speed of sound. After some manipulation, Eqs. (3.39–3.43) yield the solution for the amplitudes of the five characteristic waves as follows:

$$\mathcal{L}_1 = \lambda_1 \Big(\frac{\partial p}{\partial x_1} - \rho c \frac{\partial u_1}{\partial x_1} \Big), \tag{3.39}$$

$$\mathcal{L}_2^k = \lambda_2 \Big(c^2 \frac{\partial \rho_k}{\partial x_1} - \mathrm{Y}_k \frac{\partial p}{\partial x_1} \Big), \tag{3.40}$$

$$\mathcal{L}_3 = \lambda_3 \frac{\partial u_2}{\partial x_1}, \tag{3.41}$$

$$\mathcal{L}_4 = \lambda_4 \frac{\partial u_3}{\partial x_1}, \tag{3.42}$$

$$\mathcal{L}_5 = \lambda_5 \Big(\frac{\partial p}{\partial x_1} + \rho c \frac{\partial u_1}{\partial x_1} \Big). \tag{3.43}$$

where the velocities of these five characteristic waves as shown in Figure 3.2 are given by:

$$\lambda_1 = u_1 - c < 0, \tag{3.44}$$

$$\lambda_2 = u_1, \tag{3.45}$$

$$\lambda_3 = u_1, \tag{3.46}$$

$$\lambda_4 = u_1, \tag{3.47}$$

$$\lambda_5 = u_1 + c. \tag{3.48}$$

To simplify the problem, Poinsot and Lele (1992) [159] made the "Local One-Dimensional Inviscid" (LODI) assumption, i.e., flow on the boundaries along x_1 direction is assumed with zero velocity in the other two directions and viscous effects

neglected. Essentially, the 1D Euler equation is used to describe the flow behavior at boundary conditions. With that assumption, Eqs. (3.29–3.33) become

$$\frac{\partial \rho \mathrm{Y}_k}{\partial t} + \frac{1}{c^2}\Big[\mathcal{L}_2^k + \frac{\mathrm{Y}_k}{2}(\mathcal{L}_5 + \mathcal{L}_1)\Big] = 0, \tag{3.49}$$

$$\frac{\partial p}{\partial t} + \frac{1}{2}(\mathcal{L}_5 + \mathcal{L}_5) = 0, \tag{3.50}$$

$$\frac{\partial u_1}{\partial t} + \frac{1}{2\rho c}(\mathcal{L}_5 - \mathcal{L}_1) = 0, \tag{3.51}$$

$$\frac{\partial u_2}{\partial t} + \mathcal{L}_3 = 0, \tag{3.52}$$

$$\frac{\partial u_3}{\partial t} + \mathcal{L}_4 = 0, \tag{3.53}$$

$$\frac{\partial \mathrm{T}}{\partial t} + \frac{\mathrm{T}}{\rho c^2}\Big[-\sum_k \mathcal{L}_2^k + \frac{1}{2}(\gamma - 1)(\mathcal{L}_5 + \mathcal{L}_1)\Big] = 0. \tag{3.54}$$

With the knowledge of the characteristic waves $\mathcal{L}_i$, flow variables on the boundaries can be advanced in time using the same 4th-order Runge-Kutta scheme describe in Section 3.3. The next two sub-sections will discuss the detailed implementations applicable to subsonic inflow and outflow used in this study.

3.4.2 Subsonic inflow boundary

For an inflow boundary, knowledge about velocities, temperature and species mass fractions is often available, i.e., they are often imposed by the users. The only unknown is the density (or equivalently pressure if the equation of state is employed). As evident in Fig. 3.2, characteristic wave $\mathcal{L}_1$ is leaving the computational domain at the inflow boundary and thereby can be determined from the interior points using the one-sided approximation of Eq. (3.39). In contrast, the other four waves are entering the domain and they can only be evaluated invoking the physical boundary conditions imposed though the following steps:

$$\mathcal{L}_5 = \mathcal{L}_1 - 2\rho c \frac{du_1}{dt}, \tag{3.55}$$

$$\mathcal{L}_2 = \frac{1}{2}(\gamma - 1)(\mathcal{L}_5 + \mathcal{L}_1) + \frac{\rho c^2}{\mathrm{T}}\frac{d\mathrm{T}}{dt}, \tag{3.56}$$

$$\mathcal{L}_3 = -\frac{du_2}{dt}, \tag{3.57}$$

$$\mathcal{L}_4 = -\frac{du_3}{dt}. \tag{3.58}$$

After that, Eq. (3.29) is used to advance density to the next time-step, i.e.,

$$\frac{\partial \rho}{\partial t} = -\frac{1}{c^2}\Big[\sum_k \mathcal{L}_2^k + \frac{1}{2}(\mathcal{L}_5 + \mathcal{L}_1)\Big] - \frac{d\rho u_2}{dx_2} - \frac{d\rho u_3}{dx_3}. \tag{3.59}$$

In this case, $\mathcal{L}_3$ and $\mathcal{L}_4$ are not needed at all.

3.4.3 Subsonic outflow boundary

For a subsonic outflow boundary, four characteristic waves, i.e., $\mathcal{L}_2$, $\mathcal{L}_3$, $\mathcal{L}_4$ and $\mathcal{L}_5$, are propagating out of the domain while $\mathcal{L}_1$ is propagating inward. By employing the relations in Eqs. (3.40–3.42), the four outgoing wave amplitudes can be computed from interior nodes. However, no physical boundary condition is known to specify the last wave. Instead, a soft boundary condition is used in which the mean static pressure of the flow leaving the domain is designed to asymptotically tend towards specified values:

$$\mathcal{L}_1 = \frac{\sigma(1 - \mathrm{M}^2)c}{\mathrm{L}}(p - p_\infty). \tag{3.60}$$

Here, σ has a constant value of 0.25. M is the maximum Mach number in the flow and L is the characteristic length scale of the domain. This formulation is consistent with the physical phenomenon where the flow "senses" the acoustic waves propagating back from infinity (which is at pressure p_∞) through the outflow boundaries and adjusts its mean pressure accordingly.

3.5 Parallelization and Performance

The FLEDS code is written in Fortran90 and parallelized using the message passing interface (MPI) library. Scaling analysis has been performed by Sayeed *et al.* (2011) [163]. It was observed that as the number of processors increases while the domain size is fixed, i.e., strong scaling test, an almost ideal linear speed-up is achieved

up until 512 processors are used and speed-up efficiency of 75% is recovered when using 4096 processors. In the weak scaling analysis where the problem size increases while fixing the number of processors, excellent performance up to 32K processors was observed.

3.6 Numerics of HOLOMAC

The typical flame propagation speed under engine conditions is much slower than the propagation speed of acoustic waves and consequently the Mach number of the flow is relatively small (M $<$ 0.02). However, compressible solvers, e.g., FLEDS, enforce the constraint in the time advancement step to resolve the acoustic waves and this results in an unwarranted computational cost when the compressibility effect in the simulated flow is negligible. This has inspired the creation of HOLOMAC which makes the low-Mach number assumption thereby relieving the acoustic constraint on time step but still accounting for density variations which arise in combustion problems.

According to the dimensional analysis of the momentum equation performed by Giovangigli (1999) [164], the pressure term can be written as

$$p(\vec{x},t) = p_0(t) + \underbrace{p_1(\vec{x},t)}_{\mathcal{O}(M^2)}, \tag{3.61}$$

where $p_0(t)$ is spatially uniform and $p_1(\vec{x},t)$ is the hydrodynamic perturbation which varies with the square of the Mach number. Under the low-Mach number assumption, i.e., as M $\rightarrow$ 0, the equation of state becomes

$$p_o(t) = \rho \mathcal{R} \mathrm{T} \sum_k \frac{\mathrm{Y}_k}{\mathrm{W}_k}. \tag{3.62}$$

This implies a decoupling of the thermodynamic pressure p_0 and the fluctuating part p_1. Consequently the conservation of momentum and energy, i.e., Eqs. (3.2–3.4), can be re-written in the decoupled form:

$$\frac{\partial \rho u_i}{\partial t} = \underbrace{-\frac{\partial \rho u_j u_i}{\partial x_j}}_{\mathbf{C}_{u_i}} + \frac{\partial p_1}{\partial x_i} + \underbrace{\frac{\partial \tau_{ij}}{\partial x_j}}_{\mathbf{D}_{u_i}} + F_i, \tag{3.63}$$

$$\begin{aligned}\frac{\partial \mathrm{T}}{\partial t} = {} & \frac{1}{\rho c_p}\frac{\partial p_0}{\partial t} + \underbrace{-u_i \frac{\partial \mathrm{T}}{\partial x_i}}_{\mathbf{C}_\mathrm{T}} \\ & + \underbrace{\frac{1}{\rho c_p}\left[\frac{\partial}{\partial x_i}\left(\lambda \frac{\partial \mathrm{T}}{\partial x_i}\right)\right] + \frac{1}{\rho c_p}\left(\rho \sum_k c_{p,k} V_{i,k} \mathrm{Y}_k\right)\frac{\partial \mathrm{T}}{\partial x_i}}_{\mathbf{D}_\mathrm{T}} \underbrace{- \frac{1}{\rho c_p}\sum_k h_k \dot{\omega}_k}_{\mathbf{R}_\mathrm{T}},\end{aligned} \tag{3.64}$$

$$\frac{\partial \mathrm{Y}_k}{\partial t} = \underbrace{-u_i \frac{\mathrm{Y}_k}{x_i}}_{\mathbf{C}_\mathrm{Y}} + \underbrace{\frac{1}{\rho}\frac{\partial \rho V_{i,k} \mathrm{Y}_k}{\partial x_i}}_{\mathbf{D}_\mathrm{Y}} + \underbrace{\frac{1}{\rho}\dot{\omega}_k}_{\mathbf{R}_\mathrm{Y}}, \tag{3.65}$$

The diffusion velocities in species (and also in energy) conservation equations are given by Eq. (3.66). The second term is a correction velocity term to enforce mass conservation during species diffusion.

$$V_{i,k}\mathrm{Y}_k = D_k \frac{\partial \mathrm{Y}_k}{\partial x_i} - \mathrm{Y}_k \sum_{m=1}^{N_s} D_m \frac{\partial \mathrm{Y}_m}{\partial x_i}. \tag{3.66}$$

The overall algorithm employed in HOLOMAC consists of two parts. In the first part, temperature and species mass fractions are advanced in time using their respective conservations. This is done using a Strang operator-split scheme [165] that preserves second-order accuracy in time. Such a scheme can be represented by:

$$\mathbf{H}(t^{n+1}) = \mathcal{H}^{C-D}_{\Delta t/2}\mathcal{H}^{R}_{\Delta t}\mathcal{H}^{C-D}_{\Delta t/2}\mathbf{H}(t^n), \tag{3.67}$$

where the solution $\mathbf{H}(t^n)$ at time t^n is first integrated over half of a time step with convective and diffusion terms, i.e., $\mathcal{H}^{C-D}_{\Delta t/2}$, followed by a full time step integration of reaction rates, i.e., $\mathcal{H}^{R}_{\Delta t}$ and finished with another integration of convective and diffusion terms over the second half time step. The new density can then be computed using the equation of state in Eq. (3.62) with updated temperature and mass

fractions. In the second part, a projection-correction method is used to solve the Navier-Stokes equations. More specifically, velocity fields are integrated in time with the knowledge of the new density from previous part and corrected by solving a variable-coefficient Poisson equation to enforce the divergence condition imposed by continuity. Details of the implementation are provided in the following sub-sections. Note that the numerical methods used in HOLOMAC are built upon the open source code Incompact3D [166, 167] and the 2DECOMP&FFT algorithms [168]. More information about spatial discretization and parallelization techniques can be found in these publications.

3.6.1 Evaluation of explicit terms

Each iteration starts out with the computation of the source terms and convection terms in the momentum, energy and species equations. This is done using a 2nd-order Adams-Bashforth (AB2) scheme as follows:

$$\mathbf{S}_{u_i} = (1+\zeta_t)\mathbf{C}^n_{u_i} - \zeta_t \mathbf{C}^{n-1}_{u_i} - \frac{\partial p^n_1}{\partial x_i}, \tag{3.68}$$

$$\mathbf{S}_{\mathrm{T}} = (1+\zeta_t)\mathbf{C}^n_{\mathrm{T}} - \zeta_t \mathbf{C}^{n-1}_{\mathrm{T}} + \frac{1}{(1+\zeta_t)\rho^n c^n_p - \zeta_t \rho^{n-1} c^{n-1}_p} \frac{\partial \tilde{p}_0}{\partial x_1}, \tag{3.69}$$

$$\mathbf{S}_{\mathrm{Y}_k} = (1+\zeta_t)\mathbf{C}^n_{\mathrm{Y}_k} - \zeta_t \mathbf{C}^{n-1}_{\mathrm{Y}_k}, \tag{3.70}$$

where

$$\zeta_t = \frac{(t^{n+1}-t^n)}{2(t^n - t^{n-1})}. \tag{3.71}$$

3.6.2 Half-step integration of convective and diffusion terms

Time integration of the diffusion terms is performed using an explicit Runge-Kutta-Chebyshev (RKC) method [169]. Temperature and mass fractions are computed in each sub-step and density is updated using Eq. (3.62). The exact number of iteration steps is a user-input and is denoted by s in HOLOMAC. At the first step,

$$\mathrm{T}^1 = \mathrm{T}^0 = \tilde{\eta}_1 \frac{\Delta t}{2}\big(\mathbf{D}^0_{\mathrm{T}} + \mathbf{S}_{\mathrm{T}}\big), \tag{3.72}$$

$$\mathrm{Y}_k^1 = \mathrm{Y}_k^0 = \tilde{\eta}_1 \frac{\Delta t}{2}\big(\mathbf{D}_{\mathrm{Y}_k}^0 + \mathbf{S}_{\mathrm{Y}_k}\big), \tag{3.73}$$

$$\rho^1 = \frac{p_0^n}{\mathcal{L}\mathrm{T}^1 \sum_k \mathrm{Y}_k^1/\mathrm{W}_k^1}, \tag{3.74}$$

and subsequently,

$$\mathrm{T}^s = (1-\eta_s-\nu_s)\mathrm{T}^0 + \eta_s \mathrm{T}^{s-1} + \nu_s \mathrm{T}^{s-2} + \tilde{\eta}_s \frac{\Delta t}{2}\Big(\mathbf{D}_{\mathrm{T}}^{s-1} + \mathbf{S}_{\mathrm{T}}\Big) + \tilde{\gamma}_s \frac{\Delta t}{2}\Big(\mathbf{D}_{\mathrm{T}}^{0} + \mathbf{S}_{\mathrm{T}}\Big), \tag{3.75}$$

$$\mathrm{Y}_k^s = (1-\eta_s-\nu_s)\mathrm{Y}_k^0 + \eta_s \mathrm{Y}_k^{s-1} + \nu_s \mathrm{Y}_k^{s-2} + \tilde{\eta}_s \frac{\Delta t}{2}\Big(\mathbf{D}_{\mathrm{Y}_k}^{s-1} + \mathbf{S}_{\mathrm{Y}_k}\Big) + \tilde{\gamma}_s \frac{\Delta t}{2}\Big(\mathbf{D}_{\mathrm{Y}_k}^{0} + \mathbf{S}_{\mathrm{Y}_k}\Big), \tag{3.76}$$

$$\rho^s = \frac{p_0^n}{\mathcal{L}\mathrm{T}^s \sum_k \mathrm{Y}_k^s/\mathrm{W}_k^s}. \tag{3.77}$$

All the coefficients which appear in Eqs. (3.72–3.77) can be found in Motheau and Abraham's paper [152].

3.6.3 Integration of stiff reactive terms

In this step, chemical source terms in energy and species equations are solved over a full time-step using a stiff ordinary differential equation (ODE) solver, e.g., DVODE, similar to what is done in FLEDS. Flows inside the domain are essentially "frozen", i.e., no advection nor diffusion effects, to let chemical reactions proceed. The density is kept unchanged throughout the process and only re-distribution of mass between species is taking place. Upon the end of chemistry integration, the second half-step integrations of convective and diffusion terms are effected, following the same procedures as described in the previous sub-section.

3.6.4 Projection-correction method

After the time integration of momentum diffusion terms using the RKC method, the boundary conditions are imposed. For an inflow boundary, a simple Dirichlet type of boundary condition is employed whereas an Orlanski-type boundary is used for outflow. At this point, the velocity fields do not satisfy the divergence constraint

set by the continuity equation. The divergence constraint is described as, using the semi-discrete approach proposed by Yu *et al.* (2012) [170]:

$$\begin{aligned}\frac{\partial u_i^{n+1}}{\partial x_i} = -\frac{1}{p_0^{n+1}}\frac{dp_0}{dt}\bigg|^{n+1} &+ \frac{1}{\mathrm{T}^{n+1}}\left[(1+\zeta_t^*)\frac{D\mathrm{T}^{n+\frac{1}{2}}}{Dt} - \zeta_t^*\frac{D\mathrm{T}^{n-\frac{1}{2}}}{Dt}\right] \\ &+ \sum_k \frac{\bar{\mathrm{W}}^{n+1}}{\mathrm{W}_k}\left[(1+\zeta_t^*)\frac{D\mathrm{Y}_k^{n+\frac{1}{2}}}{Dt} - \zeta_t^*\frac{D\mathrm{Y}_k^{n-\frac{1}{2}}}{Dt}\right],\end{aligned} \tag{3.78}$$

with

$$\frac{dp_0}{dt}\bigg|^{n+1} = \frac{\Big[(\Delta t^n - \Delta t^{n-1})^2 - (\Delta t^n)^2\Big]p_0^{n+1} - (\Delta t^n + \Delta t^{n-1})^2 p_0^n + (\Delta t^n)^2 p_0^{n-1}}{\Delta t^n \Delta t^{n-1}(\Delta t^n + \Delta t^{n-1})}, \tag{3.79}$$

$$\frac{D\mathrm{T}^{n+\frac{1}{2}}}{Dt} = \frac{\mathrm{T}^{n+1} - \mathrm{T}^n}{\Delta t^n} - \big[(1+\zeta_t)\mathbf{C}_{\mathrm{T}}^n - \zeta_t \mathbf{C}_{\mathrm{T}}^{n-1}\big], \tag{3.80}$$

$$\frac{D\mathrm{Y}_k^{n+\frac{1}{2}}}{Dt} = \frac{\mathrm{Y}_k^{n+1} - \mathrm{Y}_k^n}{\Delta t^n} - \big[(1+\zeta_t)\mathbf{C}_{\mathrm{Y}_k}^n - \zeta_t \mathbf{C}_{\mathrm{Y}_k}^{n-1}\big]. \tag{3.81}$$

To enforce mass conservation, the hydrodynamic pressure needs to be solved from a variable-coefficient Poisson equation:

$$\frac{\partial}{\partial x_i}\Big(\frac{1}{\rho^{n+1}}\frac{\partial p'}{\partial x_i}\Big) = \frac{1}{\Delta t^n}\Big[\frac{\partial u_i^*}{\partial x_i} - \frac{\partial u_i^{n+1}}{\partial x_i}\Big], \tag{3.82}$$

where $p' = p_1^{(n+1)} - p_1^n$, and used to correct the provisional velocity field u_i^*. An iterative approach suggested by Nicoud (1998) [171] is employed in this work as follows:

$$\frac{\partial^2 p'_q}{\partial x_i^2} = \frac{\partial}{\partial x_i}\left[\Big(1 - \frac{\min(\rho^{n+1})}{\rho^{n+1}}\Big)\frac{\partial p'_{q-1}}{\partial x_i}\right] + \frac{\min(\rho^{n+1})}{\Delta t^n}\left[\frac{\partial u_i^*}{\partial x_i} - \frac{\partial u_i^{n+1}}{\partial x_i}\right]. \tag{3.83}$$

This can be solved exactly using a spectral solver based on Fast Fourier Transforms (FFT). Once the user-defined convergence criterion is met, the provisional velocity is corrected as follows:

$$u_i^{n+1} = u_i^* - \left[\frac{1}{\min(\rho^{n+1})}\frac{\partial p'_q}{\partial x_i} + \Big(\frac{1}{\rho^{n+1}} - \frac{1}{\min(\rho^{n+1})}\Big)\frac{\partial p'_{q-1}}{\partial x_i}\right], \tag{3.84}$$

and

$$p_1^{n+1} = p_1^n + p'. \tag{3.85}$$

After this step, a 6th-order compact spatial filter of identical form as that used in FLEDS is applied to the solution to damp out any small-scale oscillations.

3.7 Prior Validation Studies of FLEDS and HOLOMAC

In this section, prior studies in which FLEDS and HOLOMAC have been applied are summarized.

Anders *et al.* (2008) [172] carried out 2D simulations using FLEDS to study the flame-vortex interactions under diesel engine conditions in the presence of residual gases. Vortex of the size comparable to the integral length scale is imposed onto a non-premixed flame to simulate the roll-up of the flame within a vortex.

Venugopal and Abraham (2008) [173] performed 2-D DNS of vortices imposed on a diffusion layer between n-heptane and diluted air using FLEDS, to investigate extinction and re-ignition dynamics.

Owsten and Abraham (2010) [174] performed 2-D numerical studies to compare the structures of triple flames and premixed flames of H_2/air using FLEDS. The premixed flames are generated by spark-igniting a homogeneous mixture of hydrogen and air whereas the triple flames are generated from spark ignition inside initially quiescent H_2/air stratified layers.

Reddy and Abraham (2011) [175] studied the interactions of counter-rotating vortex pairs with developing ignition kernels in lean CH_4/air mixtures using FLEDS. They have also carried out DNS to evaluate the flame surface density model during the early development of ignition kernels [176].

Mukhopadhyay and Abraham (2011) [50] employed FLEDS in the studies of compositional stratification and its influence on autoignition in n-heptane/air diffusion layers.

Ameen and Abraham (2014) [177] performed large-eddy simulations (LES) of reacting diesel jets using FLEDS and compared the lift-off phenomena with those simulated using Reynolds-averaged Navier-Stokes (RANS) simulations. An unsteady flamelet progress variable (UFPV) model is used to model the turbulent combustion. The reaction source terms are tabulated as functions of mixture fraction Z, stoichio-

metric scalar dissipation rate χ_{st} and progress variable c_{st} by solving the unsteady flamelet equations.

HOLOMAC is a recently developed code. Several test cases have been carried out including the modeling of a 1-D freely propagating premixed methane flame in a periodic closed domain, autoignition of mixing layers of n-heptane and air in a closed domain and 2-D vortex-flame interactions.

4. FLAME PROPAGATION IN DUAL-FUEL MIXTURES

4.1 Introdution

In this chapter, autoignition and subsequent flame development in the dual-fuel mixtures is investigated. For our study, n-heptane (C_7H_{16}) is employed as the more reactive fuel and methane (CH_4) as the less reactive fuel. Consider a typical engine cycle of a dual-fuel engine: at the end of induction cycle, the primary fuel, i.e., methane has been introduced into the combustion chamber through the port; during the compression stroke, the gas is compressed and the pressure increases. Since there is ample time for the mixing of primary fuel and air to occur, the methane-air mixture is considered as homogeneous. At some point, the more reactive fuel, i.e., n-heptane is injected. It will diffuse into the methane-air mixture forming a molecular mixing layer before it autoignites. This configuration is schematically depicted in Fig. 4.1 in which the dotted rectangle marks the region of interest for this study. The pressure, temperature and equivalence ratio of the homogeneous mixture, and mixing layer thickness of the n-heptane/methane-air mixture are varied to study their effects on the flame development process. Our specific objective is to understand the dependence of the characteristic time required for steady flame propagation to be achieved on these parameters. In carrying out this study, laminar processes are assumed. We recognize that turbulence can alter the conclusions although it is not uncommon to assume that flame development following ignition in engines is controlled by laminar processes as reviewed through experimental observations of flame kernel growth in engines [32, 72, 178, 179, 180].

The rest of this chapter is organized as follows: Section 4.2 discusses the computational setup. Section 4.3 describes the typical autoignition and flame development process. In Section 4.4, a correlation is developed for the characteristic time to reach

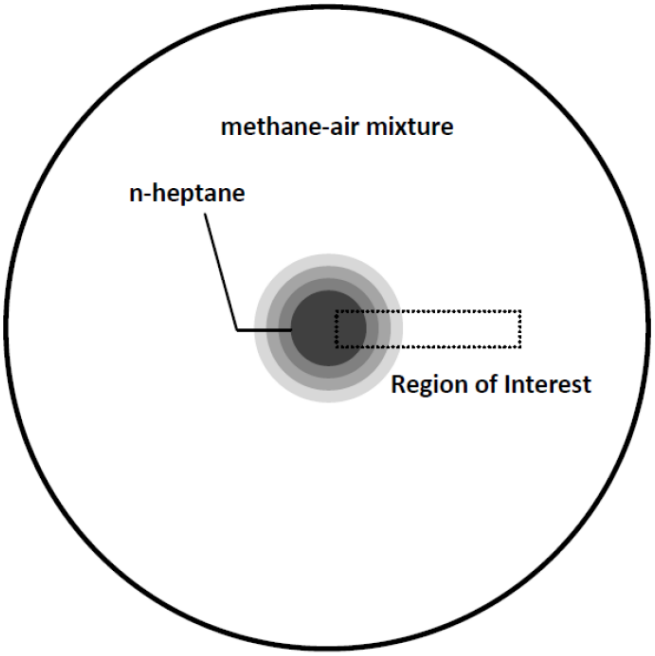

Figure 4.1. Schematic of cross-sectional view of a dual-fuel engine after the injection of pilot fuel.

steady propagation in dual-fuel mixtures. Conclusions of the study follow in Section 4.5. *This chapter borrows material from a journal paper published by Wang and Abraham* [181].

4.2 Computational Setup

For the purpose of gaining insight on the flame propagation in dual-fuel mixtures, the region of interest identified in Fig. 4.1 is isolated as the computational domain shown in Fig. 4.2. Interaction of the flame with walls is neglected because our focus is on the early flame development. The simulations are carried out using FLEDS. Subsonic non-reflective outflow boundary conditions are applied on boundaries parallel to the mixing layer (x-axis) and periodic boundary conditions are imposed on boundaries normal to the mixing layer (y-axis). The domain in Fig. 4.2 measures

0.125 and 5.000 mm in the x- and y-directions, respectively, and a uniform mesh with 25 $\times$ 1000 points is used giving a spatial resolution of 5 μm in both directions. Computations with even higher resolution of 2.5 μm have been carried out to ensure results are grid independent. Furthermore, the spatial resolution is selected to ensure not only that there are at least 10 cells within the diffusion layer [182], but also that the premixed methane flame which develops following autoignition is well resolved.

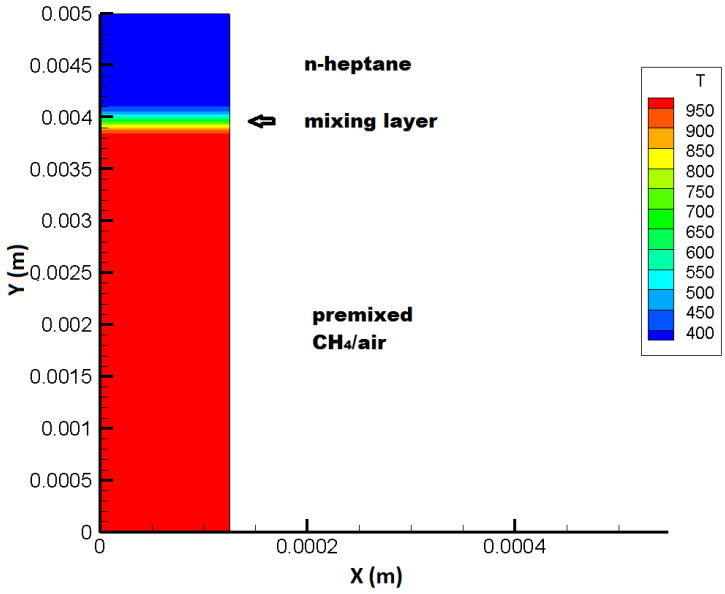

Figure 4.2. 2-D computational domain with n-heptane (top) and homogeneous mixture of methane-air (bottom).

The temperatures of n-heptane and the methane-air premixed mixture are 373 K and 900–1100 K (varies with cases), respectively. The initial compositional and thermal stratification in the heptane/methane-air mixing layer is specified using hyperbolic tangent profiles as follows:

$$f(y) = \left(\frac{f_U + f_L}{2}\right) + \left(\frac{f_U - f_L}{2}\right) \tanh\left(\frac{y - y_c}{\delta}\right), \tag{4.1}$$

where $f(y)$ is a general parameter which can represent mass fraction of n-heptane $Y_{C_7H_{16}}$ or temperature T as a function of y. f_U and f_L are the upper and lower

values, respectively, of the variable considered. y_c represents the location where $f(y)$ is half-way between the maximum and minimum values and it has been fixed at one-fifth of the distance from the top boundary. The parameter δ is a measure of the mixing layer thickness. For a hyperbolic tangent profile, the physical distance between 99 and 1 percentile of the distribution is typically three times the δ value.

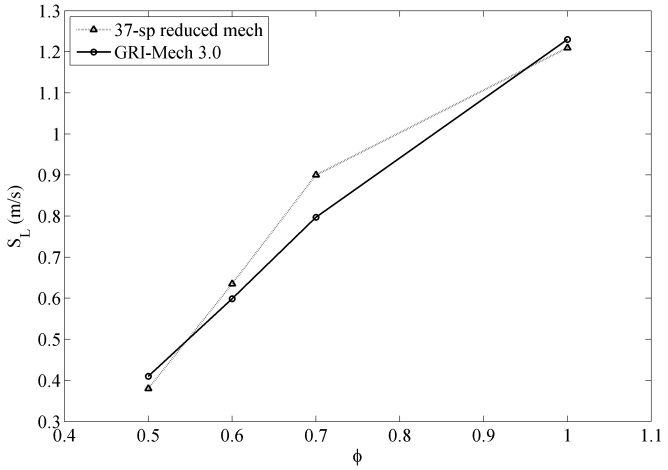

Figure 4.3. Computed laminar CH_4/air flame speeds for unburned temperature of 1000 K at pressure of 40 bar with (a) 37-species reduced mechanism [46]; (b) GRI-Mech 3.0 [183].

A 40-species, 83-step reaction mechanism is employed [46, 184]. This mechanism includes the kinetics for autoignition and high-temperature chemistry of n-heptane and methane oxidation. It has been validated using more detailed oxidation mechanisms for n-heptane [45] and has been employed in other studies [50, 107]. In addition, it has been verified as part of this work that this reduced mechanism can describe lean methane-air premixed flame propagation. Note that in the premixed mixture, the laminar flame speed and adiabatic flame temperature are the parameters of primary interest. The accuracy of this reduced kinetics has been assessed by comparing the computed flame speeds with those obtained using the comprehensive GRI-Mech 3.0 [183] for unburned gas temperature of 1000 K, pressure of 40 bar, and mixture equivalence ratios between 0.5 and 1.0. The GRI-Mech 3.0 mechanism has shown

Table 4.1. Computed adiabatic flame temperature for unburned gas temperature of 1000 K at pressure of 40 bar.

Equivalence ratio ϕ	Adiabatic flame temperature (K)	
	GRI-Mech 3.0	17-sp reduced mechanism
0.5	2052	2053
0.6	2220	2221
0.7	2374	2376
1.0	2700	2705

satisfactory agreement with experimental data at high pressure conditions up to 60 atm [185, 186]. Figure 4.3 shows that our reduced mechanism is capable of predicting flame speeds in methane-air mixture within 10% of those obtained using the GRI-Mech 3.0. The agreement in adiabatic flame temperature is also found to be within 1% of each other as listed in Table 4.1.

4.3 Flame Propagation in Dual-Fuel Mixtures

Table 4.2 lists the conditions employed for the parametric studies. We will consider Case 1 to be the baseline. Cases 2 & 3, 4 & 5, 6 & 7 and 8 & 9 will reflect changes in 1) pressure, 2) methane-air temperature, 3) premixed equivalence ratio (ϕ) and 4) initial mixing layer thickness (δ), respectively. In addition, Cases 10, 11 and 12 in which multiple parameters are simultaneously varied are performed to validate the proposed model. For the baseline, i.e., Case 1, pressure of 40 bar is used which is representative of that in a compression-ignited lean-burn engine. The temperature of 1000 K is typical of end-of-compression temperature in a compression-ignited engine. The premixed equivalence ratios of the investigated cases vary from 0.5–0.7. They fall within the range of those in lean-burn natural gas engines, but are higher than

Table 4.2. Initial pressure, temperature and equivalence ratio in the homogeneous mixture and mixing layer thickness employed for computations.

Case	Pressure (bar)	Temperature (K)	ϕ	δ (μm)
1	40	1000	0.6	90
2	30	1000	0.6	90
3	20	1000	0.6	90
4	40	1100	0.6	90
5	40	900	0.6	90
6	40	1000	0.7	90
7	40	1000	0.5	90
8	40	1000	0.6	120
9	40	1000	0.6	60
10	45	1000	0.6	180
11	40	1100	0.7	240
12	35	1100	0.7	120

those in homogeneous charge compression ignition (HCCI) engines under light and medium load conditions. The mixture-averaged diffusion coefficient is assumed to be approximately $4 \times 10^{-5}\ m^2/s$ for the stoichiometric mixture at 800 K [11]. A residence time of 0.36 ms which is representative of the ignition delay in a compression ignition engine when fuel is directly injected corresponds to a molecular mixing layer thickness of 120 μm. In other words, the mixing layer thickness is representative of the distance to which n-heptane diffuses during the ignition delay period after the start of injection (SOI). Note that this thickness can vary due to turbulent strain. Next, we will provide a detailed discussion of autoignition and flame development characteristics in dual-fuel mixtures using Case 1 as the example.

Figure 4.4 shows the initial temperature, fuel mass fractions ($Y_{C_7H_{16}}$ and Y_{CH_4}), and ϕ for the baseline case as a function of the y-coordinate of Fig. 4.2. Notice that the scaling is different for each variable on the x-axis. Figure 4.5 shows temperature, ϕ and flame front at several instances after the start of computation. For the purpose of our discussion here, we will define the point of peak heat release rate as the "flame front." Note that in reality there is a finite thickness to what we are referring to as a "front."

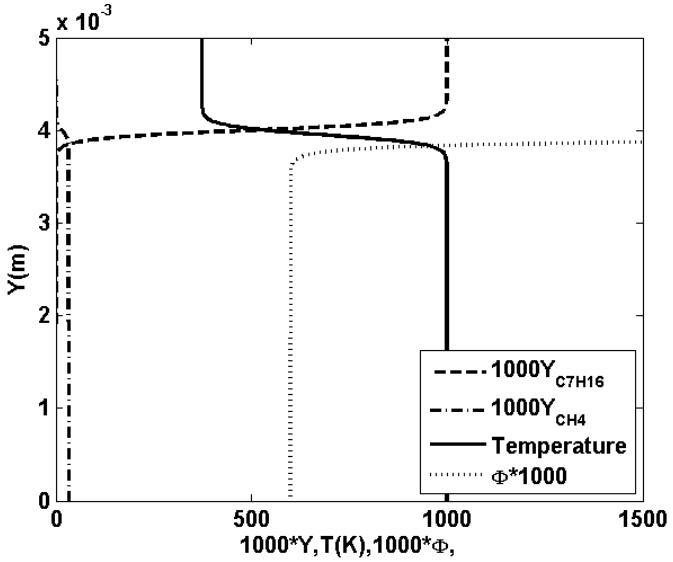

Figure 4.4. Initial profile of fuel mass fractions ($Y_{C_7H_{16}}$ and Y_{CH_4}), temperature and equivalence ratio (ϕ) inside the domain shown as a function of y-coordinate.

At 0.4 ms, the onset of autoignition in the mixing layer is evident by the small rise in temperature. Following the onset of autoignition, the temperature rises rapidly and reaches about 2760 K at 0.6 ms. This peak temperature is reached where the local mixture is close to stoichiometric. Note that the stoichiometric composition is determined by the sum of n-heptane and methane. The flame front then propagates into the premixed mixture where the equivalence ratio is lower (premixed $\phi = 0.6$) and the temperature in the burned gas behind the front drops as the local equivalence ratio decreases. The decrease in temperature suggests that as the front travels away

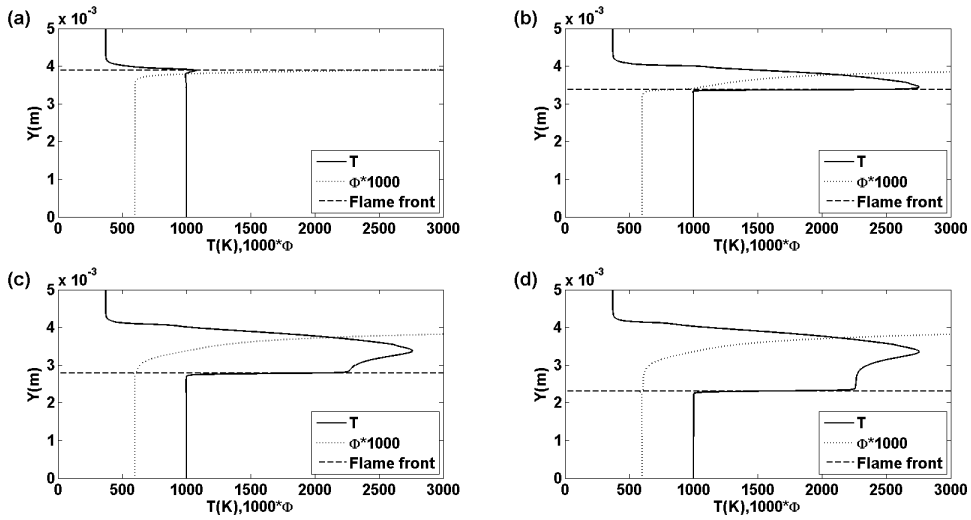

Figure 4.5. Developing profiles of temperature (T), equivalence ratio (ϕ), and flame front as a function of y-coordinate for Case 1 at time instants of (a) $t = 0.40\ ms$, (b) $t = 0.60\ ms$, (c) $t = 1.20\ ms$, and (d) $t = 1.80\ ms$.

from the mixing layer, the influence of heptane combustion on the moving flame front diminishes. At about 1.20 ms, the temperature in the burned gas is within 10% of the adiabatic flame temperature (2220 K) and the front speed within 5% of the laminar flame speed (0.60 m/s) corresponding to the homogeneous methane-air mixture. By 1.80 ms, the temperature is within 2% of the adiabatic flame temperature. Figure 4.6 shows the computed front speed as a function of time. Note that this speed in the early stages of flame development (prior to 0.7 ms) does not correspond to a flame speed. In fact, it can be seen that the peak speed is about 2.8 m/s at 0.46 ms. This occurs during the late stages of ignition, and it may correspond to an "ignition front" speed as explained by Mukhopadhyay and Abraham (2011) [50]. Beyond 1.20 ms, the flame speed is about 0.62 m/s, close to the theoretical steady-state premixed flame speed of 0.60 m/s, obtained by running CHEMKIN using the GRI-Mech 3.0.

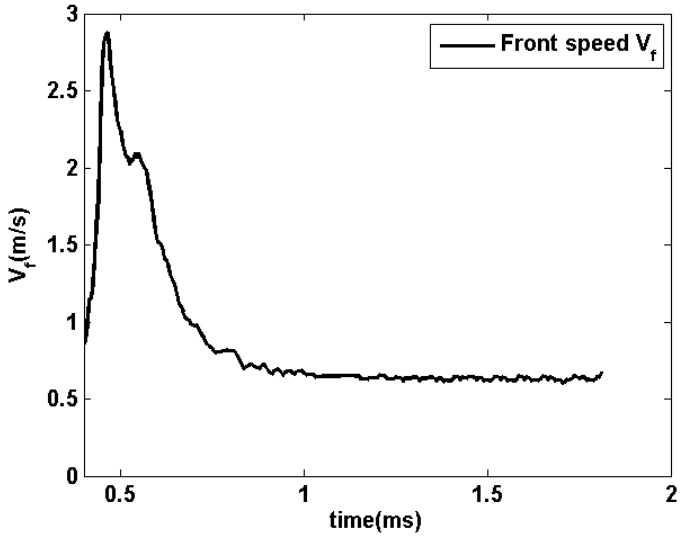

Figure 4.6. Evolution of front speed in n-heptane/methane-air dual-fuel combustion.

4.4 A Correlation for Steady Flame Propagation Time

We are now interested in understanding the dependence of the characteristic time τ_{prop} required for steady flame propagation to be achieved on 1) pressure, 2) initial methane-air temperature, 3) premixed equivalence ratio ϕ, and 4) initial mixing layer thickness δ. Based on the earlier discussion, we can characterize this time into three distinct phases:

Phase I. Time to autoignition, τ_{ig}, as defined by the time to first achieve 500 K above the initial premixed mixture temperature (usually referred to as ignition delay).

Phase II. Time to attain peak temperature following autoignition, τ_{max}.

Phase III. Time to steady flame propagation, τ_{st}, as defined by when the front speed and the temperature in the burned gas is within 2% of the laminar flame speed and adiabatic flame temperature, respectively.

The numerical values of these times are tabulated in Table 4.3. The additional information provided in Table 4.3 will be explained below as part of the discussion.

The following three subsections provide a physically-motivated correlation for the characteristic time of each stage. The characteristic time τ_{prop} required for steady flame propagation to be achieved will be the sum of all three characteristic times.

4.4.1 Autoignition delay

The characteristic time for autoignition delay in stratified mixture τ_{ig} is predominantly controlled by the chemical kinetics of the fuel and it is known to be strongly dependent on pressure and temperature. It has been suggested that autoignition delay is also dependent on the level of mixing, but it is hard to separate such dependence from the temperature effect because local mixing of fuel and air influences the local temperature in compression ignition engines where the air temperature is significantly higher than the fuel temperature. Several correlations have already been proposed in the literature [11, 49, 187]. We find that a correlation of the following form,

$$\tau_{ig}(ms) = 0.174 \cdot P^{-1.397} \cdot e^{6100/\mathrm{T}}, \tag{4.2}$$

where P and T carry the units of bars and Kelvin, respectively, provides a reasonably accurate (within 10%) fit of the computed data. The estimated τ_{ig} (est. τ_{ig}) and percentage difference are shown in columns 3 and 4, respectively, of Table 4.3.

4.4.2 Time to reach maximum temperature

The initial onset of autoignition in the mixing layer, as extensively discussed in the literature, occurs in the rich mixture at ϕ of about 3.0 [54, 188, 189]. A front then propagates into the leaner mixture and temperature increases until the peak temperature is achieved at approximately $\phi = 1.0$, i.e., where local mixture

Table 4.3. Comparison of the characteristic time (in ms) of each phase with model prediction.

Case	τ_{ig}	est. τ_{ig}	% diff	τ_{max}	est. τ_{max}	% diff	τ_{st}	est. τ_{st}	% diff
1	0.4292	0.4483	4.46%	0.2058	0.1908	-7.29%	0.8300	0.8258	-0.50%
2	0.6606	0.6701	1.44%	0.1894	0.1908	0.74%	0.7150	0.7383	3.26%
3	1.1342	1.1807	4.10%	0.1808	0.1908	5.53%	0.6450	0.6176	-4.25%
4	0.2806	0.2575	-8.23%	0.1844	0.1908	3.47%	0.5650	0.5621	-0.51%
5	0.9400	0.8830	-6.06%	0.2000	0.1908	-4.60%	1.0600	1.2398	16.96%
6	0.4288	0.4483	4.56%	0.2362	0.2211	-6.40%	0.6150	0.6207	0.92%
7	0.4299	0.4483	4.29%	0.1751	0.1605	-8.33%	1.3350	1.2065	-9.63%
8	0.4184	0.4483	7.16%	0.2466	0.2338	-5.18%	0.9400	0.9761	3.84%
9	0.4514	0.4483	-0.68%	0.1586	0.1478	-6.82%	0.7250	0.6756	-6.82%
10	0.3582	0.3803	6.18%	0.3318	0.3199	-3.60%	1.2700	1.3326	4.93%
11	0.2780	0.2575	-7.37%	0.3970	0.4362	9.87%	0.9100	0.8360	-8.13%
12	0.3349	0.3103	-7.34%	0.2401	0.2641	10.00%	0.5150	0.4921	-4.44%

is stoichiometric. Additional details about this front propagation are provided by Mukhopadhyay and Abraham (2011) [50]. We will use τ_{max} to represent the time to achieve the peak temperature. The numerical values of this time are given in Table 4.3. It is worth noting that Phase II is the fastest phase of all three and is the least important among the three times. In fact, an argument can be made that the ignition delay should be determined as the time taken to reach peak temperature rather than 500 K above the initial temperature. However, because the peak temperature is reached in the stoichiometric mixture which is also influenced by the equivalence ratio of the homogeneous mixture, it is useful to separate out the early phase of autoignition (less influenced by homogeneous mixture composition) from the later phase (more influenced by homogeneous mixture composition). By comparing Cases 1, 2 and 3 and Cases 1, 4 and 5, it is seen that as pressure or temperature is varied, τ_{max} stays approximately constant within the range of $\pm 0.010\ ms$ from $0.195\ ms$. On the other hand, altering ϕ and δ has more noticeable impact on τ_{max}: as ϕ increases from 0.5 to 0.7 and as δ increases from 60 μm to 120 μm, τ_{max} grows by approximately 35% and 50%, respectively. Based on these findings, the following correlation for τ_{max} (in ms) with ϕ and δ (in μm) fits the data:

$$\tau_{max}(ms) = 0.3029\phi + 1.434 \times 10^{-3}\delta - 0.12. \tag{4.3}$$

The dependence of τ_{max} on ϕ and δ can be explained by the fact that the time from the onset of autoignition to attain the peak temperature is predominantly controlled by the distance (d_{max}) over which the front will travel during Phase II. Here d_{max} represents the physical distance from the initial autoignition location ($\phi \approx 3$) to the location of peak temperature ($\phi \approx 1$). The location where $\phi = 1$ depends on the mixing layer thickness δ as well as the initial ϕ of the premixed mixture. Finding d_{max} requires solving equations involving hyperbolic tangent functions and a closed form analytical solution cannot be obtained. However, because of the short range of ϕ and δ which are considered, it appears reasonable to approximate d_{max} as a linear function of both ϕ and δ. Figure 4.7 shows the computed τ_{max} for several cases with various ϕ and a fixed δ of 90 μm. Figure 4.8 shows the computed τ_{max} for several

cases with various δ and a fixed ϕ of 0.6. Linear fits are seen to approximate the data well in both figures. In fact, the correlation for τ_{max} by Eq. (4.3), indicated as est. τ_{max} in Table 4.3, shows agreement with computed τ_{max} within 10%.

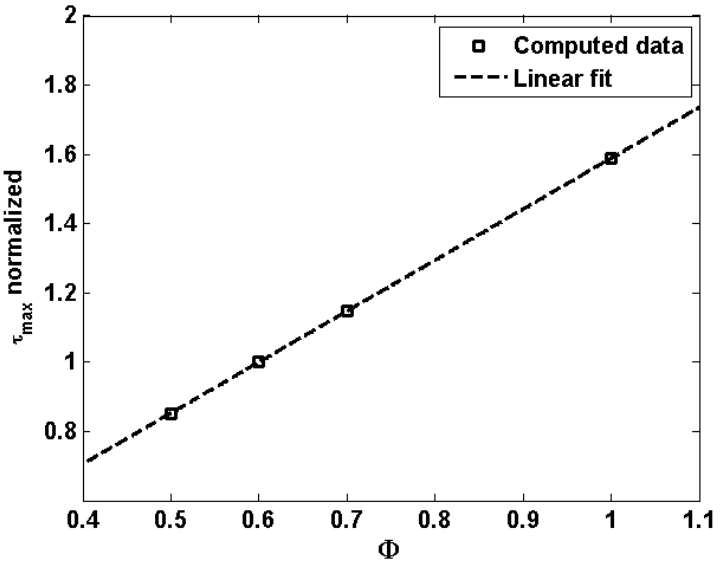

Figure 4.7. τ_{max} normalized by τ_{max} for Case 1 as a function of equivalence ratio ϕ ($\delta = 90\ \mu m$).

4.4.3 Steady flame propagation time

The next phase involves the propagation of the front into the homogeneous mixture. The time for steady flame propagation is defined as that required to achieve a burned gas temperature which is within 2% of the adiabatic flame temperature. This also corresponds approximately to the time when the front speed is within 2% of the laminar premixed flame speed. With this definition, τ_{st} is given in Table 4.3.

As discussed earlier, the moving flame front becomes progressively less affected by the n-heptane reactions and eventually develops into a premixed methane-air flame during Phase III. It is therefore reasonable that τ_{st} is some function of the steady flame speed inside the homogeneous mixture. In addition, the mixing layer thickness δ is a

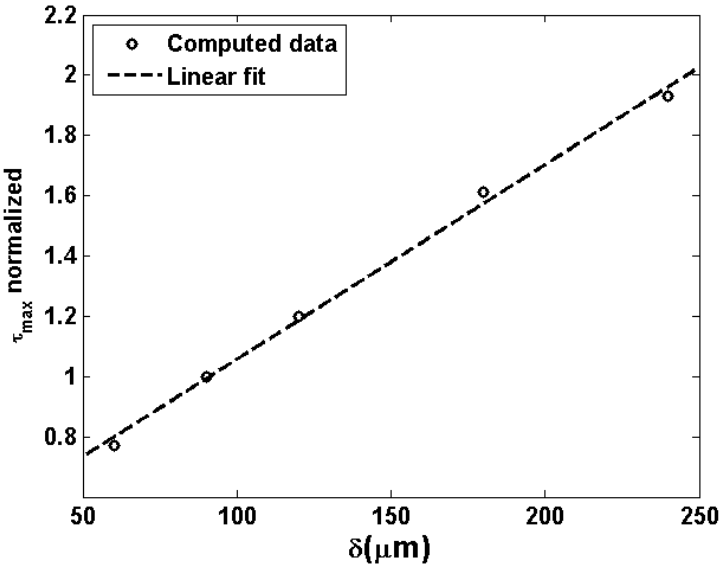

Figure 4.8. τ_{max} normalized by τ_{max} for Case 1 as a function of mixing layer thickness δ ($\phi = 0.6$).

measure of the physical length scale where n-heptane can influence front propagation. Equation (4.4) below describes the physical model we have developed for τ_{st},

$$\tau_{st}(ms) = \frac{c_1 \delta}{\mathrm{S_L}} + \frac{c_2 \delta_f}{\mathrm{S_L}}. \tag{4.4}$$

In the equation, $\mathrm{S_L}$ is the laminar flame speed in m/s, δ is the mixing layer thickness in μm, and δ_f is the laminar flame thickness in μm based on thermal diffusivity and flame speed. The first term of the expression is a measure of the time to traverse the mixing layer, i.e., for the influence of heptane to be minimized. The second term is the time required for the flame front temperature to stabilize in the absence of n-heptane, and it is derived by performing energy conservation analysis on a control volume enclosing the moving flame. A line of best-fit to the available data provides values of $c_1 = 0.003$ and $c_2 = 0.009$. Table 4.3 shows the computed τ_{st} and the estimated τ_{st} (est. τ_{st}) using Eq. (4.4). The agreement between the two is within 17%

with most cases agreeing within 10%. In sum, the time required for steady flame propagation to be achieved is

$$\tau_{prop}(ms) = 0.174 \cdot P^{-1.397} \cdot e^{6100/\mathrm{T}} + 0.3029\phi + 1.434 \times 10^{-3}\delta - 0.12 + \frac{0.003\delta + 0.009\delta_f}{\mathrm{S_L}}. \tag{4.5}$$

4.5 Summary

In this chapter, we have computationally investigated flame development in a n-heptane/methane-air mixing layer in which the higher cetane number n-heptane autoignites and causes a flame to develop and propagate into the low cetane number methane-air homogeneous mixture. Pressure and temperature conditions correspond to those in engines. The characteristic time required for steady flame propagation has been investigated and its dependence on 1) pressure, 2) initial CH_4/air temperature, 3) premixed equivalence ratio and 4) initial mixing layer thickness has been examined. There are three components to the time: ignition delay, time to attain peak temperature and time to achieve steady flame propagation. As discussed in the literature the ignition delay τ_{ig} is a function of pressure and an exponential function of temperature. The time to achieve peak temperature τ_{max} is dependent on the distance the front has to travel in the mixing layer from the point of onset of autoignition ($\phi \approx 3$) to the stoichiometric location. This time depends on the premixed equivalence ratio and the mixing layer thickness. The third component τ_{st} is shown to correlate with the time it takes for a laminar flame to traverse the mixing layer and some multiple of the thermal thickness of the laminar flame. The correlations are applicable only for lean homogenous mixtures. Additional work has to be carried out to study the behavior in stoichiometric and rich mixtures. Furthermore, prior to applying these correlations, the influence of turbulence has to be assessed. It is interesting to note, however, that the early phase of ignition and kernel growth in engines has been correlated with laminar parameters [32, 72, 178, 179, 180].

5. FEEDBACK CONTROL FOR STATISTICALLY STATIONARY FLAMES

5.1 Introduction

In the last chapter, we studied ignition and subsequent flame development in dual-fuel engines. As the flame front propagates into the homogeneous mixture of methane and air, it is influenced by the spectrum of turbulent eddies inside the combustion chamber and hence becomes a turbulent premixed flame. Subsequent work will focus on turbulent flame propagation in lean mixtures by employing direct numerical simulations (DNS).

The primary challenge with DNS of premixed turbulent combustion under engine conditions is the computational cost. Setting aside for the time being the ignition and development phases of turbulent combustion in an engine, let us consider the simulation of fully-developed flat premixed flame propagation. It requires fine resolution for resolving the smallest turbulence structures, i.e., Kolmogorov scale. Furthermore, to examine the effects of turbulence on the flame internal structure, even finer resolution may be needed to resolve the reaction zone, which is approximately 1/10 of the flame thermal thickness [62]. On the other hand, the computational domain needs to be sufficiently large. The reasons are two-fold: Firstly, the dimensions perpendicular to the flame propagation need to capture multiples of integral length scales. This is to ensure a large sample pool necessary for statistical independence. Secondly, the length of the domain along the direction of flame propagation needs to be large enough such that the flame remains inside the domain over the period of the simulation. In addition, several realizations may be required to achieve statistical convergence on the estimation of the turbulent flame speed. These constraints often entail the use of multiple millions of computational cells to resolve the flow and result

in prohibitively expensive computational cost. To reduce the computational cost, we propose a computational strategy to simulate statistically stationary premixed flames using feedback control mechanism.

The concept of a statistically stationary flame is hardly new to the experimental community. The fact that a flame may be stabilized or "held" in the wake of a bluff body is well known and used to generate V-flames and other bluff-body stabilized flames [190]. Flames can also be stabilized by recirculation zones in gas turbine engines [191]. In addition, the flame may be stabilized with an overhead stagnation plate [192]. All these stabilization techniques are commonly employed in experiments so that statistics can be collected from the turbulent flame. In numerical simulations, application of these stabilization strategies presents many challenges as geometrically complex structures are often employed which are difficult to model. They also introduce an additional level of complication in the fluid dynamics to be modeled. To account for that, Bell and Day (2006) [193] proposed a heuristic method to stabilize the flame in an effort to emulate the flame stabilization mechanisms employed in experiments to prevent blow-off and flashback. The methodology we have adopted is similar to their idea.

The rest of the chapter is organized as follows. In Section 5.2 we will describe the details of the feedback control algorithm used to simulate stationary laminar and statistically stationary turbulent flames. Various techniques for generating the turbulence in the domain will be discussed in Section 5.3. Section 5.4 will summarize the chapter.

5.2 Feedback Control Algorithm

The algorithm to simulate fully-developed premixed flames in the lean-burn engine relies on the simplification that the fully-developed flame kernel radius is relatively large and the global curvature effect of the mean flame brush can be neglected, i.e., the mean flame front can be treated as essentially planar. Once this is recognized, the

flame can be simulated as statistically stationary inside the computational domain by employing a Lagrangian framework, i.e., the frame of reference is placed on the mean flame front. An inflow/outflow configuration as shown in Fig. 5.1 is employed. Periodic boundary conditions are applied to the top/bottom and front/back boundaries which are parallel to the mean flow direction. In Fig. 5.1, inflow of unburned lean methane-air mixture is specified at the left boundary and the burned gas passes through a sponge zone and leaves the domain from the right. Non-reflective Navier-Stokes characteristic boundary conditions described in Chapter 3 are specified for the inflow and outflow boundaries. Simulations with HOLOMAC use a simple Dirichlet boundary condition for inflow and Orlanski-type boundary condition for outflow as acoustic wave propagations are not considered. If the flame speed is known *á priori*, maintaining the flame stationary would be a simple proposition. This information is, however, not readily available and is often the interest of the whole simulation. Hence, a feedback control mechanism is employed using the mean flame position $x_f(t)$ as the control output to correct the bulk inflow velocity $\mathrm{U}_0(t)$ until the flame becomes statistically stationary.

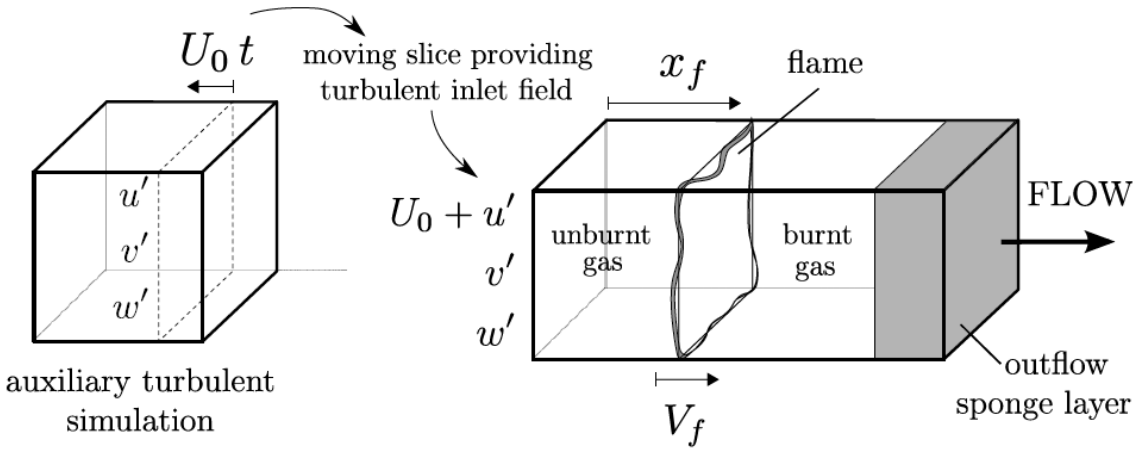

Figure 5.1. Schematic of an inflow-outflow configuration to illustrate the computational procedure.

Consider the case where a stationary laminar flame is to be simulated. The approach is to initialize a laminar flame in the domain with burned gas on one side and unburned gas on the other side of the flame. An approximation of the flame speed is specified as the initial inflow velocity U_0°. After the start of the simulation, the laminar front will move upstream or downstream depending on the sign of $(\mathrm{U}_0^\circ - \mathrm{S_L})$. For an unstrained laminar flame, the speed of the flame front will simply be

$$\mathrm{V}_f(t) = \mathrm{U}_0^\circ - \mathrm{S_L}. \tag{5.1}$$

To attain a stabilized front, the inflow velocity needs to be dynamically adjusted. In the current study, the mean flame position $x_f(t)$ is used as the control output that provides feedback into the mean inflow velocity $\mathrm{U}_0(t)$, given by

$$\mathrm{U}_0(t) = \iint u(0, y, z, t) dy dz. \tag{5.2}$$

For the laminar flame, a proportional loop is employed which can be expressed as

$$\frac{d\mathrm{U}_0(t)}{dt} = -\frac{k_p}{\tau_p}\mathrm{V}_f(t) = -\frac{k_p}{\tau_p}\frac{dx_f(t)}{dt}, \tag{5.3}$$

where $x_f(t)$ is the mean flame front location from the inflow boundary. It is given by

$$x_f(t) = \frac{1}{\mathrm{A}} \int H(c^* - c(\vec{x})) dV, \tag{5.4}$$

where $c(\vec{x})$ is the local progress variable and c^* is an arbitrarily-defined threshold progress variable used to differentiate burned from unburned gas. In this series of simulations, the progress variable is defined as the mass fraction ratio of consumed fuel to the total available fuel in the fresh gas such that $c = 0$ in the fresh gas and $c = 1$ in the burnt gas. Equation (5.3) can be written in the discrete form as

$$\mathrm{U}_0^{n+1} = \mathrm{U}_0^n - k_p \frac{\Delta t}{\tau_p}\Big(2\mathrm{V}_f^n - \mathrm{V}_f^{n-1}\Big), \tag{5.5}$$

where the flame front speed is calculated with one-sided approximation:

$$\mathrm{V}_f^n = \frac{x_f^n - x_f^{n-1}}{\tau_p}. \tag{5.6}$$

The time interval of proportional control represented by τ_p is selected to be 10-100 times the iteration time step Δt to subdue high-frequency oscillatory feedback signals which could lead to flow instabilities. Figure 5.2 shows the history of inflow velocity for five different values of non-dimensional proportional loop gain k_p used in the simulations to stabilize a laminar flame. The initial inflow velocity is deliberately set at twice the laminar flame speed. It can be seen that a proportional loop gain of value 0.1 gives the fastest convergence rate towards the correct laminar flame speed of 0.335 m/s. When k_p is set to 1 (denoted by the green line), the feedback control is unstable and results in failure of the run.

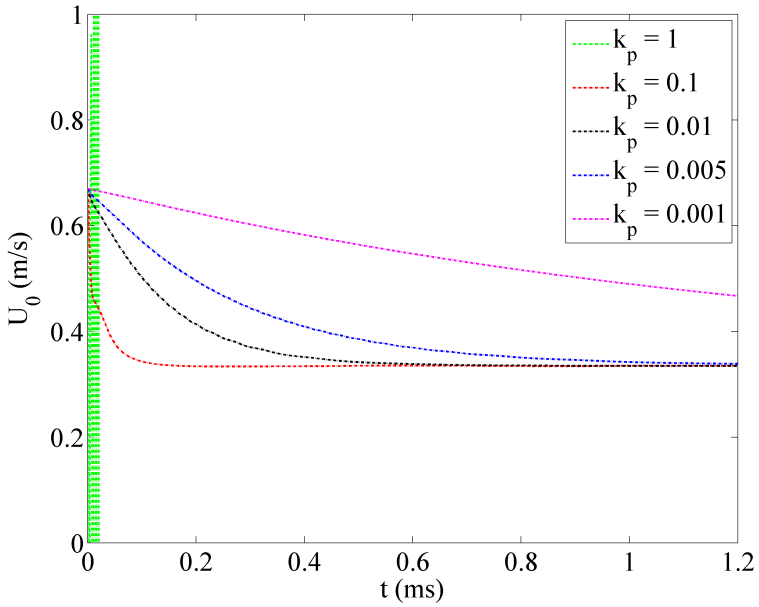

Figure 5.2. Time history of dynamically adjusted inflow velocity for k_p = 1, 0.1, 0.01, 0.005 and 0.001.

A similar approach can be adopted for 2D and 3D turbulent premixed flame simulations. A laminar flame front is initialized inside the domain but the initial flow field is specified to be an homogeneous isotropic turbulent field superimposed onto the laminar flame velocity profile. Methods to generate 2D and 3D turbulent flow fields are different and the details will be elaborated in the next section. In

addition, turbulent fluctuations are supplied at the inflow boundary to compensate for dissipation as well as turbulence advected out of the domain from the outlet, i.e.,

$$\begin{aligned} u(0,y,z,t) &= u'\Big(x_{slice}(t),y,z,t\Big) + \mathrm{U}_0(t); \\ v(0,y,z,t) &= v'\Big(x_{slice}(t),y,z,t\Big); \\ w(0,y,z,t) &= w'\Big(x_{slice}(t),y,z,t\Big); \end{aligned} \tag{5.7}$$

Here $\mathrm{U}_0(t)$ is the mean speed in the flow direction and its value is dynamically adjusted whereas u', v' and w' are the fluctuating components of a "frozen" turbulence field generated from an auxiliary simulation. The "frozen" flow is a homogeneous isotropic turbulent field with desired length scales and turbulent kinetic energy but zero net momentum. At every time step, a "slice" of this pre-generated turbulence field at location $x_{slice}(t)$ is superposed onto the bulk inflow velocity. Note that the location of this selected plane (line in the case of 2D) is advected by both the mean inflow speed $\mathrm{U}_0(t)$ and the turbulent fluctuations $u'(y,z,t)$ on the plane itself, i.e.,

$$x_{slice}(t) = \int \Big[\mathrm{U}_0(t) + \int u'(x_{slice}(t),y,z)dydz\Big]dt. \tag{5.8}$$

However, the spatial average of the turbulent fluctuations should approximately yield zero and hence the second term inside the integral in Eq. (5.8) can be neglected such that

$$x_{slice}(t) = \int \mathrm{U}_0(t)dt. \tag{5.9}$$

A proportional control loop of the same form as in Eqs. (5.3) and (5.3) is employed to correct the inflow velocity until the mean flame front is stationary. On top of that, an additional control of integral form is used:

$$\frac{d\mathrm{U}_0(t)}{dt} = \frac{k_i}{\tau_i^2}\int_0^t e^{-(t-\psi)/\tau_i}\Big[x_f(0) - x_f(\psi)\Big]d\psi, \tag{5.10}$$

where $x_f(0)$ is the initial flame front position from the inflow boundary. The integral loop is determined by the most recent history of the flame position over a characteristic time period of τ_i. The purpose of the integral control is to return the mean flame front towards its initial location. This is motivated by the concern that in some

turbulent flows, turbulence parameters such as intensities and length scales vary spatially along the inflow direction. Having the integral loop in place helps to maintain constant turbulence characteristics in the inflow with which the flame is interacting. To minimize the interference between the two forms of feedback mechanism, τ_i is selected to be much larger than the characteristic time scale of the proportional loop, i.e., τ_p in Eq. (5.3). As a result, the proportional feedback produces a "spontaneous" correction on the inflow velocity whereas the integral feedback delivers a time-averaged "long-term" control on the flame location.

Figure 5.3 shows the evolution of mean flame position and spatially-averaged inflow velocity $\mathrm{U}_0(t)$ for a typical 2D simulation using the proportional and integral feedback mechanisms. The turbulence intensity for this case is 1.5 m/s while the unstrained laminar flame speed at the given condition is 0.15 m/s. The solid line shows the average flame position inside the domain for 120 eddy turnover times while the chain-dash line tracks the dynamically adjusted inflow velocity at the boundary. The simulation reaches statistical steady-state in about 40 eddy turnover times as indicated by the inflow velocity reaching an oscillatory state. Furthermore, there is no discernible shift of the mean flame location toward either direction over time while its fluctuation remains less than one integral length of the imposed turbulent field. Evidently the flame remains statistically stationary inside the domain. Note that once the flame is (statistically) stabilized, the time average of the inflow velocity will yield the turbulent flame speed based on consumption rate.

5.3 Turbulence Generation

Simulation of 2D or 3D turbulent flames with inflow/outflow configuration requires turbulent fluctuations to be supplied at the inflow boundary. This is achieved by selecting sequential planes from an auxiliary turbulent flow field as discussed in the previous section. The most natural way to generate the auxiliary field is by using flow solutions from a Navier-Stokes solver, e.g., FLEDS and HOLOMAC. To account

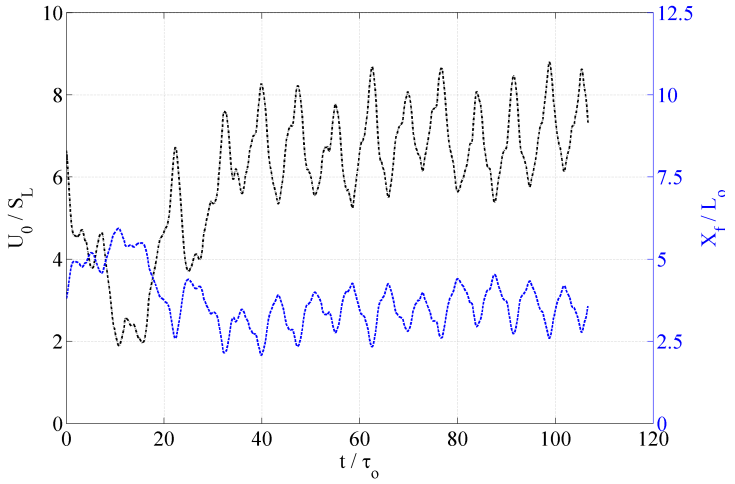

Figure 5.3. Premixed flame stabilized using the proportional and integral feedback algorithm in a turbulent flow field with an intensity of 1.5 m/s and integral length scale of 1 mm.

for turbulence dissipation, additional forcing terms are added to the Navier-Stokes equations such that the turbulence intensities are sustained, i.e., turbulent energy is non-decaying. While turbulence generated with this method is the most realistic, it is suitable only for 3D simulations but not for 2D cases. This is because 2D turbulence lacks the vortex stretching mechanism present in its 3D counterpart. Vortex stretching gives rise to the formation of smaller eddies and is responsible for the turbulence cascade. Applying forcing to 2D flows will, however, indefinitely increase the vorticity. In addition, generating turbulent flow field with high Re can be computationally expensive as the total number of grid cells scales with $Re_{\mathrm{T}}^{9/4}$. A less computationally demanding approach is to generate "synthetic" turbulence flow fields from random noises by prescribing desired turbulence characteristics. This method is suitable for generating 3D as well as 2D turbulent fields. In the following two sub-sections, we will review these methods.

5.3.1 Filtered noise method

The approach to artificially synthesize 2D turbulent fields in this work is proposed by Fathali *et al.* (2008) [194] whose work is based on the procedures of digitally filtering random signals by Klein *et al.* (2003) [195]. In essence, each velocity component is generated by a linear combination of individual uncorrelated random fields. These uncorrelated random fields are obtained by passing white noise through a spherical Gaussian filter. Autocorrelation functions and turbulence length scales can then be prescribed through specifying the coefficients of linear combination and filter width, respectively. The key mathematical formulations will be elaborated next.

For a turbulent field, the integral length scale can be considered as a quantity to describe the typical size of regions inside which correlations between velocity components are statistically significant. These correlations are quantified using the correlation function:

$$\mathrm{R}_{ij}(\mathbf{x}, \mathbf{r}, t) = \langle u_i(\mathbf{x} + \mathbf{r}, t) u_j(\mathbf{x}, t) \rangle, \tag{5.11}$$

where $\langle \cdot \rangle$ represents the temporal averages. From this two-point covariance, integral length scales can be defined as

$$\mathrm{L}_{ij}(\mathbf{x}) = \int_0^\infty \frac{\mathrm{R}_{ij}(\mathbf{x}, r\mathbf{e})}{\mathrm{R}_{ij}(\mathbf{x}, 0)} dr. \tag{5.12}$$

We can write each velocity component as a linear combination of uncorrelated random fields f_{ij} with zero mean, i.e.,

$$\begin{aligned} u &= a_{11} f_{11} + a_{12} f_{12} + a_{13} f_{13}, \\ v &= a_{21} f_{12} + a_{22} f_{22} + a_{23} f_{23}, \\ w &= a_{31} f_{13} + a_{32} f_{23} + a_{33} f_{33}. \end{aligned} \tag{5.13}$$

If we assume that $\langle f_{ij} f_{mn} \rangle = \delta_{im} \delta_{jn} r_{ij}$ and $r_{ij} \equiv \langle f_{ij}(\mathbf{x}) f_{ij}(\mathbf{x}') \rangle$ has a shape of Gaussian function which is equivalent to the autocorrelation function of homogeneous isotropic turbulence in the final period of decay, we can write each random field f_{ij} as the convolution product of the Gaussian filter F_{ij} with white noise field ξ_{ij}, i.e.,

$$f_{ij}(\mathbf{x}) = F_{ij} \circ \xi_{ij} = \int_{-\infty}^{\infty} \xi_{ij}(\mathbf{x}') F_{ij}(\mathbf{x}, \mathbf{x} - \mathbf{x}') d\mathbf{x}, \tag{5.14}$$

where

$$F_{ij}(\mathbf{x},\mathbf{r}) = \exp\Big(-\frac{\|\mathbf{r}\|^2}{\sigma_{ij}}\Big). \tag{5.15}$$

To omit the details of mathematical derivations, only the final results will be presented. For a specific target of integral length scales denoted by l_{ij} and Reynolds stress denoted by $\langle u_i u_j\rangle$, the coefficients for the linear combination used in Eq. (5.13) can be expressed as

$$\begin{aligned}
a_{11} &= \frac{\langle uu\rangle - |\langle uv\rangle| - |\langle uw\rangle|}{\sqrt{l_{uu}\langle uu\rangle - l_{uv}|\langle uv\rangle| - l_{uw}|\langle uw\rangle|}};\\
a_{22} &= \frac{\langle vv\rangle - |\langle uv\rangle| - |\langle vw\rangle|}{\sqrt{l_{vv}\langle vv\rangle - l_{uv}|\langle uv\rangle| - l_{vw}|\langle vw\rangle|}};\\
a_{33} &= \frac{\langle ww\rangle - |\langle uv\rangle| - |\langle vw\rangle|}{\sqrt{l_{ww}\langle ww\rangle - l_{uw}|\langle uw\rangle| - l_{vw}|\langle vw\rangle|}};\\
a_{12} &= \sqrt{\frac{|\langle uv\rangle|}{l_{uv}}};\\
a_{13} &= \sqrt{\frac{|\langle uw\rangle|}{l_{uw}}};\\
a_{23} &= \sqrt{\frac{|\langle vw\rangle|}{l_{vw}}};
\end{aligned} \tag{5.16}$$

while the filter width corresponding to each uncorrelated random fields f_{ij} are

$$\begin{aligned}
\sigma_{11} &= \left(\frac{2}{\pi}\right)^{\frac{1}{2}} \frac{l_{uu}\langle uu\rangle - l_{uv}|\langle uv\rangle| - l_{uw}|\langle uw\rangle|}{\langle uu\rangle - |\langle uv\rangle| - |\langle uw\rangle|};\\
\sigma_{22} &= \left(\frac{2}{\pi}\right)^{\frac{1}{2}} \frac{l_{vv}\langle vv\rangle - l_{uv}|\langle uv\rangle| - l_{vw}|\langle vw\rangle|}{\langle vv\rangle - |\langle uv\rangle| - |\langle vw\rangle|};\\
\sigma_{33} &= \left(\frac{2}{\pi}\right)^{\frac{1}{2}} \frac{l_{ww}\langle ww\rangle - l_{uw}|\langle uw\rangle| - l_{vw}|\langle vw\rangle|}{\langle ww\rangle - |\langle uw\rangle| - |\langle vw\rangle|};\\
\sigma_{12} &= \left(\frac{2}{\pi}\right)^{\frac{1}{2}} l_{uv};\\
\sigma_{13} &= \left(\frac{2}{\pi}\right)^{\frac{1}{2}} l_{uw};\\
\sigma_{23} &= \left(\frac{2}{\pi}\right)^{\frac{1}{2}} l_{vw};
\end{aligned} \tag{5.17}$$

In this work, a parallel code called GTURB has been developed using FORTRAN 90 to generate periodic 2D and 3D synthetic turbulent fields using the filtered noise

approach. Figure 5.4 illustrates the contour plot of u-component velocity from a sample 2D turbulent flow.

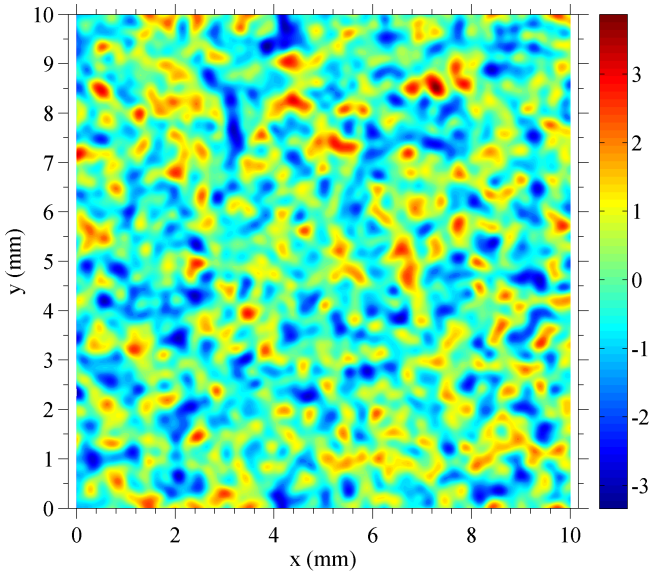

Figure 5.4. Contour of u-component velocity in a 2D homogeneous isotropic synthetic turbulence field with specified $u_{rms} = 1.0\ m/s$ and integral length scale of 1.0 mm.

5.3.2 Forced turbulence

An alternative approach to generate turbulence field is by forcing the flow. Lundgren (2003) [196] proposed the so-called "linear forcing" scheme where he has demonstrated that linear forcing in the Fourier or wavenumber space produces statistics at scales between integral and inertial subrange that resemble observations from experiment data. Later Rosales and Meneveau (2005) [197] applied the linear forcing in the physical space which makes it attractive for the simulations of this work. The idea of "linear forcing" is inspired by recognizing that the term which accounts for turbulent kinetic energy (TKE) production by the mean flow in the TKE balance equation is of the form $P = \rho \mathbf{u}' \cdot \nabla \langle \mathbf{u} \rangle$. This implies that if a term proportional to the fluctu-

ating velocity is added to momentum equation, such mechanism of TKE production in homogeneous turbulence can be mimicked. Hence, the momentum equation with forcing can be written as,

$$\frac{\partial \rho u_i}{\partial t} + \frac{\partial \rho u_j u_i}{\partial x_j} = -\frac{\partial p}{\partial x_i} + \frac{\partial \tau_{ij}}{\partial x_j} + B\rho u_i, \tag{5.18}$$

where the forcing coefficient B is given by

$$B = \frac{\epsilon + \langle \mathbf{u} \cdot \nabla p \rangle}{3\langle \rho \rangle \tilde{\mathrm{u}}_{\mathrm{rms}}^2}, \tag{5.19}$$

Here, ϵ represents the mean turbulent dissipation per unit volume. The term $\langle \mathbf{u} \cdot \nabla p \rangle$ scales with the squares of turbulent Mach number (M_t) and can be neglected for low-Ma flow.

It is found that, with this specific form of linear forcing in place, turbulence intensities can be sustained and at the steady-state, turbulent dissipation rate is related to the domain size L and the forcing coefficient by the following relations:

$$B = \frac{\epsilon^{1/3}}{0.99\mathrm{L}^{2/3}}. \tag{5.20}$$

Furthermore, it is found that the integral length scale will always converge to approximately 19% of the domain size at steady-state despite the initial conditions employed. Carroll and Blanquart (2013) [198] further modified the forcing term in Eq. (5.18):

$$f_i = B\Big(\frac{k_o}{k}\Big)\rho u_i, \tag{5.21}$$

where k is the instantaneous TKE calculated from the flow and k_o is the desired steady-state TKE. They have reported that with this modification, faster convergence rate is observed while the oscillatory amplitude of the flow solutions at steady-state is effectively reduced. In the current work, the forcing term given by Eq. (5.21) has been implemented in FLEDS and HOLOMAC and validated against the results obtained by Rosales and Meneveau (2005) [197]. Figure 5.5 shows the energy spectrum of a steady 3D homogeneous isotropic turbulence obtained from linear forcing in the wavenumber space. The result is in close agreement with the published data (green circles).

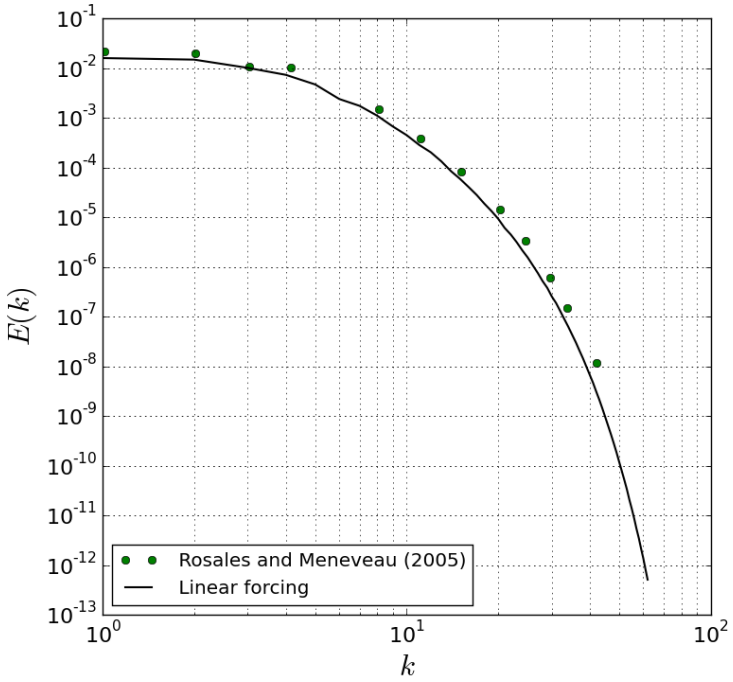

Figure 5.5. Energy spectrum as a function of wavenumber for a forced 3D homogeneous isotropic turbulence flow field.

5.4 Summary

In this chapter, a computational methodology to simulate statistically stationary turbulent premixed flames in an inflow-outflow configuration is developed. The primary motivation behind this approach is to reduce computation expenses. This is done by employing a Lagrangian framework. To keep the flame statistically stationary, the inflow velocity is dynamically adjusted and hence no prior knowledge of the turbulent flame speed is required. With the change in frame of reference, sizes of the computation domain are effectively decoupled from the physical flow time, and thus allow for statistics to be collected over a prolonged period of time for given computational resource.

Methods to generate 2D and 3D turbulence for reacting simulations have been evaluated. An inexpensive approach to generate "synthetic" turbulence is by digitally

filtering white noises and prescribing desired length scales and Reynolds stresses. This is applicable to both 2D and 3D turbulence. Another approach to generate turbulent flows is by forcing the flow to mimic the energy cascade process. It is capable of maintaining constant turbulence intensities and length scales, but is limited to only 3D simulations. In this work, auxiliary 2D turbulence is generated through the first method while 3D turbulence is obtained by applying "linear forcing".

6. EVALUATION OF FLAME SPEED IN A TWO-DIMENSIONAL DOMAIN

6.1 Introduction

In Chapter 5, a feedback control algorithm was developed for simulating statistically-stationary turbulent flames. In this chapter, we will apply this method to simulate turbulent flames for varying turbulence properties in a two-dimensional (2D) domain. Turbulent flame speeds are computed for flames with two equivalence ratios. We recognize that "two-dimensional" turbulence does not exist in reality. The work in this chapter is primarily motivated by computational cost.

Furthermore, it is important to recognize that many reported simulations of turbulent flames in the literature are still 2D because of the limitations in computational resources [175, 193, 199, 200, 201]. The validity of 2D simulations of turbulent flames has been assessed. Sreedhara and Lakshmisha (2002) [202] compared results from 2D and 3D DNS of autoignition in n-heptane/air mixing layers. They found that 2D and 3D simulations yield contradictory conclusions on how increasing turbulence intensities would affect autoignition delays. Ameen and Abraham (2015) [201] compared 2D and 3D DNS of turbulent non-reacting fuel/air mixing layers. They found that the evolution of the scalar field and its dissipation rate are different between two simulations. It is also found that the 2D results can be employed for assessing the relative accuracy of sub-grid scale models.

The next section will present some extended comments on 2D turbulence. Some of the fundamental differences between 2D and 3D turbulent flow will be highlighted. Section 6.3 will discuss the turbulent flame speeds obtained from the parametric study. Comparison with the existing correlations will also be made.

6.2 Comments on "Two-Dimensional" Turbulence

The important question is whether turbulence analyzed in a 2D framework bears some of the features of turbulence viewed in a 3D framework. With the recent development in planar experimental imaging and direct numerical simulations in 2D domains, turbulence is better understood in a 2D framework [203]. In this thesis, turbulence viewed in a 2D framework will be referred to as simply "2D turbulence" henceforth. Evidently 2D and 3D turbulence share some common attributes. Features such as cascades from large scales to small scales, the formation of coherent structures, dissipative processes and filamentation mechanisms are present in both systems. At the same time, simulating 2D turbulence in reacting flows offers drastic savings in terms of computational resources especially when detailed chemical kinetics are included in the simulations. Arguably, studying flame in 2D turbulence can provide insights if not analogies that are applicable to the general 3D problem.

The core difference of 2D from 3D turbulence is the lack of the third dimension which precludes the phenomenon known as vortex stretching. Consider the incompressible Navier-Stokes equation. Performing the curl on the equation, we get the balance equation for the vorticity, i.e., $\vec{\omega} = \nabla \times \mathbf{u}$, as follows

$$\frac{\partial \vec{\omega}}{\partial t} + \mathbf{u} \cdot \nabla \vec{\omega} = \vec{\omega} \cdot \nabla \mathbf{u} + \nu \nabla^2 \vec{\omega}. \tag{6.1}$$

The first term on the right hand side represents the stretching due to the flow velocity gradients, i.e., the vortex stretching. For a 2D flow, the vorticity equation becomes a single equation for scalar ω_z as in

$$\frac{\partial \omega_z}{\partial t} + \mathbf{u} \cdot \nabla \omega_z = \underbrace{\omega_z \cdot \nabla \mathbf{u}}_{\equiv 0} + \nu \nabla^2 \omega_z. \tag{6.2}$$

The velocity gradient $\nabla \mathbf{u}$ is in the x or y-direction which is always perpendicular to ω_z that points to the third dimension. As a result, vortex stretching term, i.e., $\omega_z \cdot \nabla \mathbf{u}$ is unconditionally zero for 2D flows. In 3D flows, vortex stretching is responsible for amplifying vorticity along vortex trajectories which leads to the formation of small intense filaments. Such mechanism is however absent in 2D turbulent flows. It is also

important to note that in the limit of inviscid flow, $\nu\nabla^2\omega_z$ equals zeros and vorticity becomes a conserved quantity on the 2D plane.

Free decay of 2D turbulence has been well documented in the literature [203, 204, 205]. It is known that the system of vortices will always evolve towards a state where large scale coherent structures dominate notwithstanding what the initial distribution of vortices is. The process of decay has been characterized by McWilliams (1990) [204] into several elementary mechanisms at play. In the initial decay phase, the weakest vortices are destroyed by the break-up process while the strongest vortices merge with one another. Throughout the process, the number of vortices decrease while the distribution of vorticity grows narrower, i.e., vortices with vorticity at both extremes disappear. However, the most probable vorticity will remain unchanged. Thin vorticity filaments are produced either during merging events or in the break-up process. At moderate Reynolds numbers these filaments disappear while at higher Reynolds numbers, these filaments would form small vortices through nucleation. Eventually, the system evolves to a state with a single pair of counter-rotating vortices, also known as the "final dipole", coexisting with the background of short-lived vortex filaments [204].

The energy cascade in 2D turbulence is different from that in 3D turbulence. In 3D flows, the mechanism accounting for energy transfer has been famously described by Richardson in the 1920s [206]. The kinetic energy is injected by external forcing which sustains the motion of the largest scale eddies. These eddies are strained by the velocity gradients until they break down into smaller eddies. This process is repeated and during the break-apart of eddies, energy is transported from large scales to smaller scales. Ultimately energy is dissipated by molecular viscosity at the smallest scales, i.e., the Kolmogorov scales. In 2D homogeneous turbulence, the turbulent kinetic energy evolves according to

$$\frac{dE}{dt} = \frac{1}{2}\frac{du^2}{dt} = -\nu Z. \tag{6.3}$$

where $Z = \langle \omega^2 \rangle$ is the enstrophy. The enstrophy equation is given as

$$\frac{DZ}{Dt} = -\nu \langle (\nabla \vec{\omega})^2 \rangle. \tag{6.4}$$

From Eq. (6.4) it is evident that in 2D turbulence, enstrophy is forced to decrease with time as the right-hand-side of the equation is non-positive. This is in contrast to 3D turbulence where enstrophy will increase with time as long as viscous effects are not dominant [203]. More importantly, in the inviscid limit, turbulent kinetic energy in 2D flow becomes conserved whereas in 3D, turbulence energy will cascade from large scale to small scale. Lesieur (1990) [207] considered a triad of wavenumber modes and the interactions between their respective energy and enstrophy densities. It can be argued that energy is transferred preferentially towards small wavenumbers, i.e., large physical scales, while enstrophy is transferred towards large wavenumbers, i.e., small physical scales. This implies the existence of an enstrophy cascade and an inverse energy cascade in 2D turbulence, which was first termed as the "double cascade process" by Kraichnan (1967) [208].

To put things in perspective, in the current 2D simulations of premixed flame, turbulent velocity fluctuations are imposed at the inflow boundary. Before the unburnt charge reaches the flame front, it essentially remains as a freely decaying 2D turbulent flow with a mean flow velocity. If the viscosity in the portion of fresh gas is "artificially" tuned to a small value representing inviscid range, we know from the previous analysis that, 1) the total vorticity and turbulent kinetic energy of every fluid parcel will be minimally affected and 2) number of vortices will decrease along the inflow direction while their sizes will grow. This implies that while turbulence intensities can be maintained, there is no effective control on the length scales of the vortices entering the flame. Nevertheless, if the flame is statistically stationary, the integral scales at the location of flame brush can be assumed to be invariant in time despite its value not being specified *á priori*. Furthermore, integral scales at the flame front can be assumed to be similar between cases, should a common computational domain be used. With this setup, series of 2D simulations have been carried out and the results will be presented in the following section.

6.3 Two-Dimensional Turbulent Flame Speeds

We will now present results from parametric studies exploring the effects of turbulence and flame scales on turbulent flame speeds under lean-burn conditions in a 2D domain. Table 6.1 lists the physical conditions we have employed. A total of eleven cases have been simulated for premixed equivalence ratio of 0.5 and seven cases for that of 0.6. Pressure is selected at 20 bar while the temperature of the unburned mixture is at 810 K. Integral length scale of the auxiliary 2D turbulence fields, i.e., at the inflow boundary, is fixed at 1.0 mm while the laminar flame thermal thicknesses are 100 and 50 μm, respectively, for $\phi = 0.5$ and 0.6. These thicknesses are measured based on the maximum temperature gradient existing inside the unstrained laminar flame profile, i.e.,

$$\delta_L = \frac{\mathrm{T_b} - \mathrm{T_u}}{\max\{d\mathrm{T}/dx\}}. \tag{6.5}$$

An alternative method to measure flame thickness is based on the physical distance between locations in the 1D laminar flame where temperature has risen 10% and 90% above the unburnt temperature, i.e.,

$$\delta'_{\mathrm{L}} = \left\| x\big|_{\mathrm{T=T_u+10\%(T_b-T_u)}} - x\big|_{\mathrm{T=T_u+90\%(T_b-T_u)}} \right\|. \tag{6.6}$$

The subscripts u and b denote the properties in the unburnt and fully-burnt mixture. Using this definition, the laminar flame thicknesses are 125 and 60 μm for the laminar flame of equivalence ratios of 0.5 and 0.6, respectively.

The turbulent Reynolds number based on integral length scale $\mathrm{L_o}$ is given by

$$Re_{\mathrm{T}} = \frac{\rho_u \mathrm{u_{rms}} \mathrm{L_o}}{\mu_u}. \tag{6.7}$$

The highest Re_{T} considered for ϕ of 0.5 and 0.6 are approximately 570 and 680. The smallest scale of turbulence η, i.e., the Kolmogorov scale, is less than the flame thermal thickness for all cases. Note that the definition of the Kolmogorov scale is ambiguous in 2D turbulence as the 2D energy cascade is of a different nature than that in 3D turbulence. The relations employed to estimate η here are the same as in 3D. The Karlovitz number of these cases ranges from 0.5 to 26.2. Recall that

Table 6.1. Simulation conditions and computed turbulent flame speeds S_T normalized by the laminar flame speed S_L.

Case	P (bar)	T (K)	ϕ	Effective u_{rms}/S_L	L_o (mm)	η (μm)	Re_T	Ka	S_T/S_L
A1	20	810	0.5	0.79	1.00	57	45.6	0.6	1.110
A2	20	810	0.5	1.47	1.00	29	114.0	2.3	1.642
A3	20	810	0.5	3.92	1.00	17	228.0	6.6	4.075
A4	20	810	0.5	6.41	1.00	13	342.0	12.2	5.114
A5	20	810	0.5	9.65	1.00	10	456.0	18.7	5.066
A6	20	810	0.5	10.58	1.00	9	570.0	26.2	6.553
A7	20	810	0.5	1.86	1.00	21	171.0	4.3	2.256
A8	20	810	0.5	5.29	1.00	14	285.0	9.3	4.964
A9	20	810	0.5	6.92	1.00	11	399.0	15.3	5.221
A10	20	810	0.5	11.07	1.00	9	513.0	22.4	6.391
A11	20	810	0.5	9.97	1.00	10	456.0	18.7	5.432
B1	20	810	0.6	0.81	1.00	29	114.0	0.5	1.439
B2	20	810	0.6	1.87	1.00	17	228.0	1.3	2.278
B3	20	810	0.6	3.01	1.00	13	342.0	2.4	3.549
B4	20	810	0.6	4.32	1.00	10	456.0	3.8	3.588
B5	20	810	0.6	5.87	1.00	9	570.0	5.3	4.758
B6	20	810	0.6	7.39	1.00	7	684.0	6.9	5.918
B7	20	810	0.6	7.58	1.00	7	684.0	6.9	6.260

Karlovitz number characterizes the ratio of chemical timescale to the time scale of the smallest eddies of turbulence and is defined as

$$Ka = \left(\frac{u_{rms}}{s_L}\right)^2 Re_T^{-0.5} \sim \left(\frac{u_{rms}}{s_L}\right)^{\frac{3}{2}} \left(\frac{\delta_L}{L_o}\right)^{\frac{1}{2}}. \tag{6.8}$$

We will first discuss the evolution of the premixed flame toward statistical steady-state using one of simulations as the baseline case. Recall that the initial flame profile is that of the 1D laminar flame. Figure 6.1 shows the evolution of temperature contours inside the domain over a course of 15 eddy turnover times for Case A5. The domain size has been non-dimensionalized by the turbulent integral length scale. It is evident that there are several eddies influencing the flame along the surface. Since the ratio of u_{rms}/S_L is relatively high (around 10), the wrinkling of the flame front is evident from the start of the simulation. Elongated structures referred to as flame fingers are formed which are then advected by the local flow field as evident in Figs. 6.1(a) and (b). At times, two branching fingers coalesce into a thicker stream (this can be inferred from Figs. 6.1(c) and (d)). Occasionally excessive strain at the base causes the finger to dislodge from the continuous flame front. Consequently, islands of burned gases can be formed which are separated from the initial flame front. Some of these islands extinguish as evident in Fig. 6.1(b) while others survive and grow into separate flame kernels as shown in Fig. 6.1(d). Pockets of fresh gases are entrained inside the burnt charge in Figs. 6.1(d), (e) and (f). However, these engulfed pockets of unburned mixture are short-lived as they are readily consumed by the surrounding flame. Local straining of the flame is also evident which is a result of two adjacent eddies moving in counter directions. When the local strain rate exceeds a threshold, local extinction occurs.

Figure 6.2 shows the turbulent flame speeds over a range of turbulence intensities estimated at the flame front for two equivalence ratios. They are obtained by averaging in time over more than 30 eddy turnover times once the flame becomes fully developed in the statistical sense. To put things in context, the physical conditions corresponding to these points are plotted in the combustion regime diagram as shown in Fig. 6.3. Note that the boundaries between various regimes in this map have not yet been confirmed and thus are not necessarily accurate in a quantitative sense. It is evident from Fig. 6.2 that for equivalence ratio of 0.5 (represented by the red squares), there are three distinct regimes spanned by the dataset. The first

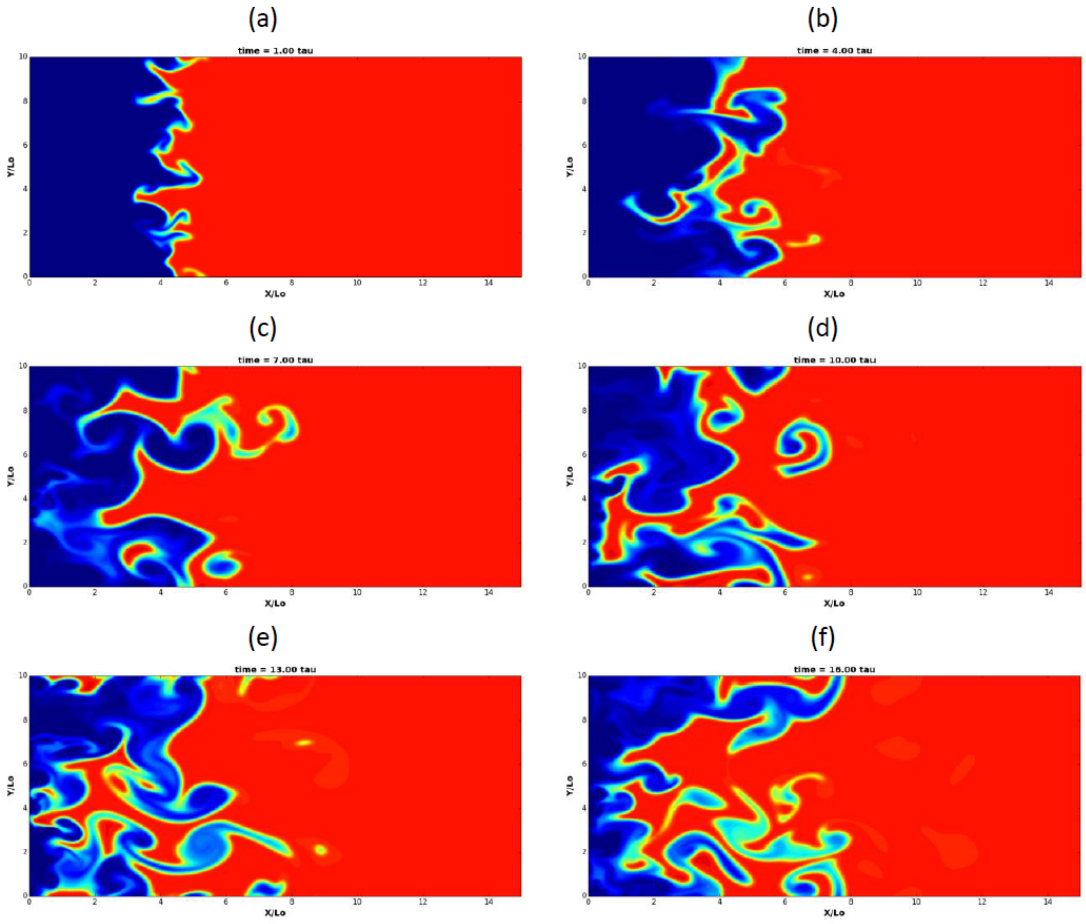

Figure 6.1. Snapshots of flame evolution of Case A5 at (a) $t = 1.0\tau_o$; (b) $t = 4.0\tau_o$; (c) $t = 7.0\tau_o$; (d) $t = 10.0\tau_o$; (e) $t = 13.0\tau_o$; (f) $t = 16.0\tau_o$.

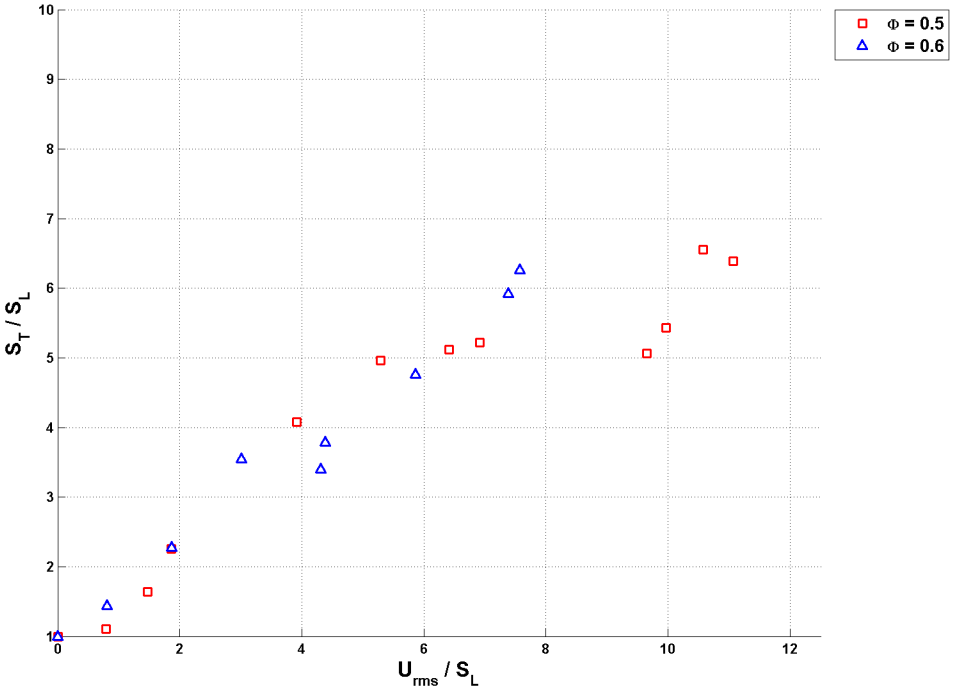

Figure 6.2. Ratio of turbulent flame speed to unstrained laminar flame speed over a range of non-dimensionalized turbulence intensities for $\phi = 0.5$ (red) and $\phi = 0.6$ (blue).

regime can be defined for $u_{rms}/S_L < 5$ where the normalized turbulent flame speeds increase with increasing turbulence intensities, and can be related to $u_{rms}/S_L < 5$ with a linear or power-law relationship. This form of correlation is commonly employed in the prior works as have been elaborated in Chapter 2. Under this condition, the flame corresponds to the weakly wrinkled or the corrugated flamelet regime shown in Fig. 6.3. In this regime, increasing turbulence will result in the generation of flame surface area through the wrinkling effect and in turn result in enhanced burning rate. The second regime can be defined for $5 < u_{rms}/S_L < 10$. It can be seen from Fig. 6.2 that the turbulent flame speed begins to plateau with further increase in turbulence intensities. There are two possible explanations for this observed trend. Damköhler (1940) [123] and later Bray and Cant (1991) [209] suggested the turbulent flame speed S_T can be related to the turbulent flame surface area A_T by

$$\frac{S_T}{S_L} = I_o\Big(\frac{A_T}{A_L}\Big), \tag{6.9}$$

where I_o is the efficiency factor to represent the effects of flame strain and curvature. The flame stretch factor can be expressed with first-order correction [210, 211] for small strain and curvature effects as

$$I_o = 1 - \mathcal{L}\Big(\kappa + \frac{a_T}{S_L}\Big), \tag{6.10}$$

where κ is the mean curvature, a_T is the tangential strain rate and $\mathcal{L}$ is the Markstein length, which depends on the unburnt mixture conditions and Lewis number (Le) of the fuel. One possible explanation is that further increasing turbulence intensities beyond a certain threshold would cease to generate any significant increase in the turbulent flame area and thereby S_T becomes flattened. Another explanation is associated with the higher strain rate which is accompanied with increasing turbulence intensity. As a result, steep gradients of temperature and species concentration are created which increases the possibility of flame quenching and thereby causing the global flame speed to flatten. The last regime is defined for u_{rms}/S_L greater than 10 where the turbulent flame speed appears to grow with further increasing u_{rms}. The flattening behavior of S_T with increasing u_{rms} will be explained in Chapter 8.

For premixed flames with equivalence ratio of 0.6 as marked by triangles in Figs. 6.2 and 6.3, a uniform trend in flame speeds is observed, i.e., increasing turbulence enhances overall burning rate. More importantly, the normalized flame speeds in the mixture of $\phi = 0.5$ and 0.6 do not appear to collapse into a single line. This suggests that the turbulent flame speed is not a function of the normalized turbulence intensity alone.

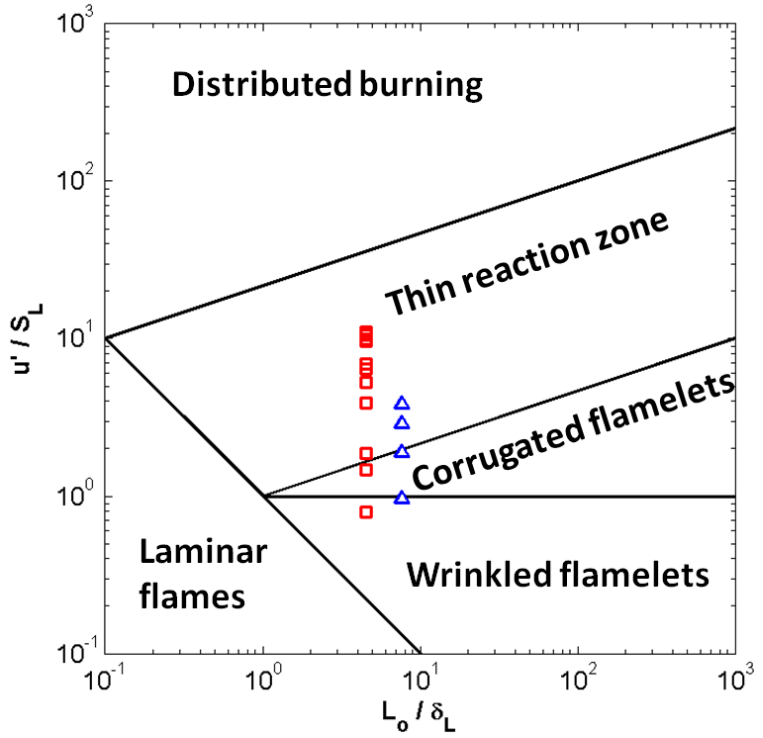

Figure 6.3. Simulation points corresponding to $\phi = 0.5$ (red) and $\phi = 0.6$ (blue) inside the combustion regime map of Peters (2002) [46].

Figure 6.4 shows a comparison between our simulated results and the turbulent flame speeds predicted by 13 correlations which we found in the literature [62, 77, 79, 105, 116, 124, 125, 127, 128, 129, 130, 132, 143]. Some of them are summarized in the literature review of this work in Chapter 2. It can be seen that there is a large variability among the predictions of the correlations. In addition, none of the existing correlations accounts for the fundamental changes in the modes of turbulence-

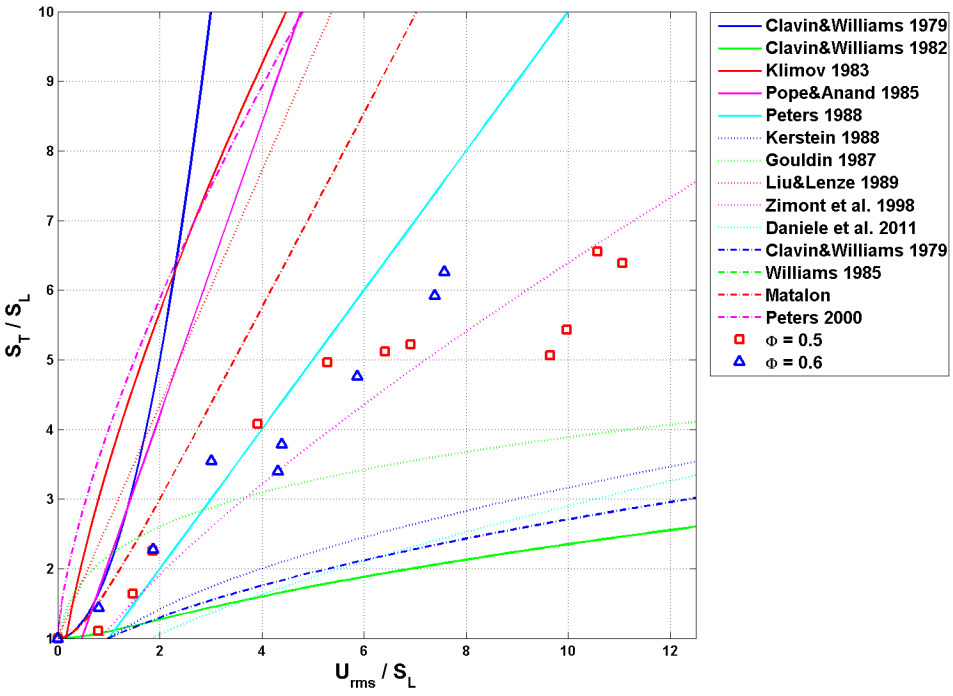

Figure 6.4. Computed turbulent flame speeds of (a) $\phi = 0.5$ (red) and (b) $\phi = 0.6$ (blue) in contrast to the predictions given by correlations in the literature.

chemistry interaction when flame transitions from one regime to another. It is also important to point out that the turbulent flame speed does not appear to be a single function of turbulence intensities, or else the simulated turbulent flame speed at equivalence ratio of 0.5 and 0.6 in Fig. 6.2 would have collapsed to one curve. It is likely to depend on Ka and/or Da which is a function of thermodynamic and chemical properties. In fact, few of the correlations proposed in the literature (only until recently) appear to recognize that such dependence is not just on turbulence intensity [116, 132], although neither of them fit the simulated data and they show significant differences among themselves.

6.4 Summary

Before any conclusion is drawn from the 2D simulations, it is important to check whether the predicted trend shown in this chapter is an accurate representation of chemistry-turbulence interaction that would occur in the 3D space. In the next chapter, 3D simulations of turbulent premixed flames will be presented. In particular, the effects of equivalence ratio on turbulent flame speed will be discussed.

7. EFFECTS OF EQUIVALENCE RATIO VARIATIONS ON TURBULENT FLAME SPEED

7.1 Introdution

In the previous chapter, we presented DNS studies of premixed flames propagating in a two-dimensional domain. Lean flames with equivalence ratio ϕ of 0.5 and 0.6 were considered. It was shown that the equivalence ratio affects the normalized turbulent flame speeds evaluated in a 2D framework. However, since 2D turbulence lacks the crucial mechanism of vortex stretching and is unphysical in nature, the validity of this conclusion needs to be further assessed. In this chapter, 3D DNS of lean premixed flames are carried out. The results are analyzed with a focus on the investigation of equivalence ratio effects on turbulent flame speed S_T. The work presented in this chapter has appeared in a journal publication by Wang *et al.* (2016) [212].

Understanding the effects of ϕ on S_T is crucial for natural gas engine applications. Efficiency and emissions considerations often require engines to operate as close to the lean limit as possible. Due to the presence of equivalence ratio variations inside the engine chamber, misfire is prone to occur especially under lean-burn conditions, which can be consequential to engine performance. Note that variations in ϕ inside engines arise from cycle-to-cycle variability and incomplete mixing that results in spatial variations. Therefore, it is important to develop better understanding of how flame propagation is dependent on equivalence ratio near the lean limit.

As discussed in Chapter 2, the turbulent flame speed S_T often appears as a direct input for several flamelet-based models [76]. Indeed, by assuming *á priori* closure for the turbulent flame speed, multi-dimensional simulations have been carried out in rather complex geometries such as combustion bombs [113], SI engines [114, 115] and industrial burners [116, 117]. It is important to note that several definitions of

turbulent flame speeds exist. To avoid ambiguity, we will define turbulent flame speed as the velocity at which the unburned mixture enters the flame zone in the direction normal to the mean flame front. Numerous correlations for S_T have been proposed in the past and a majority of the existing correlations involves the ratio of turbulence intensity to laminar flame speed (u_{rms}/S_L) [116, 125, 128, 132]. Dependencies of S_T on the ratio of the length scales (L_o/δ_L), or alternatively the Damköhler number (Da) have also been reported [116, 132]. Here, S_L and δ_L denote the flame speed and flame thickness based on the maximum temperature gradient of an unstrained laminar flame, respectively; u_{rms} and L_o represents the root-mean-square of turbulent velocity fluctuations and the integral length scale of the turbulence, respectively.

The effects of equivalence ratio ϕ on S_T normalized by the laminar flame speed S_L are still not well understood. Specifically, it is not known whether the equivalence ratio effect is exerted only through its effect on the laminar flame speed S_L and flame thickness δ_L. Limited work has been carried out to characterize the equivalence ratio effects. Bell *et al.* (2006) performed "2D" DNS of premixed methane flames at equivalence ratios $\phi = 0.55$ and 1.00 [200]. They found a change in the Markstein number as ϕ is varied which, in turn, modified the turbulent flame speed. Fru *et al.* (2011) carried out DNS of premixed methane-air flame kernels subjected to various turbulence intensities at five equivalence ratios [213]. They observed that for a fixed value of u_{rms}/S_L, S_T/S_L varies with equivalence ratios. However, neither of the two works has taken into account the effects of length scales, i.e., L_o/δ_L. In addition, the studied flames are subjected to decaying turbulence which introduces ambiguity into the definition of u_{rms}/S_L.

In this chapter, we set out to investigate the influence of equivalence ratio on the turbulent flame speed using DNS. By forcing the turbulence inside the fresh mixtures, we ensure that the premixed flame is interacting with non-decaying turbulence such that velocity and length scale ratios between the flow field and flame are clearly defined and held invariant throughout the course of simulation. The rest of the chapter is organized in the following manner. Section 7.2 discusses the numerical

methods, chemistry mechanism and the simulation setup. Section 7.3 presents the results of turbulent flame speed at various equivalence ratios. The explicit influence of ϕ on S_T is examined. Characterization of flame surface generated by turbulent eddies of various scales is performed in Section 7.4. The effect of flow strain rates with respect to the flamelet are also discussed. The chapter then closes with summary and conclusions in Section 7.5.

7.2 Computational Setup

7.2.1 The numerical model

The results presented in this study are obtained using the low-Mach code HOLOMAC [152]. As discussed in Chapter 3, the code solves the 3D conservation equations for multi-component mixtures with CHEMKIN interface for computing the chemical source terms. Spatial discretization is performed using a 6th-order implicit compact scheme [153]. The convection terms are advanced in time using a 2nd-order Adams-Bashforth (AB2) scheme while the diffusion terms are advanced using an explicit 4-step Runge-Kutta-Chebyshev (RKC) method. The divergence condition is enforced using a projection-correction method, i.e., at each time step, the hydrodynamic pressure is solved from a variable-coefficient Poisson equation using Fast Fourier Transform (FFT) and is used to correct the provisory velocity.

It is well known that DNS with multi-step chemistry is computationally intensive. In this study, a 13-species reduced mechanism developed by Sankaran *et al.* (2007) [214] is employed. In addition, the following global chemical mechanism that is able to predict the laminar flame speed is employed:

$$\dot{\omega} = A\mathrm{T}^b \left[\mathrm{CH_4}\right]^m \left[\mathrm{O_2}\right]^n e^{-E_a/R\mathrm{T}}. \tag{7.1}$$

The parameters A, b, m and n are calibrated such that the laminar flame speed is comparable to the flame speed predicted by both a 17-species, 73-step skeletal mechanism developed by Sankaran *et al.* (2007) [214] and the GRI-Mech 3.0 [183].

Specifically, the values of the constants of the global mechanism are given as $A = 3.25 \times 10^{19} cm^3/mol \cdot s$; $b = 0$; $m = n = 1$; $E_a = \mathcal{R} \cdot (40250\text{K})$. Figure 7.1 shows the computed laminar flame speeds obtained with the four mechanisms for premixed equivalence ratios between 0.39 and 0.80, the range of interest in these simulations. The results agree within 10% of each other.

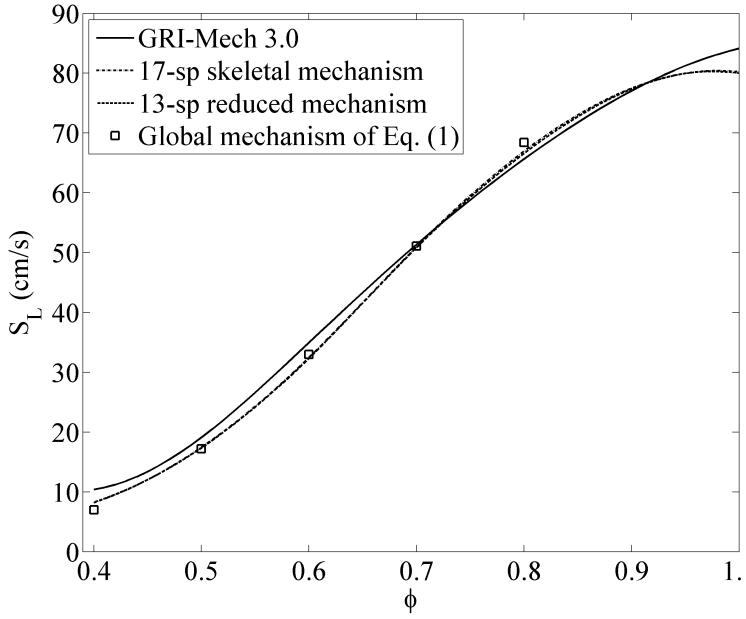

Figure 7.1. Computed laminar flame speeds as a function of ϕ for unburned temperature of 810 K at pressure of 20 bar with four mechanisms.

However, the use of global mechanism is believed to be inadequate for predicting flame response to high strain rates and hence extinction phenomena. To assess the adequacy of using the global mechanism for simulating turbulent flames, it is important to consider not only the flame speed, but also i) flame thickness, ii) flame surface wrinkling and iii) reaction rate on the flame front as a result of turbulence-chemistry interaction. In this section, the dependence on the chemistry mechanism of these three turbulent flame characteristics will be compared between flames simulated using the 13-species reduced mechanism [214] and the global mechanism for $\phi = 0.50$ at the highest turbulence intensity ($u_{rms}/S_L = 14.3$) considered in this study.

The effect of turbulence on the local flame thickness is examined first. This effect can be quantified using the mean of temperature gradient conditioned at a given temperature, i.e., $\langle \|\nabla T\| | T \rangle$ where $\langle \cdot \rangle$ involves averaging both in time and on the flame surface. Figure 7.2 shows the conditional mean of temperature gradient normalized with that across the unstrained laminar flame front as a function of temperature for flames simulated with the 13-species and the global mechanism. Note that a value less than 1 indicates "flame thickening"and a value larger than 1 indicates "flame straining". It is evident in Fig. 7.2 that both mechanisms predict thicker flame structure for T < 1700 K, i.e., inside the preheat zone, and thinner flame for T > 1700 K, i.e., inside the reaction zone. Furthermore, the effect of turbulence on the flame thickness using the two mechanisms shows agreement within 10% except at temperature close to the burnt gas temperature.

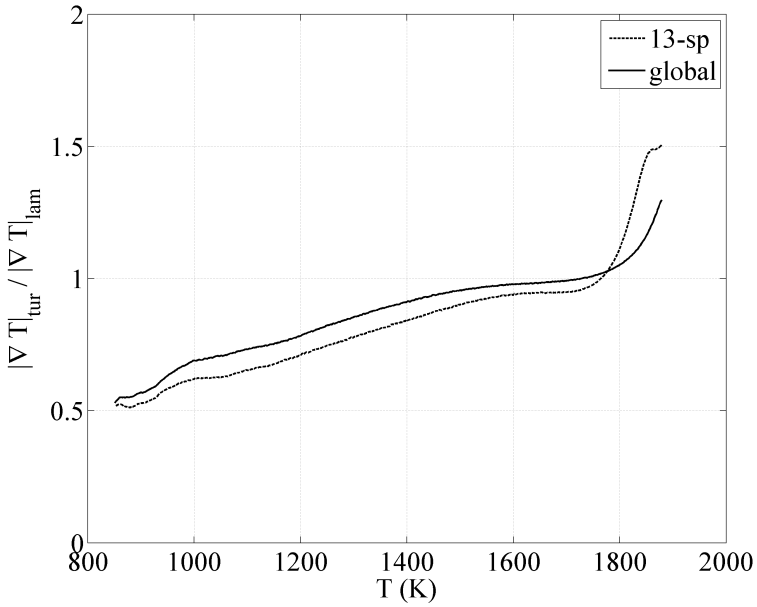

Figure 7.2. Averaged temperature gradient conditioned on flame temperature, i.e., $\langle \|\nabla T\| | T \rangle$ normalized with that of unstrained laminar flame as a function of temperature for $u_{rms}/S_L = 14.3$ (Case 1).

Flame surface wrinkling is another key feature in the modeling of turbulent premixed flames. Figure 7.3 shows the isotherm surface area A_T (T) evaluated at various

temperatures for flames simulated with the two mechanisms. The isotherm surface area is computed using a "marching cube" algorithm and averaged in time. The figure shows that the global mechanism predicts higher surface area for T > 1000 K but the difference is within 7%.

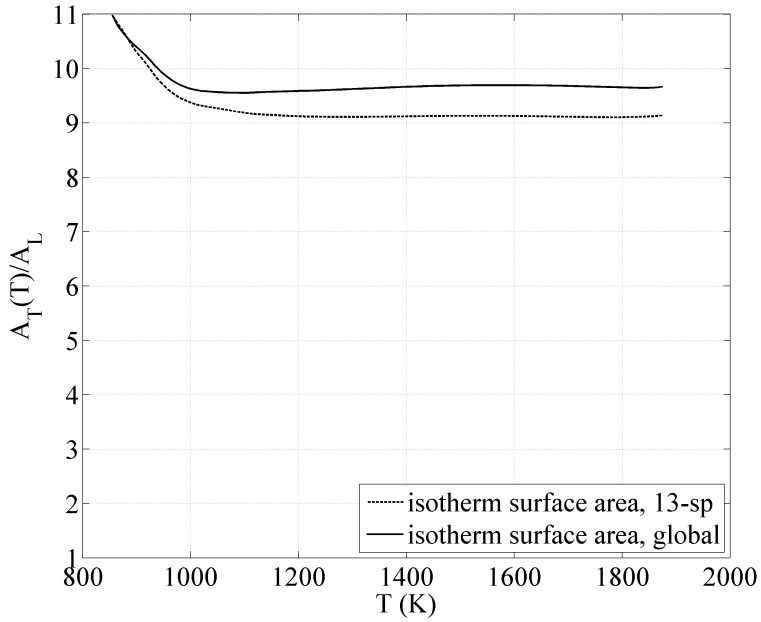

Figure 7.3. Time-averaged normalized flame surface area evaluated at T, i.e., A_T (T)/A_L as a function of temperature for $u_{rms}/S_L = 14.3$ (Case 1).

Figure 7.4 shows the comparison between the time-averaged heat release rate per unit volume conditioned on flame temperature using the 13-species and the global mechanism. The heat release rate distributions of the respective laminar flames are also plotted in solid lines. Note that the laminar profiles of heat release rate (lines) in the temperature space show noticeable differences between the two mechanisms although the differences in laminar flame speed are small as seen in Fig. 7.1. This is because the differences between heat release rate profiles in the physical space are less pronounced and it is ensured that the total heat release rate across the laminar flame front is the same for both mechanisms, hence the approximate equivalence of the laminar flame speeds. The 13-species mechanism predicts up to 5% increase in

the heat release rate compared to the laminar case whereas global mechanism predicts up to 10% increase for T > 1700 K. This increment in the heat release rate is likely a result of the "turbulence straining" of the reaction zone as illustrated in Fig. 7.2.

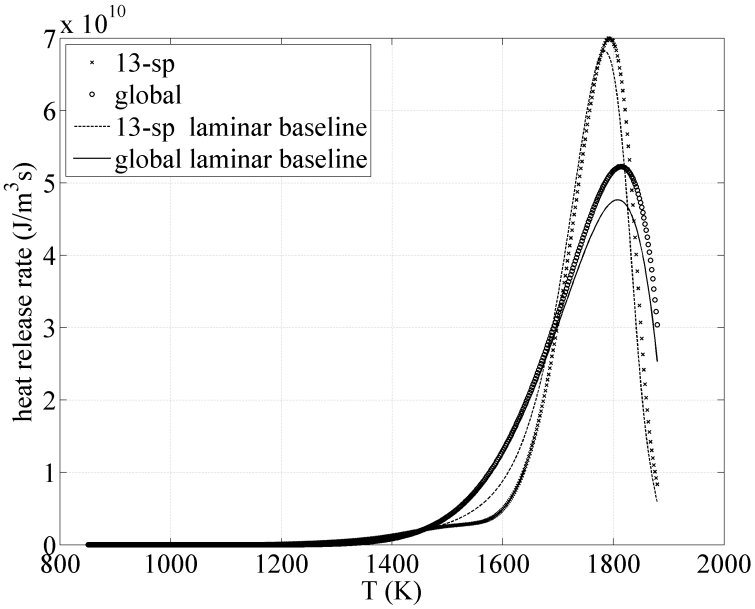

Figure 7.4. Comparison of the time-averaged heat release rate profile conditioned on flame temperature for Case 1: $u_{rms}/S_L = 14.3$ (symbols) with that of the unstrained laminar flame (lines).

It is interesting to examine the overall effects of the chemical mechanism on the computed turbulent flame speed S_T. For a fully-developed, statistically-steady flame confined in the computational domain, S_T can be computed by invoking the integral form of the conservation of energy, i.e.,

$$\rho_u A_L \Xi \cdot S_T = \langle \int \mathrm{HRR} dV \rangle_{tur} \tag{7.2}$$

where HRR is the heat release rate per unit volume and Ξ is the amount of sensible energy released per unit mass of CH_4-air mixture assuming complete combustion. Per-

forming a transformation from the physical space to the temperature space, Eq. (7.2) can be written as

$$\begin{aligned}\rho_u \mathrm{A_L} \Xi \cdot \mathrm{S_T} &= \langle \int_{\mathrm{T_u^+}}^{\mathrm{T_{ad}^-}} \overline{\mathrm{HRR}}_{tur}(\mathrm{T}) \cdot \frac{dV}{d\mathrm{T}} d\mathrm{T} \rangle \\ &= \langle \int_{\mathrm{T_u^+}}^{\mathrm{T_{ad}^-}} \overline{\mathrm{HRR}}_{tur}(\mathrm{T}) \cdot \mathrm{A_T}(\mathrm{T}) \frac{\delta s(\mathrm{T})}{\delta \mathrm{T}} d\mathrm{T} \rangle \\ &+ \langle \int_{\mathrm{T_u^+}}^{\mathrm{T_{ad}^-}} \overline{\mathrm{HRR}}_{tur}(\mathrm{T}) \cdot s \cdot \frac{\delta \mathrm{A_T}(\mathrm{T})}{\delta \mathrm{T}} d\mathrm{T} \rangle \end{aligned} \tag{7.3}$$

Here, $\langle \cdot \rangle$ denotes averaging in time and $\delta s(\mathrm{T})$ represents the infinitesimal thickness of the turbulent flame at temperature T. Notice that $\delta s(\mathrm{T})/\delta \mathrm{T}$ is the inverse of $\langle \|\nabla \mathrm{T}\| | \mathrm{T} \rangle$ shown in Fig. 7.2. In the current work, the finite thickness of flame between $\mathrm{T} \pm 1\mathrm{K}$ is used for $\delta s(\mathrm{T})$. The second term on the right-hand-side accounts for the change in $\delta \mathrm{A_T}(\mathrm{T})$ with temperature. It is found that such a term is less than 0.1% of the first term and can be neglected. Similarly, $\mathrm{S_L}$ can be constructed as

$$\begin{aligned}\rho_u \mathrm{A_L} \Xi \cdot \mathrm{S_L} &= \int_{\mathrm{T_u^+}}^{\mathrm{T_{ad}^-}} \mathrm{HRR}_{lam}(\mathrm{T}) \cdot \frac{dV}{d\mathrm{T}} d\mathrm{T} \\ &= \int_{\mathrm{T_u^+}}^{\mathrm{T_{ad}^-}} \mathrm{HRR}_{lam}(\mathrm{T}) \cdot \mathrm{A_L} \frac{\delta s(\mathrm{T})}{\delta \mathrm{T}} d\mathrm{T}. \end{aligned} \tag{7.4}$$

If we assume that flame wrinkling by turbulence, manifested by $\mathrm{A_T}(\mathrm{T})$, and the effects of turbulence on the flame front reaction rate, manifested by $\overline{\mathrm{HRR}}_{tur}(\mathrm{T}) \cdot \delta s(\mathrm{T})/\delta \mathrm{T}$, are two independent physical events, we can estimate $\mathrm{S_T}/\mathrm{S_L}$ by

$$\frac{\mathrm{S_T}}{\mathrm{S_L}} \cong \int_{\mathrm{T_u^+}}^{\mathrm{T_{ad}^-}} \langle \frac{\overline{\mathrm{HRR}}_{tur}(\mathrm{T}) / \|\nabla \mathrm{T}| \mathrm{T}\|_{tur}}{\mathrm{HRR}_{lam}(\mathrm{T}) / \|\nabla \mathrm{T}| \mathrm{T}\|_{lam}} \rangle \cdot \langle \frac{\mathrm{A_T}(\mathrm{T})}{\mathrm{A_L}} \rangle d\mathrm{T} \tag{7.5}$$

Using the relationship in Eq. (7.5), the estimated normalized turbulent flame speed $\mathrm{S_T}/\mathrm{S_L}$ using the global mechanism is only 7.8% higher than that using the 13-species mechanism for flame at $\mathrm{u_{rms}}/\mathrm{S_L} = 14.3$, the highest intensities considered in this study. This suggests that for engineering applications, the global mechanism is as capable of predicting the turbulent flame speed as the reduced mechanism over the range of conditions considered in this study.

7.2.2 Modeling of statistically stationary flames

The turbulent premixed flame is simulated as statistically stationary inside the computational domain by employing a Lagrangian framework as discussed in Chapter 5.2. The frame of reference is placed on the mean flame front and cold premixed reactants enter the flame in a turbulent flow. This setup enables the computational domain size to be decoupled from the flame propagation time, and allows for statistics to be collected over an extended period of time. The inflow-outflow configuration is shown in Fig. 7.1. Periodic boundary conditions are applied to the lateral boundaries parallel to the mean flow direction. Inflow of unburned methane-air mixture is specified at the left boundary while the burned flow passes through a sponge zone and exits from the right.

The purpose of using a sponge zone ahead of the outflow boundary shown in Fig. 5.1 is to remove any artificial effect of outflow boundary condition reflected back into the interior flow field. The sponge zone is modeled as a damper to "force" the flow into 1-D when exiting from the outflow boundary. This is done by adding a sink term with the specific form given below to the right-hand-side of the momentum equation in the y- and z-direction, i.e., perpendicular to the inflow direction:

$$s_i = \sigma(x - x_{\text{sponge}}) \cdot (0 - u_i); i = 2, 3. \tag{7.6}$$

Here, $\sigma(x - x_{\text{sponge}})$ is a hyperbolic function of the axial distance that grows gradually from 0 to some finite number as the flow enters the sponge zone. Note that the flow inside the sponge zone is unphysical and is not used in any analysis.

To maintain the flame stationary, *á priori* knowledge of the flame speed is required to specify the inflow boundary condition. This information is, however, not readily available and is the interest of the simulation. Instead, a feedback control is employed on the mean flame position $x_f(t)$ to correct the bulk inflow velocity $\mathrm{U}_0(t)$ until the flame becomes statistically stationary. In the current simulations, two forms of feedback control have been implemented. A proportional feedback is used to adjust inflow velocity until the mean flame front is stationary. In addition, an integral feed-

back is applied to return the mean flame front to its initial position. Implementation of these two forms of feedback control has been elaborately discussed in Chapter 5.2.

The turbulent flame speed $\mathrm{S_T}$ can be obtained from the time average of the bulk inflow velocity once the premixed flame becomes fully developed and is statistically stationary. $\mathrm{S_T}$ is derived through the following relation:

$$\begin{aligned} \mathrm{S_T} &\equiv \langle \frac{\dot{m}_f}{\rho_u \mathrm{A_L} \mathrm{Y_{f,u}}} \rangle \\ &= \frac{1}{t_2 - t_1} \int_{t_1}^{t_2} \frac{1}{\mathrm{A_L}} \int_{\mathrm{A_L}} \left[u(0, y, z, t) - u(\mathrm{L_x}, y, z, t) \frac{\rho_{out} \mathrm{Y}_{f,out}}{\rho_u \mathrm{Y}_{f,u}} \right] d\mathrm{A}dt. \end{aligned} \tag{7.7}$$

Here, $\mathrm{A_L}$ denotes the area of the inflow boundary. Since the length of the domain is ensured to be sufficiently long that all methane is consumed, fuel mass fraction at the outlet, i.e., $\mathrm{Y}_{f,out}$, is equal to zero. Furthermore, since the turbulent velocity fluctuations on the inflow plane come from selecting sequential cross-sectional planes of a homogeneous isotropic turbulence flow field with a zero mean, Eq. (7.7) can be further simplified as

$$\begin{aligned} \mathrm{S_T} &= \frac{1}{t_2 - t_1} \int_{t_1}^{t_2} \frac{1}{\mathrm{A_L}} \int_{\mathrm{A_L}} u(0, y, z, t) d\mathrm{A}dt \\ &= \frac{1}{t_2 - t_1} \int_{t_1}^{t_2} \mathrm{U}_0(t) dt + \langle u' \rangle \\ &= \frac{1}{t_2 - t_1} \int_{t_1}^{t_2} \mathrm{U}_0(t) dt. \end{aligned} \tag{7.8}$$

7.2.3 Turbulence forcing

The domain is initialized with a laminar flame. To obtain the desired turbulence intensity in the reactants, turbulent fluctuations are imposed on the bulk inflow velocity. These fluctuations are obtained by selecting sequential cross-sectional planes of a homogeneous no-decaying isotropic turbulence field generated in a separate auxiliary simulation as shown in Fig. 5.1. In addition, to preserve the turbulence intensity, turbulence in the reactants is forced using a "linear forcing" scheme as discussed in Chapter 5.3 [197, 198]. Specifically, a term is added to the right-hand-side of the mo-

mentum equation to represent the energy cascade from scales which are larger than the domain size. The specific form of the forcing term is given by [198]:

$$\mathrm{F}_i = \mathrm{M(T)}B\left[\frac{k_o}{k}\right]\rho u_i. \tag{7.9}$$

Here, k is the instantaneous turbulent kinetic energy (TKE) in the reactant mixture and k_o is the desired steady-state TKE. M(T) is a ramp function of temperature which decreases from 1 to 0 as T increases by 200 K above the unburned temperature. This is to prevent any artificial effect of forced turbulence on the flame structure. B is the forcing constant which is inversely proportional to the steady-state eddy turnover time. Figure 7.5 shows the time-averaged TKE spectrum in the wavenumber space for a forced turbulence with turbulent Reynolds number $Re_{\mathrm{T}} \equiv \mathrm{u_{rms}L_o}/\nu = 880$. The expected slope of -5/3 is recovered in the inertial subrange as shown in Fig. 7.5. In addition, it has been reported that the integral length scale, $\mathrm{L_o}$, of the forced turbulence will always converge to approximately 20% of the domain size independent of its initial state or the choice of the forcing constant [197]. This means that $\mathrm{L_o}$ can be maintained at a desired value by selecting an appropriate domain size.

7.3 Effects of Equivalence Ratio on Flame Speed

We will now present results from the parametric studies exploring the effects of equivalence ratio on turbulent flame speed under lean-burn conditions. Each simulation is performed over more than 80 eddy turnover times to obtain a large sample space for meaningful statistics to be collected. Pressure is selected at 20 bar and the reactant temperature at 810 K, reflective of conditions at top-dead-center (TDC) in a lean-burn natural gas engine [215, 216]. The equivalence ratio is varied from 0.39 to 0.50 while the turbulence properties are kept constant as shown in Table 7.1. Uniform grid resolution is selected and the grid size is smaller than 1.6 times the Kolmogorov length scale (η). This resolution also ensures that there are more than 16 points across the unstrained laminar flame front. Each simulation typically takes about 15 days using 256 processors.

Table 7.1. Computational parameters and turbulence conditions employed in this study. Computed normalized turbulent flame speeds S_T/S_L are also listed.

	Case 1	Case 2	Case 3
Domain size (mm^3)	8.0×3.2×3.2	8.0×3.2×3.2	8.0×3.2×3.2
ϕ	0.50	0.43	0.39
S_L (m/s)	0.1506	0.07445	0.04650
δ_L (μm)	100	200	300
u_{rms} (m/s)	**2.160**	**2.160**	**2.160**
L_o (mm)	**0.64**	**0.64**	**0.64**
Δx (μm)	12.5	12.5	12.5
η (μm)	8.27	8.27	8.27
u_{rms}/S_L	14.34	29.01	46.45
L_o/δ_L	6.40	3.20	2.13
Re_T	**315**	**315**	**315**
Da	0.45	0.11	0.05
Ka	21.5	87.4	216.8
S_T/S_L	10.2 ± 0.4	7.9 ± 0.5	6.5 ± 0.5
A_T/A_L	9.56	7.45	6.04

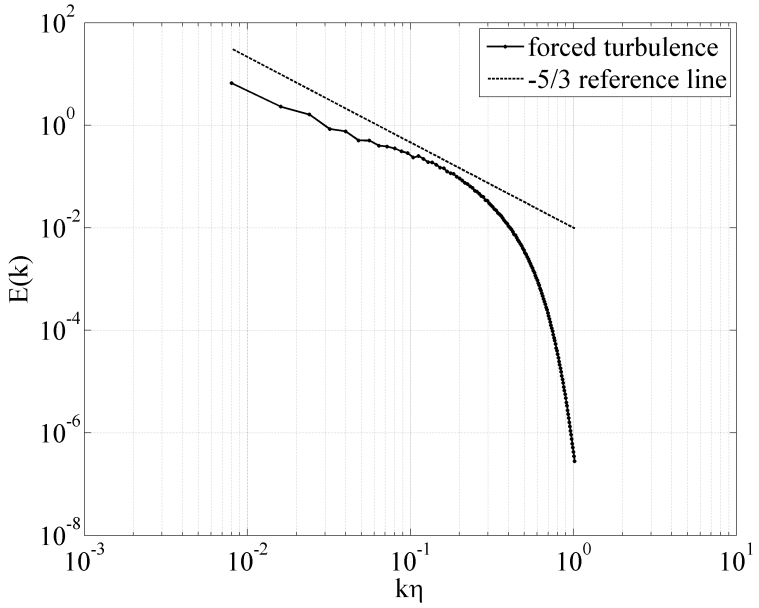

Figure 7.5. Spectrum of turbulent kinetic energy as a function of wavenumber normalized with the Kolmogorov scale for turbulence sustained by linear forcing.

The turbulent flame speed S_T is given by the time average of the bulk inflow velocity once the turbulent flame becomes fully-developed and stationary in the statistical sense, as shown in Eq. (7.8). Table 7.1 shows the turbulent flame speed S_T normalized by S_L when flames of various ϕ interact with non-decaying turbulence of identical statistically averaged properties. In particular, u_{rms} is maintained at 2.160 ms^{-1} and L_o at 0.64 mm. It can be seen that as equivalence ratio is reduced from 0.5 to 0.43 and 0.39, S_T/S_L decreases from 10.2 to 7.9 and 6.5, respectively. The reduction in S_T/S_L is predominantly controlled by the reduction in flame surface area A_T/A_L as shown in Table 7.1. Here, A_T is evaluated using a "marching cube" algorithm on the isotherm surface at the temperature corresponding to the peak heat release in the laminar flame. The reduction in S_T with decreasing ϕ is possibly because the leaner flames are thicker and hence small-scale eddies can penetrate into the flame more easily, resulting in the loss of surface area due to enhanced mixing.

This would suggest that equivalence ratio has an effect on the turbulent flame speed. At this point, the question arises as to whether this effect of equivalence ratio can be modeled through other parameters which may be influencing the speed. Note that equivalence ratio influences the laminar flame speed and thus u_{rms}/S_L is modified with different ϕ as shown in Table 7.1. Furthermore, when ϕ is changed, the chemical timescales change with respect to the turbulence timescales. Two parameters that account for this change in timescales are the Karlovitz number (Ka) and Damköhler number (Da). The Karlovitz number represents the ratio of characteristic chemical timescale to the Kolmogorov timescale while Damköhler number represents the ratio of integral eddy turnover time to the chemical timescale. Their respective definitions used in this study are given as,

$$Ka = \frac{\tau_c}{\tau_\eta} \sim \left(\frac{u_{rms}}{S_L}\right)^{\frac{3}{2}} \left(\frac{\delta_L}{L_o}\right)^{\frac{1}{2}}, \tag{7.10}$$

$$Da = \frac{\tau_t}{\tau_c} \sim \frac{S_L}{u_{rms}} \frac{L_o}{\delta_L}. \tag{7.11}$$

To understand if these parameters, rather than ϕ, can account for the change in the normalized turbulent flame speeds, the equivalence ratio is varied while the turbulence properties are also varied to keep the non-dimensional turbulence intensity, Da and Ka constant. Note that for these flames, Da can be written as a function of u_{rms}/S_L and Ka. Table 7.2 lists the physical conditions employed for these simulations. The pressure is set at 20 bar and unburned mixture temperature at 810 K as before. Turbulent velocity fluctuations are varied between $0.67 \sim 4.81\ m/s$ such that u_{rms}/S_L remains constant at 14.3. The computational domain size is selected at $80 \times 32 \times 32\delta_L$ such that L_o is always 6.4 times the laminar flame thickness. Figures 7.6(a) and 7.6(b) show the instantaneous volume rendering of the flames when ϕ is changed from 0.50 to 0.39 but u_{rms}/S_L, Da and Ka are unchanged. There is no visual difference in the extent of wrinkling of the flame surface at these two equivalence ratios despite the fact that the turbulence intensity in Fig. 7.6(a) is 3.2 times greater than that in Fig. 7.6(b). Figures 7.6(a) and 7.6(c) show instantaneous volume rendering of the flames interacting with statistically identical turbulence while ϕ is changed from 0.50

Table 7.2. Computational parameters and turbulence conditions which keep u_{rms}/S_L, Da and Ka constant. Computed normalized turbulent flame speeds S_T/S_L are also listed.

	Case 1	Case 2a	Case 3a	Case 4
Domain size (mm^3)	8.0×3.2×3.2	16.0×6.4×6.4	24.0×9.6×9.6	4.0×1.6×1.6
ϕ	0.50	0.43	0.39	0.60
S_L (m/s)	0.1506	0.07445	0.04650	0.3351
δ_L (μm)	100	200	300	50
u_{rms} (m/s)	2.160	1.068	0.667	4.806
L_o (mm)	0.64	1.28	1.92	0.32
Δx (μm)	12.5	26.7	40.0	6.67
η (μm)	8.27	16.69	26.29	3.82
u_{rms}/S_L	**14.34**	**14.34**	**14.34**	**14.34**
L_o/δ_L	**6.40**	**6.40**	**6.40**	**6.40**
Re_T	315	312	314	351
Da	**0.45**	**0.45**	**0.45**	**0.45**
Ka	**21.5**	**21.5**	**21.5**	**21.5**
S_T/S_L	10.2 ± 0.4	10.0 ± 0.5	9.9 ± 0.4	10.2 ± 0.3
A_T/A_L	9.56	9.59	9.35	9.74
I_o	1.07	1.04	1.06	1.05

to 0.39. The surface of the leaner flame appears noticeably less wrinkled, thereby generating lower flame speeds.

Figure 7.7 shows the estimated turbulent flame speeds from averaging the bulk inflow velocity over incrementally longer periods of time for Cases 1, 2a, 3a and 4. Fluctuations in the time-averaged bulk inflow velocity are also listed in Table 7.2. Self-convergence in S_T/S_L is observed in all cases. Interestingly, S_T/S_L has a similar

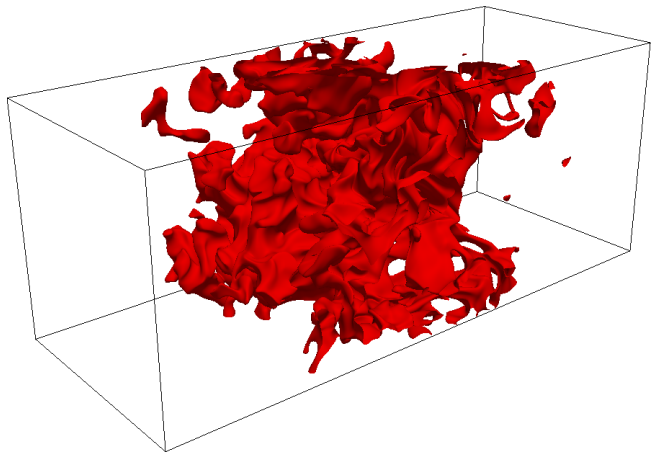

(a)

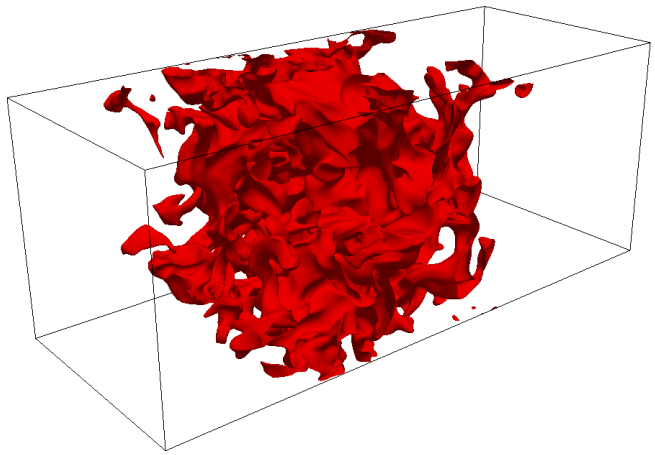

(b)

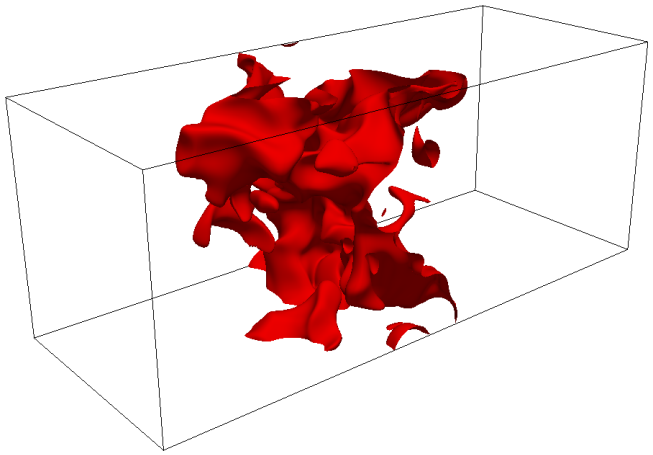

(c)

Figure 7.6. Volume rendering of temperature isosurface of T = 1400 K for DNS of flames: (a) $\phi = 0.50$, $u_{rms}/S_L = 14.3$ (Case 1), (b) $\phi = 0.39$, $u_{rms}/S_L = 14.3$ (Case 3a) and (c) $\phi = 0.39$, u_{rms} is the same as in 7.6(a) (Case 3).

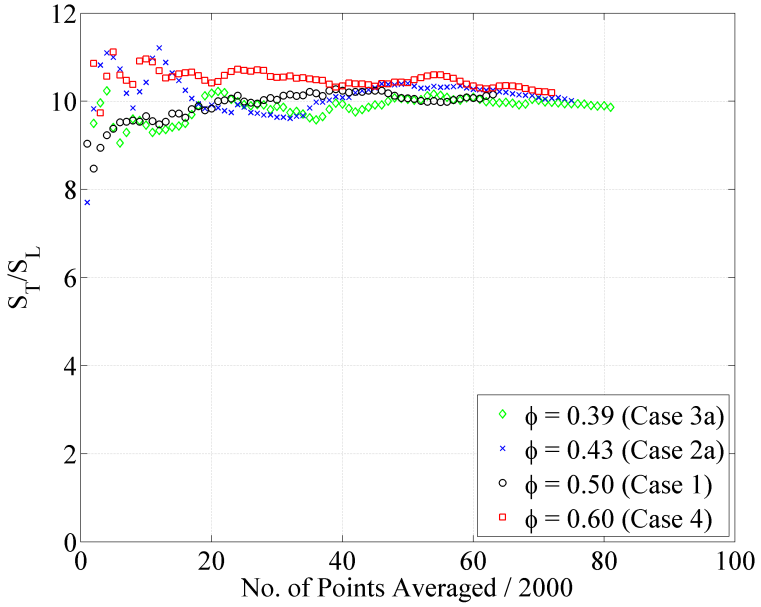

Figure 7.7. Time averages of the bulk inflow velocity $U_0(t)$ over increasingly longer periods of time for Cases 1, 2a, 3a and 4.

value around 10 (within 5%) when u_{rms}/S_L, Da and Ka are unchanged. This suggests that the primary effect of equivalence ratio on turbulent flame speed is through its influence on the laminar flame speed S_L and the Ka and/or Da. Changing ϕ while holding the turbulence constant (Case 1, 2 and 3 of Table 7.1) affects the ratios of velocities and length scales between the turbulence and the flame, i.e., u_{rms}/S_L and L_o/δ_L and consequently affects the flame speed.

To understand if changes in u_{rms}/S_L alone can account for the change in S_T/S_L shown in Table 7.1, Cases 2b and 3b are performed with u_{rms}/S_L kept constant as in Case 1, but with different Da and Ka. This is motivated by numerous existing correlations [125, 128] where S_T is expressed in the generalized form as

$$\frac{S_T}{S_L} = f\left(\frac{u_{rms}}{S_L}\right). \tag{7.12}$$

Table 7.3 lists the physical conditions employed for these simulations and the computed S_T/S_L. As ϕ is reduced from 0.5 to 0.43 and 0.39, S_T/S_L decreases from 10.2 to 6.4 and 5.2, respectively. It is evident that a correlation of the form in Eq. (7.12) is not sufficient. This suggests that the ratio of length scales, i.e., L_o/δ_L that is involved in Da and Ka, indeed plays an important role in the turbulent flame speed.

To confirm the validity of the observation that the effect of ϕ is through its influence on u_{rms}/S_L, Ka or Da, simulations are carried out with a lower normalized turbulence intensity ($u_{rms}/S_L = 8.0$) for equivalence ratio of 0.50, 0.43 and 0.39. The integral lengths scale is again selected as 6.4 times the laminar flame thickness, and consequently Da and Ka are kept constant at 0.80 and 8.9, respectively. Pressure and unburned mixture temperature are selected to be 20 bar and 810 K, respectively. Table 7.4 lists the physical conditions employed for these simulations. The normalized turbulent flame speeds S_T/S_L are also tabulated with their standard deviations in Table 7.4. It is found that S_T/S_L is again approximately constant (around 8.6) when ϕ is changed but holding u_{rms}/S_L, Da and Ka invariant.

Table 7.3. Computational parameters and turbulence conditions which keep u_{rms}/S_L constant. Computed normalized turbulent flame speeds S_T/S_L are also listed.

	Case 1	Case 2b	Case 3b
Domain size (mm^3)	8.0×3.2×3.2	8.0×3.2×3.2	8.0×3.2×3.2
ϕ	0.50	0.43	0.39
S_L (m/s)	0.1506	0.07445	0.04650
δ_L (μm)	100	200	300
u_{rms} (m/s)	2.160	1.068	0.667
L_o (mm)	**0.64**	**0.64**	**0.64**
Δx (μm)	12.5	20.0	20.0
η (μm)	8.27	14.03	19.98
u_{rms}/S_L	**14.34**	**14.34**	**14.34**
L_o/δ_L	6.40	3.20	2.13
Re_T	315	156	98
Da	0.45	0.22	0.15
Ka	21.5	30.4	37.2
S_T/S_L	10.2 ± 0.4	6.4 ± 0.8	5.2 ± 0.7
A_T/A_L	9.56	6.04	4.89

Table 7.4. Computational parameters for cases with a lower normalized turbulence intensity and constant Da and Ka. Computed normalized turbulent flame speeds are also listed.

	Case 5	Case 6	Case 7
Domain size (mm^3)	8.0×3.2×3.2	16.0×6.4×6.4	24.0×9.6×9.6
ϕ	0.50	0.43	0.39
S_L (m/s)	0.1506	0.07445	0.04650
δ_L (μm)	100	200	300
u_{rms} (m/s)	1.205	0.596	0.372
L_o (mm)	0.64	1.28	1.92
Δx (μm)	20.0	40.0	60.0
η (μm)	12.82	25.86	40.73
u_{rms}/S_L	**8.0**	**8.0**	**8.0**
L_o/δ_L	**6.40**	**6.40**	**6.40**
Da	**0.80**	**0.80**	**0.80**
Ka	**8.9**	**8.9**	**8.9**
S_T/S_L	8.7 ± 0.2	8.4 ± 0.2	8.5 ± 0.4
A_T/A_L	8.27	7.89	8.08
I_o	1.05	1.06	1.05

7.4 Analysis of Turbulence-Chemistry Interaction

The flame speeds tabulated in Tables 7.2 and 7.4 are examined within the framework of flame stretch [98, 209], i.e.,

$$\frac{\mathrm{S_T}}{\mathrm{S_L}} = \mathrm{I_o}\frac{\mathrm{A_T}}{\mathrm{A_L}}. \tag{7.13}$$

I_o, tabulated in Tables 7.2 and 7.4, is the efficiency factor representing the deviation in the burning rate per unit area from that of the laminar flame. It is found that I_o is close to unity, i.e., within 10%, in all cases. Hence, the turbulent flame speed is primarily controlled by flame surface wrinkling. The DNS data is further analyzed to characterize the flame surface generated by turbulence eddies of various scales. This is done by first sampling the DNS data with a fixed physical length Δ. The isotherm surface is then reconstructed from the sampled dataset using the "marching cube" algorithm and the surface area $\mathrm{A}(\Delta)$ is computed. To minimize variation associated with sampling at large Δ, multiple sampling are performed with the starting point selected at random. Time averaging of $\mathrm{A}(\Delta)$ is also performed over $50 \sim 100$ instantaneous snapshots. By sampling the data, wrinkling generated by eddies with a characteristic length scale $l < \Delta$ will be smoothed out. Physically, $\mathrm{A}(\Delta)$ represents the integral surface area generated by eddies larger than Δ, and $d\mathrm{A}(\Delta)/d\Delta$ is the flame surface generated by eddies with $l = \Delta$. Figure 7.8 shows the normalized $d\mathrm{A}(\Delta)/d\Delta$ as a function of eddies scale normalized by $\mathrm{L_o}$ for flames of different equivalence ratios when $Ka = 21.5$ and 8.9 (i.e., $Da = 0.45$ and 0.80), represented by the open and filled symbols, respectively. It is evident that variations in ϕ, on average, do not seem to affect the surface wrinkling generated for a fixed Da and Ka. Furthermore, wrinkling generated by large scale eddies are almost identical and independent of Ka or Da, as the open and filled symbols collapse into a single curve for $\Delta \geq 0.4\mathrm{L_o}$. This implies that the effects of Ka or Da on surface wrinkling are only present at small scales.

It is also interesting to investigate the alignment of principal strain rate directions when equivalence ratio is changed. This provides insights on whether scalar gradients

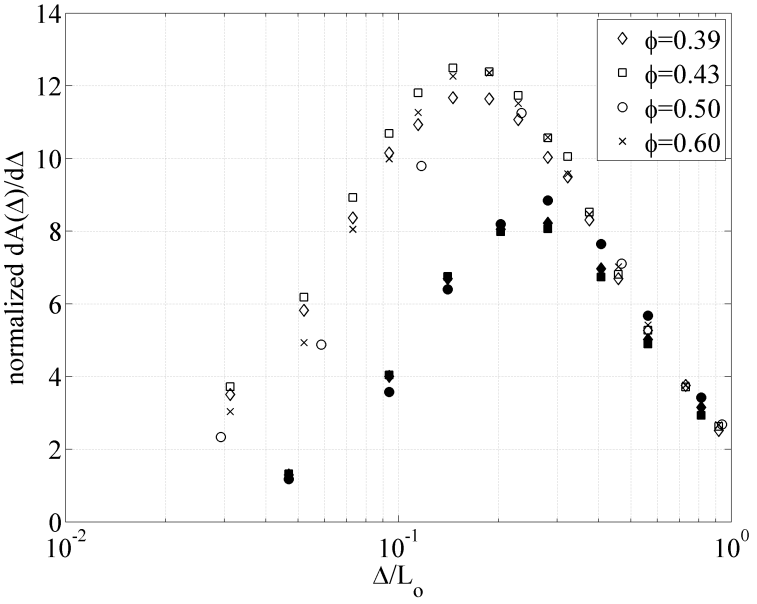

Figure 7.8. Normalized flame surface area generated by eddies with a characteristic scale of Δ for ϕ = 0.39, 0.43, 0.50 and 0.60 with Ka = 21.5 (open symbol) and Ka = 8.9 (filled symbol).

are created or destroyed by turbulence [217]. The normal strain rate a_{N} on the flame surface is given as

$$a_{\mathrm{N}} = \mathrm{n}_i \mathrm{S}_{ij} \mathrm{n}_j, \tag{7.14}$$

where n_i represents the direction normal to the flame surface and S_{ij} is the strain rate tensor given by

$$\mathrm{S}_{ij} = \frac{1}{2}\left(\frac{\partial u_i}{\partial x_j} + \frac{\partial u_j}{\partial x_i}\right). \tag{7.15}$$

In the case that a_{N} is less than zero, the isosurfaces are packed closer together and thereby facilitating steeper scalar gradients. On the other hand, when a_{N} is larger than zero, scalar gradients are reduced when interacting with turbulence. Note that a_{N} can be expressed as the linear combination of the principal strain rates, λ_1, λ_2 and λ_3, which are the three eigenvalues of S_{ij}, as follows:

$$a_{\mathrm{N}} = \cos^2\theta_1\lambda_1 + \cos^2\theta_2\lambda_2 + \cos^2\theta_3\lambda_3. \tag{7.16}$$

The largest eigenvalue, denoted as λ_1 is called the most extensive strain rate and the smallest eigenvalue λ_3 is called the most compressive strain rate. The alignment between the principal strain rate directions, denoted by $\xi_\mathbf{i}$ and flame surface normal $\mathbf{n}$ is characterized by $\cos\theta_i$ with

$$\cos\theta_i = \mathbf{n} \cdot \xi_\mathbf{i}. \tag{7.17}$$

The principal strain rates are computed from the strain rate tensor S_{ij} at three different isotherm surfaces by solving the eigenvalues. Figure 7.9 shows the probability density function (pdf) of the orientation (expressed as cosine of the angle) between the principal strain rate directions and the local flame surface normal on the temperature isosurface at T = 1694, 1394 and 1094 K for Case 2a. Here, 1694 K corresponds to the temperature where heat release rate is maximum and 1094 K corresponds to the preheat zone of the flame of $\phi = 0.43$. It is shown that the most compressive strain rate direction is preferentially aligned with the flame surface normal as evident from Fig. 7.9 that the pdf (denoted by symbols) is greater than unity when $\cos\theta$ is close to 1. On the other hand, the most extensive strain rate direction is (only weakly) preferentially perpendicular to the flame surface normal. This suggests that the flame is strained in such a way that the isosurface of temperature (and also species mass fractions) are packed closer together and thereby facilitate steeper scalar gradients. This result is consistent with PIV measurements of premixed Bunsen flames and V-flames [218, 219]. Furthermore, the alignments do not show noticeable difference at various points across the flame.

Comparisons of the alignment in the preheat zone of flames with different equivalence ratios for fixed Ka and Da are shown in Fig. 7.10. The isotherm surface where data is analyzed is at 30% of the maximum temperature rise. Similar trend is observed for all four equivalence ratios. This shows that ϕ has limited explicit influence on turbulence-flame alignment in lean premixed flames suggesting that the fundamental turbulence-flame interaction is not altered when Ka and Da are fixed. Figure 7.11 shows the pdf of the alignment between the principal strain rates and flame surface normal at an isosurface of T = 1220 K for $u_{rms}/S_L = 14.3$ and 8.0 (Case 1 and Case

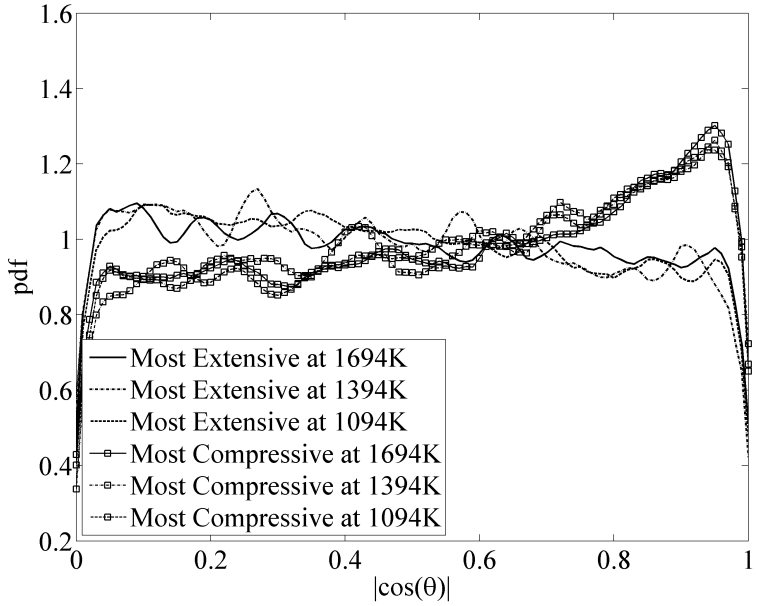

Figure 7.9. Probability density function of alignment between the principal strain rate directions and flamelet normal on the isosurface of T = 1694, 1394 and 1094 K for $\phi = 0.43$ and $u_{rms}/S_L = 14.3$ (Case 2a).

5). The alignments between the most compressive strain rate and the flamelet normal show no visual difference when turbulence intensity is changed.

7.5 Summary and Conclusions

In this study, direct numerical simulations of turbulent premixed CH_4-air flames are carried out under lean conditions using an inflow-outflow configuration. The flames are simulated as statistically stationary by dynamically adjusting the bulk inflow velocity. It is found that the normalized turbulent flame speed, i.e., S_T/S_L, does not change with equivalence ratio above the lean limit when Ka and Da are fixed. This implies that ϕ only influences S_T implicitly by affecting ratios of length scales and velocities between turbulent flow and the flame. Hence, the effect of ϕ on S_T can be modeled through Ka and Da. Analysis of flame surface area shows that surface wrinkling generated by eddies is not affected by variation in ϕ irrespective

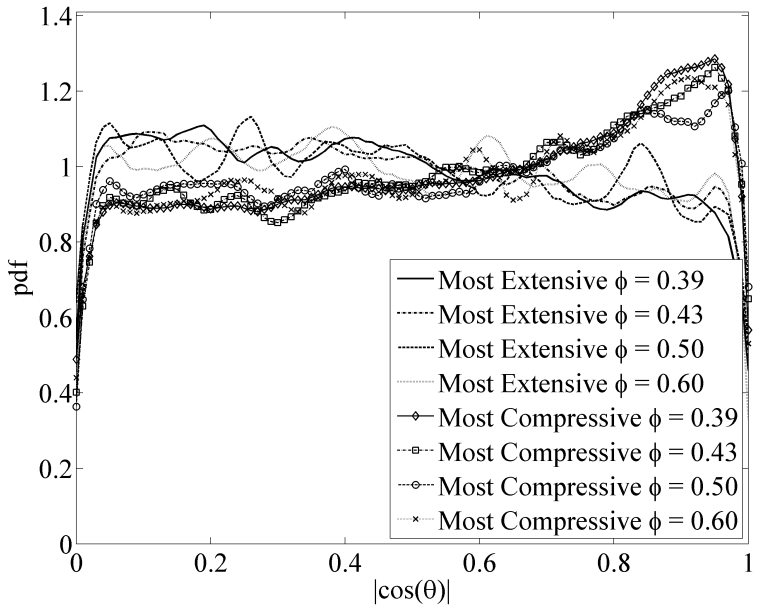

Figure 7.10. Probability density function of alignment between the principal strain rate directions and flamelet normal in the flame preheat zone for $\phi = 0.39$, 0.43, 0.50 and 0.60 and $u_{rms}/S_L = 14.3$ (Cases 1, 2a, 3a and 4).

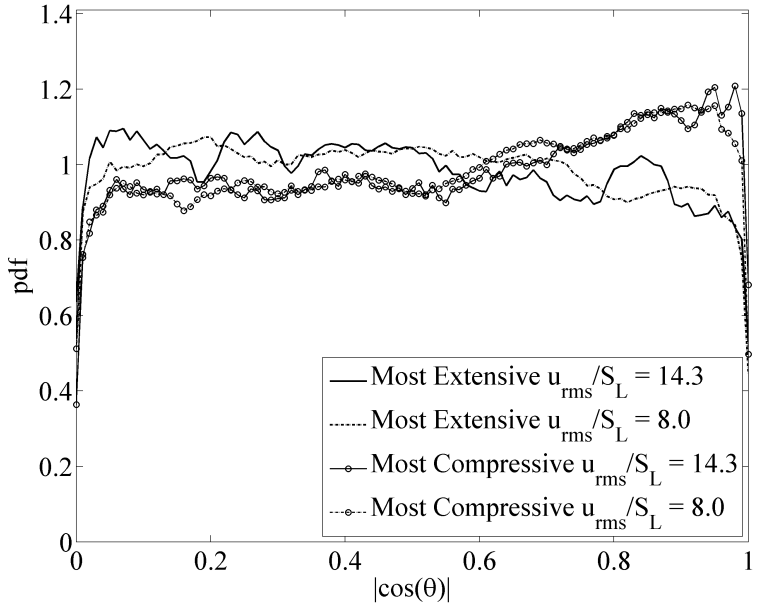

Figure 7.11. Probability density function of alignment between the principal stain rate directions and flamelet normal in the flame preheat zone for $\phi = 0.50$ and $u_{rms}/S_L = 14.3$ and 8.0 (Cases 1 and 5).

of the scales considered, provided Ka and Da are fixed. Flame surface generated by large-scale eddies is independent of Ka/Da, indicating the effect of Ka/Da on surface wrinkling is only present at smaller scales. It is also found that the most compressive strain rate in the flow is preferentially aligned to the flame surface normal. In this way, steeper passive scalar gradients are generated by turbulence. Varying equivalence ratio does not influence turbulence-flame alignment.

8. EVALUATION OF FLAME SPEED IN A THREE-DIMENSIONAL DOMAIN

8.1 Introduction

In the last chapter, the effects of equivalence ratio on the turbulent flame speeds are characterized by studying 3D DNS of lean CH_4-air flames. It is found that equivalence ratio does not affect the normalized turbulent flame speed S_T/S_L when the normalized turbulence intensities u_{rms}/S_L, Karlovitz number Ka and Damköhler number Da are fixed. This implies that u_{rms}/S_L, Ka and Da can potentially influence S_T. In this chapter, 3D DNS of lean premixed CH_4-air flames are performed to provide better understanding of flame speed dependencies under lean-burn engine relevant conditions. *The work presented in this chapter comes from a manuscript by Wang et al. (2016) which is under review for publication in Combustion and Flame.*

As discussed in Chapter 2, S_T is a key parameter employed in the modeling of premixed turbulent combustion. It reflects the impact of turbulence on accelerating combustion rates through flame surface augmentation and enhanced transport. The use of the single variable S_T greatly simplifies numerical modeling by eliminating the need to solve stiff chemical kinetic source terms within the context of modeling and it is central to several models including the G-equation model [62, 76, 77] and the Turbulent Flame Closure (TFC) model [220]. For premixed flames in the flamelet regime [77], Damköhler (1940) first proposed that S_T is primarily controlled by the increase in the flame surface area A_T [123]. The relation between S_T and A_T was then generalized through

$$\frac{S_T}{S_L} = I_o \frac{A_T}{A_L}, \tag{8.1}$$

where A_T/A_L represents the augmentation of surface area by wrinkling and I_o is the efficiency factor that represents the deviation in the burning rate per unit area from the laminar flame due to flame stretch [98, 209].

The validity of Eq. (8.1), for flames categorized in the Thin Reaction Zone (TRZ) regime shown in Fig. 2.6(b) has been studied in recent years. Note that the TRZ regime is characterized by $u_{rms}/S_L > 1$ and $Ka > 1$. For flames inside the TRZ regime, small-size eddies could penetrate the preheat zone of the premixed flame. Bell *et al.* (2002) performed DNS of premixed methane flames for $u_{rms}/S_L = 1.7$ and 4.3 [199]. They found I_o to be approximately 10% greater than unity. However, decaying turbulence is used in their study which precludes the measurement of steady-state turbulent flame speed. Hawkes and Chen (2006) performed 2D simulations of statistically flat methane flames with equivalence ratio of 0.52 and u_{rms}/S_L up to 28.5. They observed that I_o can be larger or smaller than unity but the deviation is less than 5% for pure methane/air flames [221]. Poludnenko and Oran (2011) performed three DNS of stoichiometric hydrogen-air flames subjected to high turbulence intensities ($u_{rms}/S_L = 34.5$) [146]. In their work, a spectral turbulence driving method is employed to inject turbulent kinetic energy into the domain. They observed that, in the TRZ regime, the instantaneous turbulent flame speed is primarily determined by the increase in the flame surface area. In addition, they found that the turbulent flame speed exhibits exaggerated response to flame surface augmentation and, in some cases, I_o can be 30% higher than unity. Hawkes *et al.* (2012) performed DNS of temporally developing slot jet flames of Re_T up to 1000 and Ka up to 100 [222]. They found that I_o is higher than unity and the departure from unity is non-negligible.

Efforts have been made to characterize the flame wrinkling, i.e., A_T/A_L, in Eq. (8.1) in terms of fractal properties of turbulent flames. Gouldin (1987) first proposed the use of fractals to describe the flamelet surfaces in premixed turbulent combustion [129]. Since then, combustion models based on the fractal properties of premixed flames have been developed [101, 223, 224, 225, 226]. However, the success of these models heavily relies upon the accurate prediction of the fractal dimension (D_3) as

well as the inner cut-off length (ϵ_i). Values between 2.1-2.7 for fractal dimension have been reported in the literature [227, 228, 229, 230, 231, 232]. For inner cut-off length, multiple expressions have been proposed [79, 223, 231, 233, 234]. To this day, there is no consensus on the fractal dimension of premixed flames or on the functional dependence of inner cut-off length on turbulence and flame parameters.

In all of the works cited with the exception of [146], the turbulence intensities and length scales vary spatially and/or temporally which makes it challenging to quantitatively characterize the effects of these parameters on the turbulent flame speeds. Furthermore, to the best of our knowledge, there has not been any DNS study of turbulent premixed flames at engine relevant temperature and pressure conditions. The question whether Eq. (8.1) is still applicable under engine relevant conditions will be addressed in this chapter.

In the present study, DNS of lean premixed methane flames are carried out at conditions of interest to lean-burn natural gas engines. Premixed flames are simulated as statistically stationary in a Lagrangian framework. Turbulence is forced to maintain the desired intensities and length scales in the unburned mixture. The main objective of this study is to provide deeper insight into turbulent flame speed dependencies. The validity of employing Eq. (8.1) under engine relevant conditions will be discussed. A novel approach using the "marching cube" algorithm is adopted to study flame surface wrinkling. An expression with a single degree of freedom is formulated to describe the fractal characteristics of premixed flames categorized in the TRZ regime. The effects of turbulence intensities and length scales on the flame speeds are examined, from which a physics-inspired correlation for S_T is derived.

Section 8.2 presents the computational method, including the chemical kinetic models, the approach adopted to achieve statistically stationary turbulent flames, turbulence forcing and simulation conditions used in the parametric studies. In Section 8.3, DNS results obtained by employing two different chemical mechanisms are compared. Section 8.4 discusses the flame speeds derived from the DNS data. Wrinkling of flame surface by turbulence is examined to shed light on the effects of turbulence

intensities and length scales. The chapters then ends with summary and conclusions in Section 8.5.

8.2 Computational Setup

8.2.1 The numerical model

DNS results presented in this study are obtained using the in-house code HOLOMAC (High-Order LOw-MAch number Combustion) [152]. The numerics of the code is elaborately discussed in Chapter 3. In summary, the code solves the 3D Navier-Stokes conservation equations under the low Mach-number assumption [164] for multi-component mixtures with CHEMKIN interface for computing the chemical reactions and transport properties. Spatial discretization is performed using a 6th-order implicit compact scheme [153]. The time integration is based on a Strang operator-split strategy. Convection terms are advanced in time using a 2nd-order Adams-Bashforth (AB2) scheme while the diffusion terms are integrated using a 2nd-order stabilized explicit Runge-Kutta-Chebyshev (RKC) method. The momentum equation is solved using a projection-correction method. The divergence condition is enforced up to machine precision by solving a variable-coefficient Poisson equation for pressure using a spectral solver based on Fast Fourier Transform (FFT). A 6th-order accurate spatial filter is applied to remove any spurious high-wavenumber oscillations. Mixture-averaged transport properties are used for viscosity, thermal conductivity and molecular diffusivity.

8.2.2 Chemical kinetics

It is well known that DNS with detailed chemistry is computationally very intensive. In this study, a 13-species reduced mechanism developed by Sankaran *et al.* (2007) [214] is employed. This mechanism is based on GRI-Mech 1.2 [235] and is suitable for predicting flame speeds in lean methane/air mixtures. In addition, a global

chemical mechanism that is able to predict the laminar flame speed is employed. The mechanism is formulated as follows:

$$\dot{\omega} = A\mathrm{T}^b \left[\mathrm{CH_4}\right]^m \left[\mathrm{O_2}\right]^n e^{-E_a/R\mathrm{T}}. \tag{8.2}$$

The parameters A, b, m, n, and E_a are calibrated such that the laminar flame speed is comparable to the flame speed predicted by both a 73-step skeletal mechanism with 17-species developed by Sankaran *et al.* (2007) [214] and the GRI-Mech 3.0 [183]. Specifically, the values of the constants of the global mechanism are given as $A(\phi = 0.5) = 3.25 \times 10^{19} cm^3/mol \cdot s$; $b = 0$; $m = n = 1$; $E_a = \mathcal{R} \cdot (40250\mathrm{K})$. Figure 8.1 shows the computed laminar flame speeds obtained with the four mechanisms for premixed equivalence ratios ϕ between 0.4 and 0.8, the range of interest in these simulations. The results agree within 5% of each other. However, the use of global mechanism is believed to be inadequate for predicting flame response to high strain rates. In Section 8.3, the validity of using the global mechanism for simulating turbulent premixed flames at conditions relevant to engines will be discussed at length.

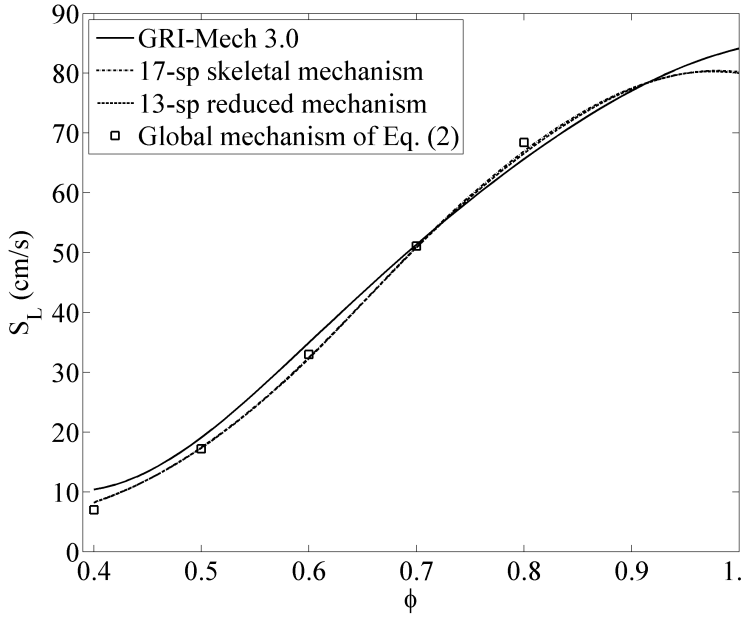

Figure 8.1. Computed laminar flame speeds as a function of ϕ for unburned temperature of 810 K at pressure of 20 bar.

8.2.3 Modeling of statistically stationary flames

In this work, turbulent premixed flames are simulated as statistically stationary inside the computational domain by employing a Lagrangian framework as discussed in Chapter 5.2. This setup enables the computational domain size to be decoupled from the flame propagation time, and allows for statistics to be collected over an extended period of time. An inflow/outflow configuration as shown in Fig. 8.2 is employed. Periodic boundary conditions are applied to the side boundaries which are parallel to the mean flow direction. In Fig. 8.2, inflow of unburned lean methane-air mixture is specified at the left boundary and the burned gas passes through a sponge zone and leaves the domain from the right. To keep the flame statistically stationary, a feedback control mechanism is employed using the mean flame position $x_f(t)$ as the control output to correct the bulk inflow velocity $\mathrm{U}_0(t)$ until the flame becomes statistically stationary. In the current simulations, a proportional feedback and an integral feedback as discussed in Chapter 5.2 are employed. The proportional feedback provides "spontaneous" correction on the bulk inflow velocity based on the mean flame front movement whereas the integral feedback delivers a "long-term" control on the flame position.

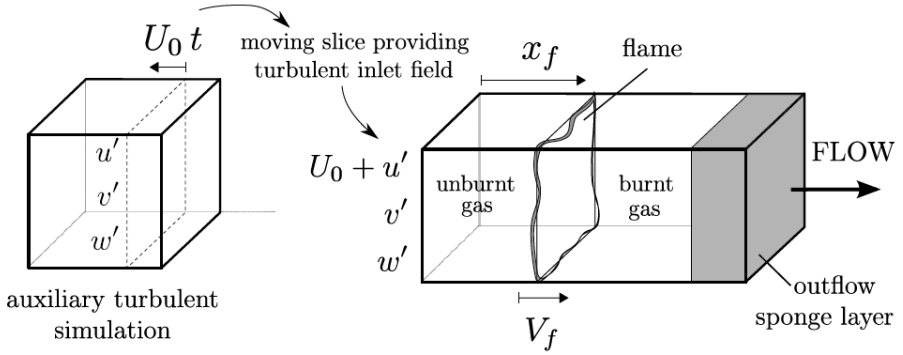

Figure 8.2. Schematic of the inflow-outflow configuration for simulation of the turbulent premixed flame as statistically stationary.

8.2.4 Turbulence forcing

The domain is initialized with a laminar flame located in the middle of the computational domain. To preserve the desired turbulence intensity in the reactants region, turbulent fluctuations are imposed on the bulk inflow velocity. These fluctuations are obtained by selecting sequential cross-sectional planes of a homogeneous no-decaying isotropic turbulence field generated in a separate auxiliary simulation as shown in Fig. 8.2. In addition, the turbulence in the reactants region is forced using the "linear forcing" scheme as discussed in Chapter 5.3 [197, 198]. Specifically, a term is added to the right-hand-side of the momentum equation to represent the energy cascade from scales which are larger than the domain size. The specific form of the forcing term is given by [198]:

$$\mathrm{F}_i = \mathrm{M(T)} B \left[\frac{k_o}{k}\right] \rho u_i. \tag{8.3}$$

Here, k is the instantaneous Turbulence Kinetic Energy (TKE) in the reactant mixture and k_o is the desired steady-state TKE. M(T) is a ramp function of temperature which decreases from 1 to 0 as T increases by 200 K above the unburned temperature. This is to prevent any artificial effect of forced turbulence on the flame structure. B is the forcing constant which is inversely proportional to the steady-state eddy turnover time. In addition, it has been reported that the integral length scale, $\mathrm{L_o}$, of the forced turbulence will always converge to approximately 20% of the domain size independent on its initial state or on the choice of the forcing constant B [197]. The significance of this is that $\mathrm{L_o}$ can be maintained at a desired value by choosing an appropriate domain size.

One caveat of using feedback control on the inflow velocity is that it may result in unwanted forcing of turbulence in the unburnt mixture. To avoid such complication, a two-step approach is used. Initially feedback control is activated to keep the flame statistically stationary inside the domain. Once the flame is fully developed and the time-averaged inflow velocity becomes self-convergent, simulation is restarted without feedback control and the bulk inflow velocity set to the converged value. Turbulence

and flame statistics are only collected during the second phase where there is no inflow forcing on the turbulence.

The turbulent flame speed S_T can be obtained from the time average of the bulk inflow velocity once the premixed flame becomes fully developed and is statistically stationary. S_T is derived through the following relation:

$$\begin{aligned} S_T &\equiv \langle \frac{\dot{m}_f}{\rho_u A_L Y_{f,u}} \rangle \\ &= \frac{1}{t_2 - t_1} \int_{t_1}^{t_2} \frac{1}{A_L} \int_{A_L} \left[u(0, y, z, t) - u(L_x, y, z, t) \frac{\rho_{out} Y_{f,out}}{\rho_u Y_{f,u}} \right] dA dt. \end{aligned} \tag{8.4}$$

Here, A_L denotes the area of the inflow boundary. Since the length of the domain is ensured to be sufficiently long that all methane is consumed, fuel mass fraction at the outlet, i.e., $Y_{f,out}$, is equal to zero. Furthermore, since the turbulent velocity fluctuations on the inflow plane come from selecting sequential cross-sectional planes of a homogeneous non-decaying isotropic turbulence flow field (see Fig. 8.2) with a zero mean, Eq. (8.4) can be further simplified as

$$\begin{aligned} S_T &= \frac{1}{t_2 - t_1} \int_{t_1}^{t_2} \frac{1}{A_L} \int_{A_L} u(0, y, z, t) dA dt \\ &= \frac{1}{t_2 - t_1} \int_{t_1}^{t_2} U_0(t) dt + \langle u' \rangle \\ &= \frac{1}{t_2 - t_1} \int_{t_1}^{t_2} U_0(t) dt. \end{aligned} \tag{8.5}$$

8.2.5 Parametric study conditions

Nine simulations are carried out for premixed methane/air flames at a pressure of 20 bar, reactant temperature of 810 K, and $\phi = 0.5$. The properties are selected to reflect conditions at top dead center (TDC) in a lean-burn natural gas engine. The adiabatic flame temperature T_{ad} under these conditions is 1906 K. Table 8.1 lists the nine cases studied with additional parameters of interest. The domain size has been selected depending on the desired L_o with the smallest $4 \times 1.6 \times 1.6$ mm and the largest $20 \times 6.4 \times 6.4$ mm. The root-mean-square turbulent velocity fluctuations u_{rms} are varied in Cases 1-7 such that the ratios of u_{rms} to the laminar flame speed

S_L, i.e., u_{rms}/S_L, vary from 2 to 25. Cases 4a and 4b are performed keeping the ratio of u_{rms}/S_L equal to 10 as in Case 4 but varying L_o of the turbulence to 0.32 and 1.28 mm, respectively, whereas $L_o = 0.64$ mm in Case 4. The grid resolution is selected to be less than 1.5 times the Kolmogorov length scale η computed from the auxiliary simulation of homogeneous non-decaying isotropic turbulence [63]. This resolution also ensures that there are more than 18 points across the unstrained laminar flame front. The Damköhler number Da, defined as the ratio of eddy turnover time to the chemical timescale, i.e., $Da = (S_L/u_{rms})(L_o/\delta_L)$, varies from 0.26 to 3.2. Here, δ_L is a measure of the unstrained laminar flame thickness and is defined based on the maximum temperature gradient, i.e., $\delta_L = (T_{ad} - T_u)/\max\{dT/dx\}$. The Karlovitz number Ka, defined as the ratio of the chemical time scale to the Kolmogorov time scale, i.e., $Ka = (u_{rms}/S_L)^{\frac{3}{2}}(\delta_L/L_o)^{\frac{1}{2}}$, is between 1.1 and 49.4. Each simulation is performed for more than 30 eddy turnover time τ after the turbulent flame front has become fully developed and stationary. Note that Case 4 ($u_{rms}/S_L = 10$) and Case 7 ($u_{rms}/S_L = 25$) are carried out using the 13-species reduced mechanism and the global mechanism whereas the rest is simulated employing the global mechanism alone. It remains to show whether the global mechanism is adequate for simulating premixed flames at the selected range of flow conditions.

8.3 Reaction Mechanism Comparison

To assess the adequacy of using the global mechanism, it is important to compare not only the turbulent flame speed, but also i) flame thickness, ii) flame surface wrinkling and iii) reaction rate on the flame front as a result of turbulence-chemistry interaction. In this section, the dependence on the chemistry mechanism of these three turbulent flame characteristics will be compared between flames simulated using the 13-species and the global mechanism at an intermediate turbulence intensity ($u_{rms}/S_L = 10$) and the highest turbulence intensity ($u_{rms}/S_L = 25$).

Table 8.1. Computational parameters and turbulence conditions employed in this study. Computed normalized turbulence flame speeds and efficiency factor I_o are also listed.

	Case 1	Case 2	Case 3	Case 4	Case 4a	Case 4b	Case 5	Case 6	Case 7
Time of flame propagation normalized by τ	180	168	100	140	180	35	78	47	130
u_{rms} (ms^{-1})	0.301	0.753	1.205	1.506	1.506	1.506	2.259	3.012	3.765
L_o (mm)	0.64	0.64	0.64	0.64	0.32	1.28	0.64	0.64	0.64
$\eta(\mu m)$	36.3	18.2	14.2	10.9	9.1	12.9	8.0	6.5	5.5
u_{rms}/S_L	2.0	5.0	8.0	10.0	10.0	10.0	15.0	20.0	25.0
L_o/δ_L	6.4	6.4	6.4	6.4	3.2	12.8	6.4	6.4	6.4
Re_T	44	110	176	220	110	440	330	440	549
Da	3.20	1.28	0.80	0.64	0.32	1.28	0.43	0.32	0.26
Ka	1.1	4.4	8.9	12.5	17.7	8.8	23.0	35.4	49.4
I_o evaluated at 1800 K	1.03	1.04	1.11	1.06	1.05	1.07	1.07	1.07	1.07
S_T/S_L	4.00 $\pm$0.02	7.63 $\pm$0.06	8.88 $\pm$0.13	8.63 $\pm$0.03	5.20 $\pm$0.06	13.34 $\pm$0.10	9.27 $\pm$0.18	10.19 $\pm$0.41	10.64 $\pm$0.12

8.3.1 Flame thickness

The effect of turbulence on the local flame thickness is examined first. This effect can be quantified using the mean of temperature gradient conditioned at a given temperature, i.e., $\langle \|\nabla \mathrm{T}|\mathrm{T}\| \rangle$ where $\langle \cdot \rangle$ involves averaging both in time and on the flame surface. Figures 8.3(a) and 8.3(b) show the conditional mean of temperature gradient normalized with that across the unstrained laminar flame front as a function of temperature for flames simulated with the 13-species and the global mechanism, respectively. Note that a value less than 1 indicates "flame thickening" and a value larger than 1 indicates "flame straining." It is evident in Fig. 8.3(a) that for $\mathrm{u_{rms}/S_L}$ = 10 (Ka = 12.5), both mechanisms predict thicker flame structure for T < 1600 K, i.e., inside the preheat zone, and thinner flame for T > 1600 K, i.e., inside the reaction zone. This is because eddies close to the Kolmogorov scale penetrate into the preheat zone which results in enhanced mixing and thus reducing the temperature gradient. Furthermore, the effect of turbulence on the flame thickness using the two mechanisms shows agreement within 5% except at temperature greater than 1800 K. For $\mathrm{u_{rms}/S_L}$ = 25 in Fig. 8.3(b) (Ka = 49.4), turbulence thickening effect is more pronounced in the preheat zone compared to Case 4. In addition, 13-species mechanism predicts up to 20% lower spatial gradient in temperature for 1100 K < T < 1800 K. Nonetheless, the effect of "flame thickening" inside the preheat zone and "turbulence straining" inside the reaction zone is qualitatively captured by the global mechanism for flames with Ka = 49.4.

8.3.2 Flame surface wrinkling

Flame surface wrinkling is another key feature in the modeling of turbulent premixed flames. Figures 8.4(a) and 8.4(b) show the isotherm surface areas $\mathrm{A_T(T)}$ evaluated at various temperatures for $\mathrm{u_{rms}/S_L}$ = 10 and 25, respectively. The isotherm surface areas are computed using a "marching cube" algorithm and averaged in time. The "marching cube" algorithm is used for extracting polygonal meshes of the isosur-

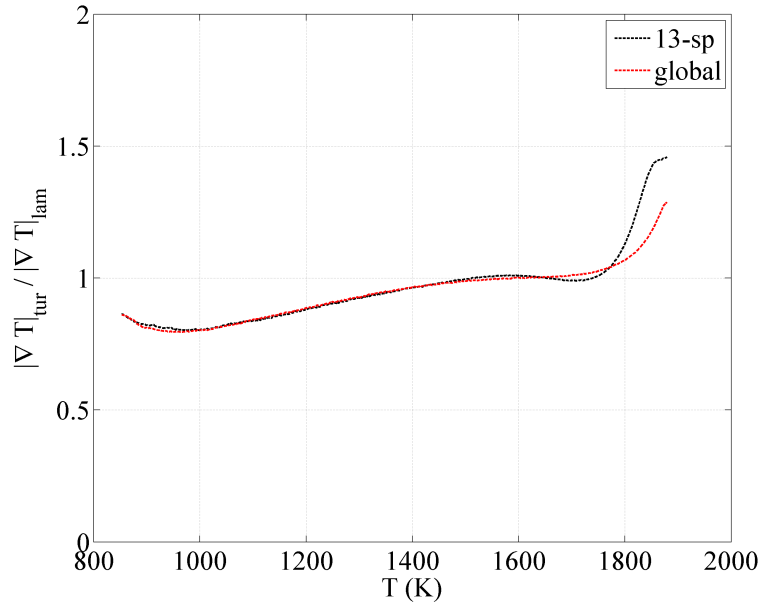

(a)

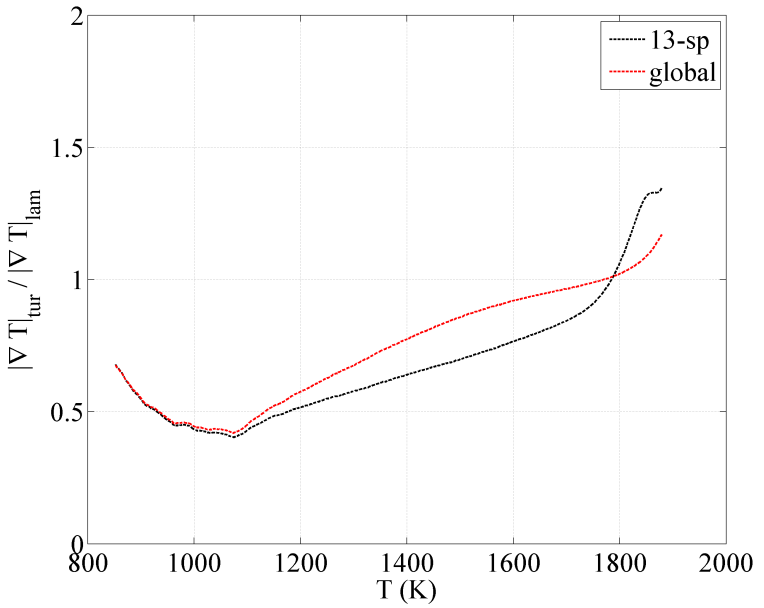

(b)

Figure 8.3. Averaged temperature gradient conditioned on flame temperature, i.e., $\langle \|\nabla T|T\| \rangle$, normalized with that in unstrained laminar flame as a function of temperature for (a) Case 4: u_{rms}/S_L = 10.0, Da = 0.64, Ka = 12.5 and (b) Case 7: u_{rms}/S_L = 25.0, Da = 0.26, Ka = 49.4.

face from the 3D discrete scalar field. Figure 8.4(a) shows that for the lower turbulence intensity, flame wrinkling predicted by the two mechanisms does not show noticeable differences across entire range of flame temperatures. For $u_{rms}/S_L = 25$, the global mechanism predicts higher surface area for T > 1200 K evident in Fig. 8.4(b) but the differences are within 7%. One possible explanation for the differences in $A_T(T)$ is that preferential diffusion of light radicals, e.g., H and OH, from the reaction zone to preheat zone is not captured by the global mechanism. Accumulation of radicals inside the preheat zone could increase the reaction rate locally on the flame surface, thereby modify the local flame displacement speed and hence the evolution of flame surface area. Nonetheless, for engineering applications, e.g., modeling combustion in engines, the global mechanism can be considered to be comparable to the 13-species mechanism as far as predicting flame wrinkling is concerned for the given range of turbulence intensities.

8.3.3 Reaction rate on the flame surface

Figures 8.5(a) and 8.5(b) show the comparison between the time-averaged Heat Release Rate (HRR) per unit volume conditioned on flame temperature using the 13-species and the global mechanism, respectively. The heat release rate distributions of the respective laminar flames are also plotted in lines. Note that the laminar profiles of heat release rate in the temperature space show noticeable differences between the two mechanisms although the differences in laminar flame speed are small as seen in Fig. 8.1. This is because the differences between heat release rate profiles in the physical space are less pronounced and it is ensured that the total heat release rates across the laminar flame front are the same for both mechanisms, hence the approximate equivalence of the laminar flame speeds. Considering Case 4 ($u_{rms}/S_L = 10$) shown in Fig. 8.5(a), the mean heat release rate inside the turbulent flame is about the same as that of their respective laminar baseline for T < 1700 K. For T > 1700 K, the 13-species mechanism predicts up to 13% increase in the heat release

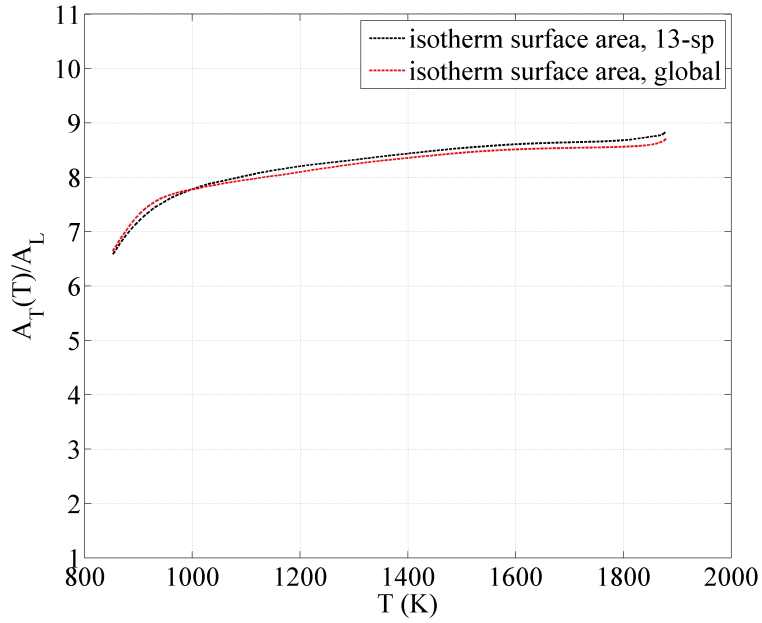

(a)

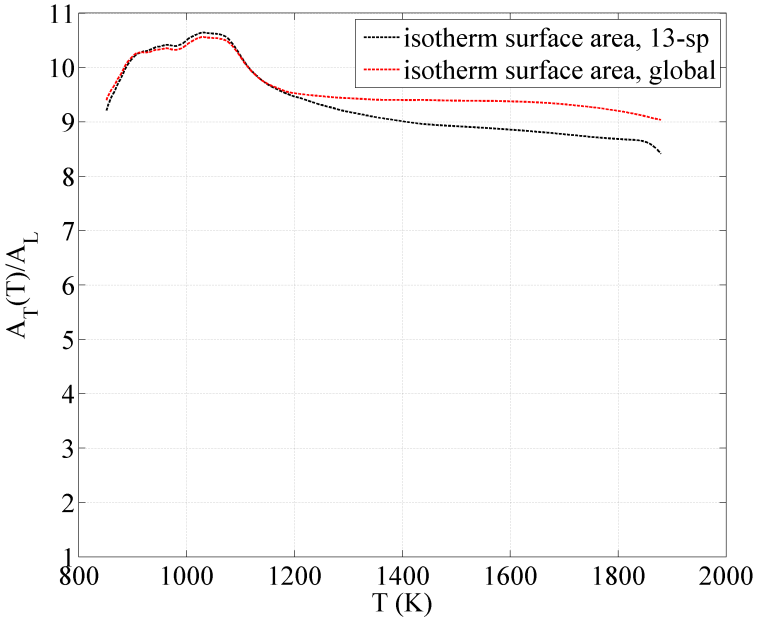

(b)

Figure 8.4. Time-averaged normalized flame surface area evaluated at T, i.e., $A_T(T)/A_L$, as a function of temperature for (a) Case 4: $u_{rms}/S_L = 10.0$, $Da = 0.64$, $Ka = 12.5$ and (b) Case 7: $u_{rms}/S_L = 25.0$, $Da = 0.26$, $Ka = 49.4$.

rate compared to the laminar case whereas global mechanism predicts up to 10% increase. This increment in the heat release rate is likely due to the straining of the reaction zone as illustrated in Figs. 8.3(a) and 8.3(b). For Case 7 ($u_{rms}/S_L = 25$) shown in Fig. 8.5(b), high fluctuations in the conditional mean heat release rate are observed for $T < 1500$ K. It is also interesting to note that, for these temperatures, the conditional mean heat release rates could be one or two orders of magnitude larger than those found in the laminar flame. This could possibly be attributed to the curvature effects present in turbulent flames. Highly curved surfaces generated by turbulence could result in the focusing of radical diffusion from the reaction zone to the preheat zone. Accumulation of these radicals in the preheat zone would drastically increase the local reaction rates without significantly affecting the mixture enthalpy. This explains the fluctuations in heat release rate on the isotherm surface evident in Fig. 8.5(b). As it will be shown in the later chapter, highly curved surfaces are more likely to occur in high *Ka* flames. Hence, fluctuations in HRR inside preheat zone are more prominent in Case 7 than in Case 4. In addition, Fig. 8.5(b) shows the maximum mean heat release rate in the turbulent flame predicted using the 13-species mechanism is 9% lower than that in the laminar flame. This is again due to enhanced diffusion of radicals away from the reaction zone, thereby reducing reaction rates inside the reaction zone. The coupled effects of radical diffusion and chemistry are, however, not predicted by the global mechanism, as shown in Fig. 8.5(b), where conditional mean heat release rates as a function of temperature are qualitatively identical to that in Fig. 8.5(a).

8.3.4 Validity of employing the global mechanism

In summary, simulation of Case 4 ($u_{rms}/S_L = 10$) using the global mechanism does not exhibit noticeable differences from that using the 13-species reduced mechanism as far as prediction of the mean turbulent flame structure, turbulent wrinkling of flame and the effects of turbulence on chemical reaction rate are concerned. For

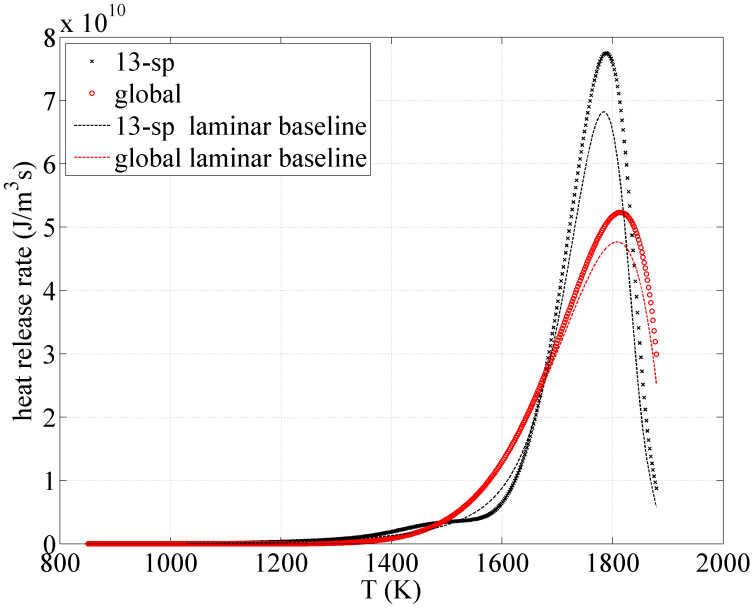

(a)

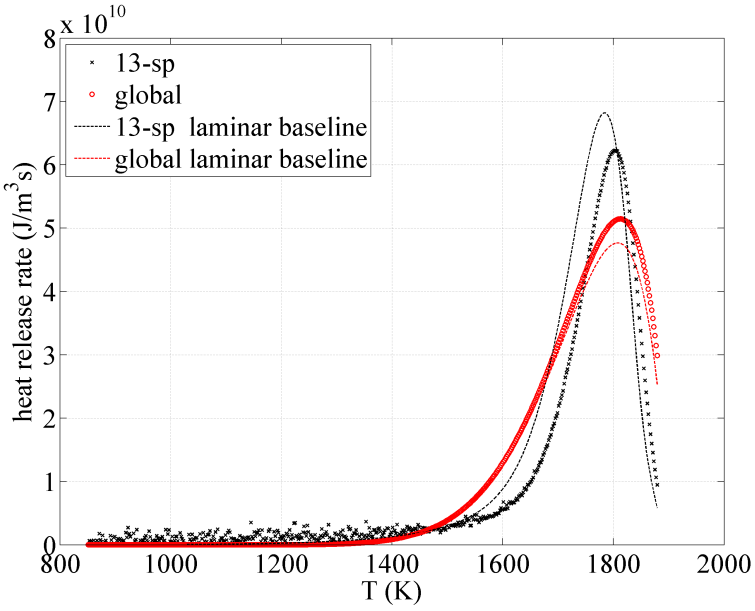

(b)

Figure 8.5. Comparison of the time-averaged heat release rate profile conditioned on flame temperature for (a) Case 4: $u_{rms}/S_L = 10.0$, $Da = 0.64$, $Ka = 12.5$ and (b) Case 7: $u_{rms}/S_L = 25.0$, $Da = 0.26$, $Ka = 49.4$ (symbols) with that of the unstrained laminar flame (lines).

higher turbulence intensities where $u_{rms}/S_L = 25$, i.e., Case 7, some differences can be observed using the global mechanism. In particular, "flame thickening" of the preheat zone is less pronounced than that using the reduced mechanism although the maximum difference is less than 20%. Global mechanism also predicts up to 7% higher in the flame surface area for $T > 1200$ K. In terms of reaction rate on the flame surface, global mechanism is inadequate for modeling the enhanced effect of radical diffusion, which results in over-prediction of heat release rates inside the reaction zone.

It is interesting to look at the overall effects of the chemical mechanism on the computed turbulent flame speed S_T. For a fully-developed, statistically-steady flame confined in the computational domain, S_T can be computed by invoking the integral form of the energy conservation:

$$\rho_u A_L \Xi \cdot S_T = \langle \int \mathrm{HRR} dV \rangle_{tur} \tag{8.6}$$

where HRR is the heat release rate per unit volume and Ξ is the amount of sensible energy released per unit mass of CH_4/air mixture assuming complete combustion. Performing a transformation from the physical space to the temperature space, Eq. (8.6) can be written as

$$\begin{aligned} \rho_u A_L \Xi \cdot S_T &= \langle \int_{T_u^+}^{T_{ad}^-} \overline{\mathrm{HRR}}_{tur}(T) \cdot \frac{dV}{dT} dT \rangle \\ &= \langle \int_{T_u^+}^{T_{ad}^-} \overline{\mathrm{HRR}}_{tur}(T) \cdot A_T(T) \frac{\delta s(T)}{\delta T} dT \rangle \\ &+ \langle \int_{T_u^+}^{T_{ad}^-} \overline{\mathrm{HRR}}_{tur}(T) \cdot s \cdot \frac{\delta A_T(T)}{\delta T} dT \rangle \end{aligned} \tag{8.7}$$

Here, $\langle \cdot \rangle$ denotes averaging in time and $\delta s(T)$ represents the infinitesimal thickness of the turbulent flame at temperature T. Notice that $\delta s(T)/\delta T$ is the inverse of $\langle \|\nabla T\| | T \rangle$ shown in Figs. 8.3(a) and 8.3(b). In the current study, the finite thickness of flame between $T \pm 1$ K is used for $\delta s(T)$. The second term on the right-hand-side accounts for the change in $\delta A_T(T)$ with temperature. It is found that such a term is

less than 0.1% of the first term and can be neglected. Similarly, laminar flame speed S_L can be constructed as

$$\begin{aligned}\rho_u A_L \Xi \cdot S_L &= \int_{T_u^+}^{T_{ad}^-} HRR_{lam}(T) \cdot \frac{dV}{dT} dT \\ &= \int_{T_u^+}^{T_{ad}^-} HRR_{lam}(T) \cdot A_L \frac{\delta s(T)}{\delta T} dT.\end{aligned} \tag{8.8}$$

If we assume that flame wrinkling by turbulence, manifested by $A_T(T)$ and the effects of turbulence on the flame front reaction rate, manifested by $\overline{HRR}_{tur}(T) \cdot \delta s(T)/\delta T$ are two independent physical events, we can estimate S_T/S_L by

$$\frac{S_T}{S_L} \cong \int_{T_u^+}^{T_{ad}^-} \langle \frac{\overline{HRR}_{tur}(T)/\|\nabla T|T\|_{tur}}{HRR_{lam}(T)/\|\nabla T|T\|_{lam}} \rangle \cdot \langle \frac{A_T(T)}{A_L} \rangle dT \tag{8.9}$$

Using the relationship in Eq. (8.9), the estimated normalized turbulent flame speed S_T/S_L using the global mechanism is only 2.8% higher than that using the 13-species mechanism for Case 7 ($u_{rms}/S_L = 25$) and 4.0% lower for Case 4 ($u_{rms}/S_L = 10$). This suggests that for engineering applications, the global mechanism is as capable of predicting the turbulent flame speed as the reduced mechanism over the range of conditions considered in this study.

8.4 Characterization of Flame Surface Wrinkling and Flame Speed

8.4.1 Turbulent flame speed and efficiency factor

So far, it has been shown using Cases 4 and 7 that the global mechanism is adequate for predicting flame surface wrinkling and also the turbulent flame speed for u_{rms}/S_L up to 25. Based on this, simulations of the other cases listed in Table 8.1 are carried out using the global mechanism. The turbulent flame speed S_T, as tabulated in Table 8.1, is obtained using Eq. (8.5) by averaging the bulk inflow velocity $U_0(t)$ over increasingly longer periods of time until self-convergence of S_T is observed. The root-mean-square of the time-averaged bulk inflow velocity is also given in Table 8.1. As u_{rms}/S_L is increased from 2 to 8 (Cases 1-3) while holding integral length

scale constant, the normalized turbulent flame speed increases by more than 120% from 4.00 to 8.88. With further increase in u_{rms}/S_L from 8 to 25 (Cases 3-7), the normalized turbulent flame speed begins to plateau as S_T/S_L is only increased by 20% from 8.88 to 10.64. The flattening of S_T with increasing u_{rms}/S_L is also observed in the 2D simulations reported in Chapter 6.3. On the other hand, when u_{rms}/S_L remains constant at 10 while integral length scale is increased from 0.32 to 0.64 and 1.28 *mm* (Cases 4a, 4 and 4b), the normalized flame speed increases from 5.20 to 8.63 and 13.34, i.e., by 66% and 156%, respectively. The trend of turbulent flame speeds with increasing turbulence intensities and integral length scales will be discussed further in Section 8.4.3.

Figure 8.6 compares the normalized turbulent flame speeds for flames simulated using a 3D framework reported in Table 8.1 and those using a 2D framework reported in Table 6.1. Flame speeds computed using a 3D framework are higher. Nonetheless, a similar trend in S_T/S_L with u_{rms}/S_L is observed for 3D and 2D turbulent flames.

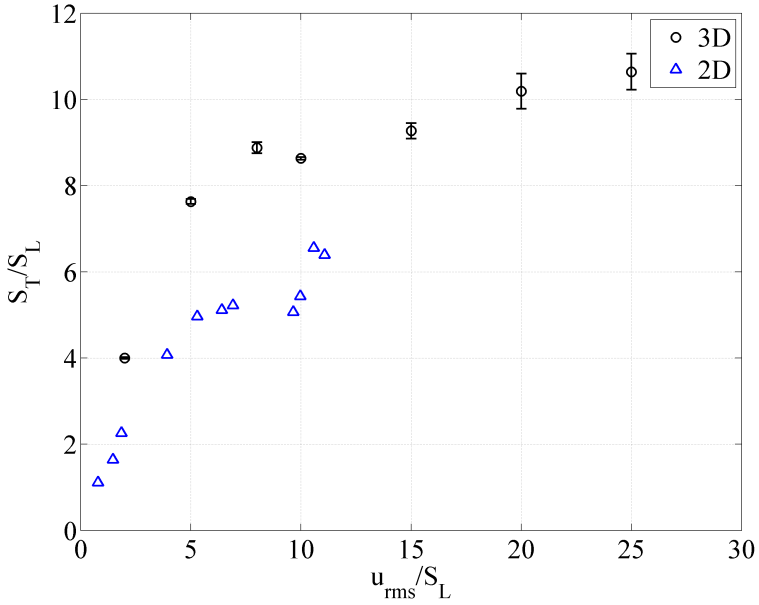

Figure 8.6. Comparison of the normalized turbulent flame speeds S_T/S_L as a function of normalized turbulence intensities u_{rms}/S_L for flames simulated in 3D and 2D framework.

These flame speed results are examined within the framework of Eq. (8.1). Note that A_T/A_L indeed varies with temperature as shown in Fig. 8.4. Table 8.1 lists the value of I_o for the various cases estimated on the isosurface of T = 1800 K corresponding to the peak heat release rate in the laminar flame. It can be seen that the value is within 1.07 ± 0.04 when u_{rms}/S_L varies from 2 to 25 and when L_o/δ_L varies from 3.2 to 12.8. For Case 4 and Case 7 simulated using the 13-species mechanism, I_o, not given in the table, is found to be 1.10 and 1.11, respectively. Hence, turbulent flame speed is primarily controlled by the flame surface generation. The efficiency factor is found to be always greater than unity and this is likely due to the non-linear effects induced by "flame straining" in the reaction zone.

8.4.2 Flame surface area

The DNS data is further analyzed on the isotherm of T = 1800 K. The data is first sampled using a fixed physical length Δ with Δ being some multiples of the actual grid size. This is possible when a uniform grid resolution is employed in the simulations. The isotherm surface is then reconstructed from the sampled dataset using the "marching cube" algorithm discussed earlier and the surface area $A(\Delta)$ is computed. To minimize variation associated with sampling at large Δ, multiple samplings are performed with the starting point selected at random. Time averaging of $A(\Delta)$ is also performed over 50$\sim$100 instantaneous snapshots. By sampling the data, wrinkling done by eddies with characteristic length scale $l < \Delta$ is smoothed out. Alternatively, $A(\Delta)$ represents the surface area generated by eddies bigger than Δ. Note that this method takes advantage of the fractal properties of premixed flames proposed by Gouldin (1987) [129], but is different from the box-counting, caliper, and circle methods [232] which are the common techniques for determining fractal dimension.

The normalized sampled flame surface area, i.e., $A(\Delta)/A_L$ is plotted against the sampling length normalized with the integral length scales, i.e., Δ/L_o for Cases 1-7

in Fig. 8.7(a) and for Cases 4, 4a and 4b in Fig. 8.7(a). Convergence of $A(\Delta)$ is evident as Δ approaches the Kolmogorov scale. More interestingly, the normalized surface area generated by the integral length scale, i.e., $A(\Delta = L_o)/A_L$ appears to be approximately a constant (3.0 ± 0.3) and independent of u_{rms} or L_o of the turbulence. This suggests that $A(\Delta = L_o)/A_L$ is likely an invariant that is specific to the problem setup (in this case, a statistically planar flame).

Figure 8.8 shows the sampled surface area $A(\Delta)$ normalized with $A(\Delta = \eta)$, which is the same as the actual flame area, i.e., $A_T(T = 1800K)$, as a function of Δ normalized by the Kolmogorov scale η for all cases. It can be seen that with this normalization, $A(\Delta)$ of all nine cases collapse into a single curve as marked by the dashed line in Fig. 8.8. In addition, when Ka is increased from 1.1 to 49.4, this curve shifts towards the upper-right direction in a monotonic fashion. This suggests that there exists a dependence of S_T on the Karlovitz number. As a result, the following expression is proposed:

$$\log_{10}\left[\frac{A(\Delta)}{A_T}\right] = f(\log_{10}\left[\frac{\Delta}{\eta}\right]) \cdot g(Ka). \tag{8.10}$$

The first function $f(x)$ on the right-hand-side of Eq. (8.10) describes the primary dependence of $A(\Delta)/A_T$ on Δ/η. The second function accounts for the slight shift of the curve when Ka is changed, i.e., the secondary dependence.

The curve $f(x)$ can be estimated using a functional form of $f(x) = \log_{10}\left[1/(1 + a \cdot x^b)\right]$. The reason for selecting this function form is that it satisfies the condition when x approaches zero, both $f(x)$ and $f'(x)$ tend toward zero. The line of best fit for $f(x)$ is obtained using Case 4a as the reference ($Ka_{ref} = 8.8$):

$$f(x) = \log_{10}\frac{1}{1 + 0.115x^{4.765}}. \tag{8.11}$$

The reference line of Eq. (8.11) is also plotted in Fig. 8.8 with the dash line. The dependence on Ka can be written in terms of

$$g(Ka) = \left(\frac{Ka}{Ka_{ref}}\right)^{-\alpha}. \tag{8.12}$$

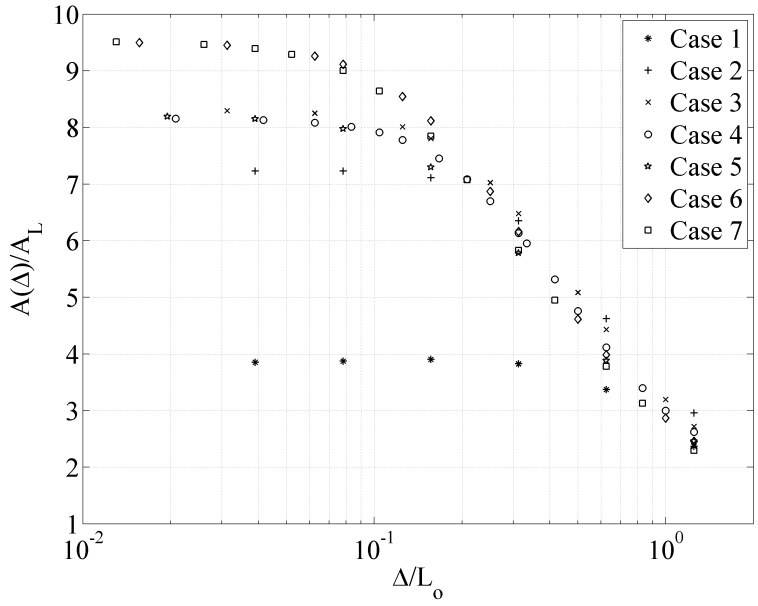

(a)

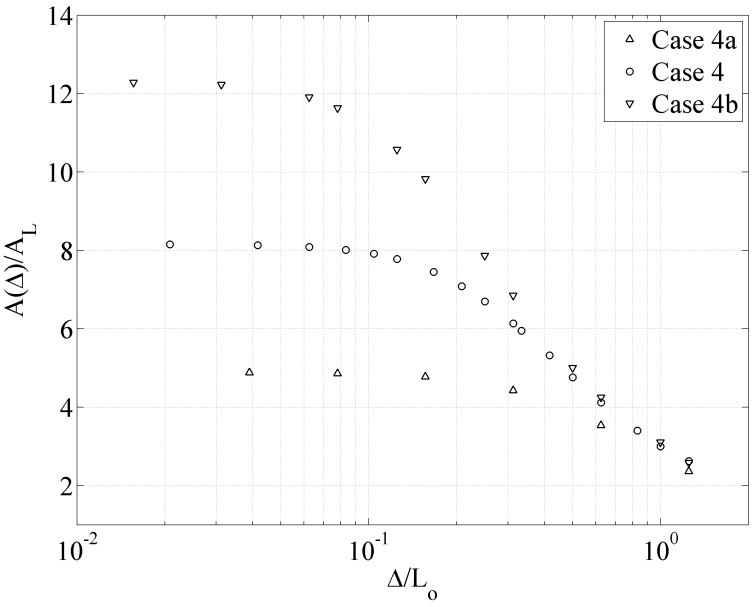

(b)

Figure 8.7. Sampled flame surface area $A(\Delta)$ of the isosurface at T = 1800 K normalized by A_L as a function of the sampling length Δ normalized by L_o for (a) Cases 1-7 where u_{rms}/S_L varies from 2 to 25 while $L_o/\delta_L = 6.4$; and (b) Cases 4, 4a and 4b where L_o/δ_L varies from 3.2 to 12.8 while $u_{rms}/S_L = 10$.

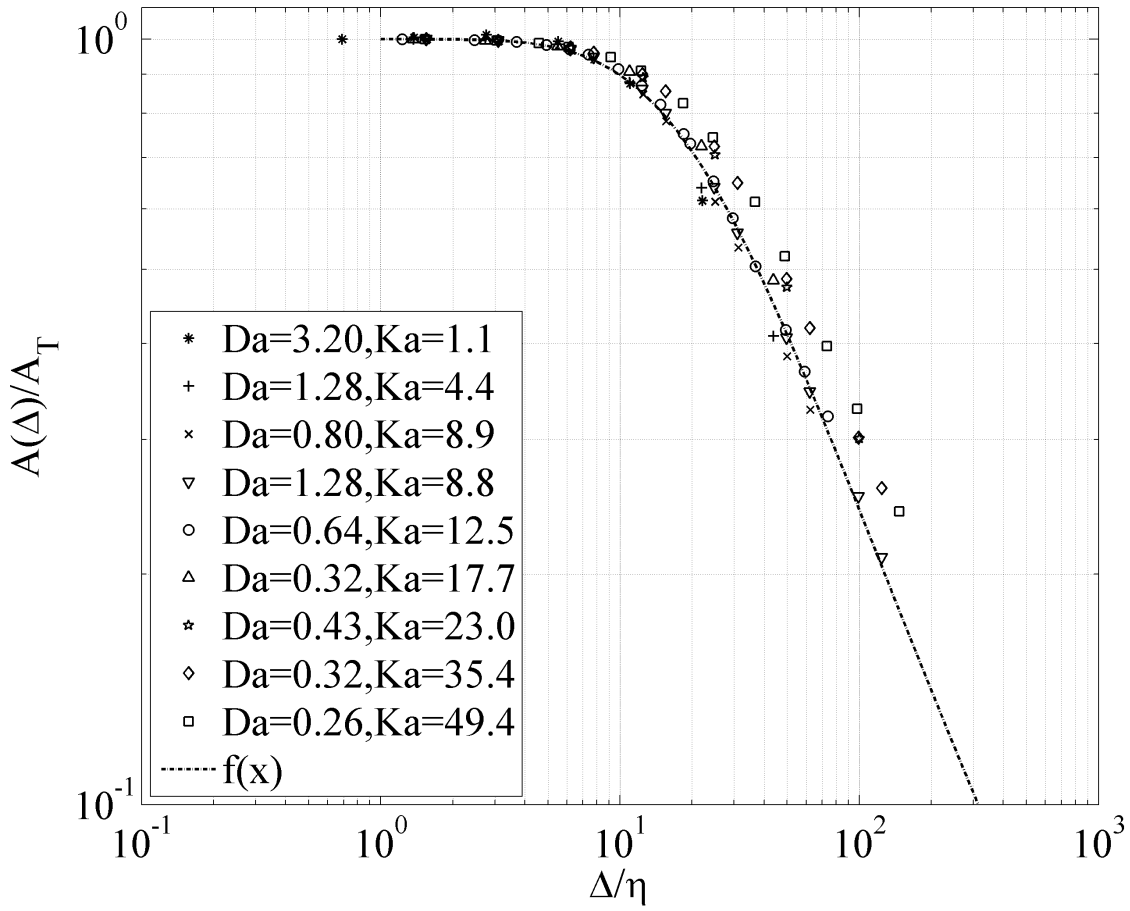

Figure 8.8. Sampled flame surface area A(Δ) of the isosurface at T = 1800 K normalized by A_T as a function of the sampling length Δ normalized by η for turbulent flames denoted by their Damköhler (Da) and Karlovitz numbers (Ka). The primary dependence of $A(\Delta)/A_T$ on Δ/η is plotted with the dash line.

The value of α is determined to be 0.1437 which minimizes the root-mean-square error of all cases considered in this study.

Finally, the correlation for S_T/S_L in Eq. (8.1) can be expressed as

$$\begin{aligned}\frac{S_T}{S_L} &= I_o \frac{A_T}{A_L} \\ &= I_o \cdot \frac{A(\Delta = L_o)}{A_L} \cdot \left[\frac{A(\Delta = L_o)}{A_T}\right]^{-1} \\ &= I_o \cdot \frac{A(\Delta = L_o)}{A_L} \cdot \left\{1 + 0.115\left[\log_{10}\left(\frac{L_o}{\eta}\right)\right]^{4.765}\right\}^{\left(\frac{Ka}{8.8}\right)^{-0.1437}}\end{aligned} \tag{8.13}$$

Here, I_o is the efficiency factor tabulated in Table 8.1. It is found to be approximately 1.07 ± 0.04 when evaluated at the temperature corresponding to the peak heat release rate in the laminar flame. The second term $A(\Delta = L_o)/A_L$ is plotted in Figs. 8.7(a) and 8.7(b). It is approximately a constant with a value of 3.0 ± 0.3 for u_{rms}/S_L between 2 and 25. The last term $[A(\Delta = L_o)/A_T]^{-1}$ is plotted in Fig. 8.8. It can be approximated using the correlation of Eq. (8.10) evaluated at $\Delta = L_o$. Note that L_o/η that appears in Eq. (8.13) can be approximated as $Re_T^{3/4}$. From a physical standpoint, the term $\{1 + 0.115[\log_{10}(L_o/\eta)]^{4.765}\}$ represents the flame surface area enhancement generated by the spectrum of length scales between L_o and η. The power coefficient, i.e., $(Ka/8.8)^{-0.1437}$, accounts for the increased interaction between the Kolmogorov-scale eddies and the flame which results in a reduction of flame surface area in high Ka flames. In other words, increasing Ka seems to "weaken" the flame. The effects of Ka on flame surface wrinkling will be discussed in details in the next chapter.

8.4.3 Discussion of the expression for S_T

It is important to explore the physical meaning of Eq. (8.10) that dictates the wrinkling of flame surface and consequentially the turbulent flame speed in Eq. (8.13). Consider the sampled flame surface area $A(\Delta)$ evaluated at T = 1800 K, i.e., inside the reaction zone. Physically it represents the overall wrinkling by all eddies larger than Δ. Now consider eddies with scales between Δ and $\Delta - \delta\Delta$. They interact with the wrinkled surface area $A(\Delta)$ and create additional surface area that is proportional to the available flame surface $A(\Delta)$ and the infinitesimal $\delta\Delta$, i.e.,

$$A(\Delta - \delta\Delta) - A(\Delta) \propto A(\Delta) \cdot \delta\Delta. \tag{8.14}$$

In addition, the wrinkling created by eddies should depend on the energy of the eddies. Hence, the wrinkling is a function of the characteristic velocity scale, or alternatively, the length scale of the eddies. Larger eddies are more energetic and are more effective at producing wrinkling than smaller eddies. Furthermore, straining and curvature effects can influence the flame surface area, which are dependent on the Karlovitz

number. In summary, surface area created by eddies with scales between Δ and $\Delta - \delta\Delta$ can be expressed as the product of the three terms as described above:

$$\delta \mathrm{A}(\Delta) \equiv \mathrm{A}(\Delta - \delta\Delta) - \mathrm{A}(\Delta) = [\mathrm{A}(\Delta) \cdot \delta\Delta] \cdot \mathcal{H}'(\Delta) \cdot g(Ka). \tag{8.15}$$

As $\delta\Delta$ approaches 0, Eq. (8.15) becomes a differential equation:

$$\frac{d\mathrm{A}(\Delta)}{d\Delta} = \mathrm{A}(\Delta) \cdot \mathcal{H}'(\Delta) \cdot g(Ka), \tag{8.16}$$

and by performing integration over Δ between $\Delta = \eta$ and $\Delta = \mathrm{L_o}$, we get

$$\int_{\mathrm{A_T}}^{\mathrm{A}(\Delta=\mathrm{L_o})} \frac{1}{\mathrm{A}} d\mathrm{A} = \int_{\eta}^{\mathrm{L_o}} \mathcal{H}'(\Delta) \cdot g(Ka) d\Delta. \tag{8.17}$$

By evaluating the integral, we get

$$\begin{aligned} \ln\left[\frac{\mathrm{A}(\Delta = \mathrm{L_o})}{\mathrm{A_T}}\right] &= [\mathcal{H}(\mathrm{L_o}) - \mathcal{H}(\eta)] \cdot g(Ka) \\ &= \left[\mathcal{F}\left(\ln(\frac{\mathrm{L_o}}{\eta})\right) - \mathcal{F}(0)\right] \cdot g(Ka) \end{aligned} \tag{8.18}$$

where $\mathcal{H}(x) = \mathcal{F}(\ln(x/\eta))$ is a simple transformation. Note that the final form of Eq. (8.18) is identical to Eq. (8.10) except that ln is used instead of $\log_{10}$. This provides a physical basis for Eq. (8.10).

Let us take a closer look at the formulation of Eq. (8.16). The term $\mathrm{A}(\Delta)$ in Eq. (8.16) is the surface area created by eddies with scales larger than Δ and its value should increase with decreasing Δ. $\mathcal{H}'(\Delta)$ in Eq. (8.16) is a measure of the effectiveness of turbulent eddies with scale Δ to create surface area. For larger Δ, the eddies are more energetic and hence $\mathcal{H}'(\Delta)$ should increase with increasing Δ. This results in two competing effects on $d\mathrm{A}(\Delta)/d\Delta$ by varying Δ. In fact, eddies that generate the maximum surface area, i.e., where $d\mathrm{A}(\Delta)/d\Delta$ is maximum, are found to have scales varying by a factor of 13 to 18 greater than the Kolmogorov scales for all cases. $g(Ka)$ is a decreasing function of Ka and accounts for surface area reduction due to strain and curvature effects.

It has been shown in Section 8.4.1 that with increasing turbulence intensities beyond $\mathrm{u_{rms}}/\mathrm{S_L} > 8$ for a fixed integral length scale, $\mathrm{S_T}$ starts to plateau. However,

when $u_{rms}/S_L = 10$ and the integral length scale is doubled, S_T increases by more than 50%. This is because increasing u_{rms} while the length scale is fixed results in two mechanisms that offset one another. On the one hand, increasing u_{rms} broadens the spectrum of turbulent eddies and thereby increases flame surface area. On the other hand, the Kolmogorov scale is reduced and hence smaller scale eddies can affect the flame surface resulting in the loss of surface area through strain and curvature effects. Hence, S_T does not change significantly beyond a certain value for turbulence intensity. When integral length scale is increased, however, both mechanisms work to increase the flame surface area by respectively broadening the spectrum of eddies that generate wrinkling and increasing the size of the Kolmogorov eddies, thereby reducing the weakening effect due to the small-scale eddies. If reaction zone thickness (δ_r) is defined as the thickness of the flame where local heat release rate is larger than 20% of its peak value, δ_r of the unstrained laminar flame following this definition is 54 μm. The plateau of S_T occurs when η/δ_r is approximately 0.2. In other words, the reduction of flame surface area due to the interaction between Kolmogorov-scale eddies and the flame becomes significant when η is less than 20% of the reaction zone thickness.

8.4.4 Wrinkling generated by large-scale eddies

The second term in Eq. (8.13), i.e., $A(\Delta = L_o)/A_L$, represents the normalized surface area generated by the integral length scale eddies. Interestingly, it is found to be approximately constant (≈ 3) for $2 < u_{rms}/S_L < 25$. This is consistent with Fig. 7.8 in the previous chapter which shows that wrinkling generated by large scale eddies are almost identical and independent of Ka or Da. However, consider the limiting case when u_{rms}/S_L approaches 0, i.e., the flame is laminar; in this case, S_T/S_L given by Eq. (8.13) should become 1. This implies that $A(\Delta = L_o)/A_L \approx 3$ would not hold true for small u_{rms}/S_L.

Table 8.2. Computational parameters and turbulence conditions employed to study wrinkling generated by large-scale eddies.

	Case 8	Case 9	Case 2a
Time of flame propagation normalized by τ	80	80	75
u_{rms} (ms^{-1})	0.075	0.151	0.753
L_o (mm)	0.64	0.64	0.27
$\eta(\mu m)$	103	61.0	13.8
u_{rms}/S_L	0.5	1.0	5.0
L_o/δ_L	6.4	6.4	2.7
Re_T	11	22	47
Da	12.8	6.40	0.54
Ka	0.14	0.40	6.8

Motivated by this observation, two additional cases with $u_{rms}/S_L = 0.5$ and 1.0 are simulated. The simulation conditions of these two cases, Cases 8 and 9, are listed in Table 8.2. Case 2a which is listed in Table 8.2 will be discussed later in this section. For Cases 8 and 9 the integral length scale is again selected as 0.64 mm and the pressure and temperature conditions are identical to the other cases. By sampling the DNS data with $\Delta = L_o$, it is found that $A(\Delta = L_o)/A_L$ is equal to 1.6 and 2.1, respectively. In the limiting case where $u_{rms}/S_L = 0$, i.e., the flame is laminar, $A(\Delta = L_o)/A_L$ should become 1. Therefore, $A(\Delta = L_o)/A_L$ is a function of the turbulence intensities for $u_{rms}/S_L < 2$ but saturates at a value of approximately 3 at larger turbulence intensities. Note that $A(\Delta = L_o)/A_L$ seems to be independent of the integral length scale itself at larger values of turbulence intensities. In other words, the effect of the integral length scale by itself on flame area enhancement is related to the effect induced by the spectrum of eddies of the turbulent cascade, i.e., the terms that are dependent on Re_T and Ka in Eq. (8.13).

It is interesting to study the influence of the computational domain on $A(\Delta = L_o)/A_L$. Note that as a result of "linear forcing", the integral length scale is always 20% of the domain size. In other words, the number of integral scale eddies is fixed on any plane perpendicular to the inflow. Naturally the question arises on whether $A(\Delta = L_o)/A_L \approx 3$ is a consequence of this specific construct. To assess this, an additional simulation (Case 2a) is performed. The simulation conditions for Case 2a are listed in Table 8.2. In this simulation, "linear forcing" is only applied to the small scale flow motions inside the unburnt mixture. This is done using Eq. (8.19) in place of Eq. (8.3):

$$F_i = M(T) B \left[\frac{k_o}{k}\right] \rho(u_i - \tilde{u}_i), \tag{8.19}$$

where $\tilde{u}_i$ is the filtered velocity. In the current study, a Gaussian filter is employed. The integral length scale of the forced turbulence using Eq. (8.19) is found to be a function of the width of the Gaussian filter employed. When filter width is equal to one third of the domain size, the resultant integral length scale of the homogeneous isotropic turbulence is 0.27 mm (equivalent to 8.4% of the domain size). With this

new forcing scheme, Case 2a is performed and $A(\Delta = L_o)/A_L$ is found to be 3.4 (again close to 3). Therefore, the conclusion that $A(\Delta = L_o)/A_L$ is approximately a constant of 3 appears not to be affected by the number of integral length scales inside the computational domain.

8.5 Summary

In the current study, a high-order numerical scheme is employed to carry out direct numerical simulations of turbulent flames propagating in lean methane/air mixtures under conditions of relevance to lean-burn natural gas engines. The pressure is selected at 20 bar, reactant temperature at 810 K, and the equivalence ratio at 0.5. A range of turbulence intensities and length scales (u_{rms}/S_L = 2-25, L_o/δ_L = 3.2-12.8) are considered. A 13-species reduced mechanism and a global mechanism are employed for the simulations.

It is shown that the global mechanism is adequate for predicting flame surface wrinkling, flame thickness and turbulent flame speed S_T compared to the reduced mechanism for normalized turbulence intensities up to 25. Furthermore, for the conditions considered, the normalized turbulent flame speeds S_T/S_L can be related to the flame area enhancement A_T/A_L resulting from turbulence interactions with the laminar flame and the efficiency factor I_o which is close to unity (1.07 $\pm$ 0.04) when evaluated at the temperature of peak heat release rate.

It is found that A_T/A_L is dependent on the turbulent Reynolds number Re_T and the Karlovitz number Ka. In particular, A_T/A_L is increased by increasing Re_T and by reducing Ka. Increasing Re_T increases the spectrum of scales that generates flame surface area. The dependence on the Ka is weaker but accounts for the change in surface area due to interaction between small-scale eddies and the flame. The wrinkling of flame surfaces generated by integral scale eddies initially increases with increasing turbulence intensities ($0 < u_{rms}/S_L < 2$) but reaches a steady value of about 3 times A_L for higher turbulence intensities ($2 < u_{rms}/S_L < 25$). The effect

of the integral length scale by itself on flame area enhancement is related to the effect induced by the spectrum of eddies of the turbulent cascade. A correlation for turbulent flame speed is proposed from the limited set of computations.

9. EFFECTS OF FLAME STRETCH ON TURBULENT PREMIXED FLAMES

9.1 Introduction

In the last two chapters, the effects of equivalence ratio (ϕ) and the effects of Karlovitz number (Ka) and turbulent Reynolds number (Re_{T}) on the turbulent flame speeds are investigated. It is observed that for flames in the thin reaction zone (TRZ) regime shown in Fig. 2.6(b), the turbulent flame speed $\mathrm{S_T}$ is primarily controlled by the generation of flame surface area through wrinkling. Furthermore, it is observed from the parametric studies in Table 8.1 that Ka influences turbulent flame surface area $\mathrm{A_T}$. More specifically, increasing Ka is found to reduce $\mathrm{A_T}$ when Re_{T} is kept constant. It is of great interest to understand the mechanism of flame surface area evolution in premixed flames in which turbulence-flame interaction plays an important role.

Consider an infinitesimal flame surface of area $\delta\mathrm{A}$ propagating in an unsteady, non-uniform flow. This flame surface is subjected to both straining by the local flow field and the curvature effects induced by the wrinkling. The fractional rate of change of the flame surface area, i.e., $\mathrm{d}(\delta\mathrm{A})/\mathrm{dt}$, can be characterized by a flame stretch rate, which was originally proposed by Karlovitz in 1953 and later generalized by Williams in 1985 [62, 236]. Flame stretch, denoted by K, is expressed as the sum of the contribution due to tangential strain rate (a_{T}) and the contribution due to curvature of the propagating surface [98, 237, 238], i.e.,

$$K \equiv \frac{1}{\delta\mathrm{A}}\frac{d(\delta\mathrm{A})}{dt} = a_{\mathrm{T}} + \mathrm{S_d}\nabla\cdot\mathbf{n}, \tag{9.1}$$

where $\mathrm{S_d}$ is the flame displacement speed and $\nabla\cdot\mathbf{n}$ is equal to twice the mean curvature κ_m. $\mathbf{n}$ is the unit vector normal to the flame surface and is defined as positive when it

points towards the unburnt gas. The transport equation for the instantaneous flame surface density Σ can be derived as [98, 238]

$$\frac{\partial \Sigma}{\partial t} + \vec{\nabla} \cdot [(\mathbf{u} + \mathrm{S_d}\mathbf{n})\Sigma] = [a_\mathrm{T} + \mathrm{S_d} \nabla \cdot \mathbf{n}]\, \Sigma, \tag{9.2}$$

where $\Sigma \equiv \delta \mathrm{A}/\delta \mathrm{V}$ is the flame surface area per unit volume. This forms the basis for the Coherent Flamelet Model (CFM) [95] and Flame Surface Density (FSD) models which can be applied to RANS [98, 239] and LES modeling [100, 103, 240].

The flame displacement speed $\mathrm{S_d}$ is defined as the speed of the flame front, defined by an iso-scalar (temperature or fuel mass fraction) surface, relative to the local convection of unburnt gas. For instance, if the flame front is defined based on fuel mass fraction $\mathrm{Y_F} = \mathrm{Y_F}^*$, flame normal is given as

$$\mathbf{n} = \vec{\nabla} \mathrm{Y_F} / \| \vec{\nabla} \mathrm{Y_F} \|, \tag{9.3}$$

and the flame displacement speed satisfies

$$\frac{d\mathrm{Y_F}}{dt}|_{\mathrm{Y_F}=\mathrm{Y_F^*}} + (\mathbf{u} + \mathrm{S_d}\mathbf{n}) \cdot \vec{\nabla} \cdot \mathrm{Y_F}|_{\mathrm{Y_F}=\mathrm{Y_F^*}} = 0. \tag{9.4}$$

Comparing Eq. (9.4) with the transport equation for the fuel in Eq. (3.4), the flame displacement speed can be derived as the sum of three components:

$$\mathrm{S_d} = \underbrace{-\frac{\dot{\omega}_\mathrm{F}}{\rho |\nabla \mathrm{Y_F}|}}_{\text{reaction}} \underbrace{-\frac{\mathbf{n} \cdot \vec{\nabla}(\rho \mathrm{D} |\nabla \mathrm{Y_F}|)}{\rho |\nabla \mathrm{Y_F}|}}_{\text{normal diffusion}} \underbrace{-\mathrm{D}(\vec{\nabla} \cdot \mathbf{n})}_{\text{tangential diffusion}} \tag{9.5}$$

The first component is due to the consumption of fuel by chemical reaction, and the second and the third components are due to normal and tangential diffusion, respectively. The density-weighted flame displacement speed $\mathrm{S_d^*}$ given by

$$\mathrm{S_d^*} = \frac{\rho|}{\rho_u} \mathrm{S_d}, \tag{9.6}$$

is often used to compare the displacement speed with the unstrained laminar flame speed $\mathrm{S_L}$. Note that for a steady unstrained flame, the density-weighted flame displacement speed is identical to the laminar flame speed everywhere inside the flame.

For weakly strained flames, i.e., when K is small, asymptotic studies [211, 241] show that S_d^* is linearly proportional to flame stretch:

$$\frac{S_d^*}{S_L} = 1 - \frac{K\mathcal{L}}{S_L}, \tag{9.7}$$

where $\mathcal{L}$ represents the Markstein length. However, for turbulent flames characterized in the TRZ combustion regime, the flame stretch generally exceeds the limit where the linear relationship of Eq. (9.7) is valid. This is partly because flame stretch due to the propagation of curved surface, i.e., $S_d \vec{\nabla} \cdot \mathbf{n}$ consists of a term proportional to the square of the mean curvature. This introduces non-linearity if the local flame surface is highly curved. In addition, due to the unsteadiness associated with turbulent flames, it is possible that the local flame displacement speed exhibits different sensitivity to the flame stretch than it would in a steady flame.

There has been some recent work on flame stretch and flame displacement speed for flames in the TRZ regime. Echekki and Chen (1999) observed that flame displacement speed decreases with increasing mean curvature [242]. Chen and Im (1998) performed 2D DNS to determine the correlation of the flame speed with the flame stretch [243]. They found two distinct branches in the correlation. Similar observations were made by Chakraborty *et al.* (2007) who studied the effects of K on flame propagation of premixed flame kernels [244]. Han and Huh (2008) studied the effects of turbulence intensities and Lewis number on the flame surface density evolution [245]. They found the propagation term to decrease with increasing turbulence intensity. Chakraborty *et al.* (2008) compared the effects of strain rate and curvature on FSD transport in CH_4-air and H_2-air flames [246]. In methane flames, the propagation term is found to correlate negatively with κ_m towards the reactant side but positively with κ_m towards the product side. In hydrogen flames, the propagation term is negatively correlated with κ_m throughout the flame brush.

In this chapter, results from DNS of the premixed CH_4-air flames listed in Table 8.1 will be analyzed with an emphasis on understanding the coupling among flame curvature κ_m, tangential strain a_T, displacement speed S_d and stretch rates K. The physical conditions employed in the DNS are applicable to lean-burn natural gas

engines. The pressure and unburnt temperature are chosen to be 20 bar and 810 K, respectively. The premixed equivalence ratio is 0.5. Normalized turbulence intensities u_{rms}/S_L range from 2 to 25. The integral length scale is fixed at 0.64 mm, i.e., 6.4 times the laminar flame thickness in Cases 1-7. Cases 4a and 4b are selected where L_o/δ_L is changed to 3.2 and 12.8, respectively. The Damköhler numbers corresponding to these cases range from 3.20 to 0.26 while the Karlovitz numbers range from 1.1 to 49.4. The main objective is to provide interpretations for the dependence of flame surface area on Karlovitz number as discussed in the previous chapter. In addition, modeling implications for the FSD transport equation in the context of Reynolds-Averaged Navier-Stokes (RANS) simulations will be discussed.

In Section 9.2, a discussion of the flame surface curvatures and shape factors is presented. Section 9.3 discusses the tangential and normal strain rates on the flame surface. Alignment of the flame surface normal with the principal strain rates is also analyzed. Section 9.4 presents the discussion of flame displacement speeds on the flame surface. The correlation between the flame displacement speed and curvature is also examined in this section. In Section 9.5, flame stretch on the flame surface and its correlation with curvature and flame displacement speed is discussed. Section 9.6 discusses a potential way to incorporate the physical insights into the modeling of FSD equation in the context of RANS simulations. Section 9.7 provides a summary of the key observations.

9.2 Curvature on the Turbulent Flame Surface

Characterizations of tangential strain rate a_T, curvature $\overrightarrow{\nabla} \cdot \mathbf{n}$ and displacement speed S_d are carried out on the progress variable isosurface c = 0.8 corresponding to the reaction zone in the laminar profile. The progress variable is defined as c = 1 - $Y_{CH_4}/Y_{u,CH_4}$ where Y_{u,CH_4} is the mass fraction of methane in the unburnt mixture. The choice of the isosurface follows the recommendation by Giannakopoulos *et al.* (2015) [247], who have shown that the flame displacement speed at an isotherm

surface close to the burned side is less dependent on the selected iso-value and hence well-conditioned. The distribution of the variables on the flame surface is first examined. Figure 9.1(a) shows the probability density function (pdf) of local curvature normalized by the laminar flame thickness δ_{L} for all flames. Evidently, the distribution of curvature spreads out with increasing Karlovitz number, i.e., it is more probable to find highly curved surface in high Ka flames. This is because as Ka increases, the Kolmogorov scale of turbulence is reduced and hence large local curvatures can be generated. In addition, the distribution of curvature on the flame surface becomes increasingly skewed towards the negative side with increasing Ka, as evident by the shift of the peak. This can be explained using the contour plot of temperature and flow vorticity shown in Fig. 9.2. Due to heat release in the reaction zone, the molecular viscosity increases by approximately 6-fold cross the reaction zone. Consequently the turbulent Reynolds number decreases and the Kolmogorov length scale increases. On average there are more small scale eddies ahead of the flame than behind. This, in turn, causes the flame front to be more concave towards the unburnt mixture, corresponding to a positive skewness in the curvature distribution. The higher the Karlovitz number, the more the number of small scale eddies in the unburnt side and the more skewed the pdf becomes.

It is interesting to study how turbulence affects flame surface topology. We introduce the shape factor, defined as the ratio of the principal curvature with the smaller magnitude to the one with the larger magnitude. The definition is expressed as follows:

$$\text{shapefactor} = \begin{cases} \kappa_1/\kappa_2, & \text{if } |\kappa_1| < |\kappa_2|; \\ \kappa_2/\kappa_1, & \text{if } |\kappa_1| \geq |\kappa_1|. \end{cases} \tag{9.8}$$

By construction, shape factor is bounded between -1 and 1. At the same time, the sign of shape factor preserves information about surface topology. If the shape factor is close to 0, the local topology is similar to that of a cylindrical surface; if the shape factor is close to 1, the local topology is similar to that of a spherical surface and finally if the shape factor is close to -1, the local topology is similar to that on a

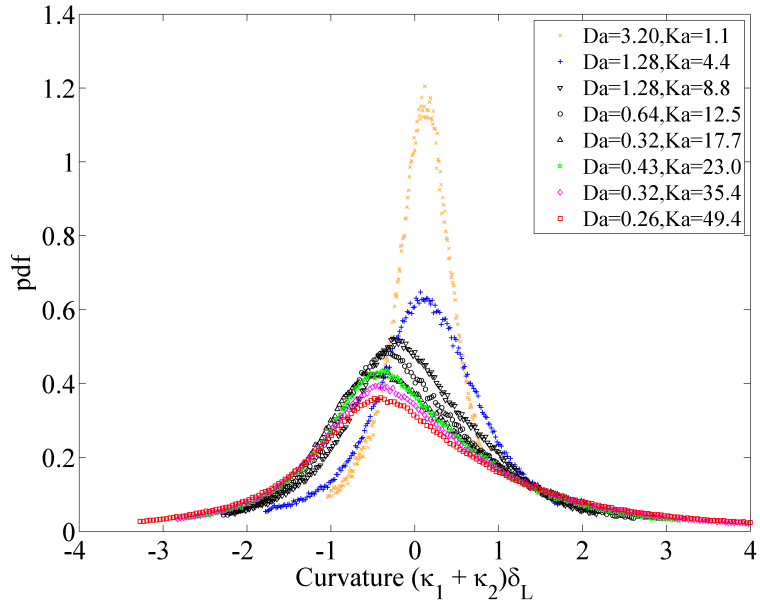

(a)

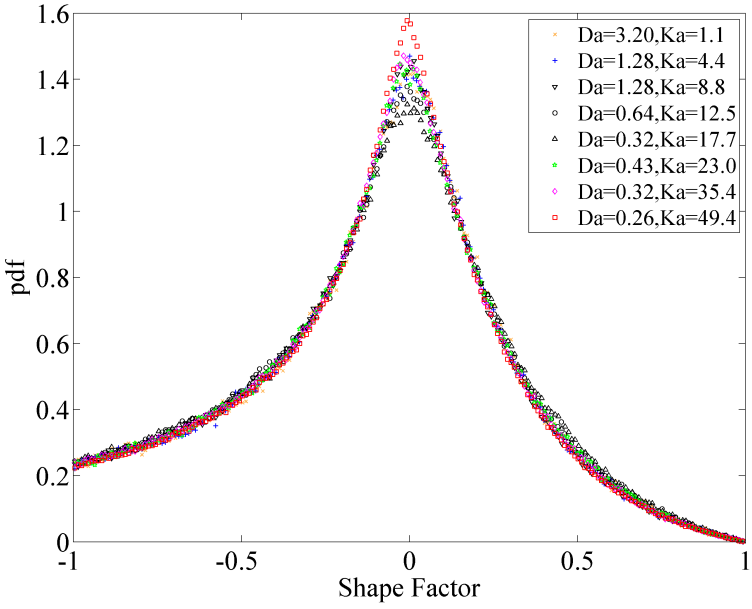

(b)

Figure 9.1. Probability density function of (a) the sum of two principal curvatures ($\kappa_1 + \kappa_2$) normalized by the laminar flame thickness δ_L and (b) shape factor on the c = 0.8 isosurface.

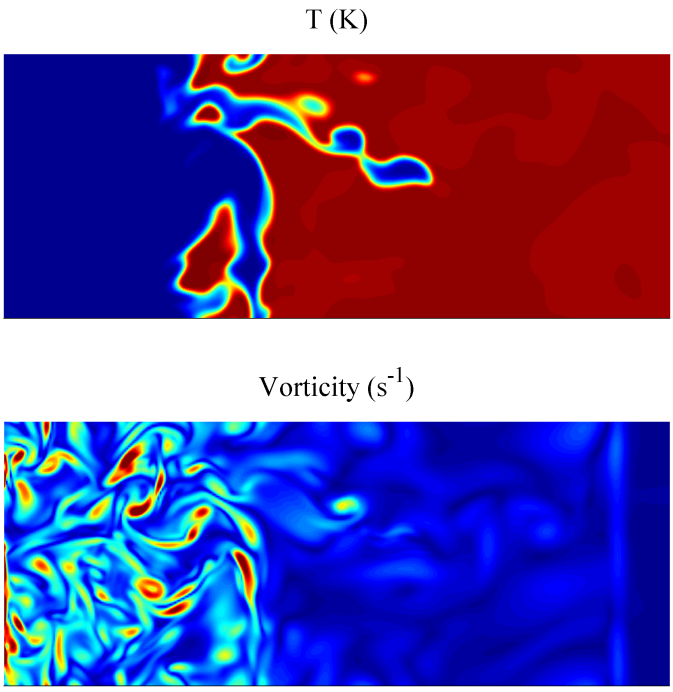

Figure 9.2. Contour plot of temperature and vorticity magnitude on a 2D x-y cut plane for Case 2: $Da = 1.28$, $Ka = 4.4$.

saddle surface. The principal curvatures κ_1 and κ_2 represent the maximum and the minimum values of the curvature at a given point. For a surface $\mathcal{S} = \{x|\phi(x) = \phi^*\}$, κ_1 and κ_2 are the roots of quadratic equation:

$$x^2 - 2\mathcal{H}x + \mathcal{K} = 0, \tag{9.9}$$

where $\mathcal{H}$ is the mean curvature given by

$$\begin{aligned}\mathcal{H} = &[\phi_x^2(\phi_{yy} + \phi_{zz}) + \phi_y^2(\phi_{xx} + \phi_{zz}) + \phi_z^2(\phi_{xx} + \phi_{yy}) - 2\phi_x\phi_y\phi_{xy} \\ &- 2\phi_x\phi_z\phi_{xz} - 2\phi_y\phi_z\phi_{yz}]/2(\phi_x^2 + \phi_y^2 + \phi_z^2)^{\frac{3}{2}},\end{aligned} \tag{9.10}$$

and $\mathcal{K}$ is the Gaussian curvature given by

$$\begin{aligned}\mathcal{K} = &[\phi_z^2(\phi_{xx}\phi_{yy} - \phi_{xy}^2) + \phi_y^2(\phi_{xx}\phi_{zz} - \phi_{xz}^2) + \phi_x^2(\phi_{yy}\phi_{zz} - \phi_{yz}^2) + 2\phi_x\phi_y(\phi_{xz}\phi_{yz} - \phi_{xy}\phi_{zz}) \\ &+ 2\phi_x\phi_z(\phi_{xy}\phi_{yz} - \phi_{xz}\phi_{yy}) + 2\phi_y\phi_z(\phi_{xy}\phi_{xz} - \phi_{yz}\phi_{xx})]/(\phi_x^2 + \phi_y^2 + \phi_z^2)^2\end{aligned} \tag{9.11}$$

Figure 9.1(b) shows the distribution of shape factor for flames over a range of Karlovitz number. It is evident that neither turbulence intensities nor Ka affects

the distribution of flame topologies on the surface. In addition, cylindrical shapes, corresponding to shape factor ~ 0, are the most probable topology, followed by saddle-like shapes (shape factor $\sim$ -1) and lastly spherical shapes (shape factor ~ 1).

9.3 Tangential and Normal Strain Rates on the Turbulent Flame Surface

Tangential strain rate a_{T} is given by Eq. (9.12) as the difference between the dilatation term $\overrightarrow{\nabla} \cdot \mathbf{u}$ and the normal strain rate $a_{\mathrm{N}} = \mathbf{n} \cdot \mathbf{S} \cdot \mathbf{n}$, i.e.,

$$a_{\mathrm{T}} = \overrightarrow{\nabla} \cdot \mathbf{u} - \mathbf{n} \cdot \mathbf{S} \cdot \mathbf{n} = (\delta_{ij} - n_i n_j)\mathrm{S}_{ij}, \tag{9.12}$$

where $\mathbf{S}$ represents the strain rate tensor given by

$$\mathrm{S_{ij}} = \frac{1}{2}\left(\frac{u_i}{x_j} + \frac{\partial u_j}{\partial x_i}\right). \tag{9.13}$$

The distribution of tangential strain rate on the flame surface is plotted in Fig. 9.3. As turbulence intensities increase and as the integral length scale decreases, the pdf becomes flatter. For flames with high Ka, even compressive tangential strain rate could be present in some locations. The surface mean of a_{T} also appears to grow when $\mathrm{u_{rms}}$ is increased or when $\mathrm{L_o}$ is decreased. This can be explained because tangential strain a_{T} is of the order $\mathcal{O}(\mathrm{u_{rms}/L_o})$ [248]. The overall effect of tangential strain rate is to generate flame surface area and this effect is promoted as Ka increases, i.e., Da decreases.

It is interesting to study the effects of turbulence intensities and length scales on the normal strain rate a_{N} where $a_{\mathrm{N}} = \mathbf{n} \cdot \mathbf{S} \cdot \mathbf{n}$. This would provide insight on whether turbulence creates or destroys passive scalar gradients. In the case that a_{N} is less than zero, the isosurfaces of progress variable are packed closer together and thereby facilitating steeper scalar gradients. On the other hand, when a_{N} is larger than zero, scalar gradients are reduced when interacting with turbulence. Chakraborty and Swaminathan (2007) performed DNS of premixed flames and observed that turbulence destroys scalar gradients in flames [217]. A similar trend was observed in experimental studies using simultaneous PIV/OH-PLIF by Hartung *et al.* (2008) [249]. On the

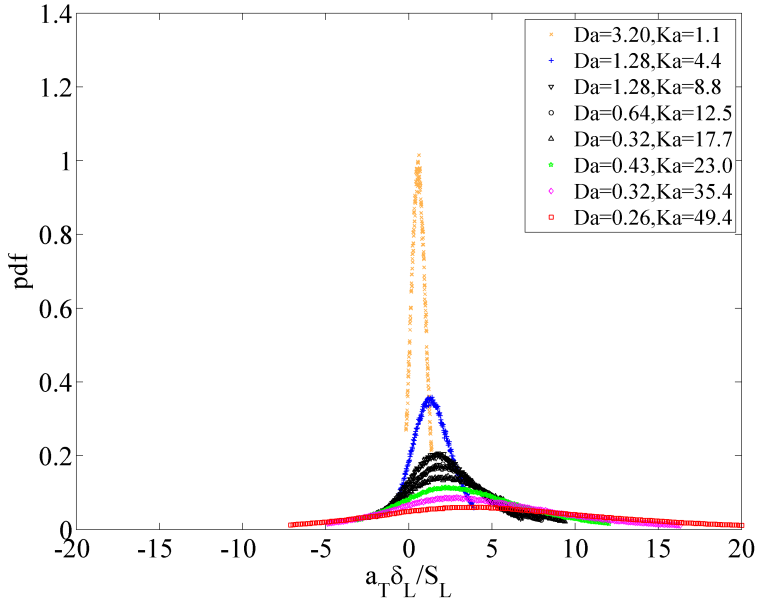

Figure 9.3. Probability density function of tangential strain rate a_{T} normalized with flame time scale $\delta_{\mathrm{L}}/\mathrm{S}_{\mathrm{L}}$ on the c = 0.8 isosurface.

other hand, PIV measurements of premixed Bunsen flames and V-flames [218, 219] report that turbulence produces steeper scalar gradients.

One way to study the normal strain rate is by examining the eigenvalues and the eigenvectors of the strain rate tensor $\mathbf{S}$. Since $\mathbf{S}$ is a real symmetric 3 by 3 matrix, the eigenvalues of $\mathbf{S}$ are real. Without the loss of generality, assume λ_1, λ_2 and λ_3 are the eigenvalues of $\mathbf{S}$ with $\lambda_1 \geq \lambda_2 \geq \lambda_3$, and $\xi_{\mathbf{1}}$, $\xi_{\mathbf{2}}$ and $\xi_{\mathbf{3}}$ are the corresponding unit eigenvectors. Note that $\xi_{\mathbf{1}}$, $\xi_{\mathbf{2}}$ and $\xi_{\mathbf{3}}$ are mutually orthogonal to each other and form the basis for $\mathbb{R}^3$. The surface normal can be written as the linear combination of the eigenvectors:

$$\mathbf{n} = \cos\theta_1 \xi_{\mathbf{1}} + \cos\theta_2 \xi_{\mathbf{2}} + \cos\theta_3 \xi_{\mathbf{3}}, \tag{9.14}$$

where

$$\cos\theta_i = \mathbf{n} \cdot \xi_{\mathbf{i}}. \tag{9.15}$$

Table 9.1. Normalized normal strain rate for flames over a range of Da and Ka.

	Case 1	Case 2	Case 4a	Case 4	Case 4b	Case 5	Case 6	Case 7
u_{rms}/S_L	2.0	5.0	10.0	10.0	10.0	15.0	20.0	25.0
L_o/δ_L	6.4	6.4	12.8	6.4	3.2	6.4	6.4	6.4
Da	3.20	1.28	1.28	0.64	0.32	0.43	0.32	0.26
Ka	1.1	4.4	8.8	12.5	17.7	23.0	35.4	49.4
$\langle\lambda_1\tau_f\rangle_s$	0.83	2.02	3.67	4.22	4.99	6.52	8.70	12.03
$\langle\lambda_2\tau_f\rangle_s$	0.14	0.13	0.16	0.21	0.24	0.27	0.36	0.46
$\langle\lambda_3\tau_f\rangle_s$	-0.60	-1.81	-3.52	-4.05	-4.84	-6.44	-8.66	-12.14
$\langle a_N\tau_f\rangle_s$	0.192	-0.84	-1.77	-2.02	-2.42	-3.27	-4.40	-6.21
$\langle a_T\tau_f\rangle_s$	0.178	1.18	2.08	2.40	2.80	3.63	4.81	6.56

The normal strain rate can then be written as

$$\begin{aligned} a_N &= [\cos\theta_1\boldsymbol{\xi_1} + \cos\theta_2\boldsymbol{\xi_2} + \cos\theta_3\boldsymbol{\xi_3}]^T \cdot \mathbf{S} \cdot [\cos\theta_1\boldsymbol{\xi_1} + \cos\theta_2\boldsymbol{\xi_2} + \cos\theta_3\boldsymbol{\xi_3}] \\ &= \cos^2\theta_1\lambda_1 + \cos^2\theta_2\lambda_2 + \cos^2\theta_3\lambda_3. \end{aligned} \tag{9.16}$$

Here, λ_1, λ_2 and λ_3 are termed the most extensive, intermediate and the most compressive principal strain rates, respectively. θ_1, θ_2 and θ_3 represent the angles between the strain rate directions, i.e., $\boldsymbol{\xi_1}$, $\boldsymbol{\xi_2}$ and $\boldsymbol{\xi_3}$, and the surface normal direction $\mathbf{n}$, respectively. The normal strain rate in Eq. (9.16) can be interpreted as the weighted-average of the principal strain rates where the weights are given by $\cos^2\theta_i$, representing the alignments between the principal strain rate directions and the surface normal.

Table 9.1 tabulates the surface average of the most extensive, intermediate and the most compressive principal strain rates normalized by the flame timescale $\tau_f = \delta_L/S_L$ for flames over a range of Ka and Da. It can be seen that the intermediate principal strain rates on average remain close to zero. The most extensive strain rates and the most compressive strain rates carry different signs with similar magnitudes. If

the flame surface normal is not preferentially aligned with any of the principal strain rate directions, the weights, i.e., $\cos^2\theta_i$ in Eq. (9.16), would be similar for all three strain rates and consequently the surface average of a_{N} would be approximately zero, suggesting that turbulence has no net influence on the scalar field gradients. Figures 9.4(a) and 9.4(b) illustrate the respective alignment of $\boldsymbol{\xi_1}$ and $\boldsymbol{\xi_3}$ with flame surface normal for a range of Ka and Da. Evidently, for flames with larger Ka ($Ka \geq 4$), the most extensive strain rates do not show any preferential alignment with the surface normal. On the other hand, the most compressive strain rates are preferentially parallel to the surface normal, i.e., $\cos\theta_3 = 1$, when Ka is large. As a result, the negative compressive strain rates λ_3 are more heavily weighted in Eq. (9.16) which causes the a_{N} to be negative in high Ka flames. Physically, this suggests that the isosurfaces of progress variable are packed closer together and thus steeper scalar gradients are produced by turbulence-flame interactions. This finding is consistent with the computed surface averages of normalized a_{N} listed in Table 9.1. The normal strains rates are on average compressive. Furthermore, their magnitudes increase as $\mathrm{u_{rms}}/\mathrm{S_L}$ is increased or when $\mathrm{L_o}/\delta_{\mathrm{L}}$ is decreased. This is because the most compressive strain rate λ_3 is increased by increasing turbulence intensities or reducing turbulence length scales as evident in Table 9.1.

An alternative way to explain the trend of a_{N} in Table 9.1 is by invoking scaling analysis. Consider a 1-D flat laminar flame. The velocity of reactants approaching the flame front is the laminar flame speed $\mathrm{S_L}$ while the velocity of burnt products leaving the flame front is $\mathrm{S_L}\rho_u/\rho_b$ (or alternatively $\mathrm{S_L T}_b/\mathrm{T}_u$) to preserve mass conservation. The change in velocity occurs over the length scale of laminar flame thickness and hence the mean dilation inside the flame $\langle\vec{\nabla}\cdot\mathbf{u}\rangle \sim (\mathrm{T}_b/\mathrm{T}_u - 1)\mathrm{S_L}/\delta_{\mathrm{L}}$. Similarly, the mean dilatation on the turbulent flame front can be estimated by $(\mathrm{T}_b/\mathrm{T}_u - 1)\mathrm{S_L}/\delta_{\mathrm{L}}$. This approximation remains valid as long as the mean flame thickness and the mean consumption rate on the flame surface do not deviate much from their values in the laminar baseline; that they do not is supported by Figs. 8.3(a), 8.3(b), 8.5(a) and

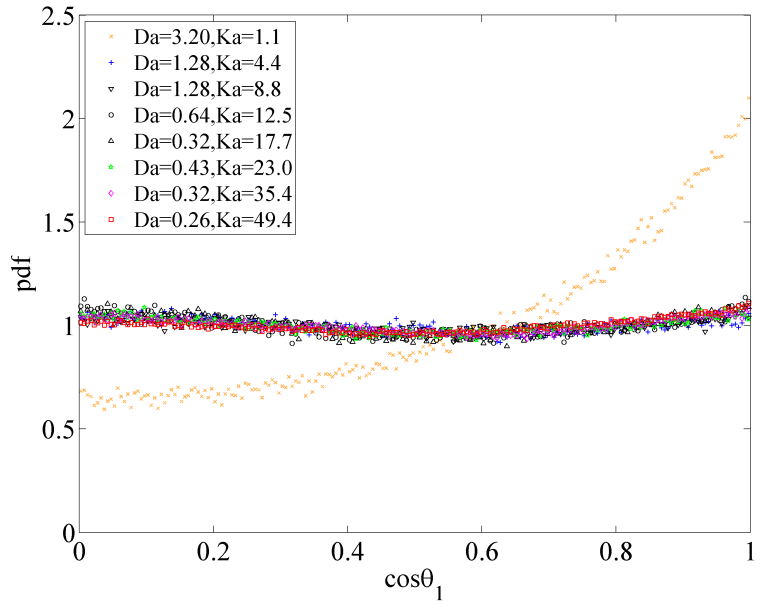

(a)

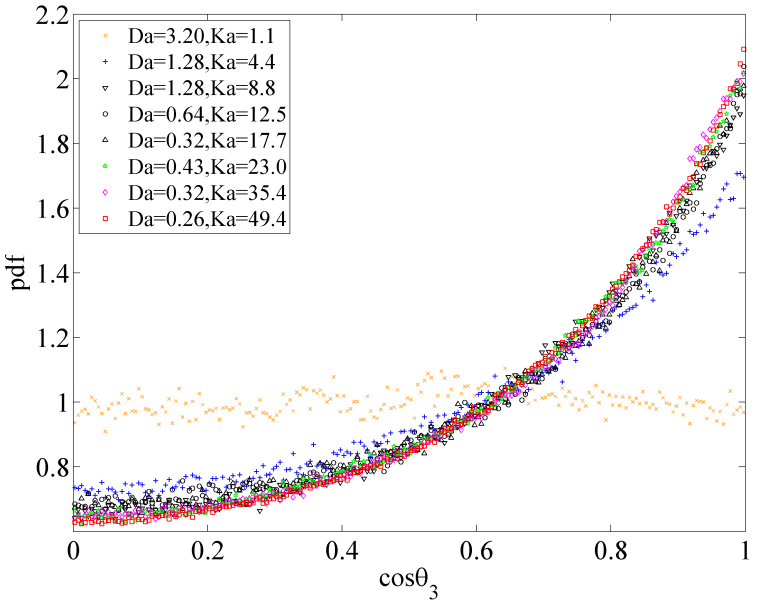

(b)

Figure 9.4. Probability density function of the alignment of the flamelet normal direction with (a) the most extensive strain rate direction and (b) the most compressive strain rate direction.

8.5(b) in Chapter 8. On the other hand, tangential strain rate scales on the order of $\mathcal{O}(\mathrm{u_{rms}/L_o})$ [248].

The ratio of tangential strain rate to the dilatation in turbulent flames can be estimated as

$$\frac{a_\mathrm{T}}{\langle \vec{\nabla} \cdot \mathbf{u} \rangle} \sim \mathcal{O}\left(\frac{\mathrm{u_{rms}}}{\mathrm{L_o}} \frac{\delta_\mathrm{L}}{\mathrm{S_L}} \frac{\mathrm{T}_u}{\mathrm{T}_b - \mathrm{T}_u} \right) \sim \mathcal{O}\left(\frac{\mathrm{T}_u}{\mathrm{T}_b - \mathrm{T}_u} Da \right). \tag{9.17}$$

Comparing Eq. (9.17) and (9.12), the following relation can be derived:

$$\frac{a_\mathrm{N}}{\langle \vec{\nabla} \cdot \mathbf{u} \rangle} \sim 1 - \mathcal{O}\left(\frac{\mathrm{T}_u}{\mathrm{T}_b - \mathrm{T}_u} Da \right). \tag{9.18}$$

Equation (9.18) signifies that if $Da < (\mathrm{T}_b - \mathrm{T}_u)/\mathrm{T}_u$ which equals to 1.35 for the cases considered in Table 9.1, the normal strain rates will be negative. This is consistent with Fig. 9.4(b) which shows that the most compressive strain rates are preferentially parallel with the flamelet normal (and hence negative a_N) for Cases with $Da \leq 1.28$. Note that Eqs. (9.17) and (9.18) appear to suggest that both tangential and normal strain rates are linearly dependent on the Damköhler number. However, comparing Cases 2 and 4(a) where Da have the same value of 1.28, the surface mean a_N and a_T differ by 71% and 55%, respectively. Comparing Cases 6 and 4(b) where $Da = 0.32$, the surface mean a_N and a_T are different by 58% and 53%, respectively. It suggests that Da does not characterize the tangential and normal strain rates very well. In fact, when a_N and a_T are plotted as a function of the Karlovitz number Ka in Fig. 9.5, a linear trend is observed. This suggests that the normal and tangential strain rates are linearly correlated with Ka rather than Da for high Ka flames. Note that Damköhler number involves the eddy turnover time whereas Karlovitz number involves the Kolmogorov timescale. Figure 9.5 indicates that the straining experienced by the infinitesimal flame surface is dictated by the small scale motion. This is expected for flames in the TRZ where Kolmogorov scale eddies are small enough to penetrate the preheat zone. These small eddies enhance mixing between the unburned and burned mixture, generating wrinkling on the scale of η. Straining experienced locally by the infinitesimal surface should also scale with the smallest eddy timescale.

Lines of best-fit are plotted in Fig. 9.5 for the surface-averaged a_{N} and a_{T}. Gradients of these line are computed to be -0.114 and 0.114, respectively. The sum of a_{N} and a_{T} yields the dilatation which is constant on a given iso-c surface, as expected.

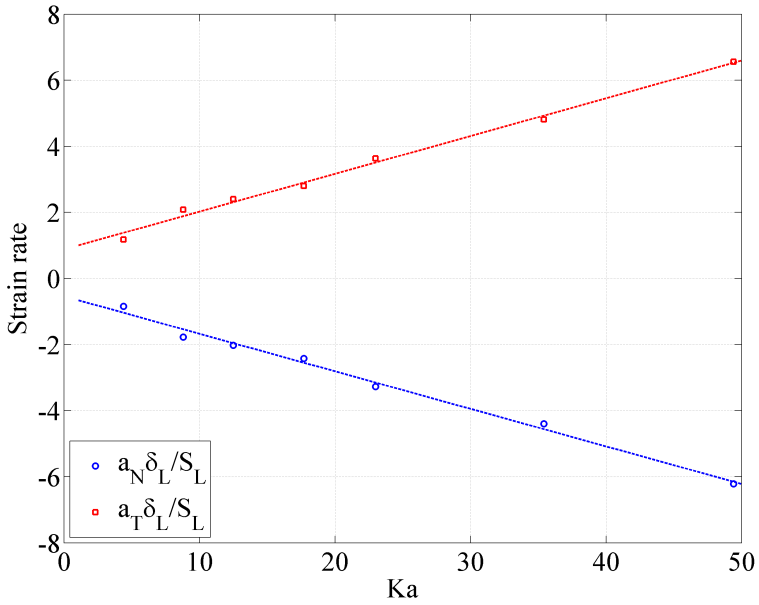

Figure 9.5. Surface averaged normal and tangential strain rates as a function of flame Karlovitz number Ka.

Figure 9.6 shows the conditional mean of normalized tangential strain rate as a function of flame curvature $\mathbf{H}$ normalized by the laminar flame thickness. For low Ka and high Da flames, the tangential strain rate is found to be negatively correlated with curvature. For flames with relatively larger Ka, a_{T} is negatively correlated with curvature on positively curved surfaces but becomes positively correlated with curvature when $\mathbf{H}\delta_{\mathrm{L}} <$ -0.5. This is consistent with prior DNS work [246, 250, 251] and experiment study [252]. A direct implication of Fig. 9.6 is that, the most extensive tangential strain rate is approximately associated with surfaces having no net curvatures in high Ka flames.

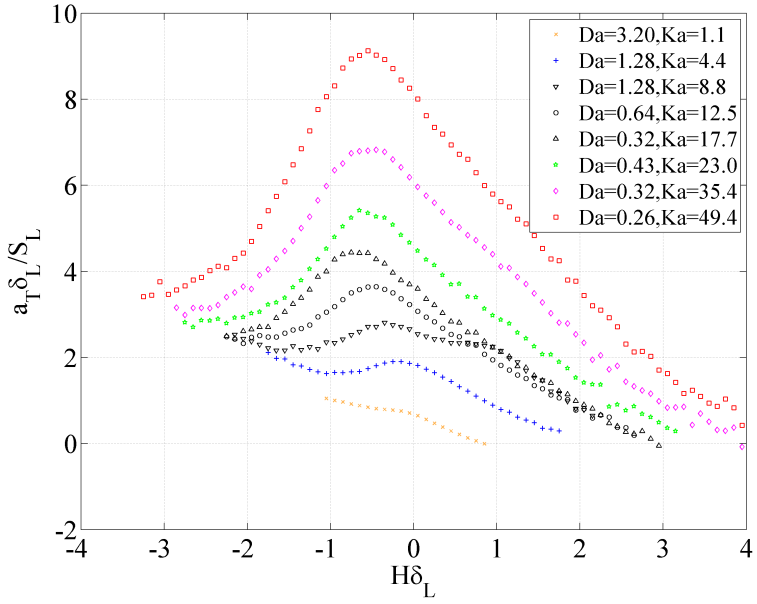

Figure 9.6. Conditional mean of normalized tangential strain rate a_T as a function of total curvature **H** normalized by laminar flame thickness.

9.4 Flame Displacement Speeds on the Turbulent Flame Surface

Flame displacement speed S_d is a measurement of the propagation speed of the iso-surface relative to its coincidental material surface in the direction normal to the material surface. It is a quantity local in both space and time. Flame displacement speed consists of three contributions as shown in Eq. (9.5). Hereafter, S_r, S_n and S_t will be used to denote the reaction, normal diffusion and tangential diffusion contributions to the flame displacement speed, respectively. In addition, S_r^*, S_n^*, S_t^* and S_d^* will represent the respective density-weighted quantity so that it can be easily compared with the laminar flame speed. Figure 9.7 presents the distribution of the density-weighted S_d, i.e., S_d^*, normalized by the laminar flame speed for flames over a range of *Da* and *Ka*. Generally with increasing *Ka*, the pdf becomes flatter, indicating that a wider range of displacement speeds are present locally on the flame surface. The peak of the pdf corresponding to the most probable S_d on the flame surface is found to be between 0.60 and 0.85 for the flames considered in this study. No clear

dependencies of the most probable S_d on Da or Ka are present. In addition, the pdf of S_d illustrates a positive skewness. This is evident by the long tail of S_d towards large positive values. This positive skewness will be explained in the next section, i.e., Section 9.4.

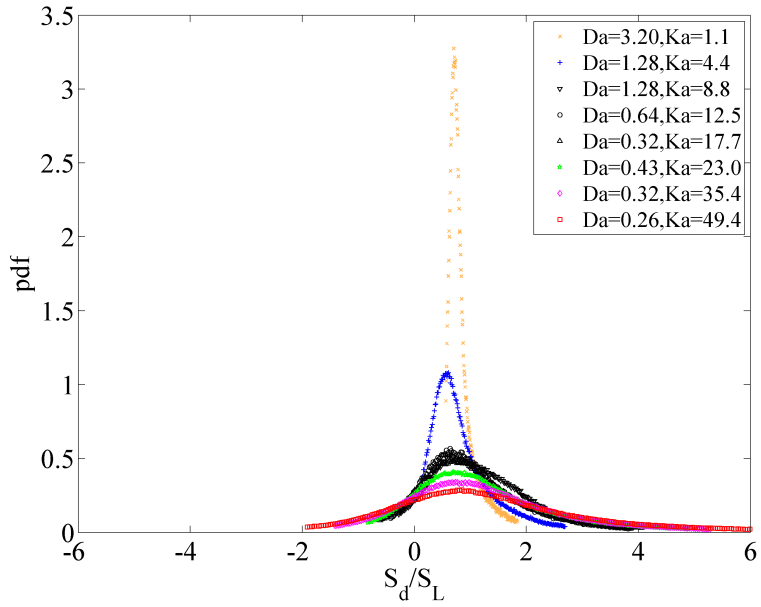

Figure 9.7. Probability density function of density-weighted flame displacement speeds on the c = 0.8 isosurface.

The effects of curvature on the flame displacement speeds are studied next. Figure 9.8(a) shows the mean density-weighted displacement speeds due to reaction and normal diffusion conditioned on the local curvature $\mathbf{H}$ where $\mathbf{H}$ is twice as the mean curvature κ_m. Note that in a flat unstrained laminar flame, the sum of S_r^* and S_n^* is equivalent to S_L while S_t is universally zero. It is evident in Figure 9.8(a) that $S_r + S_n$ exhibits a negative correlation with curvature when $\mathbf{H} < 0$ and a positive correlation with curvature when $\mathbf{H} > 0$. In other words, the displacement speeds due to reaction and normal diffusion are increased at curved surfaces, irrespective of whether the surface is concave ($\mathbf{H} < 0$) or convex ($\mathbf{H} > 0$) towards the reactants. Furthermore, it is noted that the negative branch and the positive branch of $S_r + S_n$ exhibit distinct gradients with respect to curvature. More specifically, the increment

in the displacement speed brought about by increasing the curvature magnitude is greater on concave surfaces than on convex surfaces. This can be explained as follows: When the flame surface is concave towards the reactants, there is a focusing of thermal diffusion from the product side to the c = 0.8 isosurface while there is defocusing of species diffusion from the reactants to the c = 0.8 isosurface. Since methane has a Lewis number less than air, it diffuses into the c = 0.8 isosurface faster than the other species, making the mixture locally richer. This effect offsets the defocusing of reactants due to the negative curvature. Consequently, reaction is enhanced in negatively curved regions. On the other hand, when the flame surface is convex towards the reactants, there is defocusing of thermal diffusion and focusing of species diffusion. This results in a higher concentration of reacting species despite a lower temperature. The preferential diffusion of methane also makes the mixture locally richer. This results in enhanced reaction on positively curved surfaces. Another reason that $S_r + S_n$ has a minima at $\mathbf{H} \approx 0$ is because the most extensive tangential strain rate is associated with local curvature close to zero as evident in Fig. 9.6. The normal strain rate, on the other hand, becomes the most compressive on average when $\mathbf{H} \approx 0$. Consequently, the highest normal diffusion, i.e., the most negative S_n is correlated with zero curvature, and hence the minima of $S_r + S_n$ at $\mathbf{H} \approx 0$.

Figure 9.8(b) shows the conditional mean of displacement speed due to tangential diffusion, i.e., S_t as a function of curvature $\mathbf{H}$. S_t decreases linearly with increasing curvature and this is expected from Eq. (9.5). Figure 9.8(c) shows the conditional mean of flame displacement speed S_d as a function of curvature. Overall, S_d is negatively correlated with flame curvature. When the flame surface is concave towards the reactants, both tangential diffusion and the net effect of reaction and normal diffusion contributes positively to S_d, resulting in accelerated flame propagation into the unburnt region. On the other hand, when the flame surface is highly convex towards the reactants ($\kappa_m \delta_{\mathbf{L}} > 1$), tangential diffusion of CH_4 dominates the normal diffusion and reaction, causing the flame to retract. Furthermore, it is evident that the conditional mean of S_d as a function of surface curvature is only weakly dependent on the

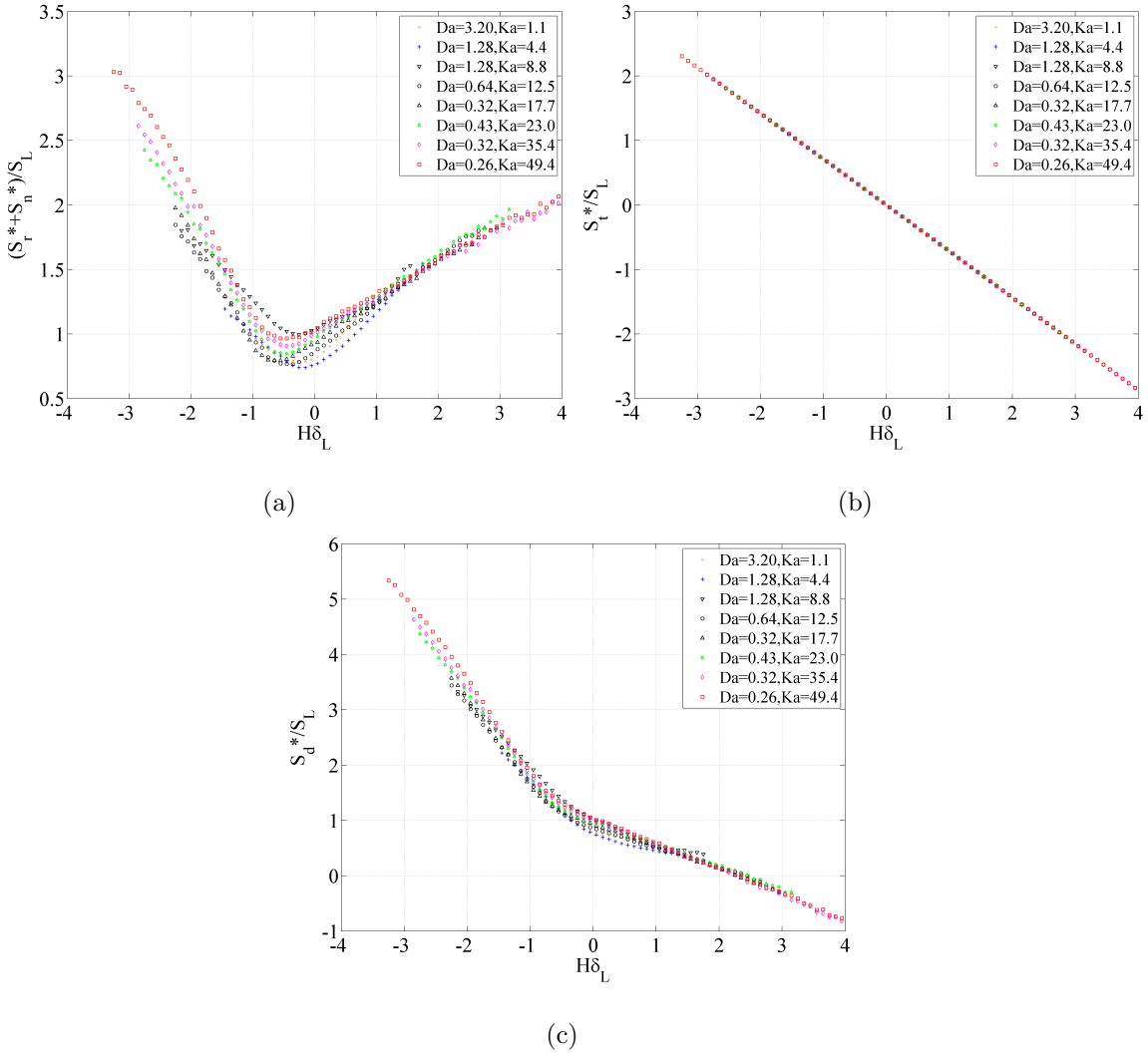

Figure 9.8. Conditional mean of (a) displacement speeds due to reaction and normal diffusion, i.e., $S_r^* + S_n^*$; (b) displacement speeds due to tangential diffusion, i.e., S_t^* and (c) flame displacement speed S_t^* as a function of total curvature **H** normalized by laminar flame thickness.

Damköhler or Karlovitz number. This indicates that the sole effect of Ka or Da on the flame displacement speed can be modeled through its influence on the curvature distribution on the flame surface, at least over the range of turbulence conditions considered in this study.

It is also interesting to observe from Fig. 9.8(c) that S_d is approximately unity within 20% when $\mathbf{H} \approx 0$. Notice that $\mathbf{H} = \kappa_1 + \kappa_2 = 0$ indicates that the two principal curvatures κ_1 and κ_2 have equal magnitude but opposite signs. This corresponds to the saddle shape with a shape factor of -1. In other words, the flame displacement speed on a saddle-like surface is similar to the flame displacement speed on a flat flame. For a flame surface in $\mathbb{R}^3$, the surface topology can be uniquely characterized by two parameters. Examples of these pairs of parameters include (κ_1, κ_2) and ($\mathbf{H}$, $\mathbf{G}$). This brings up the question whether the influence of surface topology on the displacement speed can be accounted for by using a single parameter such as the mean curvature $\kappa_m = (\kappa_1 + \kappa_2)/2$ without invoking the second degree of freedom, for instance one that is described by the shape factor or the Gaussian curvature. The analysis presented above shows that for saddle surfaces, the averaged effects of surface topology on Sd can be approximated using κ_m alone. Analysis on the cylindrical and spherical shapes will be presented next.

Figure 9.9(a) shows the conditional mean of S_d on the cylindrical surfaces alone, i.e., with a shape factor equal to 0, as a function of surface curvatures $\mathbf{H}$. In the analysis, the cylindrical surfaces are selected by isolating surfaces with a shape factor between -0.1 and 0.1, that is, the larger principal curvature is at least 10 times the smaller principal curvature. The flame displacement speeds on the cylindrical surfaces are negatively correlated with surface curvature. Furthermore, the mean S_d on the cylindrical surfaces in Fig. 9.9(a) agrees within 5% with mean Sd of all surface topologies shown in Fig. 9.8(c) when it is conditioned on the total curvature $\mathbf{H}$. Figure 9.9(b) shows the conditional mean of S_d as a function of surface curvatures $\mathbf{H}$ when considering only the spherical surfaces. The analysis is carried out on surfaces with a shape factor greater than 0.8. Again, it is evident that the conditional mean S_d on

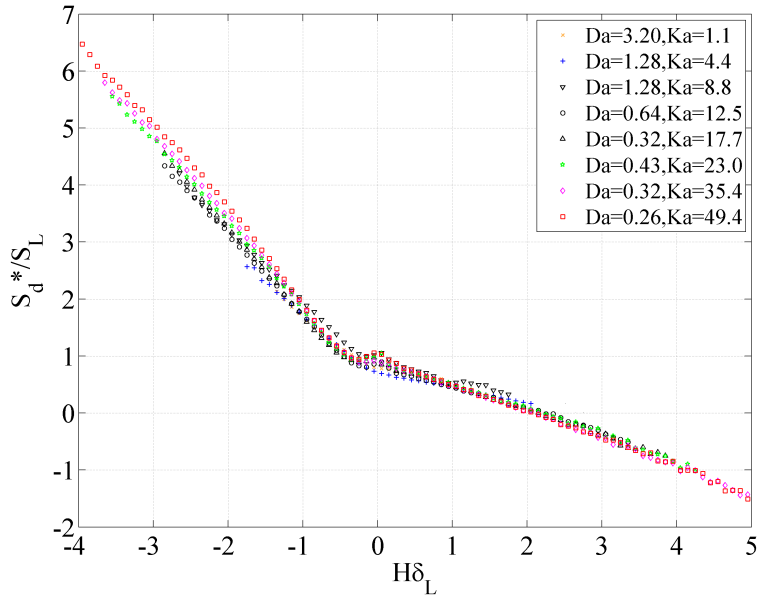

(a)

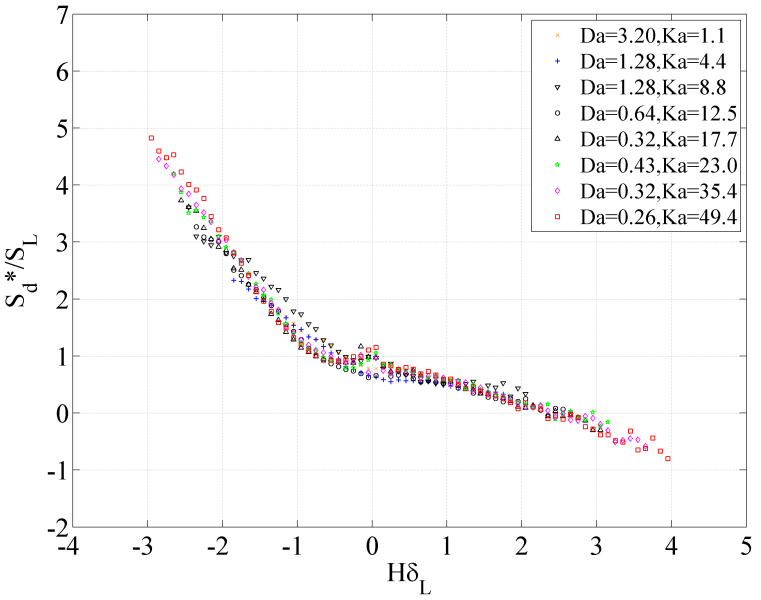

(b)

Figure 9.9. Mean flame displacement speed of (a) cylindrical shapes and (b) spherical shapes on the flame surface conditioned on total curvature **H** normalized by laminar flame thickness.

the spherical surfaces agrees well with the mean S_d when all surface topologies are considered. This suggests that flame displacement speed on average is independent of the shape factor. In other words, the total curvature **H** (or the mean curvature κ_m) alone is sufficient to account for S_d variations on the flame surface.

9.5 Flame Stretch on the Turbulent Flame Surface

In this section, analysis of flame stretch K on turbulent flame surfaces will be presented. Flame stretch denotes the fractional change of flame surface area and evidently in Eq. (9.1), it consists of a contribution due to tangential strain rate a_T which has been elaborately discussed in Section 9.2, and a contribution due to the propagation of curved surfaces. The second contribution is written as the product of flame displacement speed S_d and the total curvature **H**. Figure 9.10 presents the distribution of flame stretch due to surface curvature. It is shown that the peak of the pdf resides close to zero for flames over a range of Da and Ka. The flame stretch due to curvature remains primarily bounded between -5 and 5, which holds true for flame with Ka up to 50. This is in contrast to the tangential strain rate distribution on the flame surface as shown in Fig. 9.3, in which the pdf becomes significantly flatter as Ka is increased. In addition, the pdf of flame stretch due to curvature displays a long tail towards the negative axis, which is exaggerated in high Ka flames. This can be explained by examining Figs. 9.1(a) and 9.8(c). Figure 9.1(a) shows that as Ka is increased, there is increased probability of finding both positive and negative curvatures with relatively large magnitude. At the same time, Fig. 9.8(c) indicates that relatively large negative $\mathbf{H}\delta_L$ corresponds to positive mean flame displacement speeds (up to $S_d/S_L = 6$ for the highest Ka flame) while relatively large positive $\mathbf{H}\delta_L$ corresponds to negative mean flame displacement speeds (up to S_d/S_L = -1 for the highest Ka flame). As a result, the product of $\mathbf{H}\delta_L$ and S_d/S_L, i.e., the normalized flame stretch due to curvature, remains negative for highly curved surfaces which occur more frequently as Ka is increased.

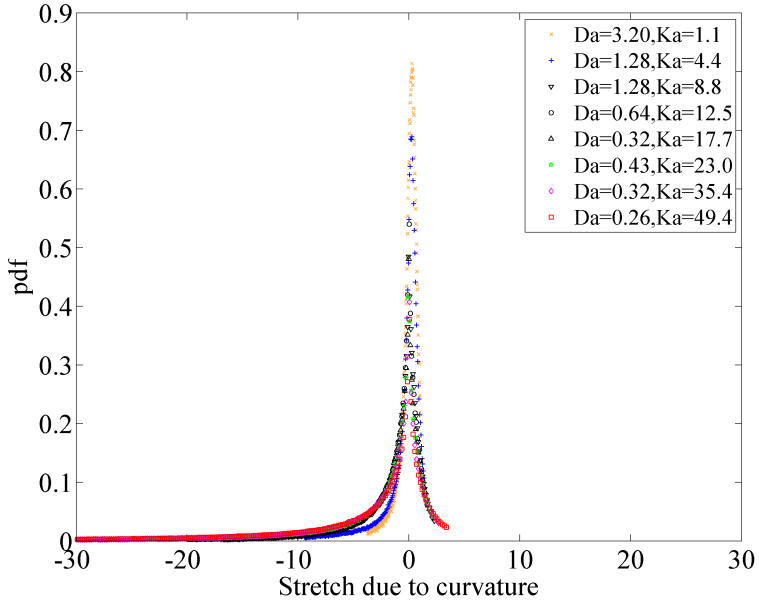

Figure 9.10. Probability density function of flame stretch due to propagation of curved surfaces on the c = 0.8 isosurface.

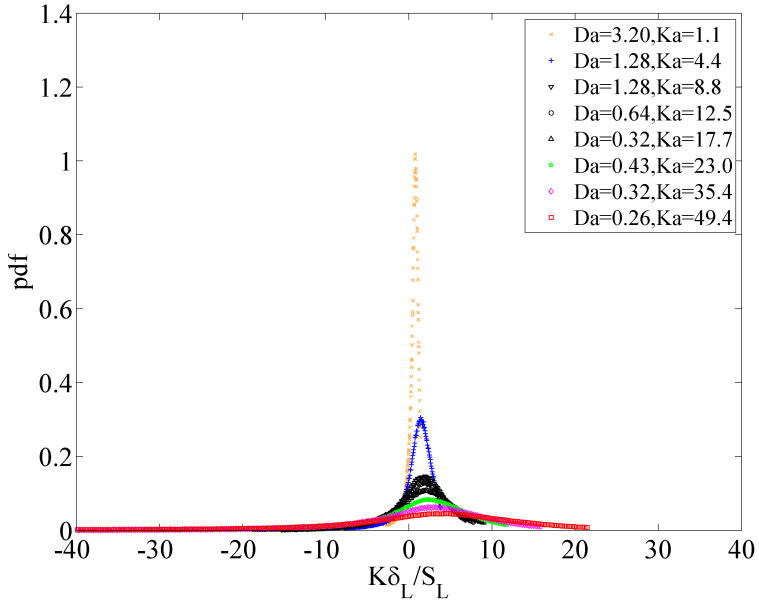

Figure 9.11. Probability density function of flame stretch K normalized by the laminar flame timescale δ_L/S_L on the c = 0.8 isosurface.

Table 9.2. Statistics of the total flame stretch K normalized by the laminar flame timescale.

	Case 1	Case 2	Case 4a	Case 4	Case 4b	Case 5	Case 6	Case 7
u_{rms}/S_L	2.0	5.0	10.0	10.0	10.0	15.0	20.0	25.0
L_o/δ_L	6.4	6.4	12.8	6.4	3.2	6.4	6.4	6.4
Da	3.20	1.28	1.28	0.64	0.32	0.43	0.32	0.26
Ka	1.1	4.4	8.8	12.5	17.7	23.0	35.4	49.4
$P(K>0)$	83.8%	77.7%	67.2%	65.8%	64.7%	63.6%	62.5%	61.3%
$\langle K\tau_f\rangle_s$	0.485	0.862	0.657	0.536	0.568	0.401	0.396	0.217
$\sigma$of $K\tau_f$	0.693	1.97	3.86	4.54	5.29	7.30	9.71	13.6
$\gamma$of $K\tau_f$	-1.87	-1.57	-1.35	-1.45	-1.38	-1.56	-1.53	-1.58

Figure 9.11 shows the distribution of total flame stretch K on the flame surfaces for a range of Da and Ka. As Ka is increased, the pdf becomes flatter while the peak value shifts towards a more positive value. This is mostly due to the increase in tangential strain rate with increasing Ka as evident in Fig. 9.3. Furthermore, the tail extending to large negative values is more prominent with increasing Ka. This is due to the propagation of highly curved surfaces as discussed in the previous paragraph. Table 9.2 lists the mean, standard deviation σ and skewness γ of the total flame stretch K normalized by the laminar flame timescale. The probability of K larger than 0 on the flame surface is also tabulated. As Karlovitz number increases, the probability of $K > 0$ decreases monotonically, indicating that the local surface area reduction is more prone to occur in high Ka flames. The surface mean of K also decreases monotonically while the standard deviation increases with increasing Ka. This is consistent with the observation that the pdf in Fig. 9.11 becomes flatter with longer tails extending to negative values.

The mean flame stretch due to curvature, i.e., S_d **H**, conditioned on flame curvature **H** is shown in Figure 9.12. The trend is non-linear since flame displacement speed due to tangential diffusion itself is proportional to **H**. In addition, the term S_d **H** only makes a positive contribution to flame stretch when $0 < \mathbf{H}\delta_L < 2$. In other words, the flame surface area is enhanced on moderately curved convex surfaces (towards the reactants) due to its own propagation, but diminished on concave or highly curved convex surfaces. This mechanism is not affected by turbulence properties as evident by its insensitivity to the change in Da or Ka. Instead, it is governed by the differential and preferential diffusion process as discussed in Section 9.3 and hence dependent on the Lewis number of the deficient specie. Chemical mechanism is also expected to play a role through coupling with the preferential diffusion which affects S_r and eventually the flame stretch due to curvature.

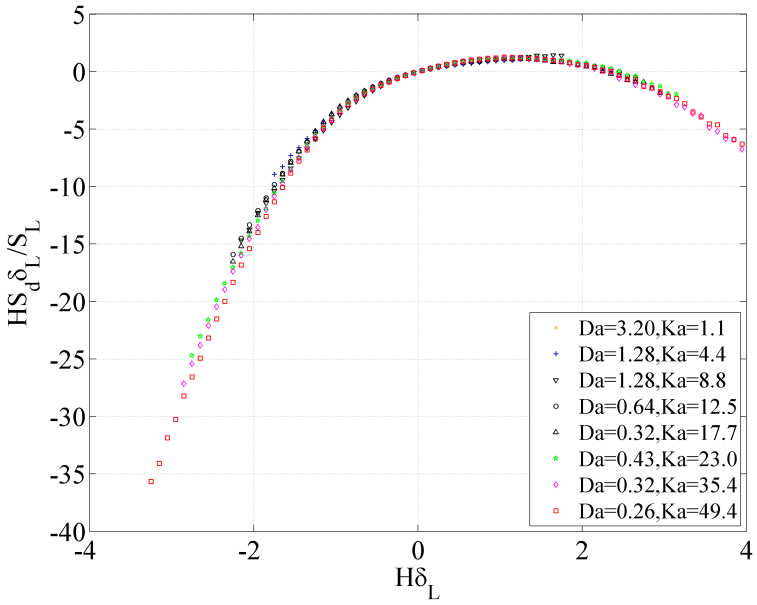

Figure 9.12. Conditional mean of normalized flame stretch due to propagation of curved surfaces as a function of total curvature **H** normalized by laminar flame thickness.

The dependence of the conditional mean flame stretch K on flame curvature **H** is shown in Fig. 9.13. Influence of Da and Ka on K are observed due to the inclusion

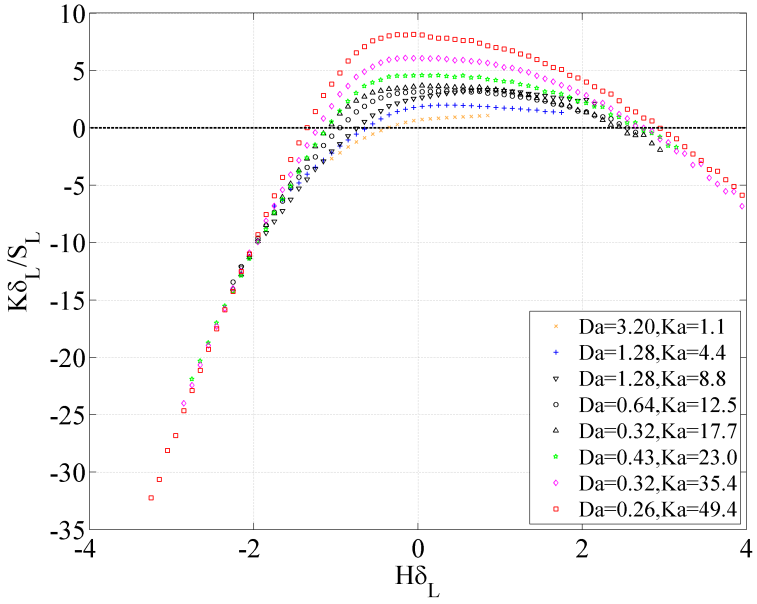

Figure 9.13. Conditional mean of normalized flame stretch as a function of total curvature **H** normalized by laminar flame thickness.

of tangential strain rate a_T. Generally a higher Ka corresponds to a higher mean flame stretch at a given curvature. On moderately curved surfaces, i.e.,-2 < $\mathbf{H}\delta_L$ < 2, the tangential strain together with surface propagation give rise to the generation of flame surface. On highly curved surfaces, irrespective of it being concave and convex, flame propagation dominates the tangential strain effect which results in the reduction of flame surface area. This provides a basis for the dependence of Ka in the correlation of flame surface area A_T, i.e., Eq. (8.10) in the previous chapter. Recall that in Figure 8.7, when sampled flame surface area A(Δ) normalized with A(Δ=η) is plotted against Δ/η, the curves exhibit a secondary dependence on Ka. More specifically, increasing Ka results in the reduction of A_T. This can be explained as follows. When Ka is small, the variation of total curvature **H** is small on the flame surface as evident in Fig. 9.1(a). For these curvatures, the flame stretch is largely positive and contributes to the generation of flame surface area. As Ka increases, the variation in **H** on the flame surface grows, or in other words, highly curved surfaces are formed. At these locations, flame stretch is relatively more negative, which, in

turn, results in the reduction of flame surface area. Note that with increase in Ka, the flame stretch at moderate curvatures also grows more positive. Such effect is attributed to the increase in tangential strain rate as shown in Fig. 9.5. However, the highly negative flame stretch due to large curvatures prevails over the increment of flame stretch at moderately curved surfaces. Ultimately, this leads to the reduction of flame surface area with increasing Ka.

It is interesting to study how flame displacement speed is correlated with flame stretch on the turbulent flame surface. Asymptotic studies have shown that for small flame stretch, S_d is linearly proportional to K as described by Eq. (9.7). Figure 9.14 plots the joint probability density function (JPDF) of normalized flame stretch with normalized flame displacement speed. Results for Cases 1, 2, 4 and 6 are presented. These cases have Da = 3.20, 1.28, 0.64 and 0.32 and Ka = 1.1, 4.4, 12.5 and 35.4, respectively. Evidently in Fig. 9.14(a) when Ka is small (i.e., Da is large), the flame displacement speed is negatively correlated with the flame stretch and the dependence is almost linear. As Ka increases, a second branch emerges in the region where S_d is negative. Along this branch, the flame displacement speed becomes positively correlated with flame stretch. A similar trend has been reported in previous DNS work [243, 244]. The appearance of two branches can be attributed to the non-linear behavior of flame stretch due to propagation of flame surfaces, i.e., S_d $\mathbf{H}$. As shown in Fig. 9.8(c), the mean S_d conditioned on $\mathbf{H}$ decreases from a positive value to a negative one but the product of S_d and $\mathbf{H}$ remains negative. Therefore, the upper branch in Figs 9.14(b)-(d) corresponds to highly concave surfaces while the lower branch corresponds to highly convex surfaces. Figure 9.15 shows the mean flame stretch conditioned on the flame displacement speed. Two branches representing the positive and negative correlation between K and S_d are apparent. Furthermore, a linear relationship appears to be insufficient to describe the dependency of S_d on K in each individual branch, let alone over the entire range of K on the flame surfaces. Hence, Eq. (9.7) would be inadequate to model turbulent flames with large Ka.

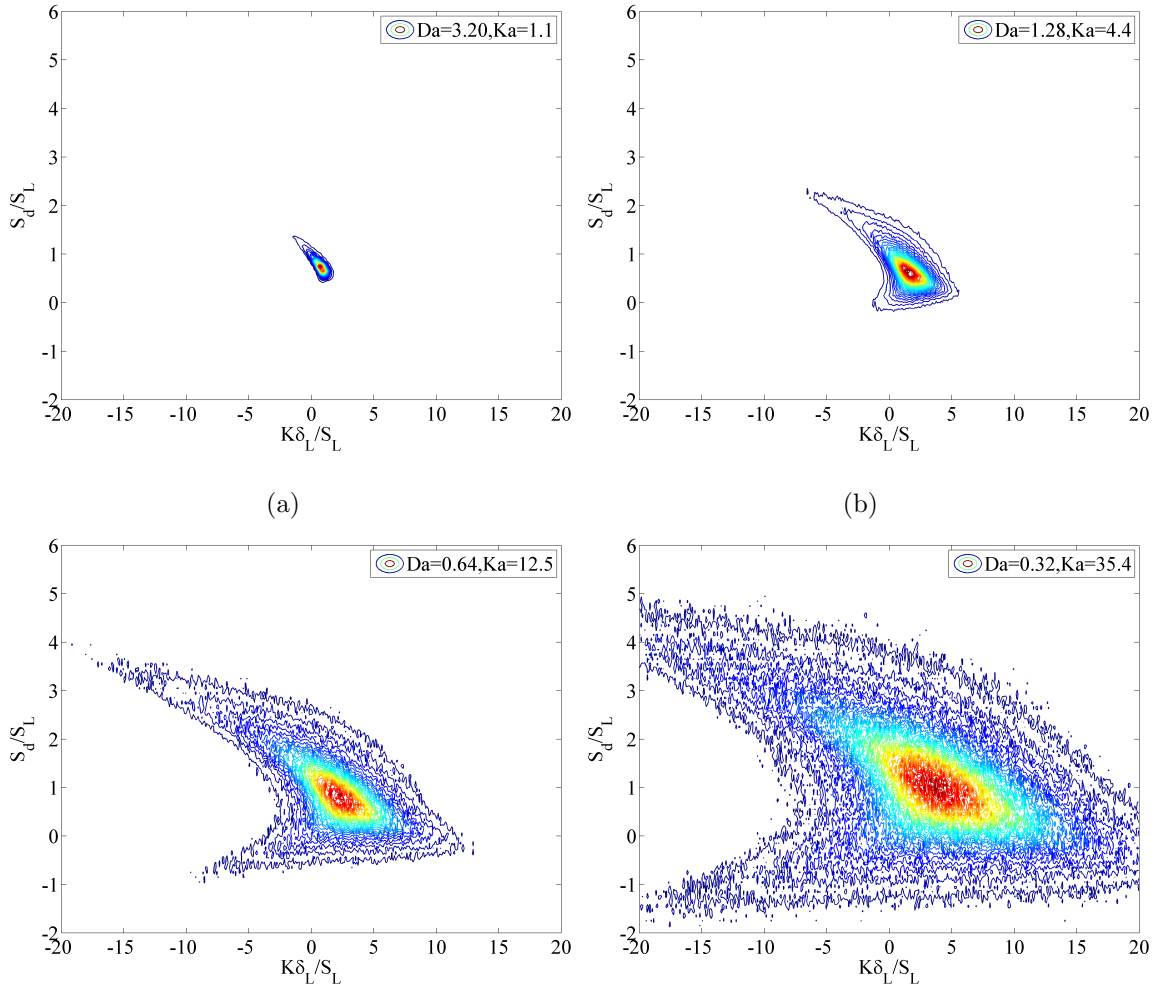

Figure 9.14. Joint probability density function of normalized flame displacement speed and normalized flame stretch for (a) Case 1: Da = 3.20, Ka = 1.1; (b) Case 2: Da = 1.28, Ka = 4.4; (c) Case 4: Da = 0.64, Ka = 12.5 and (d) Case 6: Da = 0.32, Ka = 35.4.

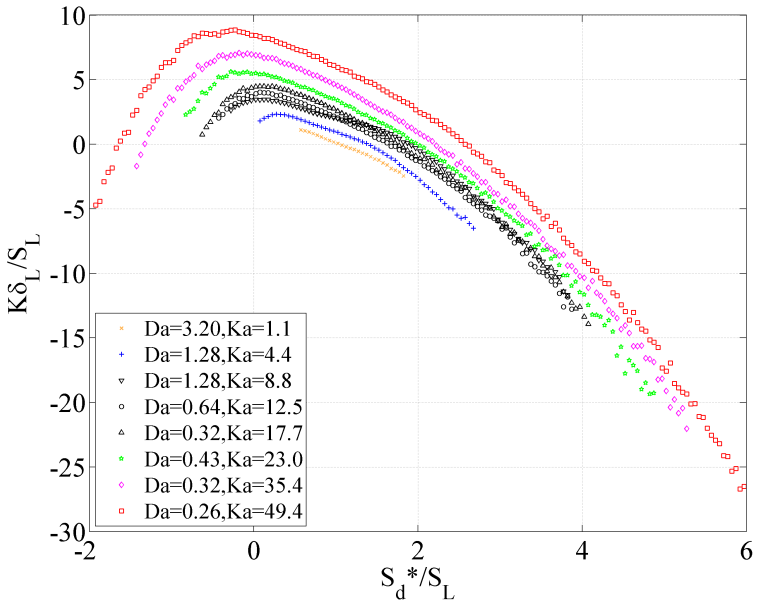

Figure 9.15. Conditional mean of normalized flame stretch as a function of normalized flame displacement speed.

9.6 Modeling FSD Transport in RANS Simulations

In this section, modeling implications for the transport of flame surface density (FSD) in the context of Reynolds-Averaged Navier-Stokes simulations are considered based on the physical insights gained by analyzing the DNS results. By taking ensemble average followed by time average of Eq. (9.1), the transport equation for the generalized FSD Σ_{gen} [100] is given as

$$\frac{\partial \Sigma_{\text{gen}}}{\partial t} + \vec{\nabla} \cdot \left[\overline{\langle \mathbf{u} \rangle_{\text{s}}} \Sigma_{\text{gen}} \right] = \overline{\langle a_{\text{T}} \rangle_{\text{s}}} \Sigma_{\text{gen}} + \overline{\langle \text{S}_{\text{d}} \nabla \cdot \mathbf{n} \rangle_{\text{s}}} \Sigma_{\text{gen}} - \vec{\nabla} \cdot \left[\overline{\langle \text{S}_{\text{d}} \mathbf{n} \rangle_{\text{s}}} \Sigma_{\text{gen}} \right] \tag{9.19}$$

where $\Sigma_{\text{gen}} = \overline{|\nabla c|}$. Here $\overline{\langle \cdot \rangle_{\text{s}}}$ denotes the Reynolds-averaging operation in addition to a FSD-weighted averaging on the surface,

$$\overline{\langle Q \rangle_{\text{s}}} = \overline{\langle Q \Sigma \rangle} / \overline{\langle \Sigma \rangle} \tag{9.20}$$

All terms on the right-hand-side of Eq. (9.19) together with the surface average of the flow velocity $\overline{\langle \mathbf{u} \rangle_{\text{s}}}$ are unclosed and require modeling.

The tangential strain rate term, i.e., $\overline{\langle a_{\mathrm{T}} \rangle_{\mathrm{s}}}$ in Eq. (9.19), has been computed and tabulated in Table 9.1 on the isosurface of c = 0.8 for all flames. As discussed in Section 9.3, the surface average of tangential strain rate is a linear function of Ka. A model for $\overline{\langle a_{\mathrm{T}} \rangle_{\mathrm{s}}}$ is proposed as

$$\overline{\langle a_{\mathrm{T}} \rangle_{\mathrm{s}}} = (a_1 Ka + a_2)/\tau_f. \tag{9.21}$$

On the CH_4-air flame surface defined by c = 0.8, the line of best-fit as shown in Fig. 9.5 gives $a_1 = 0.11$ and $a_2 = 0.88$. The proposed correlation for $\overline{\langle a_{\mathrm{T}} \rangle_{\mathrm{s}}}$ has a similar form as the one given by Cant *et al.* (1991) [253].

Modeling of the propagation of curved surfaces, i.e., $\overline{\langle \mathrm{S_d} \nabla \cdot \mathbf{n} \rangle_{\mathrm{s}}}$, is less trivial. This term involves the product of $\mathrm{S_d}$ and flame curvature. Since it has been shown in Section 9.4 that the conditional mean $\mathrm{S_d}$ as a function of curvature $\mathbf{H}$ is only weakly dependent on the Da or Ka, this implies that the sole effect of Ka or Da on $\mathrm{S_d}$ can be modeled through its influence on the curvature distribution. Furthermore, we have shown that curvature $\mathbf{H}$ alone could account for the variations in $\mathrm{S_d}$ without the need for invoking a second degree of freedom such as the shape factor. Based on these observations, we propose a model for $\overline{\langle \mathrm{S_d} \nabla \cdot \mathbf{n} \rangle_{\mathrm{s}}}$ using a pdf approach as follows,

$$\overline{\langle \mathrm{S_d} \nabla \cdot \mathbf{n} \rangle_{\mathrm{s}}} = \int_{-\infty}^{\infty} \overline{\langle \mathrm{S_d} | \mathbf{H} \rangle_{\mathrm{s}}} \cdot \mathbf{H} \cdot P(\mathbf{H}) d\mathbf{H}, \tag{9.22}$$

where $\overline{\langle \mathrm{S_d} | \mathbf{H} \rangle_{\mathrm{s}}}$ is the surface average of $\mathrm{S_d}$ conditioned on $\mathbf{H}$ as shown in Fig. 9.8(c), and $P(\mathbf{H})$ is the pdf of $\mathbf{H}$ as shown in Fig. 9.1(a). $\overline{\langle \mathrm{S_d} | \mathbf{H} \rangle_{\mathrm{s}}}$ can be further decomposed into two contributions:

$$\overline{\langle \mathrm{S_d} | \mathbf{H} \rangle_{\mathrm{s}}} = \overline{\langle \mathrm{S_r} + \mathrm{S_n} | \mathbf{H} \rangle_{\mathrm{s}}} + \overline{\langle \mathrm{S_t} | \mathbf{H} \rangle_{\mathrm{s}}}, \tag{9.23}$$

where $\overline{\langle \mathrm{S_r} + \mathrm{S_n} | \mathbf{H} \rangle_{\mathrm{s}}}$ represents the conditional mean displacement speed due to chemical reaction and normal diffusion, and $\overline{\langle \mathrm{S_t} | \mathbf{H} \rangle_{\mathrm{s}}}$ represents the conditional mean displacement speed due to tangential diffusion. $\overline{\langle \mathrm{S_t} | \mathbf{H} \rangle_{\mathrm{s}}}$ is plotted in Fig. 9.8(b) and hence can be modeled as

$$\overline{\langle \mathrm{S_t} | \mathbf{H} \rangle_{\mathrm{s}}} = -D\mathbf{H}, \tag{9.24}$$

where D is the diffusivity on the isosurface. $\overline{\langle \mathrm{S_r} + \mathrm{S_n} | \mathbf{H} \rangle_\mathrm{s}}$ is dominated by the coupled effects of differential/preferential diffusion with chemistry. Thus, it should be dependent on the Lewis number of the species, i.e.,

$$\overline{\langle \mathrm{S_r} + \mathrm{S_n} | \mathbf{H} \rangle_\mathrm{s}} = \langle (\mathrm{Le}_i) \cdot \mathrm{S_L}. \tag{9.25}$$

Since $\overline{\langle \mathrm{S_r} + \mathrm{S_n} | \mathbf{H} \rangle_\mathrm{s}}$ is only weakly dependent on the Ka or Da as shown in Fig. 9.8(a), we speculate that $\overline{\langle \mathrm{S_r} + \mathrm{S_n} | \mathbf{H} \rangle_\mathrm{s}}$ can be approximated using simulations of laminar outwardly propagating ($\mathbf{H} > 0$) and inwardly propagating ($\mathbf{H} < 0$) cylindrical flames. However, one limitation is that the laminar counterpart is only capable of simulating curved flames with -2 < $\mathbf{H}$ < 2, i.e., with a radius of curvature larger than the laminar flame thickness. Further investigation on fuels with distinct Lewis number is required for modeling this term.

The last term inside the integral in Eq. (9.22), i.e., $P(\mathbf{H})$, reflects the Ka effects on $\overline{\langle \mathrm{S_d} | \mathbf{H} \rangle_\mathrm{s}}$. This probability density function, as shown in Fig. 9.1(a) can be approximately using a skewed normal distribution as follows:

$$P(x) = \left[1 + \mathrm{erf}\,(\frac{\alpha(x-\mu)}{\sqrt{2}\sigma})\right] \exp\left(-\frac{(x-\mu)^2}{2\sigma^2}\right). \tag{9.26}$$

where μ, σ and α represent the location, scale and shape parameters, respectively. These three parameters are related to the mean ($\mathrm{S_{mean}}$), standard deviation ($\mathrm{S_{std}}$) and skewness ($\mathrm{S_{skew}}$) of the sample set of a skewed normal distribution by

$$\begin{aligned} \mathrm{S_{mean}} &= \mu + \frac{\sqrt{2/\pi}\alpha\sigma}{\sqrt{1+\alpha^2}}, \\ \mathrm{S_{std}} &= \sqrt{1 - \frac{2\alpha^2}{\pi(1+\alpha^2)}}\sigma, \\ \mathrm{S_{skew}} &= \frac{\sqrt{2}(4-\pi)\alpha^3}{[\pi + (-2+\pi)\alpha^2]^{\frac{3}{2}}}. \end{aligned} \tag{9.27}$$

Figure 9.16 shows the mean, standard deviation and skewness of flame curvature H on the flame surface as a function of the Karlovitz number Ka. It is evident that the surface mean of $\mathbf{H}$ is approximately zero, which is expected for a statistically planar flame. Furthermore, the standard deviation and the skewness of $\mathbf{H}$ increases

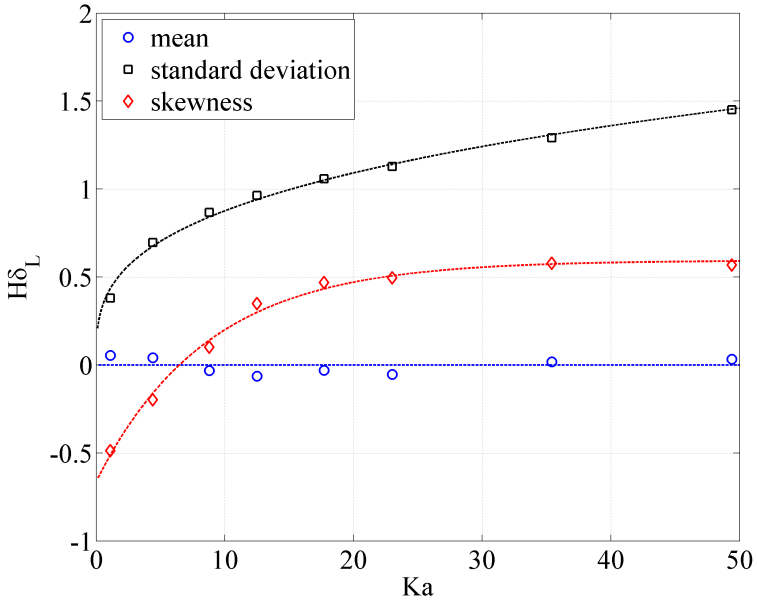

Figure 9.16. Mean, standard deviation and skewness of the normalized curvature $\mathbf{H}\delta_{\mathrm{L}}$ on the flame surface as a function of flame Karlovitz number Ka.

with Ka. By curve-fitting the data, we propose correlations for the mean, standard deviation and skewness of the distribution of $\mathbf{H}$ based on Ka:

$$\begin{aligned} \mathrm{S}_{\mathrm{mean}}(Ka) &= 0, \\ \mathrm{S}_{\mathrm{std}}(Ka) &= 0.422 \cdot Ka^{0.317}, \\ \mathrm{S}_{\mathrm{skew}}(Ka) &= 0.595 - 1.26 \cdot \exp(-0.116 \cdot Ka). \end{aligned} \tag{9.28}$$

The correlations in Eq. (9.28) are also plotted in Fig. 9.16 as dash lines. Using Eq. (9.28), the location, scale and shape parameters can be solved as functions of Ka and subsequently $P(\mathbf{H})$ in Eq. (9.22) can be closed.

Lastly, the term $\overline{\langle \mathrm{S_d}\mathbf{n}\rangle_{\mathrm{s}}}$ in the Reynolds-averaged FSD equation can again be modeled using the pdf approach as follows:

$$\overline{\langle \mathrm{S_d}\mathbf{n}\rangle_{\mathrm{s}}} \approx \overline{\langle \mathrm{S_d}\rangle_{\mathrm{s}}}\mathbf{n_m} = \int_{-\infty}^{\infty} \overline{\langle \mathrm{S_d}|\mathbf{H}\rangle_{\mathrm{s}}} \cdot P(\mathbf{H}) d\mathbf{H} \cdot \mathbf{n_m}, \tag{9.29}$$

where $\mathbf{n_m}$ represents the mean direction of flame propagation. $\overline{\langle \mathrm{S_d}|\mathbf{H}\rangle_{\mathrm{s}}}$ can be modeled using Eqs. (9.24) and (9.25), whereas $P(\mathbf{H})$ is modeled by Eq. (9.26).

9.7 Summary

In this chapter, analysis of DNS results of lean premixed CH_4-air flames of $\phi = 0.5$ is carried out on an isosurface inside the reaction zone. The range of normalized turbulent intensities, Damköhler number and Karlovitz number of the flames selected for analysis correspond to the thin reaction zone regime. Statistics of flame curvature ($\mathbf{H}$), surface topology characterized by shape factor, tangential (a_{T}) and normal strain rates (a_{N}), flame displacement speed ($\mathrm{S_d}$) and flame stretch (K) are examined on the isosurface.

It is observed that with increasing Ka, i.e., decreasing Da, there is increased probability of forming highly curved surfaces locally. However, the distribution of topological features stay almost identical independent of the ratio of velocities and length scales between the flow field and flame. The flame surface normal preferentially aligns parallel to the most compressive strain rate. This gives rise to a negative mean normal strain on the flame surface, indicating that steeper scalar gradients are on average created by turbulence. Surface-averaged tangential and normal strain rates are found to correlate linearly with Karlovitz number, rather than with Damköhler number as suggested in the past. This suggests that for flames in the thin reaction zone regime, straining experienced locally by the flame surface is dictated by the small scale motion. The correlation between strain rate and curvature shows that the most extensive (compressive) tangential (normal) strain rate is approximately associated with surfaces having no net curvatures when Ka is relatively large. This correlation impacts the mean flame displacement speed conditioned on curvature.

Flame displacement speed is studied by examining the contributions from its three components: chemical reaction ($\mathrm{S_r}$), normal ($\mathrm{S_n}$) and tangential diffusion ($\mathrm{S_t}$). $\mathrm{S_r} + \mathrm{S_n}$ is found to increase with increasing magnitude of the curvature. This is partly due to the coupled effects of differential diffusion and chemistry. In addition, correlation between curvature and normal strain rate give rise to a more negative $\mathrm{S_n}$ when the surface has no net curvature. On the other hand, $\mathrm{S_t}$ is negatively correlated with

curvature in a linear behavior. Overall, S_d manifests a negative correlation with curvature. When the flame surface is concave towards the reactants, both S_t and the net effect of $S_r + S_n$ contributes positively to S_d, resulting in accelerated flame propagation into the unburnt region. When the flame surface is highly convex towards the reactants ($\kappa_m \delta_L > 1$), S_t dominates $S_r + S_n$, causing the flame to retract. Furthermore, mean S_d conditioned on curvature is only weakly dependent on the Da or Ka, indicating that the sole effect of Ka or Da on S_d can be modeled through its influence on the curvature distribution. The shape factor is also found to have no effect on S_d, suggesting that variations of S_d on the 2D flame surface can be accounted for by using a single degree of freedom, i.e., $\mathbf{H}$.

With increasing Ka, the probability of finding positive flame stretch decreases monotonically, indicating that the local surface area reduction is more prone to occur in high Ka flames. The surface mean of K also decreases monotonically while the standard deviation increases monotonically with increasing Ka. Conditional mean of K on curvature $\mathbf{H}$ shows that flame surface area is generated only on moderately curved surfaces. On highly curved surfaces, irrespective of it being concave and convex, flame propagation dominates the tangential strain effect which results in negative K. This provides an explanation for the negative dependence of A_T on Ka as seen in the last chapter. As Ka increases, highly curved surfaces are formed. At these locations, flame stretch is relatively more negative, which, in turn, results in the reduction of flame surface area.

The physical insights derived from the analysis are applied to modeling the FSD equation in the context of RANS simulations. The tangential strain rate term $\overline{\langle a_T \rangle_s}$ is correlated with the Karlovitz number. A PDF approach is proposed for closing $\overline{\langle S_d \nabla \cdot \mathbf{n} \rangle_s}$ and $\overline{\langle S_d \mathbf{n} \rangle_s}$ in which the probability density function of curvature is modeled using a skewed normal distribution. The location, scale and shape parameters of the PDF is correlated with Ka.

10. EFFECTS OF PREMIXED COMBUSTION ON TURBULENCE

10.1 Introduction

Modeling of turbulence-chemistry interaction in premixed flames consists of two important aspects: modeling of the effects of turbulence on the premixed flame and modeling of the effects of combustion on turbulence. In the previous three chapters, the effects of turbulence on premixed combustion have been studied in detail. In the current chapter, we will examine how combustion affects turbulence. In particular, we will study how turbulence statistics of the premixed gas vary through the flame. Accurate modeling of turbulence inside the turbulent flame brush as well as inside the burned region is essential for lean-burn natural gas engine applications. Heat transfer from the burned gas to the cylinder wall and pollutant formation in the burned gas are influenced by the turbulence.

Lipatnikov and Chomiak (2010) reviewed the more recent experimental and simulation data on the effects of premixed flames on turbulence [254]. The results reveal that, in general, premixed combustion can noticeably affect both unconditioned and conditioned moments of fluctuating velocities, especially when the incident turbulence is weak, i.e., u_{rms}/S_L is low. Scurlock (1948) [255] and later Karlovitz (1953) [236] came up with the hypothesis of "flame-generated turbulence" in premixed combustion. Since then, many studies have shown evidence for "flame-generated turbulence" in premixed flames [256, 257, 258, 259, 260, 261, 262, 263]. The mechanism of "flame-generated turbulence" was attributed to the mean velocity gradient and mean pressure gradient induced by the flame [264]. On the other hand, flames can "destroy" turbulence through a different mechanism: heat release from combustion raises mixture temperature and in turn, increases the mixture viscosity. This increases kinetic energy dissipation, thereby potentially "destroying" the turbulence.

In the context of RANS simulations, the effects of premixed combustion on turbulence are often modeled by numerically solving the balance equations of turbulent kinetic energy (TKE) k, and dissipation rate ϵ [265]. The transport equation of the Favre-averaged TKE equation is given as

$$\begin{aligned}\frac{\partial \bar{\rho}\tilde{k}}{\partial t}+\frac{\partial \bar{\rho}\tilde{u}_j\tilde{k}}{\partial x_j} = & \underbrace{-\overline{\rho u_i'' u_j''}\frac{\partial \tilde{u}_i}{\partial x_j}}_{\mathrm{T}_1}\underbrace{-\overline{u_i''}\frac{\partial \bar{\mathrm{p}}}{\partial x_i}}_{\mathrm{T}_2}+\underbrace{\overline{\mathrm{p}'\frac{\partial u_k''}{\partial x_k}}}_{\mathrm{T}_3} \\ & +\underbrace{\overline{u_i''\frac{\partial \tau_{ij}}{\partial x_j}}}_{\mathrm{T}_4}\underbrace{-\overline{\frac{\partial \mathrm{p}' u_i''}{\partial x_i}}}_{\mathrm{T}_5}\underbrace{-\frac{\partial}{\partial x_i}\left(\overline{\frac{1}{2}\rho u_i'' u_k'' u_k''}\right)}_{\mathrm{T}_6}.\end{aligned} \tag{10.1}$$

Here, $\tilde{k}$ is the Favre-averaged TKE. $\tilde{u}_i$ and u'' are the Favre mean and fluctuation of velocity component, respectively. Terms T_1 and T_2 represent the production of TKE by mean velocity gradients and mean pressure gradients, respectively. Term T_3 accounts for the interaction of the pressure fluctuations with the fluctuating dilatation. Term T_4 accounts for the viscous dissipation of TKE. Terms T_5 and T_6 represent the transport of TKE by pressure fluctuation and velocity fluctuation, respectively. Zhang and Rutland (1995) evaluated the terms on the RHS of Eq. (10.1) using DNS [266]. They found that the pressure term, i.e., T_2, and T_3 in Eq. (10.1) is a dominant source of k for flames in the corrugated flamelet regime, as shown in Fig. 2.6(b). Similar findings were obtained by Nishiki *et al.* (2002) by analyzing DNS of premixed flames in the corrugated flamelet regime [267]. Chakraborty *et al.* (2011) studied the statistical behavior of TKE transport for premixed flames in decaying turbulence. The DNS analyzed in their work include flames in the corrugated flamelet regime and in the thin reaction zone regime (with $\mathrm{u_{rms}/S_L}$ up to 7.5) [268]. They observed that TKE is generated within the flame brush for flames in the corrugated flamelet regime whereas for flames in the thin reaction zone regime, TKE decays monotonically.

In this chapter, DNS of premixed flames reported in Table 8.1 of Chapter 8 will be studied with an emphasis on the TKE balance within the flame brush. The normalized turbulence intensities $\mathrm{u_{rms}/S_L}$ of flames considered in this study vary from 2.0 to 25.0. The corresponding Damköhler and Karlovitz numbers vary from 3.20 to 0.26 and from

1.1 to 49.4, respectively. The rest of the chapter is organized as follows. Section 10.2 discusses the behavior of TKE, dissipation rate, and integral length scales across the turbulent flame brush. Section 10.3 examines the budget of TKE balance across the flame brush. The scaling of individual term is also considered. The chapter then ends with summary in Section 10.4.

10.2 Turbulence Characteristics Through the Turbulent Flame Brush

As discussed in Chapter 5, the premixed turbulent flames are simulated in an inflow-outflow configuration. Without loss of generality, we will refer to the inflow direction as the x-direction. Periodic boundary conditions are imposed for boundaries which are parallel to the mean inflow direction, i.e., the y- and z-directions. With this configuration, there is no mean shear present in the flow that may complicate the analysis. Hence, the turbulent flame can be viewed as statistically planar. In addition, turbulence is homogeneous on any given y-z plane. The v and w components of velocity are isotropic. This allows us to perform spatial averaging on the y-z plane to obtain statistics of turbulence quantities. These quantities are, of course, expected to vary along the x-direction.

Performing temporal averaging of any quantity is less trivial than spatial averaging with this particular setup. This is because the mean flame position is varying in time, although the flame remains stationary in a statistical sense. This problem can be resolved by using a conditional averaging based on the planar mean progress variable $\langle c \rangle$. Here $\langle \cdot \rangle$ represents the averaging operation on the y-z plane. The progress variable c is defined as

$$c(x, y, z, t) = 1 - \frac{\mathrm{Y}_{\mathrm{CH_4}}(x, y, z, t)}{\mathrm{Y}_{\mathrm{u,CH_4}}}, \tag{10.2}$$

where $\mathrm{Y}_{\mathrm{u,CH_4}}$ is the mass fraction of $\mathrm{CH_4}$ in the unburned mixture. In other words, temporal averaging is performed on the y-z planes corresponding to a similar location within the turbulent flame brush, i.e., at $\langle c \rangle = c^*$. Mathematically, the temporal

mean of an arbitrary quantity ϕ corresponding to location c^* within the turbulence brush is given by

$$\bar{\phi}(c^*) = \overline{\phi|\langle c\rangle(x,t) = c^*}. \tag{10.3}$$

Note that progress variable c varies locally from 0 to 1 from unburned to burned mixture, respectively, whereas $\langle c\rangle$ varies from 0 to 1 across the turbulence flame brush, which is much thicker than the laminar flame thickness. For the conditional averaging on $\langle c\rangle$ to be well-posed, $\langle c\rangle$ and axial position x must possess a one-to-one correspondence. Figure 10.1 displays the planar mean progress variable $\langle c\rangle$ as a function of axial location for one instance. Evidently $\langle c\rangle$ increases with increasing x in a near monotonic behavior.

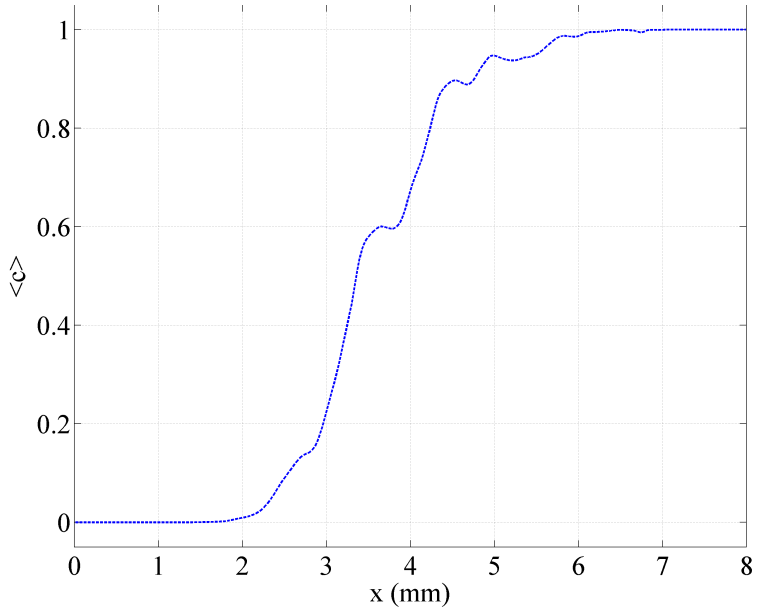

Figure 10.1. Instantaneous planar mean progress variable $\langle c\rangle$ as a function of axial location x.

The variations of the Favre-averaged turbulent kinetic energy $\tilde{k}$, its dissipation rate $\tilde{\epsilon}$ and integral length scales L_{22} and L_{33} across the turbulence flame brush are examined next. $\tilde{k}$ and $\tilde{\epsilon}$ are given by

$$\begin{aligned} \tilde{k} &= \frac{\overline{\rho u_k'' u_k''}}{2\bar{\rho}}, \\ \tilde{\epsilon} &= \mu \overline{\frac{\partial u_i''}{\partial x_j} \frac{\partial u_i''}{\partial x_j}} / \bar{\rho}. \end{aligned} \tag{10.4}$$

Figure 10.2 shows the normalized TKE as a function of $\langle c \rangle$ for eight cases. The normalization is carried out against the target steady-state TKE specified in the linear forcing term, i.e., k_o in Eq. (5.21). It can be seen that at $\langle c \rangle = 0$, Favre-averaged TKE agrees with k_o within 10%. This suggests that the use of 2D conditional statistics is adequate for predicting second moments of turbulence characteristics. As $\langle c \rangle$ increases, $\tilde{k}/k_o$ decays for all flames considered in this study. This is consistent with the observation made by Chakraborty *et al.* that $\tilde{k}$ decays monotonically across the flame brush in the thin reaction zone regime [268]. Furthermore, it is evident that there exists a correlation between the Damköhler number (Karlovitz number) and the decay in TKE. The lower (higher) the Da (Ka), the higher the decay in TKE across the turbulent flame brush. The correlation with Da and Ka will be examined in detail in Section 10.3.

Integral length scale L_o on any y-z plane can be estimated by the average of L_{22} and L_{33} which are respectively given by

$$\begin{aligned} L_{22} &= \int_0^\infty \frac{R_{22}(\vec{\mathbf{r}})}{R_{22}(0)} dr, \\ L_{33} &= \int_0^\infty \frac{R_{33}(\vec{\mathbf{r}})}{R_{33}(0)} dr, \end{aligned} \tag{10.5}$$

where R_{22} and R_{33} are the two-point correlation functions given as

$$\begin{aligned} R_{22}(\vec{\mathbf{r}}) &= \langle v''(\vec{\mathbf{x}}) v''(\vec{\mathbf{x}} + \vec{\mathbf{r}}) \rangle, \\ R_{33}(\vec{\mathbf{r}}) &= \langle w''(\vec{\mathbf{x}}) w''(\vec{\mathbf{x}} + \vec{\mathbf{r}}) \rangle, \end{aligned} \tag{10.6}$$

Figure 10.3 shows the integral length scale L_o normalized by the value of L_o at $\langle c \rangle = 0$, i.e., inside the unburned mixture, as a function of $\langle c \rangle$. It is seen that the integral

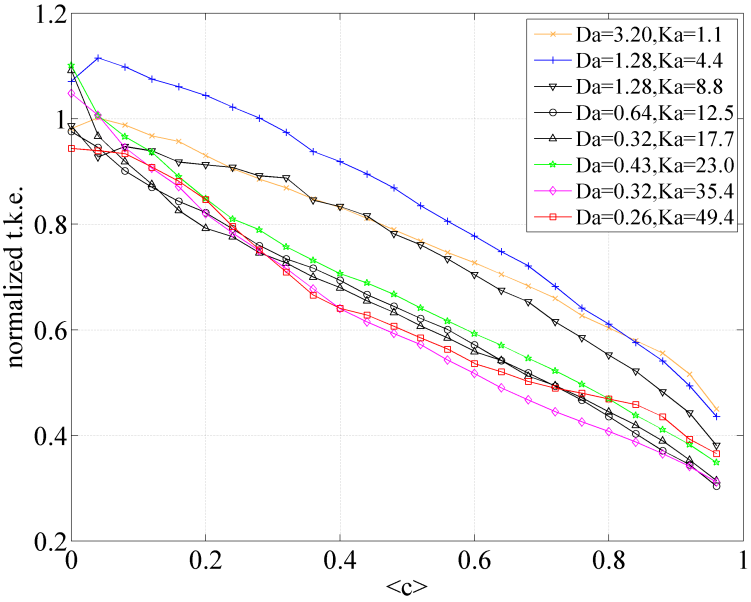

Figure 10.2. Variations of turbulence kinetic energy $\tilde{k}$ normalized by the desired steady-state k_o of the "linear forcing" scheme as a function of planar averaged progress variable $\langle c \rangle$.

length scale grows as CH_4 is consumed by the flame. The increase in L_o is more prominent in flames with low Da (high Ka). For instance, for flame with $Da = 3.20$ and $Ka = 1.1$, L_o grows by less than 60% from unburned to burned mixture whereas for flame with $Da = 0.26$ and $Ka = 49.4$, L_o grows by more than 120%. The variations in $\tilde{\epsilon}$ normalized by $\tilde{\epsilon}$ evaluated at $\langle c \rangle = 0$ are plotted in Fig. 10.4. It is seen that $\tilde{\epsilon}$ decreases across the turbulence flame brush. This is expected since ϵ scales with $k^{3/2}/L_o$. With the decay in k and growth of L_o within the flame brush, dissipation rate drops monotonically and this effect becomes more prominent in low Da, high Ka flames. The effects of Da and Ka on the variation of TKE will be discussed in the next section.

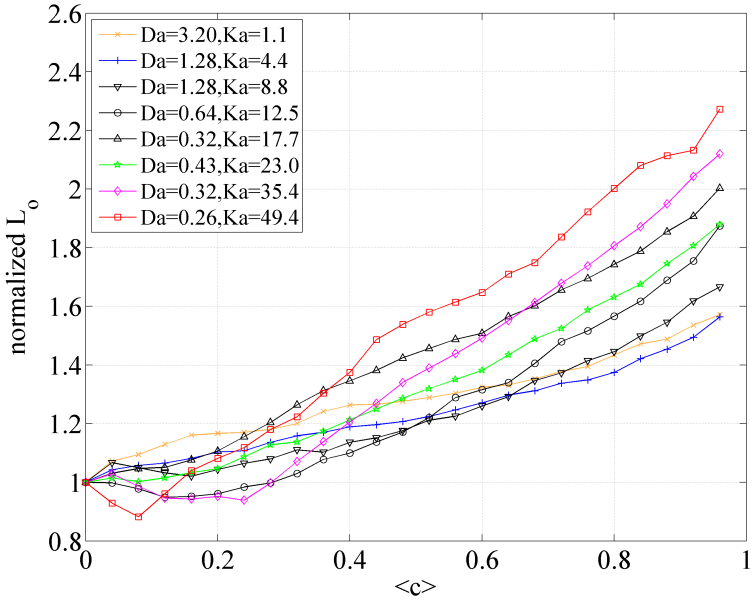

Figure 10.3. Variations of integral length scale $L_o = (L_{22} + L_{33})/2$ normalized by the value of L_o at $\langle c \rangle = 0$ as a function of planar averaged progress variable $\langle c \rangle$.

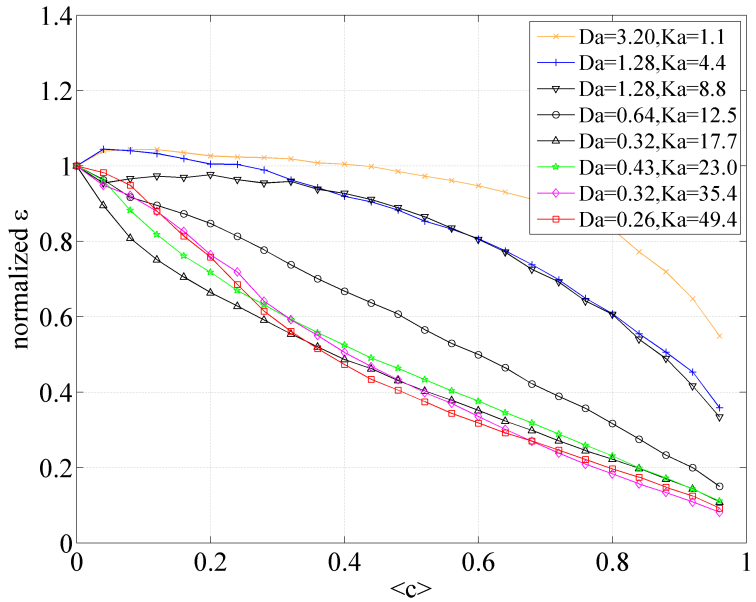

Figure 10.4. Variations of TKE dissipation rate $\tilde{\epsilon}$ normalized by $\tilde{\epsilon}$ at $\langle c \rangle = 0$ as a function of planar averaged progress variable $\langle c \rangle$.

10.3 Turbulent Kinetic Energy Budget within the Flame Brush

It is useful to examine the six terms on the RHS of Eq. (10.1) in order to better understand the variations in TKE within the turbulent flame brush. Figures 10.5(a)-10.5(d) show the mean values of T_1 to T_6 conditioned on the planar averaged progress variable $\langle c \rangle$ for four flames with normalized turbulence intensities $\mathrm{u_{rms}}/\mathrm{S_L}$ = 2, 5, 10 and 20, respectively. The corresponding Da = 3.20, 1.28, 0.64 and 0.32 and Ka = 1.1, 4.4, 12.5 and 35.4. In addition, Table 10.1 tabulates the L^2-norm of each term on the RHS of Eq. (10.1) averaged in the progress variable space using the following equation:

$$\|\mathrm{T}_i\| = \sqrt{\int_0^1 \mathrm{T}_i^2 dc}. \tag{10.7}$$

10.3.1 Term $\mathrm{T_1}$

It is evident from Fig. 10.5 that term T_1 which is responsible for the production of TKE due to the mean velocity gradients acts as a sink throughout the turbulent flame brush. This may be explained as follows: for a statistically planar flame with homogeneity in the y- and z-direction, term T_1 is reduced to $-\overline{\rho u'' u''}\partial\tilde{u}/\partial x$ where $-\overline{\rho u'' u''}$ is always negative while the mean velocity gradients remains positive due to flow acceleration by heat expansion. Therefore T_1 stays negative everywhere.

It is interesting to investigate how T_1 is influenced by changes in the turbulence intensities and length scales. Note that $-\overline{\rho u'' u''}$ should scale with $\rho_u \mathrm{u}_{\mathrm{rms}}^2$. $\partial\tilde{u}/\partial x$ is the spatial gradient of the mean velocity. In a statistically planar turbulent flame, the unburnt gas approaches the turbulent flame brush with a velocity equal to $\mathrm{S_T}$. The velocity of burned gas leaving the turbulent flame brush is then give as $\mathrm{S_T T_b}/\mathrm{T_u}$. The mean turbulent flame brush thickness δ_{T} normalized by turbulence integral length scale is plotted in Fig. 10.6. It is given as the distance between $\langle c \rangle$ = 0.5 and 0.95. Evidently, the turbulent flame brush thickness is approximately 5 times the integral

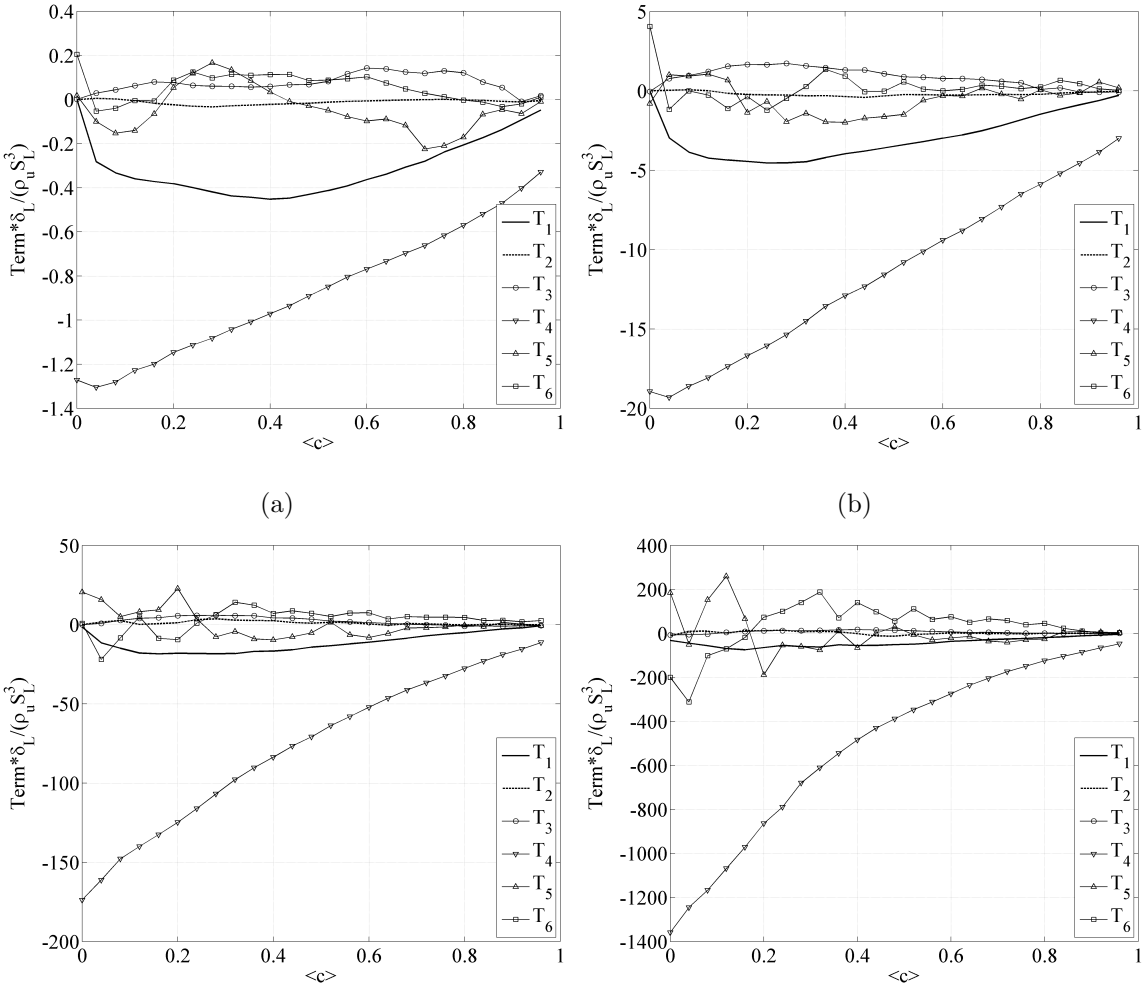

Figure 10.5. Variations of terms $T_1 \sim T_6$ across the turbulent flame brush for flames with (a) $u_{rms}/S_L = 2.0$, $Da = 3.20$, $Ka = 1.1$; (b) $u_{rms}/S_L = 5.0$, $Da = 1.28$, $Ka = 4.4$; (c) $u_{rms}/S_L = 10.0$, $Da = 0.64$, $Ka = 12.5$ and (d) $u_{rms}/S_L = 20.0$, $Da = 0.32$, $Ka = 35.4$.

Table 10.1. L^2-norms of $T_1 \sim T_6$ for flames over a range of Da and Ka.

	Case 1	Case 2	Case 4a	Case 4	Case 4b	Case 5	Case 6	Case 7
u_{rms}/S_L	2.0	5.0	10.0	10.0	10.0	15.0	20.0	25.0
L_o/δ_L	6.4	6.4	12.8	6.4	3.2	6.4	6.4	6.4
Da	3.20	1.28	1.28	0.64	0.32	0.43	0.32	0.26
Ka	1.1	4.4	8.8	12.5	17.7	23.0	35.4	49.4
$\|T_1\|\rho_u\delta_L/{S_L}^3$	0.34	3.2	12	13	12	30	46	72
$\|T_2\|\rho_u\delta_L/{S_L}^3$	0.015	0.23	1.0	1.6	2.4	4.1	7.5	32
$\|T_3\|\rho_u\delta_L/{S_L}^3$	0.084	1.0	1.9	3.2	2.2	5.6	9.2	12
$\|T_4\|\rho_u\delta_L/{S_L}^3$	0.92	13	46	92	160	290	650	1200
$\|T_5\|\rho_u\delta_L/{S_L}^3$	0.11	1.1	4.3	8.7	16	21	87	360
$\|T_6\|\rho_u\delta_L/{S_L}^3$	0.08	1.0	6.1	7.9	12	31	110	130

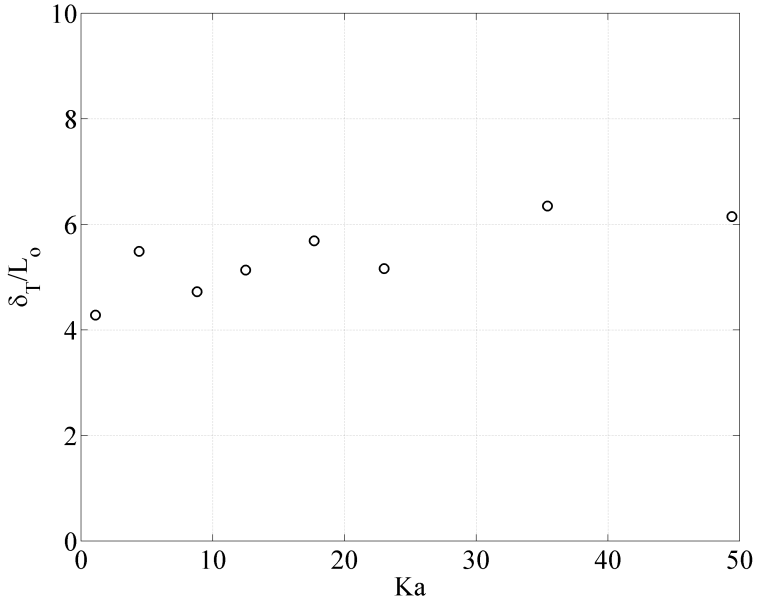

Figure 10.6. Normalized turbulent flame brush thickness as a function of Ka.

length scale. There appears to be only a weak dependence of δ_{T} on Ka. In other words, $\delta_{\mathrm{T}} \sim \mathcal{O}(\mathrm{L_o})$. The scaling of mean $\mathrm{T_1}$ across the flame brush is then given by

$$\mathrm{T_1} \sim \mathcal{O}\left(\frac{\rho_u \mathrm{u_{rms}^2 S_T}\tau}{5\mathrm{L_o}}\right), \tag{10.8}$$

where $\tau = (\mathrm{T_b} - \mathrm{T_u})/\mathrm{T_u}$ is of the order of unity for flames with high reactant temperature as in lean-burn natural gas engines. Figure 10.7 shows the comparison of the $\mathrm{L^2}$-norms of $\mathrm{T_1}$ computed using the DNS data against those from the scaling equation of Eq. (10.8) on a logarithm plot. The symbols collapse into a line with a gradient of approximately 2, suggesting the success of Eq. (10.8).

10.3.2 Term $\mathrm{T_2}$

The term $\mathrm{T_2}$ is responsible for the production of TKE due to the mean pressure gradients. Evident from Fig. 10.5, The magnitude of $\mathrm{T_2}$ is small compared to all other terms except $\mathrm{T_3}$. Note that Zhang and Rutland [266], and Nishiki *et al.* [267] found that $\mathrm{T_2}$ acts as a dominant source of TKE for flames in the corrugated flamelet

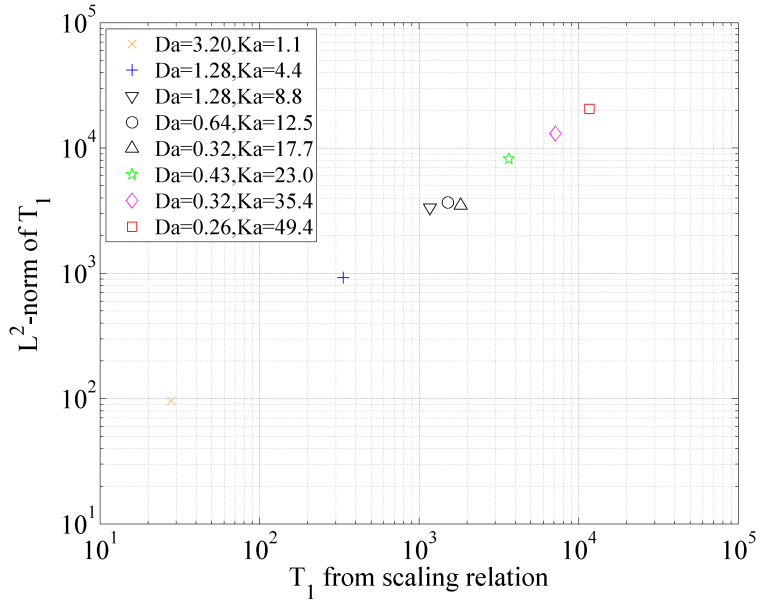

Figure 10.7. Comparison of the L^2-norms of T_1 with those obtained using the scaling equation of Eq. (10.8).

regime. As evident from Figs. 10.5(a)-10.5(d), the relative contribution of T_2 to TKE diminishes with decreasing Da and increasing Ka.

The scaling of term T_2 is examined next. Nishiki *et al.* (2002) suggested that $\overline{u''}$ can be related to the turbulent scaler flux [267] as

$$\overline{u''} = \frac{\tau}{\rho_u}\overline{\rho u'' c''}. \tag{10.9}$$

Figure 10.8 shows the comparison of $\overline{u''}$ represented by the symbols against the model of Eq. (10.9) which is plotted with lines for Cases 1, 2 ,4 and 6 where u_{rms}/S_L ranges from 2 to 20. Good agreement is observed. It is also evident that $\overline{u''}$ is of the order of the laminar flame speed. This is consistent with prior work [269] which modeled $\overline{\rho u'' c''}/\bar{\rho}$ to be proportional to S_L. The gradient of mean pressure, i.e., $d\bar{p}/dx$ is approximately the pressure drop divided by the turbulent flame brush thickness. For a laminar flame, the pressure drop across the flame is given by the Rankine-Hugoniot relations as

$$\Delta p \sim \rho_u S_L^2 \tau. \tag{10.10}$$

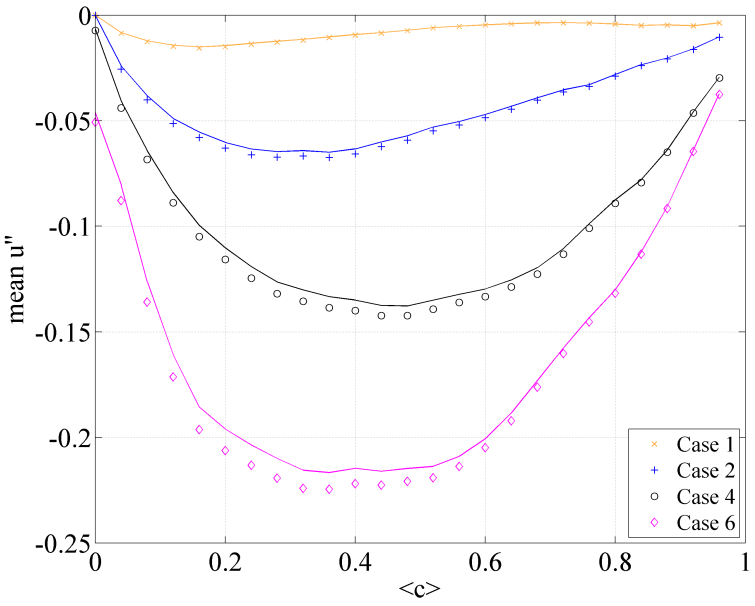

Figure 10.8. Comparison of $\overline{u''}$ (symbols) across the flame brush with the model (lines) of Nishiki *et al.* (2002) [267].

Similarly for a turbulent flame brush, the pressure drop would scale with the square of the turbulent flame speed, i.e.,

$$(\Delta \mathrm{p})_{\mathrm{tur}} \sim \rho_u \mathrm{S}_\mathrm{T}^2 \tau. \tag{10.11}$$

This implies that T_2 should scale as follows:

$$\mathrm{T}_2 \sim \mathcal{O}\left(\frac{\rho_u \mathrm{S}_\mathrm{T}^2 \mathrm{S}_\mathrm{L} \tau}{5\mathrm{L}_\mathrm{o}}\right). \tag{10.12}$$

10.3.3 Term T_4

Term T_4 represents molecular diffusion and viscous dissipation. It is evident in Fig. 10.5 that T_4 is the most dominant term and acts as a sink of TKE throughout the flame brush. The L^2-norm in Table 10.1 suggests T_4 is at least one order of magnitude larger than the other terms when Da is low (Ka is high). This explains the decay of TKE across the flame brush as shown in Fig. 10.2 for flames in the TRZ regime.

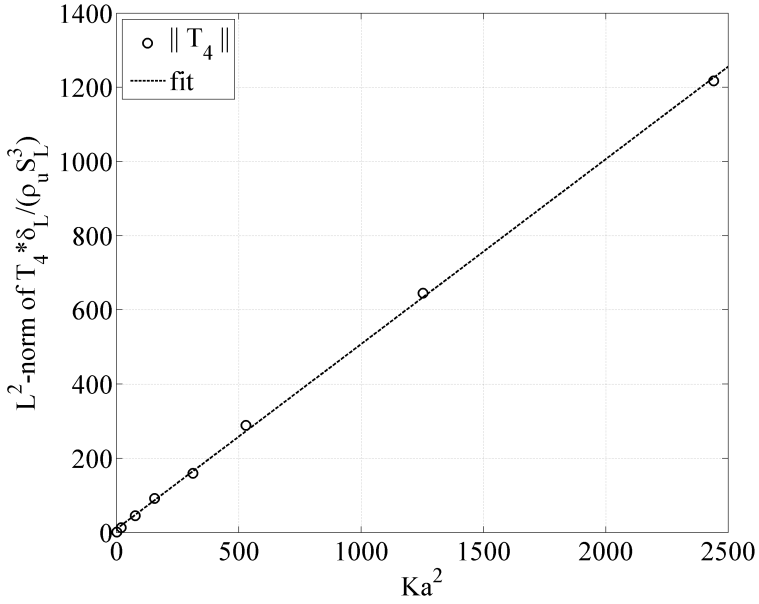

Figure 10.9. L^2-norm of normalized T_4 as a function of the squares of Ka.

By inspecting the mean values of T_4 in Table 10.1, it is seen that when the normalized turbulence intensity doubles from 5 to 10 and from 10 to 20, the L^2-norm of T_4 increases by approximately a factor of 8 in both cases. This appears to suggest that T_4 is proportional to the cube of u_{rms}. When L_o/δ_L doubles from 3.2 to 6.4 and from 6.4 to 12.8, the L^2-norm of T_4 drops by 43% and 50%, respectively, suggesting that T_4 is likely to be inversely proportional to L_o. In other words, $T_4 \propto (u_{rms}^2/L_o)$ or alternatively, $T_4 \propto Ka^2$. Figure 10.9 shows the normalized L^2-norm of T_4 as a function of the squares of the Karlovitz number. It is evident that $\|T_4\|$ scales linearly with Ka^2. The line of best-fit is plotted and the gradient is found to be 0.5. Therefore, T_4 scales with

$$T_4 \sim \mathcal{O}\left(\frac{\rho_u S_L^3}{\delta_L} Ka^2\right) = \mathcal{O}\left(\frac{\rho_u u_{rms}^3}{L_o}\right). \tag{10.13}$$

10.3.4 Term T_3 and T_5

Term T_3 which accounts for pressure dilatation stays positive within the flame brush, i.e., it acts as a source of TKE. Zhang and Rutland (1995) [266] reported that

pressure dilatation is the most important factor contributing to TKE production in corrugated flamelet regime. However in low Da and high Ka flames, the contribution of pressure dilatation remains small with respect to other terms. This is consistent with prior DNS study by Chakraborty *et al.* (2011) [268]. Term T_5 accounts for the transport of TKE by pressure fluctuations. It manifests an oscillatory behavior across the flame brush. We speculate this could be an artifact of employing the feedback control on the inflow velocity. Note that the sum of T_3 and T_5 can be written as

$$\mathrm{T}_3 + \mathrm{T}_5 = \overline{\mathrm{p}' \frac{\partial u_k''}{\partial x_k}} - \overline{\frac{\partial \mathrm{p}' u_i''}{\partial x_i}} = -\overline{u_k'' \frac{\partial \mathrm{p}'}{\partial x_k}}. \tag{10.14}$$

Launder *et al.* (1975) proposed a model for the term [270, 271] as

$$-\overline{u_k'' \frac{\partial \mathrm{p}'}{\partial x_k}} = C_1 \overline{\rho u_i'' u_i''} \frac{\partial \tilde{u}_i}{\partial x_j} - C_2 \bar{\rho} \tilde{\epsilon}, \tag{10.15}$$

where $C_1 = 1.5$ and $C_2 = 0.2$. Strahle (1983) [272] suggested that the combined contribution of T_3 and T_5 can be modeled as

$$-\overline{u_k'' \frac{\partial \mathrm{p}'}{\partial x_k}} = \frac{1}{2} C_{\mathrm{st}} \overline{\rho u_i'' u_i''} \frac{\partial \tilde{u}_i}{\partial x_j}, \tag{10.16}$$

where C_{st} is of the order of unity. Both these models suggest that $\mathrm{T}_3 + \mathrm{T}_5$ is of the order of $\overline{\rho u_i'' u_i''}(\partial \tilde{u}_i / \partial x_j)$, i.e., $\mathrm{T}_3 + \mathrm{T}_5 \sim \mathcal{O}(\mathrm{T}_1)$.

10.3.5 Term T_6

Term T_6 represents the transport of TKE by the velocity fluctuation itself. It is negative towards the unburned side but positive towards the burned side, indicating that TKE is transported from unburned to burned gas by u''. T_6 can be considered as the gradient of TKE convected by the local velocity fluctuation within the flame. Therefore, it should scale with

$$\begin{aligned} \mathrm{T}_6 &\equiv \frac{\partial}{\partial x_i} \left(\overline{\frac{1}{2} \rho u_i'' u_k'' u_k''} \right) \\ &\cong -\frac{u_u'' k_u - u_b'' k_b}{\delta_{\mathrm{T}}} \sim \mathcal{O}\left(\frac{\rho_u \mathrm{u}_{\mathrm{rms}}^3 - \rho_b \mathrm{u}_{\mathrm{rms,b}}^3}{10 \mathrm{L_o}} \right), \end{aligned} \tag{10.17}$$

where k_u and k_b represent the TKE in the unburnt and burned mixture, respectively. $u_{rms,b}$ is the root-mean-square velocity fluctuation in the product. δ_T is the turbulent flame brush thickness and is shown to be approximately 5 times the integral length scale in Fig. 10.6.

10.3.6 Relative magnitude of terms in comparison to T_4

So far, the scaling of terms $T_1 - T_6$ has been considered. It is interesting to compare the magnitude of the terms with that of T_4 in order to understand the increasing importance of T_4 in low Da, high Ka flames as observed in Figs. 10.5(a)-10.5(d). Dividing Eq. (10.8) with Eq. (10.13), we can get the ratio of T_1 and T_4, given as

$$|\frac{T_1}{T_4}| \sim \mathcal{O}\left(\frac{S_T \tau}{5 u_{rms}}\right). \tag{10.18}$$

As discussed in Chapters 8 and 9, increasing Ka reduces the flame surface area A_T and hence S_T. This effect offsets the increase in S_T due to a larger Re_T. As a result, S_T does not increase significantly beyond a certain value for u_{rms}. In other words, $S_T < u_{rms}$ in high Ka flames. This results in smaller ratio of $|T_1/T_4|$ with increasing Ka. Similarly, $T_3 + T_5$ also becomes less important with respect to T_4 in high Ka flames.

The relative magnitude of T_2 in comparison to T_4 is given by

$$|\frac{T_2}{T_4}| \sim \mathcal{O}\left(\frac{\tau}{5}\left(\frac{S_T}{u_{rms}}\right)^2 \frac{S_L}{u_{rms}}\right). \tag{10.19}$$

For high Ka flames, $S_T < u_{rms}$ and $S_L < u_{rms}$. Consequently, $|T_2/T_4|$ decreases with increasing Ka or increasing turbulence intensities. Comparing Eq. (10.19) with Eq. (10.18), it is evident that T_2 is smaller in magnitude than T_1 for flames in the TRZ regime. This is consistent with Table 10.1.

The ratio of T_6 and T_4 is computed by dividing Eq. (10.17) with Eq. (10.13) and is given as

$$|\frac{T_6}{T_4}| \sim \mathcal{O}\left(\frac{\rho_u u_{rms}^3 - \rho_b u_{rms,b}^3}{10 \rho_u u_{rms}^3}\right). \tag{10.20}$$

In the limiting case when the burned mixture becomes laminar, $|T_6/T_4|$ would be approximately 0.1. In flames with moderate Re_T, u_{rms} in the burned gas remains non-zero. In fact, Figure 10.2 shows that TKE in the burned mixture is approximately 40% of that in the reactants. This would imply that T_6 is approximately one order of magnitude lower than T_4, which is consistent with values in Table 10.1.

10.4 Summary

In this chapter, DNS results of statistically planar lean CH_4-air flames over a range of Da and Ka are examined. The focus of this study is to understand how turbulence statistics of the premixed gas vary across the flame. It is shown that turbulence kinetic energy (TKE) and its dissipation rate decreases monotonically across the flame brush while the integral length scale increases monotonically for flames in the TRZ regime. The transport equation of TKE is then examined and the scaling of each term is discussed. It is found that the term which represents molecular diffusion and viscous dissipation is the dominant term in the TKE balance. In particular, this term acts as a sink to reduce TKE across the flame and it scales with the squares of Ka. The relative importance of the other terms with respect to the dissipation term is shown to decrease with increasing Ka.

11. SUMMARY, CONCLUSIONS AND FUTURE WORK

11.1 Introduction

Lean-burn natural gas engines are attractive as they offer enhanced thermal efficiencies and reduced NOx emissions. However, achieving reliable ignition in lean natural gas is challenging because of the possibility of misfire. In addition, cycle-to-cycle variations are greater due to the slow burning velocities. The challenge to ignite the fuel can be overcome by employing a dual-fuel strategy where a pilot quantity of high CN fuel (e.g., diesel) is directly injected into the chamber that is filled with premixed natural gas and air. The pilot fuel will auto-ignite and generate multiple ignition kernels thereby accelerating the overall combustion process. This work first addresses flame ignition in dual-fuel mixtures. To reduce cycle-to-cycle variations, an improved understanding of subsequent premixed turbulent flame propagation in lean natural gas/air mixtures is vital. Such understanding can lead to the development of more accurate turbulent combustion models which can then be employed in modeling the flow and combustion in lean-burn engines. The focus of this thesis is on achieving this improved understanding of turbulent flame propagation in lean-burn mixtures.

11.2 Summary and Conclusions

A review of the literature presented in Chapter 2 shows that, while performance and emissions characteristics of dual-fuel natural gas engines with diesel injection have been studied experimentally, there is limited work discussing the ignition behavior in dual-fuel mixtures. Furthermore, turbulent flame propagation in the lean premixed natural gas is not well understood. Turbulent flame speed, in general, has been a frequent subject of inquiry as it characterizes the global effects of turbulent-chemistry interactions and it has been extensively employed in combustion modeling. Existing

correlations for premixed turbulent flame speeds are summarized but large variability is found among the correlations, as shown in Fig. 2.7. Hence, there is a need to improve the understanding of both ignition inside dual-fuel mixtures and subsequent turbulent flame propagation in lean methane-air mixtures.

The numerical tools employed in this work is described in Chapter 3. The in-house code, FLEDS, is a compressible Navier-Stokes solver with CHEMKIN-interface for solving species transport and chemical reactions. It uses a 6th-order spatial discretization and a 4th-order compact Runge-Kutta temporal scheme. A recently developed code, HOLOMAC, employs the low Mach number assumption that results in the decoupling of the thermodynamic pressure and the hydrodynamic pressure. It uses Fast Fourier Transforms (FFT) to solve the variable-coefficient Poisson equation to fulfill the divergence constraint. FLEDS and HOLOMAC are parallelized using the message passing interface (MPI) library. Speed-up efficiency up to 75% is recovered using 4096 processors in the strong scaling test and excellent performance is observed in the weak scaling test up to 32K processors.

In Chapter 4, computations are carried out of n-heptane/methane-air mixing layers under high-pressure and high-temperature conditions to provide insight into the fundamental physics of flame propagation in a lean premixed low-CN fuel/air system when ignited by autoignition of a high-CN fuel. Mixing layer thickness, pressure, and premixed fuel/air temperature and equivalence ratio are varied parametrically to understand the dependence on these variables of the characteristic time required for steady premixed flame propagation to be achieved. It is shown that the characteristic time has three components: time for autoignition to occur, time for peak temperature to be achieved following autoignition, and time for steady flame propagation in the premixed fuel/air mixture to be achieved. It is found that the autoignition time correlates well with pressure and temperature as documented in the literature. The time to achieve peak temperature is relatively short, but correlates with mixing layer thickness and premixed equivalence ratio. The time to achieve steady propagation correlates with mixing layer thickness and laminar flame speed and thickness. The

influence of turbulence is not considered as the early phase of ignition in engines is controlled by a laminar process.

Following the studies above, premixed flame propagation in turbulent flows is investigated using direction numerical simulations (DNS). To reduce the computational expenses associated with performing DNS, a novel methodology is developed to simulate turbulent premixed flames as statistically stationary in an inflow-outflow configuration using feedback control mechanism. Chapter 5 discusses the implementation of this methodology. Two forms of feedback are employed to keep the flame stationary in a statistical sense: a proportional feedback is used to produce spontaneous adjustment on the bulk inflow velocity and an integral feedback is used to shift the flame front toward a desired location. The main advantage is that the computational domain size can be decoupled from the physical flow time. This allows for statistics to be collected over an extended period of time. Methods to generate 2D and 3D turbulence for reacting simulations are also discussed in Chapter 5. An inexpensive approach which employs digital filtering of white noise and prescription of desired length scales and Reynolds stresses is used to generate 2D turbulence. Another approach discussed in Chapter 5 to generate 3D steady turbulent flows is by "linear forcing" to mimic the energy cascade process.

In Chapter 6, turbulent premixed flames in lean methane-air mixtures are simulated in a two-dimensional domain for a range of turbulent intensities (up to $u_{rms}/S_L = 11$). Turbulent flame speeds are obtained by averaging in time over more than 30 eddy turnover times once the flame becomes fully-developed. It is found that the normalized flame speeds initially increase with increasing turbulence intensities, but begin to plateau with further increase in turbulence beyond a certain threshold. Studies of premixed flames at two equivalence ratios ($\phi = 0.5$ and 0.6) show that turbulent flame speed S_T is not a function of the normalized turbulence intensity alone, but is also likely to depend on the equivalence ratio ϕ, or the Karlovitz number Ka and the Damköhler number Da. However, this conclusion could be affected by the unphysical nature of 2D turbulence which lacks the essential mechanism of vortex stretching.

In Chapter 7, 3D DNS of lean premixed flames are carried out to understand the effects of equivalence ratio on turbulent flame speed. Pressure and temperature of the reactants are selected at 20 bar and 810 K, respectively. Equivalence ratios are varied from 0.39 to 0.60. These conditions are representative of lean-burn natural gas engines. Turbulence in the reactants is forced using the "linear forcing" scheme. In this way, the velocity and length scale ratios between the flow field and the flame are held invariant throughout the course of simulation. It is found that the normalized turbulent flame speed S_T/S_L does not change with equivalence ratio above the lean limit when the Karlovitz and Damköhler number are fixed. Hence, the effect of ϕ on S_T can be modeled through Ka and Da. Analysis of flame surface area shows that surface wrinkling generated by eddies is not affected by variations in ϕ irrespective of the scales considered, provided Ka and Da are fixed. It is also found that steeper passive scalar gradients are generated by turbulence. This is resulted from the preferential alignment of the most compressive principal strain rate parallel to the flame surface normal. Varying equivalence ratio does not influence turbulence-flame alignment.

The work in Chapter 7 is extended in Chapter 8 with the objective of deriving a generalized expression for the turbulent flame speed. 3D DNS of turbulent flames propagating in lean methane/air mixtures are carried out with parametric variation of turbulence intensities (u_{rms}/S_L = 2-25) and length scales (L_o/δ_L = 3.2-12.8). The pressure is selected at 20 bar, reactant temperature at 810 K, and the equivalence ratio is selected to be 0.5. A 13-species reduced mechanism and a global mechanism are employed for the simulations. The global mechanism is found to be adequate for predicting flame surface wrinkling, flame thickness and turbulent flame speed S_T compared to the reduced mechanism.

For flames in the Thin Reaction Zone (TRZ) regime shown in Fig. 2.6(b), the normalized turbulent flame speeds S_T/S_L can be related to the flame area enhancement A_T/A_L resulting from turbulence interactions with the laminar flame and the efficiency factor I_o which is close to unity (1.07 $\pm$ 0.04) when evaluated at the tem-

perature of peak heat release rate. Furthermore, A_T/A_L is dependent on the turbulent Reynolds number Re_T and the Karlovitz number Ka. In particular, A_T/A_L is increased by increasing Re_T and by reducing Ka. Increasing Re_T increases the spectrum of scales that generates flame surface area. The dependence on the Ka is weaker but accounts for the change in surface area due to interaction between small-scale eddies and the flame. The wrinkling of the flame surface by the integral scale eddies initially increases with increasing turbulence intensities ($0 < u_{rms}/S_L < 2$) but reaches a steady value of about 3 times A_L for higher turbulence intensities ($2 < u_{rms}/S_L < 25$). A correlation for turbulent flame speed is proposed based on these observations in Section 8.4.

The effects of Karlovitz number on the evolution of flame surface area are investigated within the framework of flame stretch in Chapter 9. With increasing Ka, there is increased probability of forming highly curved surfaces locally. By examining the flame displacement speed S_d on the flame surface, it is found that on highly curved surface, irrespective of whether it is convex or concave, flame propagation dominates the tangential strain effect which results in a negative flame stretch. This, in turn, results in the reduction of flame surface area. Furthermore, conditional mean S_d on surface curvature is found to be independent of Ka or the shape factor. The physical insights derived from the analysis are applied to modeling the Flame Surface Density (FSD) equation in Section 9.6.

The effects of combustion on turbulence are investigated in Chapter 10. It is found that turbulence kinetic energy (TKE) and its dissipation rate decreases monotonically across the flame brush while the integral length scale increases monotonically for flames in the TRZ regime. The transport equation of TKE is then examined and the scaling of each term is discussed. It is found that the sink term which represents molecular diffusion and viscous dissipation is the dominant term in the TKE balance. This term is responsible for the decay of TKE across the flame brush. The relative importance of the other terms with respect to the dissipation term is shown to decrease with increasing Ka.

11.3 Future Work

It is important to assess whether the conclusions of this work are applicable for the breadth of the turbulent combustion regime map. Figure 11.1 shows the premixed combustion regime diagram by Peters (2000) [77]. The shaded rectangle represents the range of turbulence properties relative to the flame studied in this work. One suggestion for future work is to consider turbulent flames with larger integral length scales, i.e., regions on the right of the shaded rectangle. Note that the highest L_o considered in this work is 1.28 mm. In comparison, integral length scales in large lean-burn natural gas engines can be in the range of 2-5 mm. With increasing L_o, turbulent Reynolds number will increase while Karlovitz number will decrease. Based on our correlation for S_T, both of these two effects are expected to increase S_T. An important goal for the proposed study is to validate our conclusion regarding the effects of turbulent Reynolds number on flame surface wrinkling. Recall that in Figure 8.8, when the sampled flame surface area $A(\Delta)$ normalized by A_T is plotted against the sampling length Δ normalized by η, $A(\Delta)$ of all cases collapse into a single curve. More specifically, this curve represents the wrinkling generated by the spectrum of eddies from smallest scale, i.e., the Kolmogorov scale, to the largest scale, i.e., the integral length scale. A study with larger L_o and hence larger Re_T would help to validate and to improve our proposed correlation in Eq. (8.11) for describing the Re_T dependence.

Another suggestion for further work is to study turbulent flames subjected to more intense turbulence intensities and assess the potential of a transition to "distributed combustion." In Fig. 11.1, this would correspond to regions above the shaded rectangle where $Ka \gg 1$. It is argued that when $Da \ll 1$ and $Ka \gg 1$, the mode of premixed combustion becomes similar to that in a well-stirred reactor. Heat release occurs almost homogeneously throughout the flame brush, accompanied by low gradients in composition [62, 76, 273, 274]. So far, there has been no experimental evidence of distributed combustion. A fairly recent work by Aspden *et al.* (2011) considered DNS

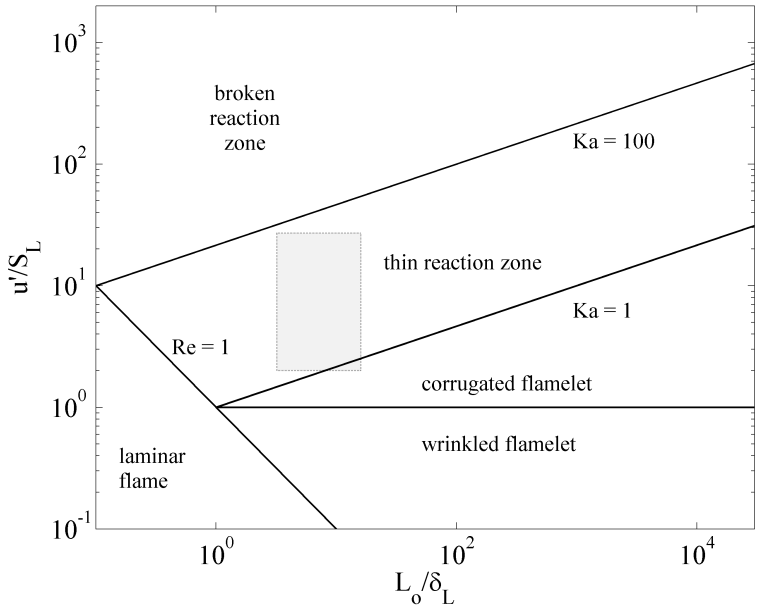

Figure 11.1. The range of turbulence conditions considered in this work on the premixed turbulent combustion regime map [77].

of premixed hydrogen-air flame with u_{rms}/S_L up to 107 and Ka up to 1562 [275]. The authors argued in favor of "a transition towards distributed combustion." It would be interesting to examine the validity of Eq. (8.1) for flames subjected to extreme turbulence. In addition, the validity of flame speed correlation presented in the thesis needs to be assessed under these conditions.

From the study of premixed flame speeds in Chapter 8, it is found that the normalized flame surface area generated by integral scale eddies reach a steady value of approximately 3 for moderate turbulence intensities. More studies are needed to elucidate the generality of this result. In other words, this result could be specific to the statistically planar flame setup that is employed in this study. It is important to examine premixed flames simulated in other geometries, such as spherical flames and V-flames, to validate this observation.

It is also important to investigate the fuel effects on the flame surface wrinkling and flame speeds. Recently, Lapointe and Blanquart (2016) considered the fuel and chemistry effects in high Ka premixed turbulent flames of n-heptane/air, toluene/air,

iso-octane/air and methane/air [276]. They found that the fuel effects on the turbulent flame speed could be essentially characterized by the set of Lewis number of all species involved in the oxidation process. In Chapter 9, we found that Lewis number plays a role in the conditional mean of $S_r + S_n$ as a function of curvature $\mathbf{H}$, and hence affects A_T/A_L and S_T/S_L. An opportunity for future study is to quantitatively characterize the Lewis effect on $S_r + S_n$. This could be done by studying the variations in $S_r + S_n$ when the Lewis number of the fuel is artificially set to some number of interests. This would provide insights on the modeling of the term $S_r + S_n$ in the context of FSD equation despite the fact that the simulated flame is unphysical.

In Chapter 4 of this thesis, ignition in the dual-fuel mixture is studied without considering the influence of turbulence. Note that at engine relevant conditions, the mixing layer thickness is of the order of 100 μm and is approximately one order of magnitude larger than the Kolmogorov scale of turbulence. The characteristic time to reach steady flame propagation reported in Chapter 4 is of the order of 1 ms. In comparison, the Kolmogorov time scale is of the order of 0.1 ms for a turbulent Reynolds number of 200. In other words, the small-scale eddies can penetrate into the mixing layer and affect local mixing under moderate turbulence levels. It is, therefore, important to assess the turbulence effects on flame development in dual-mixtures using DNS. One foreseeable challenge is associated with the computational cost. To capture the physical process of energy cascade in turbulent flows, 3D DNS is necessary. In addition, accurate modeling of the ignition behavior requires fairly detailed chemistry mechanisms to be employed.

Another opportunity to extend the study of dual-fuel ignition is to include the curvature effects. Since periodic boundary conditions are used for boundaries perpendicular to the mixing layer in Chapter 4, the mixing layer essentially remains planar. It is interesting to consider how local curvature, an effect present in 3D spaces, would influence the three phases of flame development described in Chapter 4. It is expected that curvature effect, coupled with differential diffusion, would lead to focusing/defocusing of heat and species diffusion, thereby modifying the character-

istic time scale of each individual phase identified in this work. The curvature effects can be studied by examining ignition behavior in a circular mixing layer using a 2D setup.

There is also a need to improve engine combustion models by exploiting the understanding gained in this work. Such models can then be implemented in multidimensional CFD tools to aid better design of engines.

LIST OF REFERENCES

LIST OF REFERENCES

[1] J. J. Conti. Annual energy outlook 2015. URL `www.eia.gov/forecasts/aeo`.

[2] H. M. Cho and B.-Q. He. Spark ignition natural gas enginesa review. *Energy Conversion and Management*, 48(2):608–618, 2007.

[3] T. Korakianitis, A. Namasivayam, and R. Crookes. Natural-gas fueled spark-ignition (SI) and compression-ignition (CI) engine performance and emissions. *Progress in Energy and Combustion Science*, 37(1):89–112, 2011.

[4] J. Huang and R. Crookes. Assessment of simulated biogas as a fuel for the spark ignition engine. *Fuel*, 77(15):1793–1801, 1998.

[5] U. G. Limited. Chemical composition of natural gas. URL `http://www.uniongas.com`.

[6] C. F. Blazek, J. Grimes, P. Freeman, B. K. Bailey, and C. Colucci. Fuel composition effects on natural gas vehicle emissions. *ile*, 94(3.03):0–58, 1994.

[7] NATGAS. Natural gas overview. URL `http://www.naturalgas.org`.

[8] R. Flores, J. Chen, V. Mcdonell, and G. Samuelsen. Effect of natural gas composition on the performance of a model gas turbine combustor. In *ATS Annual Workshop*, 1999.

[9] S. K. Chen and N. J. Beck. Gas engine combustion principles and applications. Technical report, SAE Technical Paper, 2001.

[10] A. Das and H. Watson. Development of a natural gas spark ignition engine for optimum performance. *Proceedings of the Institution of Mechanical Engineers, Part D: Journal of Automobile Engineering*, 211(5):361–378, 1997.

[11] J. B. Heywood. *Internal combustion engine fundamentals*, volume 930. Mcgraw-hill New York, 1988. ISBN 9780070286375.

[12] K. Varde, N. Patro, and K. Drouillard. Lean burn natural gas fueled SI engine and exhaust emissions. Technical report, SAE Technical Paper, 1995.

[13] P. Corbo, M. Gambino, S. Iannaccone, and A. Unich. Comparison between lean-burn and stoichiometric technologies for cng heavy-duty engines. Technical report, SAE Technical Paper, 1995.

[14] A. E. Hassaneen, K. S. Varde, A. H. Bawady, and A.-A. Morgan. A study of the flame development and rapid burn durations in a lean-burn fuel injected natural gas SI engine. Technical report, SAE Technical Paper, 1998.

[15] N. Kahraman, B. Çeper, S. O. Akansu, and K. Aydin. Investigation of combustion characteristics and emissions in a spark-ignition engine fuelled with natural gas–hydrogen blends. *International Journal of Hydrogen Energy*, 34(2): 1026–1034, 2009.

[16] F. Ma and Y. Wang. Study on the extension of lean operation limit through hydrogen enrichment in a natural gas spark-ignition engine. *International Journal of Hydrogen Energy*, 33(4):1416–1424, 2008.

[17] T. Sakurai, M. Iko, K. Okamoto, and F. Shoji. Basic research on combustion chambers for lean burn gas engines. Technical report, SAE Technical Paper, 1993.

[18] R. Evans. Combustion chamber design for a lean-burn SI engine. Technical report, SAE Technical Paper, 1992.

[19] B. Johansson and K. Olsson. Combustion chambers for natural gas SI engines part i: Fluid flow and combustion. Technical report, SAE Technical Paper, 1995.

[20] H. Reddy. *Numerical studies of turbulence effects on developing flames in lean methane/air homogeneous mixtures*. PhD thesis, Purdue University, 2011.

[21] Z. Chen. *Studies on the Initiation, Propagation, and Extinction of Premixed Flames*. PhD thesis, Princeton University, 2009.

[22] G. A. Karim. A review of combustion processes in the dual fuel enginethe gas diesel engine. *Progress in Energy and Combustion Science*, 6(3):277–285, 1980.

[23] G. A. Karim. Combustion in gas fueled compression: ignition engines of the dual fuel type. *Journal of Engineering for Gas Turbines and Power*, 125(3): 827–836, 2003.

[24] J. Kusaka, T. Okamoto, Y. Daisho, R. Kihara, and T. Saito. Combustion and exhaust gas emission characteristics of a diesel engine dual-fueled with natural gas. *JSAE review*, 21(4):489–496, 2000.

[25] M. Y. Selim. Pressure–time characteristics in diesel engine fueled with natural gas. *Renewable Energy*, 22(4):473–489, 2001.

[26] R. Papagiannakis and D. Hountalas. Experimental investigation concerning the effect of natural gas percentage on performance and emissions of a di dual fuel diesel engine. *Applied Thermal Engineering*, 23(3):353–365, 2003.

[27] B. Sahoo, N. Sahoo, and U. Saha. Effect of engine parameters and type of gaseous fuel on the performance of dual-fuel gas diesel enginesa critical review. *Renewable and Sustainable Energy Reviews*, 13(6):1151–1184, 2009.

[28] M. Y. Selim. Effect of engine parameters and gaseous fuel type on the cyclic variability of dual fuel engines. *Fuel*, 84(7):961–971, 2005.

[29] A. Namasivayam, R. Crookes, T. Korakianitis, and J. Olsen. Assessment of combustion in natural gas dual-fuelled compression ignition engines with dimethyl ether and rapeseed methyl ester pilot ignition. *International Journal of Engine Research*, 10(3):165–174, 2009.

[30] A. Namasivayam, R. Crookes, T. Korakianitis, and K. Bob-Manuel. Combustion characteristics of dual-fuel diesel engine using emulsified bio-fuel for pilot ignition. Technical report, SAE Technical Paper, 2009.

[31] N. Milovanovic and R. Chen. A review of experimental and simulation studies on controlled auto-ignition combustion. Technical report, SAE Technical Paper, 2001.

[32] J. Abraham, F. Bracco, and R. Reitz. Comparisons of computed and measured premixed charge engine combustion. *Combustion and Flame*, 60(3):309–322, 1985.

[33] A. Linan. The asymptotic structure of counterflow diffusion flames for large activation energies. *Acta Astronautica*, 1(7):1007–1039, 1974.

[34] H. Ciezki and G. Adomeit. Shock-tube investigation of self-ignition of n-heptane-air mixtures under engine relevant conditions. *Combustion and Flame*, 93(4):421–433, 1993.

[35] A. Chakir, M. Bellimam, J. Boettner, and M. Cathonnet. Kinetic study of n-heptane oxidation. *International Journal of Chemical Kinetics*, 24(4):385–410, 1992.

[36] P. Dagaut, M. Reuillon, and M. Cathonnet. Experimental study of the oxidation of n-heptane in a jet stirred reactor from low to high temperature and pressures up to 40 atm. *Combustion and Flame*, 101(1):132–140, 1995.

[37] J. Griffiths, K. Hughes, M. Schreiber, and C. Poppe. A unified approach to the reduced kinetic modeling of alkane combustion. *Combustion and Flame*, 99(3): 533–540, 1994.

[38] R. Minetti, M. Carlier, M. Ribaucour, E. Therssen, and L. Sochet. A rapid compression machine investigation of oxidation and auto-ignition of n-heptane: measurements and modeling. *Combustion and Flame*, 102(3):298–309, 1995.

[39] K. Sahetchian, R. Rigny, and S. Circan. Identification of the hydroperoxide formed by isomerization reactions during the oxidation of n-heptane in a reactor and cfr engine. *Combustion and Flame*, 85(3):511–514, 1991.

[40] W. R. Leppard. The autoignition chemistries of primary reference fuels, olefin/paraffin binary mixtures, and non-linear octane blending. Technical report, SAE Technical Paper, 1992.

[41] A. Cavaliere, A. Ciajolo, A. D'anna, R. Mercogliano, and R. Ragucci. Autoignition of n-heptane and n-tetradecane in engine-like conditions. *Combustion and Flame*, 93(3):279–286, 1993.

[42] H. Curran, P. Gaffuri, W. J. Pitz, and C. K. Westbrook. A comprehensive modeling study of n-heptane oxidation. *Combustion and Flame*, 114(1):149–177, 1998.

[43] C. Callahan, T. Held, F. Dryer, R. Minetti, M. Ribaucour, L. Sochet, T. Faravelli, P. Gaffuri, and E. Rani. Experimental data and kinetic modeling of primary reference fuel mixtures. In *Symposium (International) on Combustion*, volume 26, pages 739–746. Elsevier, 1996.

[44] P. Lignola and E. Reverchon. A jet stirred reactor for combustion studies: design and characterization. *Combustion Science and Technology*, 60(4-6):319–333, 1988.

[45] R. Seiser, H. Pitsch, K. Seshadri, W. Pitz, and H. Gurran. Extinction and autoignition of n-heptane in counterflow configuration. *Proceedings of the Combustion Institute*, 28(2):2029–2037, 2000.

[46] N. Peters, G. Paczko, R. Seiser, and K. Seshadri. Temperature cross-over and non-thermal runaway at two-stage ignition of n-heptane. *Combustion and Flame*, 128(1):38–59, 2002.

[47] F. Maroteaux and L. Noel. Development of a reduced n-heptane oxidation mechanism for HCCI combustion modeling. *Combustion and Flame*, 146(1): 246–267, 2006.

[48] C. S. Yoo, T. Lu, J. H. Chen, and C. K. Law. Direct numerical simulations of ignition of a lean n-heptane/air mixture with temperature inhomogeneities at constant volume: Parametric study. *Combustion and Flame*, 158(9):1727–1741, 2011.

[49] S. Liu, J. C. Hewson, J. H. Chen, and H. Pitsch. Effects of strain rate on high-pressure nonpremixed n-heptane autoignition in counterflow. *Combustion and Flame*, 137(3):320–339, 2004.

[50] S. Mukhopadhyay and J. Abraham. Influence of compositional stratification on autoignition in n-heptane/air mixtures. *Combustion and Flame*, 158(6): 1064–1075, 2011.

[51] G. Bansal, H. G. Im, and S.-R. Lee. Autoignition of non-premixed n-heptane/air counterflow subjected to unsteady scalar dissipation rate. *Proceedings of the Combustion Institute*, 32(1):1083–1090, 2009.

[52] E. Mastorakos, T. Baritaud, and T. Poinsot. Numerical simulations of autoignition in turbulent mixing flows. *Combustion and Flame*, 109(1):198–223, 1997.

[53] H. Pitsch and N. Peters. Investigation of the ignition process of sprays under diesel engine conditions using reduced n-heptane chemistry. Technical report, SAE Technical Paper, 1998.

[54] V. Gopalakrishnan and J. Abraham. An investigation of ignition behavior in diesel sprays. *Proceedings of the Combustion Institute*, 29(1):641–646, 2002.

[55] V. Gopalakrishnan and J. Abraham. Effects of multicomponent diffusion on predicted ignition characteristics of an n-heptane diffusion flame. *Combustion and Flame*, 136(4):557–566, 2004.

[56] E. Mastorakos. Ignition of turbulent non-premixed flames. *Progress in Energy and Combustion Science*, 35(1):57–97, 2009.

[57] L. Shenghua, Z. Longbao, W. Ziyan, and R. Jiang. Combustion characteristics of compressed natural gas/diesel dual-fuel turbocharged compressed ignition engine. *Proceedings of the Institution of Mechanical Engineers, Part D: Journal of Automobile Engineering*, 217(9):833–838, 2003.

[58] A. Carlucci, A. Ficarella, and D. Laforgia. Control of the combustion behaviour in a diesel engine using early injection and gas addition. *Applied Thermal Engineering*, 26(17):2279–2286, 2006.

[59] R. Crookes and K. Bob-Manuel. Rme or dme: a preferred alternative fuel option for future diesel engine operation. *Energy Conversion and Management*, 48(11): 2971–2977, 2007.

[60] E. Khalil and G. Karim. A kinetic investigation of the role of changes in the composition of natural gas in engine applications. *Journal of Engineering for Gas Turbines and Power*, 124(2):404–411, 2002.

[61] Z. Liu and G. Karim. An examination of the ignition delay period in gas-fueled diesel engines. *Journal of Engineering for Gas Turbines and Power*, 120(1): 225–231, 1998.

[62] F. Williams. *Combustion Theory: The Fundamental Theory of Chemically Reacting Flow Systems*. Perseus Books Group, 1985. ISBN 9780201407778.

[63] S. B. Pope. *Turbulent flows*. Cambridge university press, 2000.

[64] B. E. Launder and D. Spalding. The numerical computation of turbulent flows. *Computer Methods in Applied Mechanics and Engineering*, 3(2):269–289, 1974.

[65] J. Smagorinsky. General circulation experiments with the primitive equations: I. the basic experiment*. *Monthly Weather Review*, 91(3):99–164, 1963.

[66] J. Ferziger. Subgrid-scale modeling. *Large eddy simulation of complex engineering and geophysical flows*, pages 37–54, 1993.

[67] C. Fureby, G. Tabor, H. Weller, and A. Gosman. A comparative study of subgrid scale models in homogeneous isotropic turbulence. *Physics of Fluids (1994-present)*, 9(5):1416–1429, 1997.

[68] C. Fureby. Large eddy simulation of rearward-facing step flow. *AIAA journal*, 37(11):1401–1410, 1999.

[69] A. Yoshizawa. Statistical theory for compressible turbulent shear flows, with the application to subgrid modeling. *Physics of Fluids (1958-1988)*, 29(7): 2152–2164, 1986.

[70] J. Ghojel. Review of the development and applications of the wiebe function: a tribute to the contribution of ivan wiebe to engine research. *International Journal of Engine Research*, 11(4):297–312, 2010.

[71] R. J. Tabaczynski, C. R. Ferguson, and K. Radhakrishnan. A turbulent entrainment model for spark-ignition engine combustion. Technical report, SAE Technical Paper, 1977.

[72] G. Beretta, M. Rashidi, and J. Keck. Turbulent flame propagation and combustion in spark ignition engines. *Combustion and Flame*, 52:217–245, 1983.

[73] F. V. Bracco. Introducing a new generation of more detailed and informative combustion models. Technical report, SAE Technical Paper, 1975.

[74] T. Butler and P. O'rourke. A numerical method for two dimensional unsteady reacting flows. In *Symposium (International) on Combustion*, volume 16, pages 1503–1515. Elsevier, 1977.

[75] P. A. Libby and F. Williams. Some implications of recent theoretical studies in turbulent combustion. *AIAA Journal*, 19(3):261–274, 1981.

[76] J. Abraham, F. A. Williams, and F. V. Bracco. A discussion of turbulent flame structure in premixed charges. Technical report, SAE Technical Paper, 1985.

[77] N. Peters. *Turbulent combustion*. Cambridge university press, 2000.

[78] R. Borghi and D. Escudie. Assessment of a theoretical model of turbulent combustion by comparison with a simple experiment. *Combustion and Flame*, 56(2):149–164, 1984.

[79] N. Peters. Laminar flamelet concepts in turbulent combustion. In *Symposium (International) on Combustion*, volume 21, pages 1231–1250. Elsevier, 1988.

[80] D. Spalding. Mixing and chemical reaction in steady confined turbulent flames. In *Symposium (International) on Combustion*, volume 13, pages 649–657. Elsevier, 1971.

[81] B. Magnussen and B. Hjertager. Sixteenth symposium (international) on combustion. *The Combustion Institute, Pittsburgh*, page 719, 1976.

[82] F. Grasso and F. Bracco. Evaluation of a mixing-controlled model for engine combustion. *Combustion Science and Technology*, 28(5-6):185–210, 1982.

[83] S.-C. Kong, N. Ayoub, and R. D. Reitz. Modeling combustion in compression ignition homogeneous charge engines. Technical report, SAE Technical Paper, 1992.

[84] Z.-X. Hou and J. Abraham. Three-dimensional modeling of soot and no in a direct-injection diesel engine. Technical report, SAE Technical Paper, 1995.

[85] A. R. Wadhwa, V. Gopalakrishnan, and J. Abraham. A mixture fraction averaged approach to modeling no and soot in diesel engines. Technical report, SAE Technical Paper, 2001.

[86] A. Zur Loye and F. Bracco. Two-dimensional visualization of ignition kernels in an ic engine. *Combustion and Flame*, 69(1):59–69, 1987.

[87] J. Mantzaras, P. G. Felton, and F. V. Bracco. Three-dimensional visualization of premixed-charge engine flames: islands of reactants and products; fractal dimensions; and homogeneity. Technical report, SAE Technical Paper, 1988.

[88] F. Bracco. Structure of flames in premixed-charge ic engines. *Combustion Science and Technology*, 58(1-3):209–230, 1988.

[89] K. Bray, P. A. Libby, and J. Moss. Unified modeling approach for premixed turbulent combustionpart i: General formulation. *Combustion and Flame*, 61 (1):87–102, 1985.

[90] T. Mantel and R. Borghi. A new model of premixed wrinkled flame propagation based on a scalar dissipation equation. *Combustion and Flame*, 96(4):443–457, 1994.

[91] V. Yakhot. Propagation velocity of premixed turbulent flames. *Combustion Science and Technology*, 60(1-3):191–214, 1988.

[92] Z. Tan and R. D. Reitz. Modeling ignition and combustion in spark-ignition engines using a level set method. Technical report, SAE Technical Paper, 2003.

[93] J. Ewald and N. Peters. On unsteady premixed turbulent burning velocity prediction in internal combustion engines. *Proceedings of the Combustion Institute*, 31(2):3051–3058, 2007.

[94] W. K. Cheng and J. A. Diringer. Numerical modelling of SI engine combustion with a flame sheet model. Technical report, SAE Technical Paper, 1991.

[95] F. E. Marble and J. E. Broadwell. The coherent flame model for turbulent chemical reactions. Technical report, DTIC Document, 1977.

[96] P. Boudier, S. Henriot, T. Poinsot, and T. Baritaud. A model for turbulent flame ignition and propagation in spark ignition engines. In *Symposium (International) on Combustion*, volume 24, pages 503–510. Elsevier, 1992.

[97] X. Zhao, R. D. Matthews, and J. L. Ellzey. Three-dimensional numerical simulation of flame propagation in spark ignition engines. Technical report, SAE Technical Paper, 1993.

[98] S. M. Candel and T. J. Poinsot. Flame stretch and the balance equation for the flame area. *Combustion Science and Technology*, 70(1-3):1–15, 1990.

[99] D. Veynante, J. Piana, J. Duclos, and C. Martel. Experimental analysis of flame surface density models for premixed turbulent combustion. In *Symposium (International) on Combustion*, volume 26, pages 413–420. Elsevier, 1996.

[100] M. Boger, D. Veynante, H. Boughanem, and A. Trouvé. Direct numerical simulation analysis of flame surface density concept for large eddy simulation of turbulent premixed combustion. In *Symposium (International) on Combustion*, volume 27, pages 917–925. Elsevier, 1998.

[101] F. Charlette, C. Meneveau, and D. Veynante. A power-law flame wrinkling model for les of premixed turbulent combustion part i: non-dynamic formulation and initial tests. *Combustion and Flame*, 131(1):159–180, 2002.

[102] C. Angelberger, D. Veynante, F. Egolfopoulos, and T. Poinsot. Large eddy simulations of combustion instabilities in premixed flames. In *Proc. of the Summer Program*, pages 61–82. Citeseer, 1998.

[103] E. Hawkes and R. Cant. A flame surface density approach to large-eddy simulation of premixed turbulent combustion. *Proceedings of the Combustion Institute*, 28(1):51–58, 2000.

[104] E. O'brien. The probability density function (pdf) approach to reacting turbulent flows. In *Turbulent Reacting Flows*, pages 185–218. Springer, 1980.

[105] S. Pope. Pdf methods for turbulent reactive flows. *Progress in Energy and Combustion Science*, 11(2):119–192, 1985.

[106] H. Pitsch and M. Ihme. An unsteady/flamelet progress variable method for les of nonpremixed turbulent combustion. *AIAA paper*, 557:2005, 2005.

[107] C. Bajaj, M. Ameen, and J. Abraham. Evaluation of an unsteady flamelet progress variable model for autoignition and flame lift-off in diesel jets. *Combustion Science and Technology*, 185(3):454–472, 2013.

[108] B. Fiorina, O. Gicquel, L. Vervisch, S. Carpentier, and N. Darabiha. Premixed turbulent combustion modeling using tabulated detailed chemistry and pdf. *Proceedings of the Combustion Institute*, 30(1):867–874, 2005.

[109] J. Galpin, A. Naudin, L. Vervisch, C. Angelberger, O. Colin, and P. Domingo. Large-eddy simulation of a fuel-lean premixed turbulent swirl-burner. *Combustion and Flame*, 155(1):247–266, 2008.

[110] J. Galpin, C. Angelberger, A. Naudin, and L. Vervisch. Large-eddy simulation of h2–air auto-ignition using tabulated detailed chemistry. *Journal of Turbulence*, (9):N13, 2008.

[111] G. Albouze, T. Poinsot, and L. Gicquel. Chemical kinetics modeling and les combustion model effects on a perfectly premixed burner. *Comptes Rendus Mécanique*, 337(6):318–328, 2009.

[112] B. Lewis and G. von Elbe. *Combustion, Flames and Explosives of Gases*. Academic Press, 1961.

[113] T.-W. Lee, G. North, and D. Santavicca. Curvature and orientation statistics of turbulent premixed flame fronts. *Combustion Science and Technology*, 84(1-6): 121–132, 1992.

[114] R. Paul and K. Bray. Study of premixed turbulent combustion including landaudarrieus instability effects. In *Symposium (International) on Combustion*, volume 26, pages 259–266. Elsevier, 1996.

[115] Y. D'angelo, G. Joulin, and G. Boury. On model evolution equations for the whole surface of three-dimensional expanding wrinkled premixed flames. *Combustion Theory and Modelling*, 4(3):317–338, 2000.

[116] V. Zimont, W. Polifke, M. Bettelini, and W. Weisenstein. An efficient computational model for premixed turbulent combustion at high reynolds numbers based on a turbulent flame speed closure. In *ASME 1997 International Gas Turbine and Aeroengine Congress and Exhibition*, pages V002T06A054–V002T06A054. American Society of Mechanical Engineers, 1997.

[117] P. Flohr and H. Pitsch. A turbulent flame speed closure model for les of industrial burner flows. In *Proceedings of the summer program*, pages 169–179, 2000.

[118] V. Zimont. To computations of turbulent combustion of partially premixed gases. *Chemical Physics of Combustion and Explosion Processes. Combustion of Multi-Phase and Gas Systems*, pages 77–80, 1977.

[119] J. F. Driscoll. Turbulent premixed combustion: Flamelet structure and its effect on turbulent burning velocities. *Progress in Energy and Combustion Science*, 34(1):91–134, 2008.

[120] A. Lipatnikov and J. Chomiak. Turbulent flame speed and thickness: phenomenology, evaluation, and application in multi-dimensional simulations. *Progress in Energy and Combustion Science*, 28(1):1–74, 2002.

[121] S. H. Kim and R. W. Bilger. Iso-surface mass flow density and its implications for turbulent mixing and combustion. *Journal of Fluid Mechanics*, 590:381–409, 2007.

[122] H. Kolla, J. Rogerson, and N. Swaminathan. Validation of a turbulent flame speed model across combustion regimes. *Combustion Science and Technology*, 182(3):284–308, 2010.

[123] G. Damköhler. Der einfluß der turbulenz auf die flammengeschwindigkeit in gasgemischen. *Zeitschrift für Elektrochemie und angewandte physikalische Chemie*, 46(11):601–626, 1940.

[124] P. Clavin and F. Williams. Theory of premixed-flame propagation in large-scale turbulence. *Journal of Fluid Mechanics*, 90(03):589–604, 1979.

[125] P. Clavin and F. Williams. Effects of molecular diffusion and of thermal expansion on the structure and dynamics of premixed flames in turbulent flows of large scale and low intensity. *Journal of Fluid Mechanics*, 116:251–282, 1982.

[126] A. R. Kerstein and W. T. Ashurst. Passage rates of propagating interfaces in randomly advected media and heterogeneous media. *Physical Review E*, 50(2): 1100, 1994.

[127] A. Klimov. Premixed turbulent flames-interplay of hydrodynamic and chemical phenomena. *Flames, Lasers, and Reactive Systems*, 1:133–146, 1983.

[128] A. R. Kerstein. A linear-eddy model of turbulent scalar transport and mixing. *Combustion Science and Technology*, 60(4-6):391–421, 1988.

[129] F. Gouldin. An application of fractals to modeling premixed turbulent flames. *Combustion and Flame*, 68(3):249–266, 1987.

[130] Y. Liu and B. Lenze. The influence of turbulence on the burning velocity of premixed ch 4-h 2 flames with different laminar burning velocities. In *Symposium (International) on Combustion*, volume 22, pages 747–754. Elsevier, 1989.

[131] Ö. L. Gülder. Turbulent premixed flame propagation models for different combustion regimes. In *Symposium (International) on Combustion*, volume 23, pages 743–750. Elsevier, 1991.

[132] S. Daniele, P. Jansohn, J. Mantzaras, and K. Boulouchos. Turbulent flame speed for syngas at gas turbine relevant conditions. *Proceedings of the Combustion Institute*, 33(2):2937–2944, 2011.

[133] D. Ballal and A. Lefebvre. The structure and propagation of turbulent flames. In *Proceedings of the Royal Society of London A: Mathematical, Physical and Engineering Sciences*, volume 344, pages 217–234. The Royal Society, 1975.

[134] D. Ballal. The structure of a premixed turbulent flame. *Proceedings of the Royal Society of London. A. Mathematical and Physical Sciences*, 367(1730):353–380, 1979.

[135] I. Shepherd, E. Bourguignon, Y. Michou, and I. Gökalp. The burning rate in turbulent bunsen flames. In *Symposium (International) on Combustion*, volume 27, pages 909–916. Elsevier, 1998.

[136] K. Smith and F. Gouldin. Turbulence effects on flame speed and flame structure. *AIAA Journal*, 17(11):1243–1250, 1979.

[137] S. Chaibongsai, T. Kadota, and N. Henein. The burning velocity in a cfr engine with different turbulent flow fields generated by intake valves. Technical report, SAE Technical Paper, 1980.

[138] S. Li, P. A. Libby, and F. Williams. Experimental investigation of a premixed flame in an impinging turbulent stream. In *Symposium (International) on Combustion*, volume 25, pages 1207–1214. Elsevier, 1994.

[139] B. Leisenheimer and W. Leuckel. Self-generated acceleration of confined deflagrative flame fronts. *Combustion Science and Technology*, 118(1-3):147–164, 1996.

[140] H. Kobayashi. Experimental study of high-pressure turbulent premixed flames. *Experimental Thermal and Fluid Science*, 26(2):375–387, 2002.

[141] S. R. Muppala, N. K. Aluri, F. Dinkelacker, and A. Leipertz. Development of an algebraic reaction rate closure for the numerical calculation of turbulent premixed methane, ethylene, and propane/air flames for pressures up to 1.0 mpa. *Combustion and Flame*, 140(4):257–266, 2005.

[142] J. Ritzinger, T. Koch, J. Lehmann, and K. Boulouchos. Influence of fuel composition and combustion process on thermodynamic parameters of SI engines. Technical report, SAE Technical Paper, 2012.

[143] F. Creta and M. Matalon. Propagation of wrinkled turbulent flames in the context of hydrodynamic theory. *Journal of Fluid Mechanics*, 680:225–264, 2011.

[144] M. Tanahashi, S. Kikuta, N. Shiwaku, and T. Miyauchi. Local flame structure of ch4-air turbulent premixed flames. In *Proceedings of The Sixteenth International Symposium on Transport Phenomena*, volume 400, 2005.

[145] A. Y. Poludnenko and E. S. Oran. The interaction of high-speed turbulence with flames: Global properties and internal flame structure. *Combustion and Flame*, 157(5):995–1011, 2010.

[146] A. Y. Poludnenko and E. S. Oran. The interaction of high-speed turbulence with flames: Turbulent flame speed. *Combustion and Flame*, 158(2):301–326, 2011.

[147] A. Aspden, M. Day, and J. Bell. Turbulence-chemistry interaction in lean premixed hydrogen combustion. *Proceedings of the Combustion Institute*, 35 (2):1321–1329, 2015.

[148] Y.-S. Shim, N. Fukushima, M. Shimura, Y. Nada, M. Tanahashi, and T. Miyauchi. Radical fingering in turbulent premixed flame classified into thin reaction zones. *Proceedings of the Combustion Institute*, 34(1):1383–1391, 2013.

[149] J. Abraham and V. Magi. Exploring velocity and density ratio effects in a mixing layer using dns. *International Journal of Computational Fluid Dynamics*, 8(2): 147–151, 1997.

[150] A. Viggiano and V. Magi. A 2-d investigation of n-heptane autoignition by means of direct numerical simulation. *Combustion and Flame*, 137(4):432–443, 2004.

[151] J. W. Anders. *Turbulence and residual gas effects in pulsed diesel jets*. PhD thesis, Purdue University, 2006.

[152] E. Motheau and J. Abraham. A high-order numerical algorithm for dns of low-mach-number reactive flows with detailed chemistry and quasi-spectral accuracy. *Journal of Computational Physics*, 313:430–454, 2016.

[153] S. K. Lele. Compact finite difference schemes with spectral-like resolution. *Journal of Computational Physics*, 103(1):16–42, 1992.

[154] S. Conte and C. de Boor. *Elementary Numerical Analysis: An Algorithmic Approach*. McGraw-Hill Book Company, 1972. ISBN 9780070851290.

[155] B. Carnahan, H. Luther, and J. Wilkes. *Applied numerical methods*. Wiley, 1969.

[156] S. Gill. A process for the step-by-step integration of differential equations in an automatic digital computing machine. In *Mathematical Proceedings of the Cambridge Philosophical Society*, volume 47, pages 96–108. Cambridge Univ Press, 1951.

[157] R. Courant, K. Friedrichs, and H. Lewy. Über die partiellen differenzengleichungen der mathematischen physik. *Mathematische Annalen*, 100(1):32–74, 1928.

[158] T. Poinsot, C. Le Chatelier, S. Candel, and E. Esposito. Experimental determination of the reflection coefficient of a premixed flame in a duct. *Journal of Sound and Vibration*, 107(2):265–278, 1986.

[159] T. J. Poinsot and S. Lele. Boundary conditions for direct simulations of compressible viscous flows. *Journal of Computational Physics*, 101(1):104–129, 1992.

[160] K. W. Thompson. Time dependent boundary conditions for hyperbolic systems. *Journal of Computational Physics*, 68(1):1–24, 1987.

[161] J. Anders, V. Magi, and J. Abraham. Large-eddy simulation in the near-field of a transient multi-component gas jet with density gradients. *Computers & Fluids*, 36(10):1609–1620, 2007.

[162] J. C. Strikwerda. Initial boundary value problems for incompletely parabolic systems. *Communications on Pure and Applied Mathematics*, 30(6):797–822, 1977.

[163] M. Sayeed, V. Magi, and J. Abraham. Enhancing the performance of a parallel solver for turbulent reacting flow simulations. *Numerical Heat Transfer, Part B: Fundamentals*, 59(3):169–189, 2011.

[164] V. Giovangigli. *Multicomponent Flow Modeling*. Birkhäuser Boston, 1999. ISBN 9780817640484.

[165] G. Strang. *Introduction to Applied Mathematics*. Wellesley-Cambridge Press, 1986. ISBN 9780961408800.

[166] S. Laizet and E. Lamballais. High-order compact schemes for incompressible flows: A simple and efficient method with quasi-spectral accuracy. *Journal of Computational Physics*, 228(16):5989–6015, 2009.

[167] S. Laizet and N. Li. Incompact3d: A powerful tool to tackle turbulence problems with up to o (105) computational cores. *International Journal for Numerical Methods in Fluids*, 67(11):1735–1757, 2011.

[168] N. Li and S. Laizet. 2decomp&fft–a highly scalable 2d decomposition library and fft interface. In *Cray User Group 2010 conference*, pages 1–13, 2010.

[169] J. G. Verwer, B. P. Sommeijer, and W. Hundsdorfer. Rkc time-stepping for advection–diffusion–reaction problems. *Journal of Computational Physics*, 201 (1):61–79, 2004.

[170] R. Yu, J. Yu, and X.-S. Bai. An improved high-order scheme for dns of low mach number turbulent reacting flows based on stiff chemistry solver. *Journal of Computational Physics*, 231(16):5504–5521, 2012.

[171] F. Nicoud. Numerical study of a channel flow with variable properties. *Center for Turbulent Research, Annual Research Briefs*, pages 289–309, 1998.

[172] J. Anders, V. Magi, and J. Abraham. A computational investigation of the interaction of pulses in two-pulse jets. *Numerical Heat Transfer, Part A: Applications*, 54(11):999–1021, 2008.

[173] R. Venugopal and J. Abraham. A 2-d dns investigation of extinction and reignition dynamics in nonpremixed flame–vortex interactions. *Combustion and Flame*, 153(3):442–464, 2008.

[174] R. Owston and J. Abraham. Structure of hydrogen triple flames and premixed flames compared. *Combustion and Flame*, 157(8):1552–1565, 2010.

[175] H. Reddy and J. Abraham. A numerical study of vortex interactions with flames developing from ignition kernels in lean methane/air mixtures. *Combustion and Flame*, 158(3):401–415, 2011.

[176] H. Reddy and J. Abraham. Two-dimensional direct numerical simulation evaluation of the flame-surface density model for flames developing from an ignition kernel in lean methane/air mixtures under engine conditions. *Physics of Fluids (1994-present)*, 24(10):105108, 2012.

[177] M. M. Ameen and J. Abraham. Rans and les study of lift-off physics in reacting diesel jets. Technical report, SAE Technical Paper, 2014.

[178] S. Hires, R. Tabaczynski, and J. Novak. The prediction of ignition delay and combustion intervals for a homogeneous charge, spark ignition engine. Technical report, SAE Technical Paper, 1978.

[179] J. C. Keck. Turbulent flame structure and speed in spark-ignition engines. In *Symposium (International) on Combustion*, volume 19, pages 1451–1466. Elsevier, 1982.

[180] J. A. Gatowski, J. B. Heywood, and C. Deleplace. Flame photographs in a spark-ignition engine. *Combustion and Flame*, 56(1):71–81, 1984.

[181] Z. Wang and J. Abraham. Fundamental physics of flame development in an autoigniting dual fuel mixture. *Proceedings of the Combustion Institute*, 35(1): 1041–1048, 2015.

[182] L. Vervisch and T. Poinsot. Direct numerical simulation of non-premixed turbulent flames. *Annual Review of Fluid Mechanics*, 30(1):655–691, 1998.

[183] G. Smith, D. Golden, M. Frenklach, N. Moriarty, B. Eiteneer, M. Goldenberg, C. Bowman, R. Hanson, S. Song, W. Gardiner, V. Lissianski, and Z. Qin. Grimech 3.0. URL `http://www.me.berkeley.edu/gri_mech/`.

[184] T. Yoshikawa and R. D. Reitz. Development of an improved nox reaction mechanism for low temperature diesel combustion modeling. Technical report, SAE Technical Paper, 2008.

[185] X. Gu, M. Haq, M. Lawes, and R. Woolley. Laminar burning velocity and markstein lengths of methane–air mixtures. *Combustion and Flame*, 121(1): 41–58, 2000.

[186] G. Rozenchan, D. Zhu, C. Law, and S. Tse. Outward propagation, burning velocities, and chemical effects of methane flames up to 60 atm. *Proceedings of the Combustion Institute*, 29(2):1461–1470, 2002.

[187] S. Aggarwal, O. Awomolo, and K. Akber. Ignition characteristics of heptane–hydrogen and heptane–methane fuel blends at elevated pressures. *International Journal of Hydrogen Energy*, 36(23):15392–15402, 2011.

[188] P. F. Flynn, R. P. Durrett, G. L. Hunter, A. O. zur Loye, O. Akinyemi, J. E. Dec, and C. K. Westbrook. Diesel combustion: an integrated view combining laser diagnostics, chemical kinetics, and empirical validation. 1999.

[189] C. K. Westbrook. Chemical kinetics of hydrocarbon ignition in practical combustion systems. *Proceedings of the Combustion Institute*, 28(2):1563–1577, 2000.

[190] S. Correa and A. Gulati. Measurements and modeling of a bluff body stabilized flame. *Combustion and Flame*, 89(2):195–213, 1992.

[191] D. G. Lilley. Swirl flows in combustion: a review. *AIAA journal*, 15(8):1063–1078, 1977.

[192] P. Cho, C. Law, R. Cheng, and I. Shepherd. Velocity and scalar fields of turbulent premixed flames in stagnation flow. In *Symposium (International) on Combustion*, volume 22, pages 739–745. Elsevier, 1989.

[193] J. Bell, M. Day, J. Grcar, and M. Lijewski. Active control for statistically stationary turbulent premixed flame simulations. *Communications in Applied Mathematics and Computational Science*, 1(1):29–51, 2007.

[194] M. Fathali, M. Klein, T. Broeckhoven, C. Lacor, and M. Baelmans. Generation of turbulent inflow and initial conditions based on multi-correlated random fields. *International Journal for Numerical Methods in Fluids*, 57(1):93–117, 2008.

[195] M. Klein, A. Sadiki, and J. Janicka. A digital filter based generation of inflow data for spatially developing direct numerical or large eddy simulations. *Journal of Computational Physics*, 186(2):652–665, 2003.

[196] T. Lundgren. Linearly forced isotropic turbulence. *Annual Research Briefs*, pages 461–473, 2003.

[197] C. Rosales and C. Meneveau. Linear forcing in numerical simulations of isotropic turbulence: Physical space implementations and convergence properties. *Physics of Fluids (1994-present)*, 17(9):095106, 2005.

[198] P. L. Carroll and G. Blanquart. A proposed modification to lundgren's physical space velocity forcing method for isotropic turbulence. *Physics of Fluids (1994-present)*, 25(10):105114, 2013.

[199] J. B. Bell, M. S. Day, and J. F. Grcar. Numerical simulation of premixed turbulent methane combustion. *Proceedings of the Combustion Institute*, 29(2): 1987–1993, 2002.

[200] J. B. Bell, M. S. Day, J. F. Grcar, and M. J. Lijewski. A computational study of equivalence ratio effects in turbulent, premixed methane-air flames. In *Proc. ECCOMAS-CFD*, 2006.

[201] M. M. Ameen and J. Abraham. Are 2d dns results of turbulent fuel/air mixing layers useful for assessing subgrid-scale models? *Numerical Heat Transfer, Part A: Applications*, pages 1–13, 2015.

[202] S. Sreedhara and K. Lakshmisha. Autoignition in a non-premixed medium: Dns studies on the effects of three-dimensional turbulence. *Proceedings of the Combustion Institute*, 29(2):2051–2059, 2002.

[203] P. Tabeling. Two-dimensional turbulence: a physicist approach. *Physics Reports*, 362(1):1–62, 2002.

[204] J. C. McWilliams. The vortices of two-dimensional turbulence. *Journal of Fluid Mechanics*, 219(361-385):102, 1990.

[205] J. Miller. Statistical mechanics of euler equations in two dimensions. *Physical Review Letters*, 65(17):2137, 1990.

[206] L. Richardson. *Weather prediction by numerical process*. University Press, 1922.

[207] M. Lesieur. Turbulence in fluids: stochastic and numerical modeling. *NASA STI/Recon Technical Report A*, 91:24106, 1990.

[208] R. H. Kraichnan. Inertial ranges in two-dimensional turbulence. Technical report, DTIC Document, 1967.

[209] K. Bray and R. Cant. Some applications of kolmogorov's turbulence research in the field of combustion. In *Proceedings of the Royal Society of London A: Mathematical, Physical and Engineering Sciences*, volume 434, pages 217–240. The Royal Society, 1991.

[210] P. Pelce and P. Clavin. Influence of hydrodynamics and diffusion upon the stability limits of laminar premixed flames. *Journal of Fluid Mechanics*, 124: 219–237, 1982.

[211] M. Matalon and B. Matkowsky. Flames as gasdynamic discontinuities. *Journal of Fluid Mechanics*, 124:239–259, 1982.

[212] Z. Wang, E. Motheau, and J. Abraham. Effects of equivalence ratio variations on turbulent flame speed in lean methane/air mixtures under lean-burn natural gas engine operating conditions. *Proceedings of the Combustion Institute*, 36, 2016.

[213] G. Fru, D. Thévenin, and G. Janiga. Impact of turbulence intensity and equivalence ratio on the burning rate of premixed methane–air flames. *Energies*, 4 (6):878–893, 2011.

[214] R. Sankaran, E. R. Hawkes, J. H. Chen, T. Lu, and C. K. Law. Structure of a spatially developing turbulent lean methane–air bunsen flame. *Proceedings of the Combustion Institute*, 31(1):1291–1298, 2007.

[215] S. Thipse, S. Rairikar, K. Kavathekar, and P. Chitnis. Development of a six cylinder hcng engine using an optimized lean burn concept. Technical report, SAE Technical Paper, 2009.

[216] P. A. Atibeh, P. A. Dennis, P. J. Orbaiz, M. J. Brear, and H. C. Watson. Lean burn performance of a natural gas fuelled, port injected, spark ignition engine. Technical report, SAE Technical Paper, 2012.

[217] N. Chakraborty and N. Swaminathan. Influence of the damköhler number on turbulence-scalar interaction in premixed flames. i. physical insight. *Physics of Fluids (1994-present)*, 19(4):045103, 2007.

[218] A. M. Steinberg, J. F. Driscoll, and N. Swaminathan. Statistics and dynamics of turbulence–flame alignment in premixed combustion. *Combustion and Flame*, 159(8):2576–2588, 2012.

[219] T. Sponfeldner, I. Boxx, F. Beyrau, Y. Hardalupas, W. Meier, and A. Taylor. On the alignment of fluid-dynamic principal strain-rates with the 3d flamelet-normal in a premixed turbulent v-flame. *Proceedings of the Combustion Institute*, 35(2):1269–1276, 2015.

[220] V. L. Zimont. Gas premixed combustion at high turbulence. turbulent flame closure combustion model. *Experimental Thermal and Fluid Science*, 21(1): 179–186, 2000.

[221] E. R. Hawkes and J. H. Chen. Comparison of direct numerical simulation of lean premixed methane–air flames with strained laminar flame calculations. *Combustion and Flame*, 144(1):112–125, 2006.

[222] E. R. Hawkes, O. Chatakonda, H. Kolla, A. R. Kerstein, and J. H. Chen. A petascale direct numerical simulation study of the modelling of flame wrinkling for large-eddy simulations in intense turbulence. *Combustion and Flame*, 159 (8):2690–2703, 2012.

[223] Ö. L. Gülder and G. J. Smallwood. Inner cutoff scale of flame surface wrinkling in turbulent premixed flames. *Combustion and Flame*, 103(1):107–114, 1995.

[224] R. Knikker, D. Veynante, and C. Meneveau. A priori testing of a similarity model for large eddysimulations of turbulent premixed combustion. *Proceedings of the Combustion Institute*, 29(2):2105–2111, 2002.

[225] C. Fureby. A fractal flame-wrinkling large eddy simulation model for premixed turbulent combustion. *Proceedings of the Combustion Institute*, 30(1):593–601, 2005.

[226] N. K. Aluri, S. R. Muppala, and F. Dinkelacker. Substantiating a fractal-based algebraic reaction closure of premixed turbulent combustion for high pressure and the lewis number effects. *Combustion and Flame*, 145(4):663–674, 2006.

[227] A. R. Kerstein. Fractal dimension of turbulent premixed flames. *Combustion Science and Technology*, 60(4-6):441–445, 1988.

[228] G. North and D. Santavicca. The fractal nature of premixed turbulent flames. *Combustion Science and Technology*, 72(4-6):215–232, 1990.

[229] G. J. Smallwood, Ö. Gülder, D. R. Snelling, B. Deschamps, and I. Gökalp. Characterization of flame front surfaces in turbulent premixed methane/air combustion. *Combustion and Flame*, 101(4):461–470, 1995.

[230] Ö. Gülder, G. J. Smallwood, R. Wong, D. Snelling, R. Smith, B. Deschamps, and J.-C. Sautet. Flame front surface characteristics in turbulent premixed propane/air combustion. *Combustion and Flame*, 120(4):407–416, 2000.

[231] Y. Shim, S. Tanaka, M. Tanahashi, and T. Miyauchi. Local structure and fractal characteristics of h 2–air turbulent premixed flame. *Proceedings of the Combustion Institute*, 33(1):1455–1462, 2011.

[232] O. Chatakonda, E. R. Hawkes, A. J. Aspden, A. R. Kerstein, H. Kolla, and J. H. Chen. On the fractal characteristics of low damköhler number flames. *Combustion and Flame*, 160(11):2422–2433, 2013.

[233] T. Poinsot, D. Veynante, and S. Candel. Diagrams of premixed turbulent combustion based on direct simulation. In *Symposium (international) on Combustion*, volume 23, pages 613–619. Elsevier, 1991.

[234] W. L. Roberts, J. F. Driscoll, M. C. Drake, and L. P. Goss. Images of the quenching of a flame by a vortexto quantify regimes of turbulent combustion. *Combustion and Flame*, 94(1):58–69, 1993.

[235] M. Frenklach, H. Wang, C. Yu, M. Goldenberg, C. Bowman, R. Hanson, D. Davidson, E. Chang, G. Smith, D. Golden, W. Gardiner, and V. Lissianski. Gri-mech 2.1. URL `http://www.me.berkeley.edu/gri_mech/`.

[236] B. Karlovitz, D. Denniston, D. Knapschaefer, and F. Wells. Studies on turbulent flames: A. flame propagation across velocity gradients b. turbulence measurement in flames. In *Symposium (International) on Combustion*, volume 4, pages 613–620. Elsevier, 1953.

[237] M. Matalon. On flame stretch. *Combustion Science and Technology*, 31(3-4): 169–181, 1983.

[238] S. Pope. The evolution of surfaces in turbulence. *International Journal of Engineering Science*, 26(5):445–469, 1988.

[239] S. Candel, D. Veynante, F. Lacas, E. Maistret, N. Darabiha, and T. Poinsot. Coherent flamelet model: applications and recent extensions. *Recent Advances in Combustion Modelling*, 6:19–64, 1990.

[240] E. Hawkes and R. Cant. Implications of a flame surface density approach to large eddy simulation of premixed turbulent combustion. *Combustion and Flame*, 126(3):1617–1629, 2001.

[241] P. Clavin. Dynamic behavior of premixed flame fronts in laminar and turbulent flows. *Progress in Energy and Combustion Science*, 11(1):1–59, 1985.

[242] T. Echekki and J. H. Chen. Analysis of the contribution of curvature to premixed flame propagation. *Combustion and Flame*, 118(1):308–311, 1999.

[243] J. H. Chen and H. G. Im. Correlation of flame speed with stretch in turbulent premixed methane/air flames. In *Symposium (International) on Combustion*, volume 27, pages 819–826. Elsevier, 1998.

[244] N. Chakraborty, M. Klein, and R. Cant. Stretch rate effects on displacement speed in turbulent premixed flame kernels in the thin reaction zones regime. *Proceedings of the Combustion Institute*, 31(1):1385–1392, 2007.

[245] I. Han and K. Y. Huh. Roles of displacement speed on evolution of flame surface density for different turbulent intensities and lewis numbers in turbulent premixed combustion. *Combustion and Flame*, 152(1):194–205, 2008.

[246] N. Chakraborty, E. Hawkes, J. Chen, and R. Cant. The effects of strain rate and curvature on surface density function transport in turbulent premixed methane–air and hydrogen–air flames: A comparative study. *Combustion and Flame*, 154 (1):259–280, 2008.

[247] G. K. Giannakopoulos, A. Gatzoulis, C. E. Frouzakis, M. Matalon, and A. G. Tomboulides. Consistent definitions of flame displacement speed and markstein length for premixed flame propagation. *Combustion and Flame*, 162(4):1249–1264, 2015.

[248] C. Meneveau and T. Poinsot. Stretching and quenching of flamelets in premixed turbulent combustion. *Combustion and Flame*, 86(4):311–332, 1991.

[249] G. Hartung, J. Hult, C. Kaminski, J. Rogerson, and N. Swaminathan. Effect of heat release on turbulence and scalar-turbulence interaction in premixed combustion. *Physics of Fluids (1994-present)*, 20(3):035110, 2008.

[250] D. Haworth and T. Poinsot. Numerical simulations of lewis number effects in turbulent premixed flames. *Journal of Fluid Mechanics*, 244:405–436, 1992.

[251] N. Chakraborty and S. Cant. Unsteady effects of strain rate and curvature on turbulent premixed flames in an inflow–outflow configuration. *Combustion and Flame*, 137(1):129–147, 2004.

[252] B. Renou, A. Boukhalfa, D. Puechberty, and M. Trinité. Effects of stretch on the local structure of preely propagating premixed low-turbulent flames with various lewis numbers. In *Symposium (International) on Combustion*, volume 27, pages 841–847. Elsevier, 1998.

[253] R. Cant, S. Pope, and K. Bray. Modelling of flamelet surface-to-volume ratio in turbulent premixed combustion. In *Symposium (International) on Combustion*, volume 23, pages 809–815. Elsevier, 1991.

[254] A. Lipatnikov and J. Chomiak. Effects of premixed flames on turbulence and turbulent scalar transport. *Progress in Energy and Combustion Science*, 36(1): 1–102, 2010.

[255] A. Scurlock. *Flame stabilization and propagation in high-velocity gas streams*. PhD thesis, Massachusetts Institute of Technology, 1948.

[256] P. Moreau and A. Boutier. Laser velocimeter measurements in a turbulent flame. In *Symposium (International) on Combustion*, volume 16, pages 1747–1756. Elsevier, 1977.

[257] A. Gulati and J. Driscoll. Flame-generated turbulence and mass fluxes: effect of varying heat release. In *Symposium (International) on Combustion*, volume 21, pages 1367–1375. Elsevier, 1988.

[258] J. Driscoll and A. Gulati. Measurement of various terms in the turbulent kinetic energy balance within a flame and comparison with theory. *Combustion and Flame*, 72(2):131–152, 1988.

[259] R. Cheng and I. Shepherd. Intermittency and conditional velocities in premixed conical turbulent flames. *Combustion Science and Technology*, 52(4-6):353–375, 1987.

[260] R. Cheng. Conditional sampling of turbulence intensities and reynolds stress in premixed turbulent flames. *Combustion Science and Technology*, 41(3-4): 109–142, 1984.

[261] J. Furukawa, Y. Noguchi, T. Hirano, and F. A. Williams. Anisotropic enhancement of turbulence in large-scale, low-intensity turbulent premixed propane–air flames. *Journal of Fluid Mechanics*, 462:209–243, 2002.

[262] Y.-C. Chen and R. W. Bilger. Turbulence and scalar transport in premixed bunsen flames of lean hydrogen/air mixtures. *Proceedings of the Combustion Institute*, 28(1):521–528, 2000.

[263] S. Pfadler, A. Leipertz, and F. Dinkelacker. Systematic experiments on turbulent premixed bunsen flames including turbulent flux measurements. *Combustion and Flame*, 152(4):616–631, 2008.

[264] K. Bray and P. A. Libby. Interaction effects in turbulent premixed flames. *Physics of Fluids (1958-1988)*, 19(11):1687–1701, 1976.

[265] W. Jones and B. Launder. The calculation of low-reynolds-number phenomena with a two-equation model of turbulence. *International Journal of Heat and Mass Transfer*, 16(6):1119–1130, 1973.

[266] S. Zhang and C. J. Rutland. Premixed flame effects on turbulence and pressure-related terms. *Combustion and Flame*, 102(4):447–461, 1995.

[267] S. Nishiki, T. Hasegawa, R. Borghi, and R. Himeno. Modeling of flame-generated turbulence based on direct numerical simulation databases. *Proceedings of the Combustion Institute*, 29(2):2017–2022, 2002.

[268] N. Chakraborty, M. Katragadda, and R. S. Cant. Statistics and modelling of turbulent kinetic energy transport in different regimes of premixed combustion. *Flow, Turbulence and Combustion*, 87(2-3):205–235, 2011.

[269] N. Chakraborty and R. Cant. Effects of lewis number on turbulent scalar transport and its modelling in turbulent premixed flames. *Combustion and Flame*, 156(7):1427–1444, 2009.

[270] B. Launder, G. J. Reece, and W. Rodi. Progress in the development of a reynolds-stress turbulence closure. *Journal of Fluid Mechanics*, 68(03):537–566, 1975.

[271] K. Bray, M. Champion, and P. A. Libby. Premixed flames in stagnating turbulence part iv: a new theory for the reynolds stresses and reynolds fluxes applied to impinging flows. *Combustion and Flame*, 120(1):1–18, 2000.

[272] W. C. Strahle. Velocity-pressure gradient correlation in reactive turbulent flows. *Combustion Science and Technology*, 32(5-6):289–305, 1983.

[273] S. Pope and M. Anand. Flamelet and distributed combustion in premixed turbulent flames. In *Symposium (International) on Combustion*, volume 20, pages 403–410. Elsevier, 1985.

[274] K. Bray. Turbulent transport in flames. In *Proceedings of the Royal Society of London A: Mathematical, Physical and Engineering Sciences*, volume 451, pages 231–256. The Royal Society, 1995.

[275] A. Aspden, M. Day, and J. Bell. Turbulence–flame interactions in lean premixed hydrogen: transition to the distributed burning regime. *Journal of Fluid Mechanics*, 680:287–320, 2011.

[276] S. Lapointe and G. Blanquart. Fuel and chemistry effects in high karlovitz premixed turbulent flames. *Combustion and Flame*, 167:294–307, 2016.

LIST OF PUBLICATIONS

LIST OF PUBLICATIONS

Refereed Journal Publications

- Wang, Z. and Abraham, J., Effects of Karlovitz number on flame surface wrinkling in turbulent lean premixed methane-air flames. *In preparation.*

- Wang, Z. and Abraham, J., Effects of Karlovitz number on turbulent kinetic energy transport in turbulent lean premixed methane-air flames. *In preparation.*

- Wang, Z., Magi, V. and Abraham, J., Turbulent flame speed dependencies in lean methane-air mixtures under engine relevant conditions. *Submitted to Combustion and Flame, revision in preparation.*

- Wang, Z., Motheau, M. and Abraham, J., Effects of equivalence ratio variations on turbulent flame speed in lean methane/air mixtures under lean-burn natural gas engine operating conditions. *Proceedings of the Combustion Institute, in press.*

- Wang, Z. and Abraham, J., Fundamental physics of flame development in an autoigniting dual fuel mixture. *Proceedings of the Combustion Institute*, 35(1):1041-1048, 2015.

Conference Publications

- Wang, Z., Ameen, M., Som, S. and Abraham, J., Assessment of large-eddy simulations of turbulent round jets using low-order numerical schemes. *SAE World Congress 2017, submitted.*

- Wang, Z., Motheau, M. and Abraham, J., Equivalence ratio effects on turbulent premixed flames in lean methane/air mixtures. *Australian Combustion Symposium 2015*, Melbourne, Australia, Dec 2015.

- Wang, Z. and Abraham, J., Numerical simulations of turbulent premixed flames in lean methane/air mixtures. *10th Asian-Pacific Conference on Combustion*, Beijing, China, July 2015.

- Wang, Z., Scalo, C., Magi, V. and Abraham, J., Towards DNS of statistically stationary turbulent premixed flames in lean methane/air mixtures. *Proceedings of the 9th Joint Meeting of the US Sections of the Combustion Institute*, Cincinnati, Ohio, May 2015.

- Wang, Z. and Abraham, J., Ignition and flame development in mixing layers with applications to CI engines. *Proceedings of the 8th Joint Meeting of the US Sections of the Combustion Institute*, Salt Lake City, Utah, May 2013.

VITA

VITA

Zhiyan Wang was born in Wuhan, Hubei, China on September 9th, 1988. He studied in Raffles Institution and Raffle Junior College in Singapore for 6 years before coming to the States in 2007. He graduated from Vassar College with a Bachelor of Art degree with Higher Distinction and Subject Distinction in 2011 and a Bachelor of Engineering from Dartmouth College in 2012. He joined Purdue University in August 2012 to pursue graduate studies in Professor John Abraham's research group in the School of Mechanical Engineering. He also spent one semester at Argonne National Laboratory as a Research Aide in 2016. His work has focused on the autoignition in the dual-fuel mixtures and premixed flame propagation in the lean natural-gas mixtures. This work employed state-of-art simulation techniques, such as DNS, and has resulted in two archival journal publications, three journal paper submissions, four papers in conference proceedings and one conference paper submission.